



HAL
open science

QCD resummation in the light of the Run 3 of LHC

Yehudi Simon

► **To cite this version:**

Yehudi Simon. QCD resummation in the light of the Run 3 of LHC. Physics [physics]. Sorbonne Université, 2023. English. NNT: . tel-04452749v1

HAL Id: tel-04452749

<https://theses.hal.science/tel-04452749v1>

Submitted on 12 Feb 2024 (v1), last revised 12 Feb 2024 (v2)

HAL is a multi-disciplinary open access archive for the deposit and dissemination of scientific research documents, whether they are published or not. The documents may come from teaching and research institutions in France or abroad, or from public or private research centers.

L'archive ouverte pluridisciplinaire **HAL**, est destinée au dépôt et à la diffusion de documents scientifiques de niveau recherche, publiés ou non, émanant des établissements d'enseignement et de recherche français ou étrangers, des laboratoires publics ou privés.

**THÈSE DE DOCTORAT
DE SORBONNE UNIVERSITÉ**

Spécialité : Physique

École doctorale n°564: Physique en Île-de-France

réalisée

au Laboratoire de physique théorique et hautes énergies

sous la direction de Benjamin Fuks

présentée par

Yehudi SIMON

pour obtenir le grade de :

DOCTEUR DE SORBONNE UNIVERSITÉ

Sujet de la thèse :

Resommation en QCD à l'aune du Run 3 du LHC

soutenue le 14 Décembre 2023

devant le jury composé de :

Pr. Tilman Plehn	Rapporteur
Pr. J.A. Aguilar-Saavedra	Rapporteur
Pr. Anna Kulesza	Examinatrice
Dr. Eleni Vryonidou	Examinatrice
Pr. Bertrand Laforge	Président du jury
Pr. Benjamin Fuks	Directeur de thèse
Dr. Hua-Sheng Shao	Co-encadrant

Dans cette section, je voudrais remercier tout ce qui a rendu possible la rédaction et la défense de ce manuscrit.

Je tiens d'abord à remercier mes encadrants de thèse, Benjamin et Hua-Sheng. Bien évidemment, sans vous ce projet n'aurait pas été possible. Outre l'aide incommensurable que vous m'avez apportée, chacun à votre manière, je voulais vous remercier pour m'avoir permis de travailler sur ce sujet si passionnant. J'ai beaucoup appris durant ces trois années, tout n'a pas été facile mais j'ai toujours pu me raccrocher à la beauté et l'immense intérêt de ce domaine de recherche. Je ne sais pas si mon travail comptera pour la QCD mais il est certain que la QCD comptera toujours beaucoup pour moi.

J'aimerais ensuite remercier ma famille. Chacun pourra se reconnaître si je vous remercie collectivement pour ne pas "trop" m'avoir posé de questions délicates comme «Et la thèse ça se passe comment?». Je remercie en particulier mes parents pour avoir failli à leur rôle et m'avoir laissé m'engager dans une voie plus qu'incertaine et dépourvue de débouchés. Pire encore, vous avez su me soutenir dans mes choix (discutables) et me permettre de me sentir en sécurité. Sans votre inconscience je n'aurais pas pu m'épanouir autant, merci infiniment. Merci à ma petite sœur pour avoir réveillé mes vieux souvenirs de chimie et m'avoir fait goûter au travail non rémunéré, j'en aurai certainement besoin à l'avenir. Merci à mes grands parents pour être si parfaits, je ne trouve pas quel second degré pourrait rendre hommage à votre soutien indéfectible et la fierté que vous placez en moi.

Je voudrais également remercier tous les amis qui m'entourent aujourd'hui. J'ai la chance d'avoir gardé les amitiés de certains depuis de longues années désormais. Les relations plus récentes n'en sont pas moins fortes à mes yeux. Je tiens à remercier plus particulièrement tous les doctorants du LPTHE et toutes les partitions des divers ensembles dans le voisinage. En particulier les camarades de ma génération sont plus incroyables les uns que les autres. Merci Andriani pour tes réflexions, Wenqi pour ta confiance, Francesco (C) pour ton sourire, Max pour ton humour, Andrei pour être Andrei, Vincent pour ta pugnacité, Francesco (M) pour ton style inimitable, Pierre pour tes anecdotes et Simon pour tous nos échanges. Merci aussi à mes collègues de l'indéniable meilleur bureau du labo, Jordan, Greivin, Carlo, Grégoire, vous avez rendu mon quotidien meilleur. Je n'oublie pas les personnes incroyables que sont Yann, Anthony, Diyar, Mathis, Léo, Tom, Jules. Je ne peux pas conclure ce paragraphe sans mentionner mes amis de l'ENS Cachan. En particulier les autres membres du Trimôme, merci Corentin et Manon, je vous dois beaucoup et plus encore, vous le savez. Enfin je voudrais remercier Thierry sans lequel je ne serais pas celui que je suis devenu aujourd'hui et sans lequel cette thèse n'aurait pas vu le jour.

Contents

0	Introduction	5
1	Perturbative Quantum Chromodynamics	15
1.1	QCD features	17
1.1.1	α_s renormalisation group running	17
1.1.2	The parton model	19
1.2	Parton Distribution Functions and factorisation	19
1.2.1	Factorisation theorem	19
1.2.2	Dokshitzer–Gribov–Lipatov–Altarelli–Parisi equations	20
1.2.3	LHAPDF for practical use	27
1.3	Colour Algebra	29
1.3.1	Colour tensor basis	29
1.3.2	Minimal set of colour factors	33
1.3.3	Expression in colour tensor basis	36
2	Soft gluon threshold resummation	38
2.1	Leading logarithm and exponentiation	40
2.1.1	Eikonal approximation and soft gluon emission	40
2.1.2	Factorisation and Mellin transform	42
2.1.3	Toy resummation	43
2.1.4	Power counting	46
2.2	General expression	47
2.2.1	Total cross section and PDF factorisation	47
2.2.2	Partonic cross section and Hard/Soft factorisation	49
2.3	Colour matrices	52
2.3.1	Soft matrix	52
2.3.2	Soft anomalous dimension matrix	56
2.3.3	Beam functions	60
2.3.4	Hard matrix	61

2.4	General expression and implementation	63
2.4.1	Resummation formula	63
2.4.2	Implementation of PDFs	63
2.4.3	Physical result in direct space	66
3	Drell-Yan like processes: VLL & Seesaw	69
3.1	BSM and exotic leptons searches	71
3.2	Theoretical models and their implementation	72
3.2.1	A simplified model for VLL phenomenology	72
3.2.2	An effective Type-III seesaw Lagrangian	75
3.2.3	From Lagrangian to events at the LHC	79
3.3	Improving theory accuracy beyond NLO: threshold resummation	80
3.4	Cross sections for extra lepton production at the LHC	82
3.4.1	Total cross sections at the LHC	82
3.4.2	Invariant mass distributions	86
3.4.3	Transverse momentum spectra	90
3.5	Conclusion	91
4	Colourful processes: top pair(s) production	93
4.1	Pair production: $pp \rightarrow t\bar{t}$	95
4.1.1	Absolute threshold <i>vs</i> invariant mass threshold	95
4.1.2	Differential cross section	96
4.2	Increasing multiplicity: $pp \rightarrow t\bar{t}t\bar{t}$	99
4.2.1	NLO prediction	100
4.2.2	Feynman diagrams and partonic channels	100
4.2.3	Colour Basis	101
4.2.4	Soft function and anomalous dimension	103
4.2.5	Resummation results	103
5	Conclusion	106
A	Appendix	111
A.1	Lagrangian and Feynman rules	113
A.1.1	Lagrangian	113
A.1.2	Feynman rules	113
A.2	SU(N_c) colour algebra	114
A.2.1	SU(N_c) relations	114

A.2.2	Colour Factors	115
A.3	Spinors and polarisation tensors	115
A.4	PDF Evolution	116
A.4.1	Decoupling, singlets and non-singlet states	117
A.4.2	Evolution operators	118
A.5	Mellin transform	120
A.5.1	Miscellaneous	120
A.5.2	Splitting kernels	122
A.6	Subtraction method	123
A.7	Soft and Anomalous dimension color matrices	124
A.7.1	Soft color matrix	125
A.7.2	Soft anomalous dimension color matrix	125
A.8	Sudakov factor	126
A.8.1	Derivation	126
A.8.2	Expansion $\mathcal{O}(\alpha_s)$	131
A.8.3	Collinearly improved resummation	131
A.9	Resummation coefficients	132
A.10	Four top production tree level diagrams	135
A.10.1	Quark channel	135
A.10.2	Gluon channel	135

B Bibliography **136**

List of Tables

2.1	SCET power counting	47
2.2	Eikonal coefficients Ω	54
3.1	VLL gauge eigenstates	74
3.2	VLL mass eigenstates	74
3.3	VLL couplings	75
3.4	Type-III seesaw gauge eigenstates	78
3.5	Type-III seesaw mass eigenstates	78
3.6	Type-III seesaw parameters	79

Table of Figures

1	ATLAS Experiment at CERN, 1 st collision of Run 3	7
2	Illustration of the elementary particles of the Standard Model	9
3	ATLAS preliminary summary of SM data/theory comparison [5]	10
4	Example of generic loop diagrams for 0, 1 and 2 loops	11
5	ATLAS preliminary summary of top physics [25]	13
1.1	α_s running fit to various data [10]	18
1.2	LHAPDF CT18NLO set [49] displayed for $\mu_F = 10$ GeV	28
2.1	Ratio of direct and inverse Mellin transformed fits to CT18NLO gluon PDF	65
2.2	N integration path for the inverse Mellin transform	66
3.1	Total cross sections for the production of charged leptons typical from VLL and Type-III seesaw models	84
3.2	Total NLO+NNLL cross sections for the production of VLL and Type-III seesaw leptons	85
3.3	Invariant mass spectrum of VLL pair production	87
3.4	Invariant mass spectrum for Type-III seesaw leptons pair production	88
3.5	Transverse momentum spectrum for VLL pair production	89
3.6	Transverse momentum spectrum for Type-III seesaw lepton pair production	91
4.1	(M^2, \hat{s}) phase space and different threshold regions	96
4.2	Resummation scale uncertainty reduction	97
4.3	Resummation(s) compared to ATLAS data	98
4.4	Fixed order MG5AMC output	99
4.5	Four top NLL matched to NLO differential cross section, $\mu_0 = M/4$	103
4.6	Four top NLL matched to NLO differential cross section, $\mu_0 = M/2$	104

0

Introduction

It doesn't matter how beautiful your theory is, it doesn't matter how smart you are. If it doesn't agree with experiment, it's wrong

Richard Feynman



Cosmic Spring, 1913-1914, František Kupka

THIS preliminary chapter allows us to give an introduction to the subject of this document. After providing a brief overview of the physical model on which particle physics is based, we review the state of the art in theoretical predictions before introducing Quantum Chromodynamics. In the next chapters we will focus in more detail on Quantum Chromodynamics and resummation techniques in the context of soft gluon threshold resummation. The final chapters provide physical results of cross sections related to BSM searches or top pair(s) production.

The main purpose of physics is to understand, describe and predict the behaviours realised in Nature. The first step of the physicist is to observe, to be amazed by the productions of Nature. Without this first ontological look there is no physics.

Naturally, we strive to apprehend the essence of the phenomena and decipher the underlying mechanisms at work. To this effect, experiments are indispensable on the journey towards physical knowledge as they emulate the phenomenon we are examining. Experiments are the embodiment of our understanding of Nature, as well as tools to deepen our knowledge. As a theoretical physicist, it is more the theoretical framework, the mindset that we build to look at Nature in a humanly understandable way, that I will insist on. Before proceeding, I must reiterate the paramount importance of observation in physics which is more connected to experimentation than theories.

Particle physics offers a unique opportunity to unveil a plethora of new phenomena that would be otherwise unattainable. In this context, physics is itself unveiling our eyes to look at its complex and beautiful ramifications.

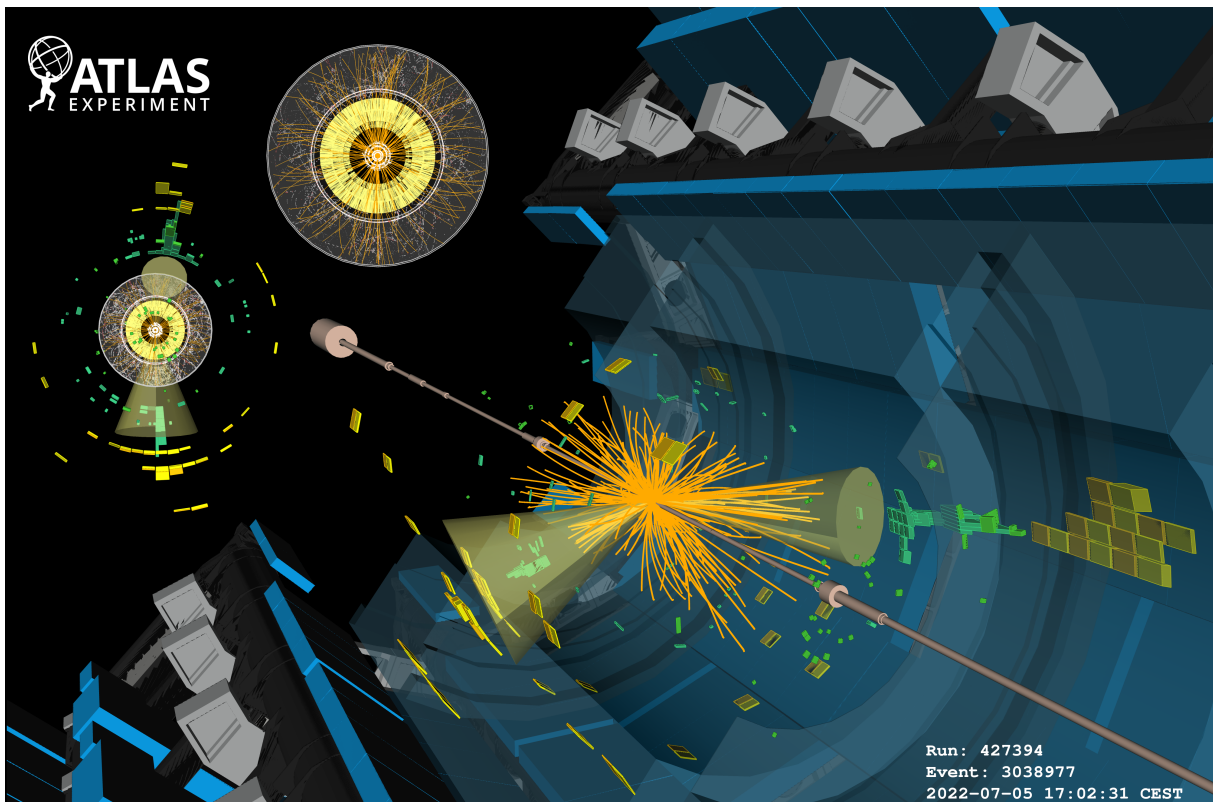


Figure 1: ATLAS Experiment at CERN, 1st collision of Run 3

One of the primary objectives of physics (and chemistry) is to describe the elementary constituents of the universe. Since the end of the XVIIIth century, various classifications have been proposed in order to rationally describe the elements present in Nature. From

Lavoisier to Mendeleev and Chancourtois, the systematization of classification has been pushed further and further. The elegance of the modern periodic table of the elements lies in the fact that it encapsulates the periodic laws of chemical behaviour and predicts those of elements yet to be discovered.

However, at the beginning of the XXth century, the discovery of the electron opened the way to a new kind of classification. As chemistry reaches its limits, particle physics takes over: the chemical elements are no longer elementary!

To uncover and comprehend the fundamental elements of Nature, we must crack the unbreakable *atoms* and search for the elementary particles.

Through the Planck-Einstein relation, it is known that energy scales inversely with wavelength or spatial dimension:

$$E = h\nu = \frac{hc}{\lambda} . \quad (1)$$

In natural units with $\hbar = c = 1$, the dimension of energy is simply the inverse of the wavelength. This dimensional analysis reveals that to investigate increasingly small spatial scales, we will have to use increasingly large energies.

Thanks to technological advancements in the latter half of the XXth century both in colliders technology and cosmic rays detection, and the subsequent exploration of a wider range of energies, numerous new particles were discovered. Substantial efforts were made to construct a model that defines the behaviour and interactions of elementary particles, now known as the Standard Model (SM) of particle physics [1–4]. The SM not only classifies the building blocks of matter but also presents a Lagrangian theory describing their interactions. In figure 2, the elementary particles of the SM are shown, with their properties encoded in graphical representations. The fermions are arranged by family on the left-hand side, with leptons located at the bottom and quarks at the top. Vector bosons can be found to the right, with the Higgs boson occupying the central position in the illustration. The electric charge is represented by plain blue (red) colour for negative (positive) charges respectively. Additionally, we can observe that the quarks on the left and the gluon on the right exhibit some internal colour, representing the colour charge that we will discuss later in this introduction. Apart from its particle content, the Standard Model is largely successful in predicting various phenomena. Its unparalleled accuracy in predictions across different orders of magnitude makes it an exceptional achievement in physics. Figure 3 outlines several predictions and measurements from ATLAS [5] in relation to the SM. Figure 3 shows the diverse range of phenomena investigated within particle physics, spanning a wide range of orders of magnitude. We do not claim to be exhaustive here, but rather illustrate the predictive power of the SM. We can also note that in the lower part of the plot, where the cross sections become smaller than 1 pb, the error bars tend to become quite large as the measurements are more and more difficult to perform.

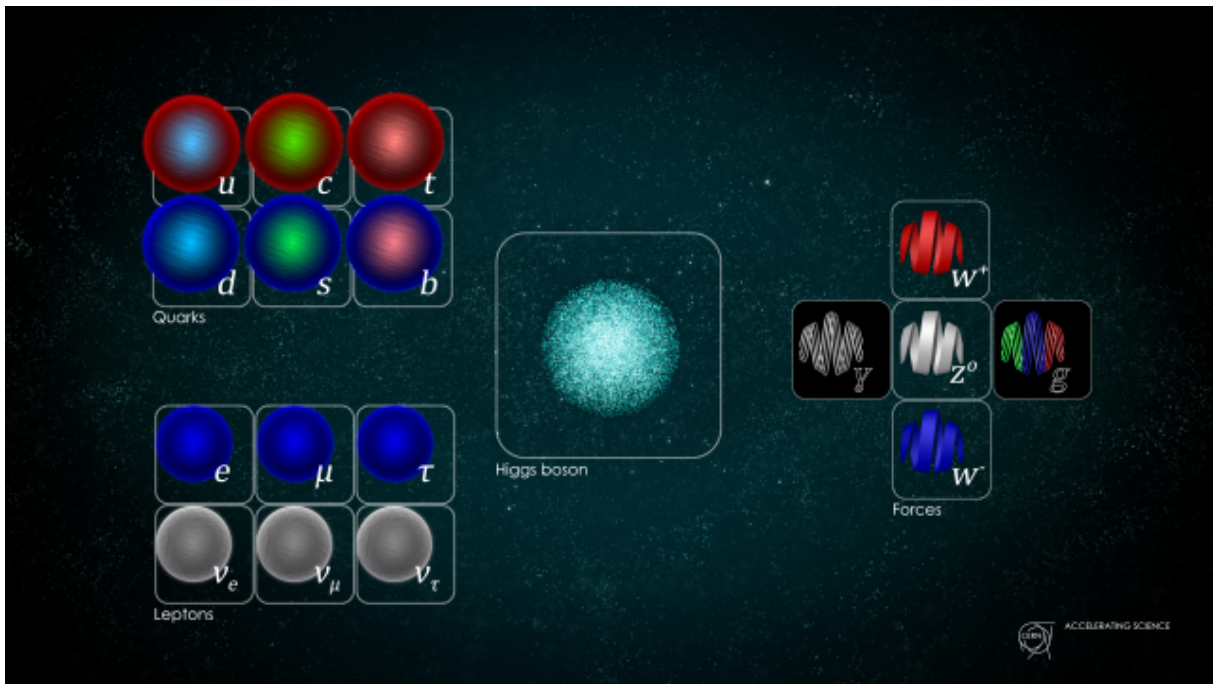


Figure 2: Illustration of the elementary particles of the Standard Model
<https://home.cern/fr/science/physics/standard-model>

However, as good as a theory can be, it never holds the absolute truth. While we physicists search for evidence to falsify the SM and uncover hints of New Physics (NP) beyond the Standard Model (BSM), we must also acknowledge its theoretical limitations. By excluding gravitation alone, we know that the SM is not a complete theory. It must rather be recognized as an effective theory with relevance limited to a particular energy range. In addition, within the current energy range, numerous questions remain unanswered, including the unnatural hierarchy between the electroweak and the Planck scales, the origins of electroweak symmetry breaking, particle masses or the nature of dark matter. Although there is certainty that BSM physics exists, its discovery still eludes us. However, there are two predominant strategies for searching for NP, each with its own advantages and disadvantages.

- Direct searches → increase the energy scale. Increasing the energy scale is expected to reveal new phenomena and possibly detect deviations from the SM, like hints of supersymmetry, compositeness of Higgs. The hadron-hadron Future Circular Collider [6,7] (FCC-hh) project would be designed for this purpose, with an expected increase in available energy by a factor of 7 compared to the Large Hadron Collider (LHC). This would allow to probe the $\mathcal{O}(10)$ TeV range for the masses of potential new particles, including new Z' weak boson, excited quark states Q^* or massive gravitons. However, it presents significant material, and human resources costs [8].

Standard Model Production Cross Section Measurements

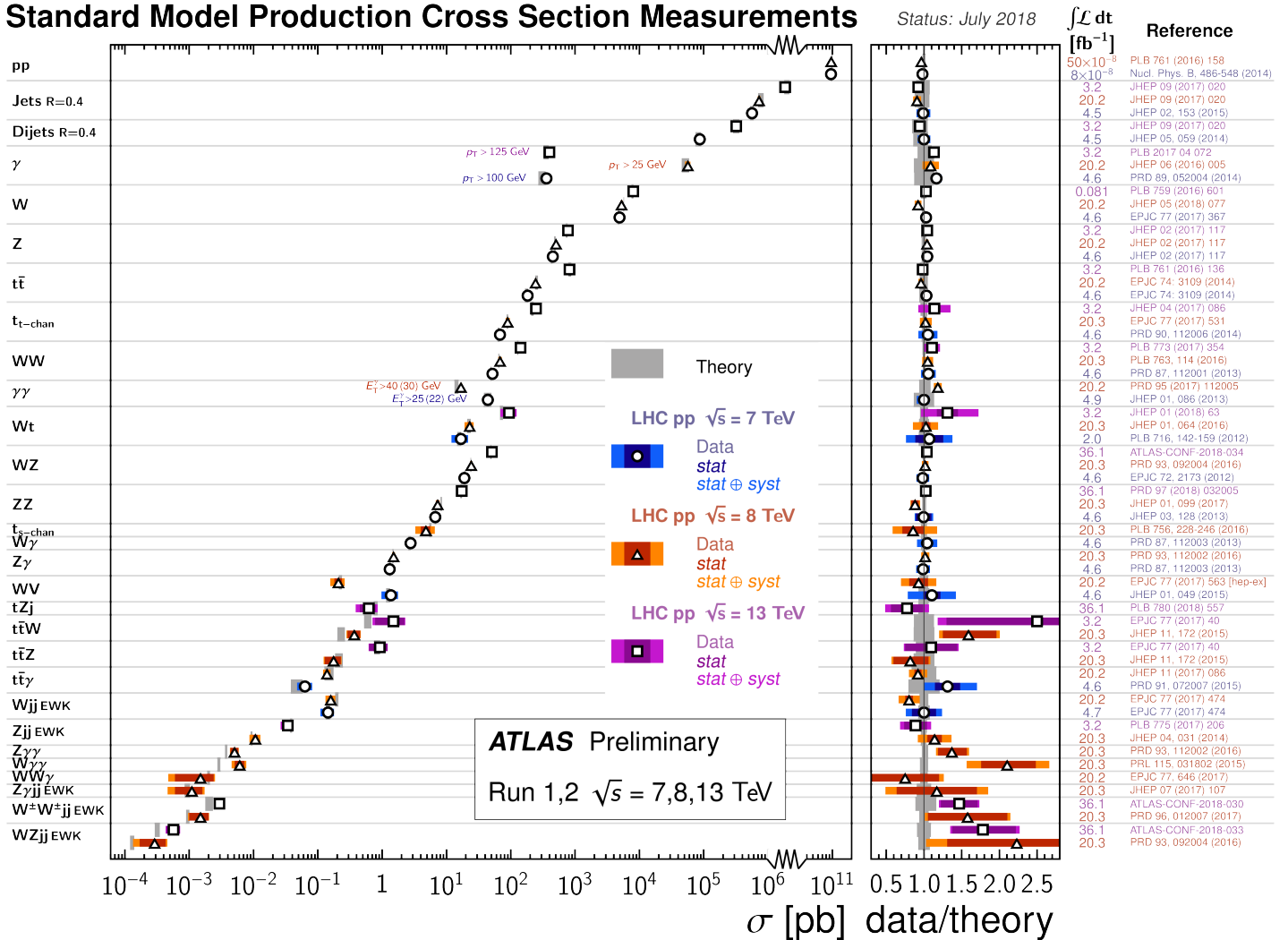


Figure 3: ATLAS preliminary summary of SM data/theory comparison of total cross sections for several observed processes [5]

- Indirect searches → increase the precision. It is possible that we are already capable of detecting new physics within the present energy range. However, separating SM from BSM contributions requires a high accuracy both on the theoretical and experimental sides. The High Luminosity LHC [9] will be crucial in achieving this, as it is expected to increase the integrated luminosity by a factor of 10 compared to the LHC, over the course of its operation. This results in significantly improved statistics, thereby reducing statistical error. Achieving such high trigger rates, data collection, and processing present a technical challenge. The electronic part of the FCC project (FCC-ee) would also go in this direction with the precision program. For example, it would explore the Higgs cross section in great depth and improve measurements by orders of magnitude in precision.

Given the scale at stake, it seems that if the NP materialises solely around the Planck scale $E_P = \sqrt{c^5 \hbar / G} \simeq 10^{28}$ eV, it is likely to remain beyond the reach of human experiments. Nevertheless, even without going to very high energies, we can have a contribution from higher energy scales through virtual loops, with Feynman diagrams such as in figure 4.

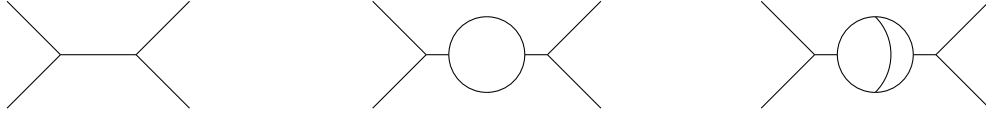


Figure 4: Example of generic loop diagrams for 0, 1 and 2 loops

Indeed, to calculate physical observables in particle physics (such as the cross section), we use an asymptotic expansion in terms of the relevant couplings that arise in the process. If this progression quickly converges, we can limit the expansion to a certain order to ultimately provide a prediction. Diagrammatically, this means that we stop the computation at a certain loop order: 0 for tree level or Leading Order (LO), 1 for Next-to-Leading Order (NLO), and so on. The particles appearing in these loops are not observable, hence the virtual adjective, and can involve states inaccessible otherwise.

It is assumed that each order has a smaller impact than the preceding one, and the truncated series offers a reasonable estimate of the actual value from the theory. The truncation of the asymptotic expansion introduces theoretical uncertainties due to the missing higher orders. The more orders are included the smaller the theoretical uncertainties are expected to be. As we will discuss in section 2.4.3, these theoretical uncertainties are usually evaluated by varying the arbitrary scales introduced by the truncation, see section 1.1.1 for more details. Parton distribution functions (see section 1.2) uncertainties are sometimes included in theoretical uncertainties but in this document we will not consider them and focus only on scale variation induced error bars. As we can see in figure 3, most of the theory predictions reach the $\mathcal{O}(1\%)$ precision level. However for some rare processes, theory still display quite large error bars, above $\mathcal{O}(10\%)$ uncertainty as the right hand side of figure 5.

Incorporating loop terms results in the inclusion of certain virtual contributions in the calculation. The unobservable particles emerging in these loops actually have an impact on the result, and their contribution depends on their inherent properties (mass, charge, spin...). Let us assume the existence of a highly massive particle in some NP spectrum. If it is coupled to the SM particles, this loop contribution could lead to a significant deviation from the SM predictions. Therefore, indirect detection necessitates precise experimental measurements and accurate theoretical predictions of the observables, so that we can identify any deviation from pure SM physics.

From an experimental perspective, this results in a race for precision (both systematic and statistical). On the theoretical side, there is a striving towards accuracy and precision in predictions, involving increasingly intricate calculations. This thesis is inscribed in this

context. We aim to provide accurate and precise predictions for both SM observables and BSM searches. Increasing the SM prediction precision would be useful in the context of indirect detection when searching for discrepancies between theory and experiments. For BSM searches, it is important to have an expectation of a potential signal in a direct detection scenario. Precise predictions also allow to reject BSM models if the experiments have a negative result in a signal region.

In the following paragraph, we review the current status of SM predictions. Section 9 of [10] provides an extensive review of fixed-order predictions, from which we extract a few key points as an illustration.

Firstly, we present the fixed-order predictions, *i.e.* calculations with α_s contributions treated up to a certain fixed-order in perturbation theory. As reported in [10], most of the hadron collider $2 \rightarrow 1$ and $2 \rightarrow 2$ processes have been computed at N²LO: $pp \rightarrow ZZ$ [11], W^+W^- [12], $\gamma\gamma$ [13], $Z\gamma$ [14], $\gamma/W/Z/H+\text{jet}$ [15–17], $t\bar{t}$ [18–20], *etc.*

For (di-)Higgs production or Drell-Yan processes, predictions can go up to N³LO [15, 21]. On the contrary, as the multiplicity of the final state increases, the fixed-order predictions available tend to include fewer orders, as the complexity increases dramatically. For example, $2 \rightarrow 3$ processes like 3γ [22], 3 jets [23] or $2\gamma + \text{jet}$ [24] are known at N²LO.

While increasing the loop order can be very difficult, requiring years of process-specific technical development, another approach is to use resummation techniques. Further detail on resummation will be provided in chapter 2. However, we take this opportunity to examine the current state of the art in this section. Without delving into too much detail, resummation aims to improve predictions without requiring an additional loop order. Numerous resummation methods have been developed, depending on both the observable and the regime of interest [26–28]. Nevertheless, it is always assumed that certain scale ratios manifest themselves in the observable expansion at a fixed-order. In regimes where the ratios are significant, they tend to spoil the asymptotic convergence of the series. For instance, the resummation of transverse momentum q_T treats logarithmic terms like $\ln M^2/q_T^2$ in the small (compared to the invariant mass M) q_T region, while threshold resummation handles terms such as $\ln(s - M^2)/(s - M^2)$ when M goes to the center of mass energy \sqrt{s} , and so on. Resumming such kind of terms to all orders through exponentiation can remedy the pathological behaviour of fixed-order prediction and improve the final result.

The $pp \rightarrow t\bar{t}\bar{t}\bar{t}$ process provides a clear example of the benefits of resummation. This high multiplicity process is only known at NLO, due to the extremely complex nature of the N²LO calculation. Experimentally, this process has only recently been measured [29, 30] around 20 fb and has still quite large error bars of the order of $\pm 25\%$. Including only NLO, the theoretical prediction is precise at the $\mathcal{O}(25\%)$ level for a total cross section around 12 fb. However, it is possible to improve the theoretical prediction as in [31], by including threshold resummation at NLL accuracy and gain an order of magnitude in precision.

Top Quark Production Cross Section Measurements

Status: September 2023

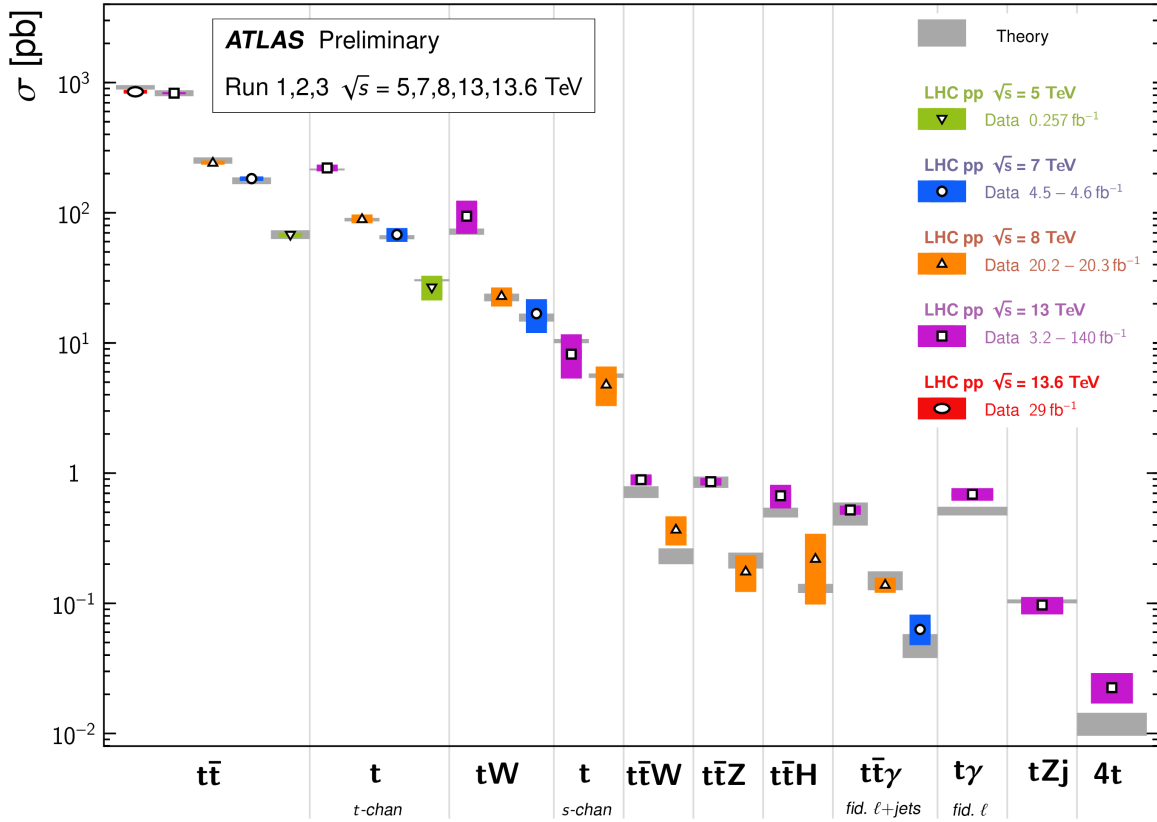


Figure 5: ATLAS preliminary summary of top physics, the cross section is displayed on the right axis and the corresponding process on the bottom axis [25]

This is especially relevant for top physics, as it is a sector of interest for both SM and BSM searches. Figure 5 outlines the present situation regarding top sector predictions and measurements. The considerable uncertainty associated with four-top production is apparent from both the theoretical and experimental sides. Moreover, there is a slight tension between the prediction and the measurement, so it is of paramount importance to increase the precision to validate or dismiss any discrepancies. Even in the case of processes such as Higgs production known at high-order, the precision of predictions can be improved through resummation techniques, as demonstrated in [32–34] up to next-to-next-to-next-to-leading logarithmic (N³LL) accuracy.

As we can note from the review in [10], high-order corrections are calculated using Quantum Chromodynamics (QCD) even in cases where the tree-level process is purely electro-weak. It could seem counter intuitive that we need QCD to make accurate predictions for processes involving only non-coloured particles in the final state. However, as previously discussed, loop contributions may result in contributions of particles that are not present at tree-level. Furthermore, within the context of LHC physics, proton collisions induce

parton-initiated processes, which means that the initial particles are always coloured. To better understand why these contributions are important, let us look more closely at QCD, which will be our focus throughout this document.

QCD characterises the strong interaction which binds quarks and gluons inside hadrons. This force introduces a new quantum number called “colour” carried by the particles sensitive to the strong interaction. The main observation about QCD is that it does indeed describe the strongest interaction of the Standard Model. One way to illustrate this is to evaluate the ratio of the coupling “constants”, α_s for QCD, and α for QED, at the mass of the Z boson:

$$\frac{\alpha_s(m_Z)}{\alpha(m_Z)} \approx 0.118 \cdot 128 \approx 15.1 \gg 1, \quad \alpha_s = \frac{g_s^2}{4\pi}, \quad (2)$$

where g_s is the coupling appearing in the QCD Lagrangian (A.3). Therefore, when studying particles sensitive to the effects of this interaction, QCD is likely to be the dominant contribution. As a result, it is crucial to consider the inclusion of QCD effects when predicting observables for hadron collision, as it is the case in LHC physics.

QCD has numerous notable traits beyond its magnitude. One such feature arises from the underlying non-Abelian group $SU(N_c)$ ($N_c = 3$), namely the gluon self-coupling (see A.6). We postpone the discussion on the group theory details of $SU(N_c)$ to the section 1.3 and the appendix A.2.

Another aspect worth mentioning is confinement [35]. It is impossible to directly observe the colour charge of a single coloured particle. Experimentally, we can only access particles that are neutral in terms of colour charge, whether they are bound states or colourless elementary particles. Gluons and quarks are confined within hadrons at low-energy scales and cannot display their charge, unlike electrons and the nucleus in atoms. Nonetheless, we can have access to the internal structure of hadrons at high energy with experiments such as deep inelastic scattering (DIS). Indeed, asymptotic freedom [3] allows to consider coloured particles individually in the context of hard scatterings, as detailed in chapter 1. The aim of this chapter 1 is to provide the key QCD concepts at the foundation of perturbative computations.

However, our work does not aim to compute higher orders to improve the available fixed-order predictions. Instead, we have implemented soft gluon threshold resummation, using the framework presented in detail in chapter 2, to improve the precision of some current fixed-order predictions. Chapter 3 presents the results obtained using this approach for the pair production of exotic leptons arising in different BSM models. In chapter 4 we continue this investigation by studying processes involving massive coloured final states of the top sector. First, we recover results similar to those found in the literature for top pair production, before presenting preliminary results on the application of soft gluon resummation to four top production process.

1

Perturbative Quantum Chromodynamics

Summary

1.1	QCD features	17
1.1.1	α_s renormalisation group running	17
1.1.2	The parton model	19
1.2	Parton Distribution Functions and factorisation	19
1.2.1	Factorisation theorem	19
1.2.2	Dokshitzer–Gribov–Lipatov–Altarelli–Parisi equations	20
1.2.3	LHAPDF for practical use	27
1.3	Colour Algebra	29
1.3.1	Colour tensor basis	29
1.3.2	Minimal set of colour factors	33
1.3.3	Expression in colour tensor basis	36

The force is strong in this one
Master Yoda



A.I. (DALL.E) generated image for colour flux

IN this chapter, we shift our focus to the most colourful part of the Standard Model: Quantum Chromodynamics (QCD). Indeed, QCD characterises the strong interaction, which binds the quarks and gluons inside the hadrons. This force introduces a new quantum number known as colour, carried by particles sensitive to the strong interaction. Throughout this chapter, we consider some key aspects of QCD, shedding light on coloured particles and how they interact. This leads us to consider the running of the strong coupling, the parton model and the corresponding parton distribution functions. Finally, we discuss a few points on the underlying $SU(3)$ group theory and tensor space, necessary to describe high energy scattering processes. The material presented in this chapter is mainly based on [10, 35–39] refer directly to chapters 3 and 4 for original results.

1.1 QCD features

We overviewed a few characteristics of QCD in introduction. In this section we provide more details on the QCD coupling α_s and its renormalisation group running. Subsequently, we introduce the parton model, a key concept at the basis of the perturbative QCD computations.

1.1.1 α_s renormalisation group running

Indeed, α_s is not constant and depends on the energy scale we are considering. The renormalisation group running of the coupling is not unique to the QCD case: it follows from the fact that the perturbative approach contains infinities that need to be renormalised. The renormalisation procedure introduces an arbitrary scale dependence μ_R for the coupling. Thus, we have the following renormalisation group equation (RGE) imposing the running of the renormalised α_s with the scale μ :

$$\frac{d\alpha_s(\mu)}{d \ln(\mu^2)} = \beta(\alpha_s) = -\alpha_s \sum_{k=0} \beta_k \left(\frac{\alpha_s}{2\pi} \right)^{k+1}, \quad (1.1)$$

where β_k are the $(k+1)$ -loop β function coefficients. Their actual value depends on the particle content of the theory. In this document, we restrict ourselves to the modified minimal subtraction scheme ($\overline{\text{MS}}$) [40] for renormalisation. We can formally solve (1.1) order by order:

$$\frac{\alpha_s(\mu)}{2\pi} = \sum_{k=0} \left(\frac{\alpha_s(\mu_R)}{2\pi} \right)^{k+1} g_k(\alpha_s(\mu_R), \mu, \mu_R, \{\beta_i\}_{i \leq k}), \quad (1.2)$$

where the g_k functions depend on the initial and final scales and the β coefficients up to $(k+1)$ -loop. The computations of β_k and g_k are completely decoupled, the latter being just functional forms to be determined order by order and parametrised by the β_k coefficients. Here are the results up to two-loop order (see [41] for more terms):

$$\begin{aligned} \beta_0 &= \frac{11}{6}C_A - \frac{2}{3}T_F n_f, & g_0(x) &= \frac{1}{x}, & \text{with } x(\mu) &= 1 + \frac{\alpha_s(\mu_R)}{2\pi} \beta_0 \ln \left(\frac{\mu^2}{\mu_R^2} \right), \\ \beta_1 &= \frac{17}{6}C_A^2 - \frac{1}{3}T_F n_f (5C_A + 3C_F), & g_1(x) &= \frac{\beta_1 \ln(x)}{\beta_0 x^2}, \end{aligned} \quad (1.3)$$

with the $\text{SU}(N_c)$ group theory invariants:

$$C_F = \frac{N_c^2 - 1}{2N_c} \underset{N_c=3}{=} \frac{4}{3}, \quad C_A = N_c \underset{N_c=3}{=} 3, \quad T_F = \frac{1}{2}. \quad (1.4)$$

From the previous results, we can conclude that, for a number of active quark flavours $n_f \leq 16$, the one-loop coefficient $\beta_0 > 0$, which ensures $\beta(\alpha_s) < 0$. Since, in the Standard

Model, there are at most $n_f = 6$ quark flavours available, the condition is always satisfied. In this document, we consider that $n_f = 5$. Indeed, the top flavour is too heavy to be considered massless compared to typical LHC energy scales. The sign of the QCD β function, different from that of QED, is the origin of asymptotic freedom [42]. Namely, at asymptotically large momentum exchange, the effective coupling vanishes, $\alpha_s \rightarrow 0$. Figure 1.1 displays a summary [10] of the current measurements of $\alpha_s(Q)$, showing the decrease of the coupling with the energy scale Q .

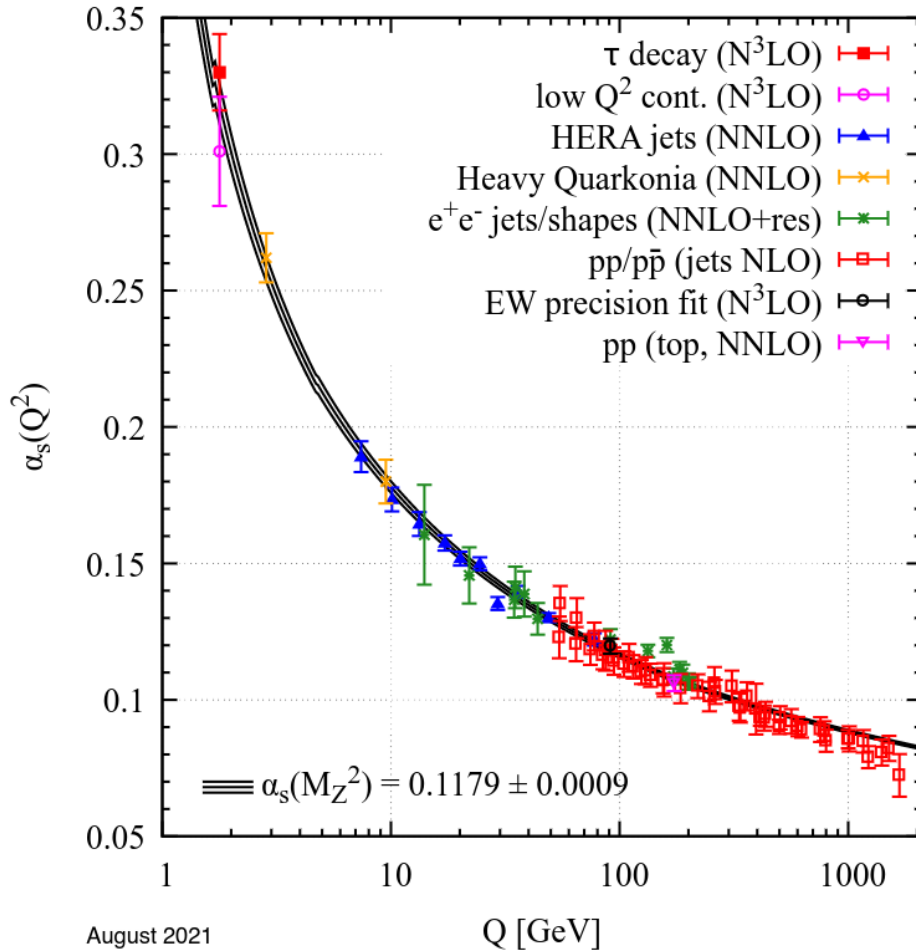


Figure 1.1: α_s running fit to various data [10]

From the low- Q region of the plot, it is clear that the coupling becomes larger and larger as we decrease the energy scale, ultimately leading to the break down of the perturbative approach as α_s gets close to 1. The energy scale below which the perturbative theory ceases to make sense is $\Lambda_{\text{QCD}} \approx 200$ MeV. On the contrary in the high- Q region, the plot illustrates the asymptotical freedom that allows to consider coloured particles individually at high energies. As shown in the following section, the parton model is particularly helpful to study the specific behaviour of these particles.

1.1.2 The parton model

Originally introduced by Feynman [43], the parton model aims to describe the components of hadrons and characterise their properties through their interaction with light. Although it has been introduced quite independently from the quark model of Gell-Mann and Zweig [44, 45] (almost a decade later), partons were quickly identified as the quarks and gluons inside hadrons. If, in principle, we can apply the parton model to QED, electrons and photons [46], when referring to partons we mostly have in mind coloured particles.

Partons are virtual states constituting the hadrons, held together by their mutual interactions. The complete structure of these states is inaccessible to an external observer. However, in the case where we can neglect the parton-parton interactions, we can describe their scattering with an external particle. Careful readers would recognise the QCD features mentioned in the previous section: confinement and the non-perturbative low-energy regime, asymptotic freedom and the potential perturbative approach at high energies.

As in [36], we can intuitively understand these features as the effect of Lorentz boosts inside the hadron. Indeed, in the centre-of-mass frame, if a high-energy particle exchanges a substantial amount of momentum with a hadron, the hadron contracts in the direction of the collision, while its internal interactions are time-dilated. As a result, the lifetime of the virtual states, the partons, increases, while the time required for the high-energy particle to travel through the hadron decreases. At a certain energy threshold, the hadron’s parton composition appears effectively immobilised to the high-energy particle, allowing it to scatter with a single parton that has well-defined properties. Indeed, the time for scattering is considerably shorter than the time scale associated with the parton-parton interaction. In this regime, partons cannot exchange momentum with anything else than the probing particle and can be considered as free particles. Thus, we can define distributions describing the momentum carried by a parton. These so-called “parton distribution functions” (PDFs) are a key ingredient for perturbative QCD computations, as we will see in section 1.2.

1.2 Parton Distribution Functions and factorisation

1.2.1 Factorisation theorem

The most important consequences of the parton model are the factorising properties emerging from it. Due to the significant differences in the physical time scales governing parton interactions and scattering, there is no quantum interference between them. Therefore, it is possible to combine probability densities in place of amplitudes. Thus, the hard

scattering between the hadron H and the particle λ can be written at the differential level at scale μ_F as [36]:

$$d\sigma_{\lambda H}(x, Q^2, \mu_F) = \sum_a \int_x^1 d\xi f_{a/H}(\xi, \mu_F) d\hat{\sigma}_{\lambda a}(Q^2, x/\xi, \mu_F), \quad (1.5)$$

where $x = Q^2/2p_H \cdot p_\lambda$ is the Bjorken variable, Q the momentum transfer, p_H and p_λ are the respective momenta of the hadron and the high-energy particle. $f_{a/H}(\xi)$ represents the PDF, at lowest order that can be understood as the density probability to have the parton a carrying the momentum fraction ξ inside of H . μ_F represents the scale that is introduced through the renormalization of PDFs to eliminate divergences. Just as μ_R is introduced for α_s in (1.1), the renormalisation of PDFs introduces a new arbitrary scale μ_F . $d\hat{\sigma}_{\lambda a}$ is the differential partonic cross section, it encodes the cross section when considering the interaction between the incoming λ and the parton a inside H . One of the goals of perturbative QCD (pQCD), is to determine this partonic cross section as accurately as possible. On the other hand, in the context of DIS, this relation can be used to determine experimentally the PDF for the measure of the total cross section, assuming that the partonic cross section is known, up to some order in perturbation theory.

From there, the generalisation to hard parton-parton collision is quite natural. Indeed, the generic particle λ can also be a parton from another hadron. The reasoning is the same: the hadronic internal interactions occur on a timescale much longer than that of the scattering. For the same reason, any potential interactions between the remaining partons in the final state and the hard scattering are excluded. Then, we can formally write the factorisation formula for hadronic collisions:

$$d\sigma_{AB}(\tau, Q^2) = \sum_{a,b} \int_0^1 d\xi_A d\xi_B f_{a/A}(\xi_A, \mu_F) f_{b/B}(\xi_B, \mu_F) d\hat{\sigma}_{ab}(Q^2, \tau/\xi_A \xi_B, \mu_F) \Theta(\xi_1 \xi_2 - \tau), \quad (1.6)$$

where $\tau = Q^2/s$, with s the hadronic center of mass energy squared. The Heaviside distribution Θ ensures that the squared partonic center of mass energy $\hat{s} = s\xi_A \xi_B$ is greater than Q^2 . As they have to be renormalised, PDFs satisfy corresponding RGEs that describe their evolution with μ_F . In the following section, we focus on these RGEs and derive the corresponding splitting kernels at first order in α_s .

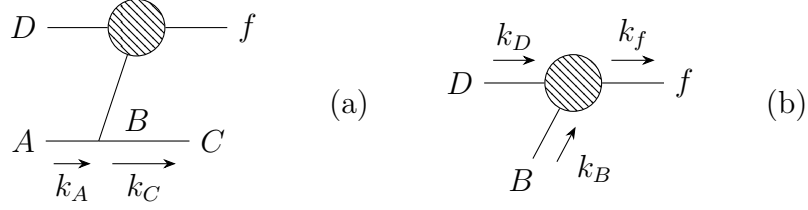
1.2.2 Dokshitzer–Gribov–Lipatov–Altarelli–Parisi equations

In this section, our aim is to recover explicitly Dokshitzer–Gribov–Lipatov–Altarelli–Parisi (DGLAP) equations, and their solutions for PDF evolution in QCD at one-loop. To do so, we consider the matrix elements describing parton splittings. From there we can

recover the DGLAP equations and deduce explicitly the splitting kernels [47, 48] (or Altarelli-Parisi splitting functions).

Splitting

We begin by considering the two generic diagrams:



where A is the parton splitting into B and C while D is a given spectator particle, f any final state and the k_i are the corresponding four-momenta. We define the differential cross section $d\sigma$ for the generic process $a b \rightarrow \{f\}$:

$$d\sigma_{ab \rightarrow f} = \frac{1}{4E_a E_b |\vec{v}_a - \vec{v}_b|} \overline{\sum} |\mathcal{M}_{ab \rightarrow f}|^2 d\Phi_f, \quad (1.7)$$

where E_i and $\vec{v}_i = \vec{p}_i/E_i$ are respectively the energy and velocity of the particle i , $d\Phi_f$ is the phase space corresponding to the final state $\{f\}$ and \mathcal{M} is the matrix element amplitude. For simplicity, we consider the final state f in (a) and (b) as a single particle, but including multiple final states would not affect the reasoning. The sum $\overline{\sum}$ indicates averaging over initial quantum numbers (spin, helicity, colour...) and sum over the final ones. We can express the differential cross sections before the sum, in the center of mass frame, where $|\vec{v}_a - \vec{v}_b| = 2$ for diagrams (a) and (b), similarly to section 4 of [47]:

$$\begin{aligned} d\sigma_b &= \frac{1}{8E_B E_D} \frac{d^3 k_f}{(2\pi)^3 2E_f} (2\pi)^4 \delta^{(4)}(k_B + k_D - k_f) |\mathcal{M}_{B+D \rightarrow f}|^2, \\ d\sigma_a &= \frac{1}{8E_A E_D} \frac{d^3 k_f}{(2\pi)^3 2E_f} \frac{d^3 k_C}{(2\pi)^3 2E_C} (2\pi)^4 \int d^4 k_B \delta^{(4)}(k_B + k_D - k_f) \delta^{(4)}(k_B - k_A + k_C) \\ &\quad \overline{\sum} |\mathcal{M}_{A \rightarrow B+C}|^2 \frac{1}{k_B^4} |\mathcal{M}_{B+D \rightarrow f}|^2 \\ &= \frac{1}{8E_A E_D} \frac{d^3 k_f}{(2\pi)^3 2E_f} \frac{d^3 k_C}{(2\pi)^3 2E_C} (2\pi)^4 \delta^{(4)}(k_A + k_D - k_f - k_C) \\ &\quad |\mathcal{M}_{A \rightarrow B+C}|^2 \frac{1}{(k_A - k_C)^4} |\mathcal{M}_{B+D \rightarrow f}|^2, \end{aligned} \quad (1.8)$$

To obtain the final expression of $d\sigma_a$, we integrated over the internal momentum k_B . If we label the momentum k_B as $k_A - k_C$ in the Dirac δ distribution of $d\sigma_b$, the two processes are related by:

$$d\sigma_a = d\sigma_b \frac{d^3 k_C}{(2\pi)^3 2E_C} \frac{E_B}{E_A} |\mathcal{M}_{A \rightarrow B+C}|^2 \frac{1}{(k_A - k_C)^4} \equiv d\sigma_b d\mathcal{P}_{BA}(z) dz, \quad (1.9)$$

where z is the longitudinal momentum fraction from A carried by B and where we introduced the probability of transition from A to B: $d\mathcal{P}_{BA}$. We can parametrise the momenta of interest with the z variable, p the momentum of A and a transverse momentum magnitude p_\perp . In the collinear approximation, we have $p_\perp/p \ll 1$ so we can approximate the momenta by :

$$\begin{aligned} \bullet k_A^\mu &= (E_A, \vec{p}_A) = (p, \vec{0}, p), \\ \bullet k_B^\mu &\simeq (pz, \vec{p}_\perp, pz - \frac{p_\perp^2}{2zp}), \\ \bullet k_C^\mu &\simeq (p(1-z), -\vec{p}_\perp, p(1-z) - \frac{p_\perp^2}{2(1-z)p}), \end{aligned} \quad (1.10)$$

which ensures that we deal with massless particles, with a breach of momentum conservation of order $\delta p = \mathcal{O}(p_\perp^2/p)$. With this, we can express quantities in term of z , p_\perp , p :

$$d^3 k_C = \pi dz dp_\perp^2 p, \quad \frac{E_B}{E_A} = z, \quad \frac{1}{(k_A - k_C)^4} = \frac{(1-z)^2}{p_\perp^4}. \quad (1.11)$$

If we consider the unpolarised transition probability, we need to sum or average over the relevant degrees of freedom:

$$d\mathcal{P}_{BA}(z) = \frac{dp_\perp^2}{p_\perp^2} \frac{z(1-z)}{16\pi^2 p_\perp^2} \overline{|\mathcal{M}_{A \rightarrow B+C}|^2} \equiv \frac{dp_\perp^2}{p_\perp^2} \frac{\alpha_s}{2\pi} P_{BA}^{(1)}(z). \quad (1.12)$$

From splitting functions to DGLAP equations

The DGLAP [47] equations describe how the distribution functions evolve with energy scale. They can be derived directly from the previous splitting process at first order. $\mathcal{P}_{BA}(z)$ can be interpreted as the probability for the particle A to emit a particle B carrying a fraction z of its momentum. The evolution of the PDF $f_{B/H}$ can be described by a simple evolution equation, using (1.12):

$$\begin{aligned} \Delta f_{B/H}(x, Q) &= \int_0^1 dx' \int_0^1 dz \frac{\alpha_s}{2\pi} \frac{\Delta Q^2}{Q^2} P_{BA}^{(1)}(x') f_{A/H}(z, Q) \delta(x - zx') \\ \implies \frac{df_{B/H}(x, Q^2)}{d \ln(Q^2)} &= \int_x^1 \frac{dz}{z} \frac{\alpha_s}{2\pi} P_{BA}^{(1)}(x/z) f_{A/H}(z, Q^2). \end{aligned} \quad (1.13)$$

In (1.13), we can take the partial differential as the total one at first-order because the correcting term has a magnitude of $\mathcal{O}(\alpha_s^2)$.

$$\frac{d}{d \ln(Q^2)} = \frac{\partial}{\partial \ln(Q^2)} + \frac{d\alpha_s}{d \ln(Q^2)} \frac{\partial}{\partial \alpha_s} = \frac{\partial}{\partial \ln(Q^2)} - \beta_0 \frac{\alpha_s^2}{2\pi} \frac{\partial}{\partial \alpha_s} + \mathcal{O}(\alpha_s^3). \quad (1.14)$$

Of course we have complementary processes $B \longleftrightarrow A$, so that DGLAP equations are actually coupled to one another. Since in this document we will always refer to proton-proton collision, we will no longer specify the hadron in the notation of the PDF. Once all taken into account we find the DGLAP equations for QCD at first order in α_s :

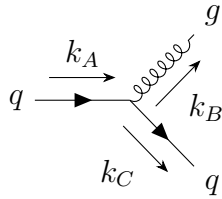
$$\frac{\partial}{\partial \ln(Q^2)} \begin{pmatrix} f_q(x, Q^2) \\ f_g(x, Q^2) \end{pmatrix} = \frac{\alpha_s(Q^2)}{2\pi} \int_x^1 \frac{dz}{z} \begin{pmatrix} P_{qq}^{(1)}(x/z) & P_{qg}^{(1)}(x/z) \\ P_{gq}^{(1)}(x/z) & P_{gg}^{(1)}(x/z) \end{pmatrix} \begin{pmatrix} f_q(z, Q^2) \\ f_g(z, Q^2) \end{pmatrix}. \quad (1.15)$$

Here the sum over quark (anti)flavours is implicit. To solve the DGLAP equations, we only miss the derivation of the splitting kernels $P_{BA}^{(1)}$.

Explicit derivation

We now have to evaluate the corresponding $\overline{\sum} |\mathcal{M}_{A \rightarrow B+C}|^2$ in order to compute the splitting functions. For QCD, we have four functions to find (for all possible transitions between q and g) but not all of them are independent. For conciseness, we detail only the computations for the $g \rightarrow q\bar{q}$, $g \rightarrow gg$ and $q \rightarrow qg$ vertices.

- $q \rightarrow qg$



$$i\mathcal{M}_{q \rightarrow g+q} = -ig_s \bar{u}_h(k_C) \mathbf{T}^a \gamma_\mu u_{h'}(k_A) \epsilon_T^{*\mu}(k_B),$$

where the spinors $u_{h'}$ and \bar{u}_h are respectively carrying the helicities of the incoming and outgoing quarks. ϵ_T^* is the polarisation vector of the outgoing gluon, γ_μ is a Dirac matrix in $d = 4$ dimension [48]. For details on the polarisation sum, refer to appendix A.3. Using the Lorenz gauge, in the case of transverse polarisation vectors, we can make the replacement, as in [47]:

$$\sum_{T=\pm} \epsilon_T^\mu(k_B) \epsilon_T^{*\nu}(k_B) = \delta^{ij} - \frac{k_B^i k_B^j}{k_B^2}. \quad (1.16)$$

We denote the space-only indices by Latin letters like i, j , and Lorentz indices with Greek letters like μ, ν . For example the four momentum k can be written as: $k^\mu = (E_k, k^i)$

$$\begin{aligned}
 \overline{\sum} |\mathcal{M}_{q \rightarrow g+q}|^2 &= \frac{\text{Tr}(\mathbf{T}^a \cdot \mathbf{T}^a)}{2N_c} g_s^2 \sum_{\substack{h=\pm \\ h'=\pm}} \text{Tr} \left(\not{k}_A \gamma_\mu \not{k}_C \gamma_\nu \frac{1 + h h' + (h + h') \gamma^5}{4} \right) \sum_{T=\pm} \epsilon_T^\mu \epsilon_T^{*\nu} \\
 &= 2g_s^2 C_F (k_{Ai} k_{Cj} + k_{Aj} k_{Ci} + \delta_{ij} k_A \cdot k_C) \left(\delta^{ij} - \frac{k_B^i k_B^j}{\vec{k}_B^2} \right) \\
 &= 2g_s^2 C_F \left(2\vec{k}_A \cdot \vec{k}_C + 2k_A \cdot k_C - 2 \frac{(\vec{k}_A \cdot \vec{k}_B)(\vec{k}_B \cdot \vec{k}_C)}{\vec{k}_B^2} \right).
 \end{aligned} \tag{1.17}$$

From the previous formula, we can see that we need scalar products of three-momenta. We can compute these relevant scalar products from (1.10). It follows that:

$$\begin{aligned}
 \vec{k}_A \cdot \vec{k}_C + k_A \cdot k_C &= E_A E_C = p^2(1-z), \quad \vec{k}_A \cdot \vec{k}_B = zp^2 - \frac{p_\perp^2}{2z}, \quad \vec{k}_B^2 = z^2 p^2, \\
 \vec{k}_B \cdot \vec{k}_C &= p^2 z(1-z) - p_\perp^2 \left(1 + \frac{z}{2(1-z)} + \frac{1-z}{2z} \right).
 \end{aligned} \tag{1.18}$$

Injecting these solutions in (1.17), we obtain:

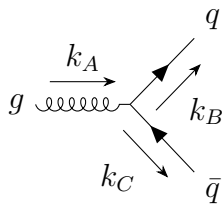
$$\begin{aligned}
 \overline{\sum} |\mathcal{M}_{q \rightarrow g+q}|^2 &= 2g_s^2 C_F \left[2p^2(1-z) - \frac{2}{p^2 z^2} \left(p^4 z^2(1-z) - \frac{p_\perp^2 p^2(1-z)}{2} - p^2 p_\perp^2 \frac{1}{2(1-z)} \right) \right] \\
 &= \frac{2g_s^2 C_F p_\perp^2}{z(1-z)} \left(\frac{1 + (1-z)^2}{z} \right).
 \end{aligned} \tag{1.19}$$

Finally we can write $P_{gq}^{(1)}$, the splitting kernel corresponding to the transition $q \rightarrow g$ (notice that the indices are swapped compared to the ordering in the transition), at first order:

$$P_{gq}^{(1)}(z) = C_F \frac{2g_s^2 p_\perp^2}{z(1-z)} \left(\frac{1 + (1-z)^2}{z} \right) \frac{8\pi^2}{g_s^2} \frac{z(1-z)}{16\pi^2 p_\perp^2} = C_F \left(\frac{1 + (1-z)^2}{z} \right). \tag{1.20}$$

In the same way we can consider the $g \rightarrow q\bar{q}$ splitting for the $g \rightarrow q$ transition.

- $g \rightarrow q\bar{q}$



$$i\mathcal{M}_{g \rightarrow q+\bar{q}} = -ig_s v_h(k_C) \mathbf{T}^a \gamma_\mu \bar{u}_{h'}(k_B) \epsilon_T^\mu(k_A).$$

With a similar calculation to the previous vertex,

$$\begin{aligned}
 \overline{\sum} |\mathcal{M}_{g \rightarrow q + \bar{q}}|^2 &= \frac{1}{2} \frac{\text{Tr}(\mathbf{T}^a \cdot \mathbf{T}^a)}{N_c^2 - 1} g_s^2 \sum_{\substack{h=\pm \\ h'=\pm}} \text{Tr} \left(\not{k}_C \gamma_\mu \not{k}_A \gamma_\nu \frac{1 - hh' + (h' - h)\gamma^5}{4} \right) \sum_{T=\pm} \epsilon_T^\mu \epsilon_T^{*\nu} \\
 &= 2g_s^2 T_F (k_{Bj} k_{Cj} + k_{Bj} k_{Ci} + \delta_{ij} k_B \cdot k_C) \left(\delta^{ij} - \frac{k_A^i k_A^j}{k_A^2} \right) \\
 &= 2g_s^2 T_F \left(2E_B E_C - 2 \frac{(\vec{k}_A \cdot \vec{k}_C)(\vec{k}_B \cdot \vec{k}_A)}{k_A^2} \right).
 \end{aligned} \tag{1.21}$$

For these products we have:

$$\begin{aligned}
 E_B E_C &= p^2 z(1-z), & \vec{k}_A \cdot \vec{k}_C &= p^2(1-z) - \frac{p_\perp^2}{2(1-z)}, \\
 \vec{k}_B \cdot \vec{k}_A &= zp^2 - \frac{p_\perp^2}{2z}, & \vec{k}_A^2 &= p^2.
 \end{aligned} \tag{1.22}$$

Thus, after injecting the scalar products we obtain the squared matrix element:

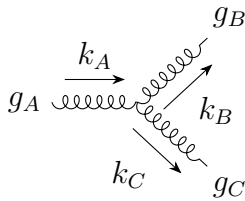
$$\begin{aligned}
 \overline{\sum} |\mathcal{M}_{g \rightarrow q + \bar{q}}|^2 &= 2T_F g_s^2 \left(2p^2 z(1-z) - 2p^2 z(1-z) + p_\perp^2 \frac{1}{z(1-z)} (z^2 + (1-z)^2) \right) \\
 &= 2T_F g_s^2 \frac{p_\perp^2}{z(1-z)} (z^2 + (1-z)^2).
 \end{aligned} \tag{1.23}$$

And finally we can identify the splitting function for the $g \rightarrow q$ transition:

$$P_{qg}^{(1)}(z) = 2g_s^2 T_F p_\perp^2 \frac{1}{z(1-z)} (z^2 + (1-z)^2) \frac{8\pi^2 z(1-z)}{g_s^2 16\pi^2 p_\perp^2} = T_F (z^2 + (1-z)^2). \tag{1.24}$$

- $g \rightarrow gg$

The last matrix element that we need to compute is the tree-gluon vertex, which arises from the non-Abelian nature of QCD.



$$\begin{aligned}
 i\mathcal{M}_{g \rightarrow g+g} &= ig_s f^{abc} \epsilon_{h_1 \mu}(k_A) \epsilon_{h_2 \nu}^*(k_B) \epsilon_{h_3 \rho}^*(k_C) \\
 &\left(-g^{\mu\rho}(k_A + k_C)^\nu + g^{\mu\nu}(k_A + k_B)^\rho + g^{\rho\nu}(k_C + k_B)^\mu \right).
 \end{aligned}$$

Here we have to specify the polarisation tensors. They must be transverse with respect to

the momentum they carry *i.e.* $\epsilon(p) \cdot p = 0$.

$$\begin{aligned}\epsilon_{\pm}^{\mu}(k_A) &= \frac{1}{\sqrt{2}}(0, 1, \pm i, 0), \\ \epsilon_{\pm}^{\nu}(k_B) &= \frac{1}{\sqrt{2}}\left(0, 1, \pm i, -\frac{p_{\perp}}{zp}\right), \\ \epsilon_{\pm}^{\rho}(k_C) &= \frac{1}{\sqrt{2}}\left(0, 1, \pm i, \frac{p_{\perp}}{(1-z)p}\right).\end{aligned}\tag{1.25}$$

The expression of the momenta k_i can be found in (1.10) so the transversality of the polarisation tensor can be checked explicitly. We give here some useful contractions:

$$\begin{aligned}(\vec{k}_A + \vec{k}_C) \cdot \epsilon^*(k_B) &= -\sqrt{2}\frac{p_{\perp}}{z}, & \epsilon_{h_1}(k_A) \cdot \epsilon_{h_3}^*(k_C) &= \delta_{h_1 h_3}, & (\vec{k}_C - \vec{k}_B) \cdot \epsilon(k_A) &= -\sqrt{2}p_{\perp}, \\ (\vec{k}_A + \vec{k}_B) \cdot \epsilon^*(k_C) &= \sqrt{2}\frac{p_{\perp}}{1-z}, & \epsilon_{h_1}(k_A) \cdot \epsilon_{h_2}(k_B)^* &= \delta_{h_1 h_2}, & \epsilon_{h_2}^*(k_B) \cdot \epsilon_{h_3}^*(k_C) &= \delta_{-h_2 h_3}.\end{aligned}\tag{1.26}$$

Injecting these results we can compute the matrix element amplitude:

$$\begin{aligned}i\mathcal{M}_{g \rightarrow g+g} &= ig_s f^{abc} \left(-\sqrt{2}\frac{p_{\perp}}{z}\delta_{h_1 h_3} - \sqrt{2}\frac{p_{\perp}}{1-z}\delta_{h_1 h_2} + \sqrt{2}p_{\perp}\delta_{-h_2 h_3} \right) \\ &= -ig_s f^{abc} \sqrt{2}p_{\perp} \left(\frac{\delta_{h_1 h_3}}{z} + \frac{\delta_{h_1 h_2}}{1-z} - \delta_{-h_2 h_3} \right).\end{aligned}\tag{1.27}$$

so that the squared matrix element reads:

$$\begin{aligned}\overline{\sum} |\mathcal{M}_{g \rightarrow g+g}|^2 &= 2C_A g_s^2 p_{\perp}^2 \frac{1}{2} \sum_{h_i=\pm} \left(\frac{\delta_{h_1 h_3}}{z} + \frac{\delta_{h_1 h_2}}{1-z} - \delta_{-h_2 h_3} \right)^2 \\ &= 4C_A g_s^2 \frac{p_{\perp}^2}{z(1-z)} \left(\frac{1-z}{z} + \frac{z}{1-z} + z(1-z) \right).\end{aligned}\tag{1.28}$$

We can notice that a divergent part arises when $z \rightarrow 1$. To regularise this divergence, we make use of the + distribution prescription (refer to A.45). Therefore, introducing the collinear anomalous dimension for gluons γ_g , that we will derive later:

$$P_{gg}^{(1)}(z) = 2C_A \left(\frac{1-z}{z} + z \frac{1}{1-z} \Big|_+ + z(1-z) \right) + \gamma_g \delta(1-z).\tag{1.29}$$

Deductions

As we stated earlier, splittings kernels are related in more than one way. We can recycle the previous results to find the other splitting kernels. First, we can deduce $P_{qq}^{(1)}(z)$ from our computation of $P_{gq}^{(1)}(z)$. Since they appear in the same vertex, we just need to perform

the exchange $z \longleftrightarrow 1 - z$ and regularise the resulting divergence as $z \rightarrow 1$ by introducing the $+$ distribution and the resulting collinear anomalous dimension for quarks γ_q .

$$P_{qq}^{(1)}(z) = C_F \left((1+z^2) \frac{1}{1-z} \Big|_+ + \frac{\gamma_q}{C_F} \delta(1-z) \right). \quad (1.30)$$

We only miss the collinear anomalous dimensions to fully determine the splitting functions: γ_q , γ_g . To obtain these constants, we can apply the sum rules that encode respectively probability and momentum conservation inside the proton:

$$\begin{aligned} \int_0^1 dz P_{qq}^{(1)}(z) = 0 &\implies \frac{\gamma_q}{C_F} = - \int_0^1 dz \frac{1+z^2-2}{1-z} = \frac{3}{2}, \\ \int_0^1 dz z \left(P_{gg}^{(1)}(z) + \sum_{i=1}^{2n_f} P_{qig}^{(1)}(z) \right) = 0 &\implies \gamma_g = \frac{11C_A}{6} - \frac{2n_f T_F}{3} = \beta_0. \end{aligned} \quad (1.31)$$

In the end we have all the splitting functions for QCD at first order in α_s :

$$\begin{aligned} \bullet P_{qq}^{(1)}(z) &= C_F \left((1+z^2) \frac{1}{1-z} \Big|_+ + \frac{3}{2} \delta(1-z) \right), \\ \bullet P_{qg}^{(1)}(z) &= T_F \left(z^2 + (1-z)^2 \right), \\ \bullet P_{gq}^{(1)}(z) &= C_F \left(\frac{1+(1-z)^2}{z} \right), \\ \bullet P_{gg}^{(1)}(z) &= 2C_A \left(\frac{1-z}{z} + z \frac{1}{1-z} \Big|_+ + z(1-z) \right) + \beta_0 \delta(1-z). \end{aligned} \quad (1.32)$$

The splitting functions demonstrate invariance to quark flavour and do not discriminate between particles and anti-particles. With the essential components in place, we can solve the DGLAP equations and determine the first-order evolution of PDFs. For the explicit solving of the equations, see the appendix A.4. In the broader scope of this document, the DGLAP evolution in itself is not necessary for the resummation formalism. However, in appendix A.8, we reuse the expression of the first order splitting functions, and more specifically the collinear anomalous dimensions, to derive the Sudakov factor that is part of the resummation framework.

1.2.3 LHAPDF for practical use

Now that we have described how PDFs are defined and evolve, let us focus on their actual implementation for phenomenological use. As previously mentioned, PDFs encompass the partonic behaviour, which is not completely accessible through a perturbative approach. Some collaborations attempt to produce *ab initio* PDF fits from lattice computations [50,51], but most of the available PDFs come from experimental fits [37,49,52].

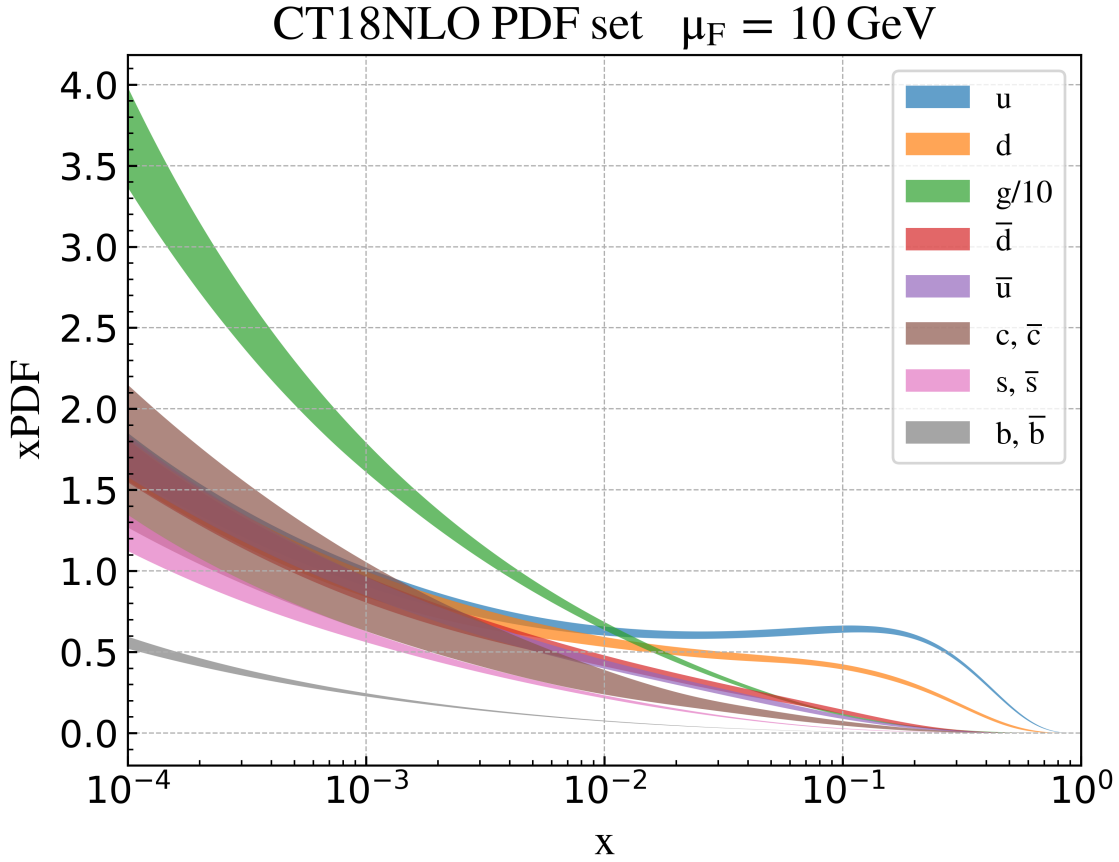


Figure 1.2: LHAPDF CT18NLO set [49] displayed for $\mu_F = 10 \text{ GeV}$

For the physics community to use the results of PDFs in a standardised way, the Les Houches Accords PDF (LHAPDF) [53] library was introduced. The collaboration maintains a PDF database from which anyone can download their preferred PDF set corresponding to their specific needs. The PDF sets are labeled with a unique identification number (LHAPDF ID). All the results in this document were produced using the PDF sets CT18NLO (ID 14400) [49], MSTW2008nlo68cl (ID 21100) or MSTW2008nnlo68cl (ID 21200) [37]. Other PDF sets are available, encompassing a various number of approaches (analytic parameterisation, neural network and Monte-Carlo representation, meta-analysis...), schemes (general/zero mass, fixed/varying flavour number...) and input data (HERA, ATLAS, CMS, LHCb, Tevatron...). We chose the previous sets for their adequacy with the chosen parameterisation (see section 2.4.2) and their extensive use in the literature. We do not pretend to have performed an extensive review of the available PDF sets that could be suitable for our study. Future studies could consist in comparing the different PDF sets and their influence on the results presented in this document, similarly to what has been done in [54, 55].

In figure 1.2, the proton PDFs from the CT18NLO set, for the gluon and the $n_f = 5$ active quark flavours are shown, similarly to figure 2 in [49]. The y-axis represents the PDF multiplied by the momentum fraction x . We can notice that there is a distinction between sea quarks and valence quarks (u and d). Sea quarks and anti-quarks share the same distribution due to symmetric pair production and annihilation, while valence quarks u and d have a different distributions from their anti-particle partners. The gluon PDF is approximately an order of magnitude larger than the quark PDFs in most of the x range. This illustrates the proton's rich parton content with numerous gluons and sea quarks contributing to its momentum.

In the context of perturbative QCD computations, using directly the PDF sets provided by LHAPDF is enough for phenomenological applications. However, when using resummation techniques, such as the work presented in this document, we need to introduce the Mellin transform of the PDF. For more details about the implementation in this scenario, refer to section 2.4.2.

1.3 Colour Algebra

After exploring the parton model and its implications on perturbative QCD computations, let us address the question of the underlying symmetry. Indeed, the QCD Lagrangian detailed in A.3 is invariant under local $SU(N_c)$ gauge transformation. In the Standard Model, $N_c = 3$ but we maintain a general N_c dependence whenever possible. To thoroughly understand scattering processes involving coloured particles, we need to familiarise ourselves with some elements of group theory relative to $SU(N_c)$. This enables us to generate explicitly the tensor spaces on which the matrix elements of the processes span, as well as computing the colour factor arising from the symmetry group. To depict the colour structure of a process, we need a tensorial basis $\{C_j^{\{c_k\}_{k \leq n}}\}_{1 \leq j \leq N}$ on which to span the coloured matrix element amplitudes, and the colour factors $\{\mathbf{t}_k \cdot \mathbf{t}_l\}_{1 \leq k, l \leq n}$ which will be useful in section 2.3.1. We denote n the number of coloured particles involved (incoming or outgoing) in the process with their respective colour indices c_k , and N is the dimension of the tensor basis. Let us first focus on the tensorial basis.

1.3.1 Colour tensor basis

In the upcoming section, we outline the general procedure for constructing the colour tensor basis. It is noteworthy that an extensive mathematical proof or a comprehensive treatment will not be undertaken in this study. Instead, we mainly follow the reasoning presented in [38] and provide the minimal set of mathematical details required for our purpose.

SU(N_c): group, representation and Lie algebra

SU(N_c) is the special unitary group of $N_c \times N_c$ matrices. It belongs to the category of Lie groups, and its Lie algebra, denoted by $\mathfrak{su}(N_c)$, is $(N_c^2 - 1)$ -dimensional. The Lie algebra consists of traceless, Hermitian matrices (or anti-Hermitian, up to a global factor i) in the fundamental representation. For the case of $N_c = 3$, the generators are related to the Gell-Mann matrices λ_i by the relation: $\mathbf{T}^i = \lambda_i/2$. Hereafter, we distinguish between \mathbf{t}^i , which represents generic generators for any representation, and \mathbf{T}^i , which is specific to the fundamental representation. Furthermore, we have the following definitions for the structure constants:

$$\mathbf{T}^i \cdot \mathbf{T}^j = \frac{\delta^{ij}}{2N_c} \mathbb{1}_{N_c} + \frac{if^{ijk} + d^{ijk}}{2} \mathbf{T}^k, \quad (1.33)$$

$$[\mathbf{T}^i, \mathbf{T}^j] = if^{ijk} \mathbf{T}^k, \quad \{\mathbf{T}^i, \mathbf{T}^j\} = \frac{\delta^{ij}}{N_c} \mathbb{1}_{N_c} + d^{ijk} \mathbf{T}^k, \quad (1.34)$$

or equivalently :

$$f^{abc} = -2i \text{Tr}([\mathbf{T}^a, \mathbf{T}^b] \mathbf{T}^c), \quad d^{abc} = 2 \text{Tr}(\mathbf{T}^a \{\mathbf{T}^b, \mathbf{T}^c\}),$$

with f^{abc} representing the completely antisymmetric structure constant and d^{abc} the symmetric one. For more relations involving these objects, refer to A.2. If \mathbf{T}^i are the generators of the fundamental representation, the adjoint is generated by the antisymmetric structure constants: $\mathbf{t}_{\alpha\beta}^i = -if^{i\alpha\beta}$.

It is essential to note that the generators in the fundamental representation are Hermitian matrices. Therefore, in general $\mathbf{T}_{ab}^i \neq \mathbf{T}_{ba}^i$. The first index a belongs to the fundamental representation, while the second index b belongs to the conjugate space. To construct consistent tensors utilizing these generators, it is crucial to keep track of the number of indices in each space. To do this, we describe the irreducible representations of SU(3) using the notation (m, n) where m is the number of indices in the fundamental representation, and n the number of indices in the conjugate space. We can treat them similarly to covariant and contravariant indices for the Lorentz group, but we should remember that they are related through complex conjugation. The dimension of an irreducible representation (m, n) is given by:

$$\dim((m, n)) = \frac{(m+1)(n+1)(m+n+2)}{2}. \quad (1.35)$$

We can try this formula on some example (not) chosen at random:

$$\begin{aligned}
 \dim((1, 0)) &= \frac{2 \times 3}{2} = 3 \equiv \dim(\underline{\mathbf{3}}) , \\
 \dim((0, 1)) &= \frac{2 \times 3}{2} = 3 \equiv \dim(\overline{\mathbf{3}}) , \\
 \dim((1, 1)) &= \frac{2 \times 2 \times 4}{2} = 8 \equiv \dim(\mathbf{8}) .
 \end{aligned} \tag{1.36}$$

The attentive reader would certainly recognise the definitions of the fundamental, conjugate and adjoint representations. The “name” of a representation directly comes from its dimension. The underlying or overlying notations indicate representations with indices on one side only. It is worth noting that this is can be ambiguous for high-dimensional representations but is not be problematic for most practical cases in this document.

Now that we have described the parameterisation of irreducible representations, let us address the question of direct product of irreducible representations. As a direct product of (irreducible) representations is a representation itself, it can be decomposed as a direct sum of irreducible representations. In the case of $SU(3)$, these Clebsch–Gordan series can be described in a compact way. Introducing the intermediate notation:

$$(m, m'; n, n') = \bigoplus_{i=0}^{\min(m, m')} (m' + m - 2i, n' + n + i) \bigoplus_{j=1}^{\min(m, m')} (m' + m + j, n' + n - 2j) . \tag{1.37}$$

We can write in a concise way:

$$(m, n) \otimes (m', n') = \bigoplus_{i=0}^{\min(m, n')} \bigoplus_{j=0}^{\min(m', n)} (m - i, m' - j; n - j, n' - i) . \tag{1.38}$$

It is useful to build an intuition for these formula on examples:

$$\begin{aligned}
 \underline{\mathbf{3}} \otimes \overline{\mathbf{3}} &= (1, 0) \otimes (0, 1) = (1, 0; 0, 1) \oplus (0, 0; 0, 0) = (1, 1) \oplus (0, 0) = \mathbf{8} \oplus \mathbf{1} , \\
 \mathbf{8} \otimes \mathbf{8} &= (1, 1) \otimes (1, 1) = (1, 1; 1, 1) \oplus (1, 0; 0, 1) \oplus (0, 1; 1, 0) \oplus (0, 0; 0, 0) \\
 &= \left((2, 2) \oplus (0, 3) \oplus (3, 0) \right) \oplus (1, 1) \oplus (1, 1) \oplus (0, 0) \\
 &= \mathbf{27} \oplus \underline{\mathbf{10}} \oplus \overline{\mathbf{10}} \oplus \mathbf{8} \oplus \mathbf{8} \oplus \mathbf{1} .
 \end{aligned} \tag{1.39}$$

Of course, in the end the dimensions should be the same on both sides of the equation, and this can be easily verified with the explicit notation displaying the dimension of each irreducible representation.

When analysing the colour structure of a process, we decompose the tensor product of the initial particles’ representations into a direct sum of irreducible representations. This

summed space yields the colour tensor basis used to describe the process. We must stress that, in general, not all resulting representations are populated, as further constraints may arise from the time inversion of the process. In other words, when exchanging incoming and outgoing particles, we should be able to account for all the irreducible representations involved in the process. For example, in the case of $q\bar{q} \rightarrow t\bar{t}$, there is no ambiguity, we have $\underline{\mathbf{3}} \otimes \bar{\underline{\mathbf{3}}} = \mathbf{8} \oplus \mathbf{1}$ for both direct and reverse time flow. However in the case of $gg \rightarrow t\bar{t}$, we have: $\mathbf{8} \otimes \mathbf{8} = \underline{\mathbf{27}} \oplus \underline{\mathbf{10}} \oplus \bar{\underline{\mathbf{10}}} \oplus \mathbf{8} \oplus \mathbf{8} \oplus \mathbf{1}$ but $\underline{\mathbf{3}} \otimes \bar{\underline{\mathbf{3}}} = \mathbf{8} \oplus \mathbf{1}$, so that we know that $\underline{\mathbf{27}} \oplus \underline{\mathbf{10}} \oplus \bar{\underline{\mathbf{10}}}$ do not enter the colour tensor basis for this process.

It is useful to understand the underlying irreducible representation to build the colour tensor basis, but it does not directly provide a basis for further computations. Nevertheless, it proves highly valuable to intuitively find one. For instance, in $q\bar{q} \rightarrow t\bar{t}$, the colour tensor basis can be explicitly expressed as singlet and octet components (2.65). Similarly, for $gg \rightarrow t\bar{t}$, the basis can be decomposed into the singlet case and two octets, one symmetric and the other antisymmetric (2.67). In general, we can also generate a colour basis by considering all possible combinations of colour indices dressing baseline colour tensors such as δ^{ij} , \mathbf{T}_{ab}^i or f^{ijk} . We then reduce this set of tensors to an orthogonal basis through the Gram-Schmidt orthogonalisation algorithm. However, it is essential to note that the resulting basis is not unique, as a permutation in the original non-orthogonal basis can lead to a different orthogonal basis. For more details about the general construction of orthogonal colour basis (and predicting its dimension), refer to [56].

In the following sections of this document, we use the Hermitian scalar product as the natural choice for colour tensor products:

$$\langle \cdot | \cdot \rangle : A, B \mapsto \langle A | B \rangle = A^\dagger \cdot B . \quad (1.40)$$

To better understand this, let us describe an explicit example for one colour basis.

$gg \rightarrow t\bar{t}\bar{t}$ colour basis construction

In this example, we have two gluon indices g_1 and g_2 , two quarks t_1, t_2 and two antiquarks \bar{t}_1, \bar{t}_2 . We must stress that all (anti)quarks are outgoing so that their indices belong respectively to the (conjugate) fundamental representation. We are now ready to build a colour basis from the combination of the relevant colour indices. First we can pair the gluon indices in $\delta^{g_1 g_2}$, this leaves only two possibilities to pair the remaining indices in $\mathbf{T}_{q\bar{q}}^i \cdot \mathbf{T}_{q'\bar{q}'}^i$, with $(q, q') \in (t_1, t_2)$: $\delta^{g_1 g_2} \mathbf{T}_{t_1 \bar{t}_1}^i \cdot \mathbf{T}_{t_2 \bar{t}_2}^i$ and $\delta^{g_1 g_2} \mathbf{T}_{t_1 \bar{t}_2}^i \cdot \mathbf{T}_{t_2 \bar{t}_1}^i$. Once this case is settled, we have to enumerate the remaining combinations where the gluon indices are used in the \mathbf{T} generators. Since the product is not symmetric in general, we have two possibilities: $\mathbf{T}^{g_1} \cdot \mathbf{T}^{g_2}$ or $\mathbf{T}^{g_2} \cdot \mathbf{T}^{g_1}$. Let us choose the first case and just multiply the counting of the possible tensors by two in the end to account for both cases. Once the adjoint indices are fixed, we need to allocate the (anti)quark indices in the corresponding

generators. Like in the previous case, there are again two possibilities: $\mathbf{T}_{t_1 \bar{t}_1}^{g_1} \cdot \mathbf{T}_{t_2 \bar{t}_2}^{g_2}$ and $\mathbf{T}_{t_1 \bar{t}_2}^{g_1} \cdot \mathbf{T}_{t_2 \bar{t}_1}^{g_2}$.

However we must remember that the quark indices can also be contracted within δ functions. We covered the case where there are no δ contraction for quarks, and zero or one contraction for gluons. We can already rule out the cases where we have one pair of gluon indices contracted and one pair of (anti)quark indices contracted since it leads to another δ for the remaining (anti)quark indices (see A.7). Similarly, having two pairs of quark indices contracted imposes that the gluon indices are also contracted. In addition, from the first relation in (A.8), we can see that the cases where we have the gluon indices contracted and zero or two pair contractions for the (anti)quark indices are equivalent. It would be redundant to take them both into account. In the end we only miss the case with one pair of (anti)quark indices contracted and no contraction for the gluons. This implies four new possibilities for the choice of the pair of indices contracted. The allocation of the contracted indices leaves only two options because of the tracelessness of the generators. However, due to the symmetry resulting from the contraction $\mathbf{T}_{t_i \alpha}^{g_1} \cdot \mathbf{T}_{\alpha \bar{t}_j}^{g_2} = \mathbf{T}_{\alpha \bar{t}_j}^{g_2} \cdot \mathbf{T}_{t_i \alpha}^{g_1}$, it does not affect the count. The final count reads: $2 \times (1 + 2 + 4) = 14$, and the tensor basis appears as:

$$\left\{ \begin{aligned} & \delta^{g_1 g_2} \mathbf{T}_{t_1 \bar{t}_1}^i \cdot \mathbf{T}_{t_2 \bar{t}_2}^i ; \delta^{g_1 g_2} \mathbf{T}_{t_1 \bar{t}_2}^i \cdot \mathbf{T}_{t_2 \bar{t}_1}^i ; \mathbf{T}_{t_1 \bar{t}_1}^{g_1} \cdot \mathbf{T}_{t_2 \bar{t}_2}^{g_2} ; \mathbf{T}_{t_1 \bar{t}_2}^{g_1} \cdot \mathbf{T}_{t_2 \bar{t}_1}^{g_2} ; \mathbf{T}_{t_1 \bar{t}_1}^{g_2} \cdot \mathbf{T}_{t_2 \bar{t}_2}^{g_1} ; \mathbf{T}_{t_1 \bar{t}_2}^{g_2} \cdot \mathbf{T}_{t_2 \bar{t}_1}^{g_1} ; \\ & \delta_{t_1 \bar{t}_1} \left(\mathbf{T}^{g_1} \cdot \mathbf{T}^{g_2} \right)_{t_2 \bar{t}_2} ; \delta_{t_2 \bar{t}_1} \left(\mathbf{T}^{g_1} \cdot \mathbf{T}^{g_2} \right)_{t_1 \bar{t}_2} ; \delta_{t_1 \bar{t}_2} \left(\mathbf{T}^{g_1} \cdot \mathbf{T}^{g_2} \right)_{t_2 \bar{t}_1} ; \delta_{t_2 \bar{t}_2} \left(\mathbf{T}^{g_1} \cdot \mathbf{T}^{g_2} \right)_{t_1 \bar{t}_1} ; \\ & \delta_{t_1 \bar{t}_1} \left(\mathbf{T}^{g_2} \cdot \mathbf{T}^{g_1} \right)_{t_2 \bar{t}_2} ; \delta_{t_2 \bar{t}_1} \left(\mathbf{T}^{g_2} \cdot \mathbf{T}^{g_1} \right)_{t_1 \bar{t}_2} ; \delta_{t_1 \bar{t}_2} \left(\mathbf{T}^{g_2} \cdot \mathbf{T}^{g_1} \right)_{t_2 \bar{t}_1} ; \delta_{t_2 \bar{t}_2} \left(\mathbf{T}^{g_2} \cdot \mathbf{T}^{g_1} \right)_{t_1 \bar{t}_1} \end{aligned} \right\}. \quad (1.41)$$

As previously stated, this basis is not unique. We could also have made the choice of expanding the $\mathbf{T}^i \mathbf{T}^i$ products in terms of δ products using (A.8). Furthermore, we need to orthogonalise this basis for practical usage. For the final basis, with $N_c = 3$, refer to (4.3). This basis will be used in the context of four top production, treated in chapter 4.

1.3.2 Minimal set of colour factors

Now that we have an explicit tensorial colour basis, we can focus on the determination of the colour factors that arise from generator products in QCD scattering, as we will see in chapter 2. These factors encode the colour structure of the process, expressed in the tensor space previously mentioned. As such they depend on the choice of the basis, but also the nature of the coloured partons entering the process. In appendix A. of [39], there is a description of how the colour algebra factorises (or not) depending on the numbers of coloured partons entering the process. For a n coloured parton, we have n individual generators \mathbf{t}_i , hence n possible squared generators \mathbf{t}_i^2 and $n(n-1)/2$ products $\mathbf{t}_i \cdot \mathbf{t}_j$. These

products are symmetric in (i, j) , as argued in the above example. Then, we can consider implicitly $i < j$ to describe the generator products. However, there are some constrains, namely the n definitions of quadratic Casimir operators relative to each particle i :

$$\forall i \quad \mathbf{t}_i^2 = C_i \mathbb{1} , \quad (1.42)$$

and the n colour conservation constrains:

$$\forall i \quad \mathbf{t}_i \cdot \sum_{j=1}^n \mathbf{t}_j = 0 . \quad (1.43)$$

In total, we have $n + n(n-1)/2 - n - n = n(n-3)/2$ independant non-trivial operator products to determine. It is clear that the case $n = 3$ is the limit where we should expect factorisability to fall apart. Below $n = 3$, the algebra is overconstrained, and all the colour factors can be expressed as combinations of Casimir operators resulting in matrices proportional to $\mathbb{1}$ in colour space.

Factorising algebras

We can describe quickly the factorising algebras for $n \leq 3$, as they are quite easy to recover.

- For $n = 1$, the colour algebra is trivial: $\mathbf{t}_1^2 = C_1 \mathbb{1}$.
- For $n = 2$, the colour algebra is also quite simple: $\mathbf{t}_1 + \mathbf{t}_2 = 0 \Rightarrow \mathbf{t}_1 \cdot \mathbf{t}_2 = -C_1 \mathbb{1} = -C_2 \mathbb{1}$.

We can take the example of the Drell-Yan process $q\bar{q} \rightarrow l^+l^-$ for $n = 2$. Then, we have $\mathbf{t}_1 = \mathbf{t}_q$ and $t_2 = t_{\bar{q}}$. Of course the quadratic Casimir operators definition still holds, so that: $\mathbf{t}_q^2 = \mathbf{t}_{\bar{q}}^2 = C_F \mathbb{1}$. The only colour tensor product in this case is $\mathbf{t}_q \cdot \mathbf{t}_{\bar{q}} = -C_F \mathbb{1}$, as we will see in (2.10).

- The case $n = 3$ still factorises but is less trivial. First, we can express colour conservation as:

$$\forall k \quad 0 = \sum_{i=1}^3 \mathbf{t}_i = \mathbf{t}_k \cdot \sum_{i=1}^3 \mathbf{t}_i = \left(\sum_{i=1}^3 \mathbf{t}_i \right)^2 = \sum_{i=1}^3 \left[C_i + 2\mathbf{t}_i \cdot \sum_{j>i}^3 \mathbf{t}_j \right] . \quad (1.44)$$

If we exploit the colour conservation conditions successively for $k = 1, 2, 3$, we can express the products $\mathbf{t}_k \cdot \mathbf{t}_i$ solely in terms of quadratic Casimir operators:

$$\forall (i, j, k) \in (1, 2, 3) \quad 2\mathbf{t}_k \cdot \mathbf{t}_i = (C_j - C_k - C_i) \mathbb{1} . \quad (1.45)$$

Non factorisable algebras

For $n \geq 4$, we need to examine the situation more closely. First of all, we must choose a minimal set of colour operators that we consider as independant from each other and that we should determine individually. This choice is arbitrary but the resulting set must be linearly independant. A possible choice is the set of the $n(n-3)/2$ first products excluding Casimir operators and $\mathbf{t}_i \cdot \mathbf{t}_n$. This set contains $n-3$ subfamilies, each one corresponding to a choice of i , with j going up to $n-1$. It can be expressed as follow:

$$\{\mathbf{t}_i \cdot \mathbf{t}_j\}_{\substack{1 \leq i \leq n-3 \\ i < j \leq n-1}} .$$

The remaining products not in this minimal set are $\mathbf{t}_{n-2} \cdot \mathbf{t}_{n-1}$ and the $n-1$ products involving \mathbf{t}_n : $\mathbf{t}_i \cdot \mathbf{t}_n$. We can express these products in term of the Casimirs and the minimal set operators. For the first $n-3$ $\mathbf{t}_i \cdot \mathbf{t}_n$ products, we can simply use the colour conservation regarding the i^{th} parton (all the other generator products are in the minimal set):

$$\forall i, 1 \leq i \leq n-3 \quad \mathbf{t}_i \cdot \mathbf{t}_n = -C_i \mathbb{1} - \sum_{\substack{j=1 \\ j \neq i}}^{n-1} \mathbf{t}_i \cdot \mathbf{t}_j . \quad (1.46)$$

At this stage we only miss 3 products to describe all operators in terms of the minimal subset : $\mathbf{t}_{n-2} \cdot \mathbf{t}_{n-1}$, $\mathbf{t}_{n-2} \cdot \mathbf{t}_n$ and $\mathbf{t}_{n-1} \cdot \mathbf{t}_n$. We can use the three final colour conservation constraints :

$$\forall (i, j, k) \in (n-2, n-1, n) \quad \mathbf{t}_k \cdot \mathbf{t}_i + \mathbf{t}_k \cdot \mathbf{t}_j = -C_k \mathbb{1} - \sum_{l=1}^{n-3} \mathbf{t}_l \cdot \mathbf{t}_k . \quad (1.47)$$

Combining these equations, we can single out the three remaining products in term of the others:

$$2\mathbf{t}_i \cdot \mathbf{t}_j = -(C_i + C_j - C_k) \mathbb{1} - \sum_{l=1}^{n-3} \mathbf{t}_l \cdot (\mathbf{t}_i + \mathbf{t}_j - \mathbf{t}_k) . \quad (1.48)$$

We only need to replace the products outside of the minimal set with their expressions in terms of the minimal set operators. The only products falling into this category are the $\mathbf{t}_l \cdot \mathbf{t}_n$. Now, we must distinguish between the case where $k = n$ and the other two cases:

$$\begin{aligned}
 \mathbf{t}_{n-2} \cdot \mathbf{t}_{n-1} &= \frac{1}{2} \left(C_n - \sum_{j=1}^{n-1} C_j \right) \mathbb{1} - \sum_{i=1}^{n-3} \sum_{j=i+1}^{n-1} \mathbf{t}_i \cdot \mathbf{t}_j, \\
 \forall i \in (n-2, n-1) \quad \mathbf{t}_i \cdot \mathbf{t}_n &= \frac{1}{2} \left(\sum_{\substack{j=1 \\ j \neq i}}^{n-1} C_j - C_n - C_i \right) \mathbb{1} + \sum_{l=1}^{n-3} \sum_{\substack{j=l+1 \\ j \neq i}}^{n-1} \mathbf{t}_l \cdot \mathbf{t}_j.
 \end{aligned} \tag{1.49}$$

Having expressed all the colour factors in terms of the minimal subset, our computations are significantly improved, particularly for colour-rich systems such as $g_1 g_2 \rightarrow t_3 \bar{t}_4 t_5 \bar{t}_6$. In this case, $n = 6$ so there are 30 non trivial colour tensor products to determine, each one being a 13×13 matrix (5070 coefficients) for $N_c = 3$ (see 4.3). With the minimal set of tensor products this reduces to 9 products (1521 coefficients left to compute):

$$\left\{ \mathbf{t}_1 \cdot \mathbf{t}_2; \mathbf{t}_1 \cdot \mathbf{t}_3; \mathbf{t}_1 \cdot \mathbf{t}_4; \mathbf{t}_1 \cdot \mathbf{t}_5; \mathbf{t}_2 \cdot \mathbf{t}_3; \mathbf{t}_2 \cdot \mathbf{t}_4; \mathbf{t}_2 \cdot \mathbf{t}_5; \mathbf{t}_3 \cdot \mathbf{t}_4; \mathbf{t}_3 \cdot \mathbf{t}_5 \right\}. \tag{1.50}$$

Again, this minimal set will be used in chapter 4 to reduce the number of colour factors to derive.

1.3.3 Expression in colour tensor basis

Now that we have established the minimal set of colour factors necessary to describe the colour content of the process, we can proceed to find their actual expressions in the colour tensor basis determined in section 1.3.1. As we will see in (2.56), we need to compute colour factors expressed in the tensor basis as follows:

$$\frac{\langle C_k | \mathbf{t}_i \cdot \mathbf{t}_j | C_l \rangle}{\langle C_k | C_k \rangle}. \tag{1.51}$$

In general, $|C_l\rangle$ is a tensor with m indices in the adjoint representation $\{g_p\}_{1 \leq p \leq m}$ (octet), q in the fundamental and conjugate representation $\{\alpha_a\}_{1 \leq a \leq q}$, $\{\beta_b\}_{1 \leq b \leq q}$ (triplet and anti-triplet). The colour generator \mathbf{t}_i carries the colour indices c_{a_i} and c'_{a_i} to be contracted with $|C_l\rangle$ where c_{a_i} has been replaced by c'_{a_i} :

$$\mathbf{t}^i |C_l\rangle = C_l(\{c_1, c_2, \dots, c_{a_{i-1}}, c'_{a_i}, c_{a_{i+1}}, \dots\}) \mathbf{t}_{c_{a_i} c'_{a_i}}^i. \tag{1.52}$$

The c_{a_i} can belong to any subset of colour indices (triplet, anti-triplet or octet). With this prescription, the order of c_{a_i} and c'_{a_i} depends on the actual nature of this colour index (it might be swapped for an anti-triplet, for example). Using this approach, we are now able to derive the actual expressions of colour factors in a given colour tensor basis. Let us detail an explicit determination in the case of the quark channel of top pair production.

$$q_1 \bar{q}_2 \longrightarrow t_3 \bar{t}_4$$

First of all, we need to specify the colour basis. We choose the singlet-octet basis, motivated by the representation decomposition of (1.39):

$$\{|C_1\rangle; |C_2\rangle\} = \{\delta_{c_2 c_1} \delta_{c_3 c_4}; \mathbf{T}_{c_2 c_1}^i \mathbf{T}_{c_3 c_4}^i\}. \quad (1.53)$$

We need $n(n-3)/2 = 2$ matrices in $\mathcal{M}_{2 \times 2}(\mathbb{R})$ to describe all colour factors of the process: $\mathbf{t}_q \cdot \mathbf{t}_{\bar{q}}$ and $\mathbf{t}_q \cdot \mathbf{t}_t$. We focus on the determination on $\mathbf{t}_q \cdot \mathbf{t}_{\bar{q}}$ for simplicity. The four components of the matrix can be computed using (1.52). We have:

$$\begin{aligned} \frac{\langle C_1 | \mathbf{t}_q \cdot \mathbf{t}_{\bar{q}} | C_1 \rangle}{\langle C_1 | C_1 \rangle} &= -\frac{\delta_{\alpha c_2} \delta_{c_4 c_3} \delta_{\beta c_1} \delta_{c_3 c_4} \mathbf{T}_{c_1 \alpha}^i \mathbf{T}_{c_2 \beta}^i}{N_c^2} = -\frac{\text{Tr}(\mathbf{T}^i \cdot \mathbf{T}^i)}{N_c} = -C_F, \\ \frac{\langle C_1 | \mathbf{t}_q \cdot \mathbf{t}_{\bar{q}} | C_2 \rangle}{\langle C_1 | C_1 \rangle} &= -\frac{\delta_{\alpha c_2} \delta_{c_4 c_3} \mathbf{T}_{\beta c_1}^j \mathbf{T}_{c_3 c_4}^j \mathbf{T}_{c_1 \alpha}^i \mathbf{T}_{c_2 \beta}^i}{N_c^2} \propto \text{Tr}(\mathbf{T}^j) = 0, \\ \frac{\langle C_2 | \mathbf{t}_q \cdot \mathbf{t}_{\bar{q}} | C_1 \rangle}{\langle C_2 | C_2 \rangle} &= -\frac{\mathbf{T}_{\alpha c_2}^j \mathbf{T}_{c_4 c_3}^j \delta_{\beta c_1} \delta_{c_3 c_4} \mathbf{T}_{c_1 \alpha}^i \mathbf{T}_{c_2 \beta}^i}{C_F N_c T_F} \propto \text{Tr}(\mathbf{T}^j) = 0, \\ \frac{\langle C_2 | \mathbf{t}_q \cdot \mathbf{t}_{\bar{q}} | C_2 \rangle}{\langle C_2 | C_2 \rangle} &= -\frac{\mathbf{T}_{\alpha c_2}^k \mathbf{T}_{c_4 c_3}^k \mathbf{T}_{\beta c_1}^j \mathbf{T}_{c_3 c_4}^j \mathbf{T}_{c_1 \alpha}^i \mathbf{T}_{c_2 \beta}^i}{C_F N_c T_F} = \frac{\text{Tr}(\mathbf{T}^j \cdot \mathbf{T}^i \cdot \mathbf{T}^j \cdot \mathbf{T}^i)}{C_F N_c} = \frac{C_A}{2} - C_F. \end{aligned} \quad (1.54)$$

For more examples, refer to A.2.2.

In the previous sections we introduced the fundamental concepts underlying perturbative QCD calculations. The parton model, PDFs, factorisation theorem and colour structure are necessary to understand the fixed order computations of observables constituting many of the current predictions both in the SM and beyond. However, we can go further than fixed order computations by introducing resummation techniques in the aim of producing even more accurate predictions. In the next chapter, we detail the general framework of soft gluon threshold resummation that will be used in the rest of the document.

2

Soft gluon threshold resummation

Summary

2.1	Leading logarithm and exponentiation	40
2.1.1	Eikonal approximation and soft gluon emission	40
2.1.2	Factorisation and Mellin transform	42
2.1.3	Toy resummation	43
2.1.4	Power counting	46
2.2	General expression	47
2.2.1	Total cross section and PDF factorisation	47
2.2.2	Partonic cross section and Hard/Soft factorisation	49
2.3	Colour matrices	52
2.3.1	Soft matrix	52
2.3.2	Soft anomalous dimension matrix	56
2.3.3	Beam functions	60
2.3.4	Hard matrix	61
2.4	General expression and implementation	63
2.4.1	Resummation formula	63
2.4.2	Implementation of PDFs	63
2.4.3	Physical result in direct space	66

*Never gonna let you down***Exponential Rick Astley to the soft logarithms**

Resummation illustration, Akenium

THIS chapter focuses on soft-gluon resummation, and specifically on that of the associated threshold logarithms. Firstly, we introduce resummation through a didactic example to better understand its underlying concepts. Subsequently, Mellin space factorisation properties are used to derive a general formula for resumming soft gluon emission at the level of differential cross sections. Once the formal framework is established, we detail the explicit derivation of the universal soft components involved in QCD resummation calculations. Finally, practical insights into the numerical implementation are presented. This chapter is mainly based on the work presented in references [57–59]. In this chapter, we aim to provide a pedagogical presentation of resummation and have a clear understanding of the key ingredients of the formalism.

2.1 Leading logarithm and exponentiation

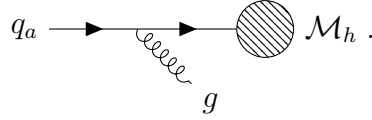
The goal of this section is to provide a clear understanding of the definitions, key concepts and objects involved in soft gluon resummation. With this, we will be able to settle the general framework in section 2.2.

2.1.1 Eikonal approximation and soft gluon emission

We use individual emissions to introduce the theoretical foundations necessary for resummation calculations. Doing so, we introduce the soft and collinear limits to achieve resummation with Leading Logarithmic (LL) precision.

Motivational example: single emission

Similarly to [59], let us consider an emission originating from an incoming quark q_a within a generic process. The corresponding matrix element for this process is denoted as \mathcal{M}_h . Diagrammatically, it gives:



From this, we can proceed to calculate the overall matrix element \mathcal{M}_e . By keeping \mathcal{M}_h general, we ensure its dependence solely through an emission factor:

$$\mathcal{M}_e = \mathcal{M}_h \frac{i(\not{p}_a - \not{k} + m_a)}{(p_a - k)^2 - m_a^2 + i\epsilon} (-ig_s \mathbf{T}^a \gamma^\mu) u(p_a) \epsilon_\mu^*(k), \quad (2.1)$$

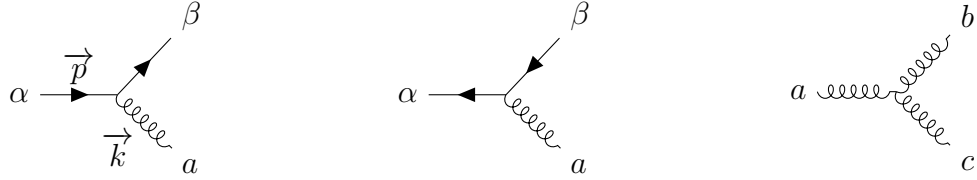
with p_a and k the respective momenta of the incoming quark and emitted gluon, m_a the mass of the quark. In practice, we set $m_a = 0$ for incoming quarks but the derivation remains identical in the massive case. Using the anticommutation relations of γ matrices, $\{\gamma^\mu, \gamma^\nu\} = 2g^{\mu\nu}$, and the relations $(\not{p}_a - m_a)u(p_a) = 0 = k \cdot \epsilon^*(k)$, we can write:

$$\mathcal{M}_e = \mathcal{M}_h g_s \frac{\gamma^\mu \not{k} + 2p_a^\mu}{k^2 - 2p_a \cdot k + i\epsilon} \mathbf{T}^a u(p_a) \epsilon_\mu^*(k).$$

In cases where the momentum of the emitted gluon is significantly smaller than the other momentum scales, we can use the so-called *eikonal approximation* [60]:

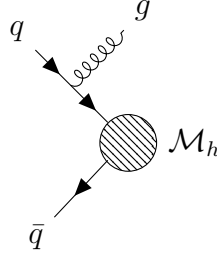
$$\mathcal{M}_e \xrightarrow{k \ll p} \mathcal{M}_h g_s \mathbf{T}^a \frac{-p_a^\mu}{p_a \cdot k - i\epsilon} u(p_a) \epsilon_\mu^*(k). \quad (2.2)$$

Within the soft regime ($k \ll p$), this approximation yields the formulation of effective eikonal Feynman rules governing the emission of gluons from an incoming parton:



$$-\mathbf{T}_{\beta\alpha}^a g_s \frac{p^\mu}{p \cdot k - i\epsilon}, \quad \mathbf{T}_{\alpha\beta}^a g_s \frac{p^\mu}{p \cdot k - i\epsilon}, \quad -if^{abc} g_s \frac{p^\mu}{p \cdot k - i\epsilon}.$$

In the case of outgoing particles, $-i\epsilon$ is changed to $+i\epsilon$, and the SU(3) generators for quarks and anti-quarks are exchanged. We can now express the differential cross section in the eikonal approximation. For simplicity, we will consider a quark-antiquark initiated process with a colour-singlet final state, so that only the initial (anti-)quarks radiate soft gluons.



Using the kinematics of the eikonal cross section, in the centre of mass frame and omitting the regularisation factors ϵ for the sake of brevity, we can link the differential cross section including the soft emission $d\sigma_e$ and the generic one $d\sigma_h$:

$$d\sigma_e \propto -d\sigma_h \frac{p_q \cdot p_{\bar{q}}}{(p_q \cdot k)(p_{\bar{q}} \cdot k)} = -d\sigma_h \frac{2p_q \cdot p_{\bar{q}}}{E_q E_{\bar{q}} E_k^2 (1 - \cos^2(\theta))}. \quad (2.3)$$

Here, θ represents the angle formed between the momenta of the quarks and the (on-shell) radiated gluon, characterised by its energy E_k . p_q , E_q and $p_{\bar{q}}$, $E_{\bar{q}}$ are the momenta and energies of the incoming particles. Equation (2.3) encapsulates two distinct categories of infrared divergences stemming from soft radiation: the first emerges due to the factor $1/E_k^2$ as $E_k \rightarrow 0$, while the second arises as a collinear divergence when $\theta \rightarrow 0$ or π .

2.1.2 Factorisation and Mellin transform

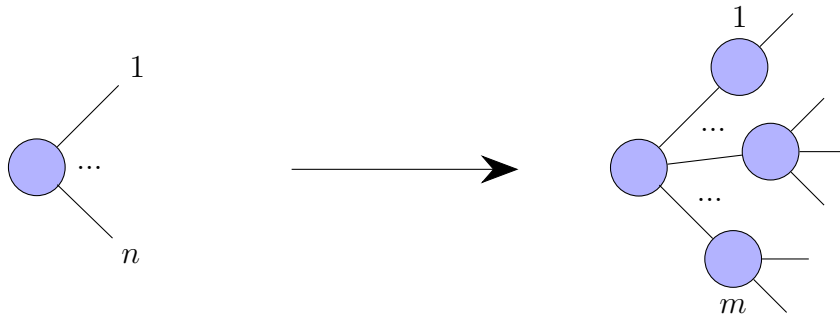
So far, our attention has been focused on single emission, which yields a radiation factor that multiplies the Born cross section. However, in order to deal with multiple emissions within the soft limit, it becomes imperative to use factorisation properties that include both kinematic aspects and the associated phase space. Regarding kinematics, factorisability in the soft limit arises directly from the eikonal Feynman rules. As an example, we can consider two emissions with momenta k_1 and k_2 from the same leg carrying momentum p :

$$\frac{p^\mu}{p \cdot k_1} \frac{p^\nu - k_1^\nu}{(p - k_1) \cdot k_2} \underset{k_i \ll p}{\simeq} \frac{p^\mu p^\nu}{(p \cdot k_1)(p \cdot k_2)}. \quad (2.4)$$

The emissions are not ordered, for n emissions all $n!$ permutations contribute with the same probability, and should be averaged over. While factorisable kinematics constitutes a crucial aspect, it is not sufficient to establish complete factorisability. It is also imperative to incorporate the underlying phase space. Here is the general definitions for a n -body phase space:

$$d\Phi_n(P; \{p_i\}_{1 \leq i \leq n}) = (2\pi)^{4-3n} \delta^{(4)}\left(P - \sum_{i=1}^n p_i\right) \prod_{i=1}^n d^4 p_i \delta(p_i^2 - m_i^2) \Theta(E_i), \quad (2.5)$$

where P is the centre-of-mass four-momentum of the process with individual final particle's four-momenta $\{p_i\}$ of respective mass m_i . If we start from (2.5), similarly to [61], we can split it in m arbitrary sub-phase-spaces:



$$d\Phi_n(P; \{p_i\}_{1 \leq i \leq n}) = \prod_{i=1}^m \left(\frac{dQ_i^2}{2\pi} d\Phi_{n_i}(Q_i; \{p_k^{(i)}\}_{1 \leq k \leq n_i}) \right) d\Phi_m(P; \{Q_j\}_{1 \leq j \leq m}). \quad (2.6)$$

In the case of the $n + 1$ particles, we can split the phase space into a n -particles subspace which corresponds to Born-level and a 1 particle phase space with momentum k :

$$\begin{aligned}
 d\Phi_{n+1}(P; \{p_i\}_{1 \leq i \leq n}, k) &= \frac{dQ^2}{2\pi} d\Phi_n(Q; \{p_j\}_{1 \leq j \leq n}) \frac{dQ'^2}{2\pi} d\Phi_1(Q'; k) d\Phi_2(P; Q, Q') \\
 &= d\Phi_n(Q; \{p_j\}_{1 \leq j \leq n}) d^4Q \delta^{(4)}(k + Q - P) dQ^2 \delta(Q^2 - M^2) \frac{d^4k}{(2\pi)^3} \delta(k^2) \\
 &= d\Phi_n(M; \{p_j\}_{1 \leq j \leq n}) \frac{d^3k}{(2\pi)^3 2E_k} dM^2 \delta\left((P - k)^2 - M^2\right).
 \end{aligned} \tag{2.7}$$

M symbolises the invariant mass of the final state composed of n particles. In the case of multiple emissions, we simply have $\{k_i\}$ gluons. Introducing the threshold parameters, $z = M^2/\hat{s}$ and for each emitted gluon i , $x_i = 2E_i/\sqrt{\hat{s}} = 1 - z_i$, we can make the factorisation explicit in the soft limit and the centre-of-mass frame:

$$\begin{aligned}
 \delta\left(\left[P - \sum_i k_i\right]^2 - M^2\right) &= \delta\left(\hat{s} - 2\sqrt{\hat{s}} \sum_i E_i + \left[\sum_i k_i\right]^2 - M^2\right) \\
 &\simeq \delta\left(\hat{s} - 2\sqrt{\hat{s}} \sum_i E_i - M^2\right) = \frac{1}{\hat{s}} \delta\left(1 - \sum_i x_i - z\right) \\
 &\simeq \frac{1}{\hat{s}} \delta\left(\prod_i (1 - x_i) - z\right) = \frac{1}{\hat{s}} \delta\left(z - \prod_i z_i\right),
 \end{aligned} \tag{2.8}$$

where we have neglected terms of order $\mathcal{O}(k^2)$. The factorisation of the cross section is manifest in Mellin space (refer to A.35):

$$d\Phi_{n+1}(N) \propto \int_0^1 dz z^{N-1} \delta\left(\prod_i (1 - x_i) - z\right) = \prod_i (1 - x_i)^{N-1} = \prod_i z_i^{N-1}. \tag{2.9}$$

2.1.3 Toy resummation

In order to perform resummation, as a first approximation, we will focus on the LL accuracy. This involves computing the fixed order cross section resulting from single emission, as mentioned in section 2.1.1. We already described the kinematics involved in the matrix element in (2.3) and the phase space in (2.7). Let us simply collect the results and compute the real and virtual contributions to the cross section in the eikonal approximation. This section is motivated by pedagogical reasons. We do not pretend to introduce resummation in a rigorous way. For more details, refer to section 2.2.

Real emission contribution

With the factorisation of phase space, we can express the real emission, with $z_k = 1 - 2E_k/\sqrt{\hat{s}}$:

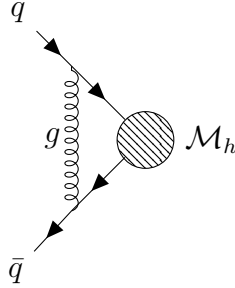
$$\frac{d\sigma_R}{d\Phi_n dM^2} = -g_s^2 \mathbf{T}^q \cdot \mathbf{T}^{\bar{q}} \frac{d\sigma_B}{d\Phi_n dM^2} \int \frac{d^3k}{(2\pi)^3 2E_k} \frac{2p_q \cdot p_{\bar{q}}}{(k \cdot p_q)(k \cdot p_{\bar{q}})} \delta(z_k - z). \quad (2.10)$$

Using (A.7), we can write after a Mellin transform with respect to z :

$$\frac{d\sigma_R(N)}{d\Phi_n dM^2} = g_s^2 C_F \frac{d\sigma_B}{d\Phi_n dM^2} \int \frac{d^3k}{(2\pi)^3 2E_k} \frac{2p_q \cdot p_{\bar{q}}}{(k \cdot p_q)(k \cdot p_{\bar{q}})} z_k^{N-1}. \quad (2.11)$$

Virtual contribution

We also need the virtual emission contribution to cancel the infrared divergences stemming from real emission (refer to A.6). This term will share the same phase space as the Born-level cross section. We can draw the corresponding diagram:



So that we have the virtual contribution:

$$\frac{d\sigma_V}{d\Phi_n dM^2} = g_s^2 C_F \frac{d\sigma_B}{d\Phi_n dM^2} \int \frac{d^4k}{(2\pi)^4} \frac{2p_q \cdot p_{\bar{q}}}{(k \cdot p_q)(k \cdot p_{\bar{q}})} \frac{-i}{k^2} \delta(1 - z). \quad (2.12)$$

At this stage, the generic gluon momentum k can be off-shell, since it is integrated in a loop. Furthermore, we can write in the centre-of-mass frame after Mellin transformation:

$$\begin{aligned} \frac{d\sigma_V(N)}{d\Phi_n dM^2} &= g_s^2 C_F \frac{d\sigma_B}{d\Phi_n dM^2} \int \frac{d^3\vec{k}}{(2\pi)^3} \frac{2p_q \cdot p_{\bar{q}}}{E_q E_{\bar{q}} (E_k^2 - |\vec{k}|^2 \cos^2(\theta))} \frac{dE_k}{E_k^2 - |\vec{k}|^2} \frac{-i}{2\pi} \\ &= -g_s^2 C_F \frac{d\sigma_B}{d\Phi_n dM^2} \int \frac{d^3\vec{k}}{(2\pi)^3 2E_k} \frac{2p_q \cdot p_{\bar{q}}}{E_q E_{\bar{q}} E_k^2 (1 - \cos^2(\theta))}. \end{aligned} \quad (2.13)$$

Exponentiation and Leading Logarithm accuracy

In the eikonal approximation, we can then write the combination of virtual and real emission:

$$\begin{aligned}
 \frac{d\sigma_e(N)}{d\Phi_n dM^2} &= C_F \frac{d\sigma_B}{d\Phi_n dM^2} \int \frac{d^3 \vec{k}}{(2\pi)^3 2E_k E_q E_{\bar{q}} E_k^2 (1 - \cos^2(\theta))} (z_k^{N-1} - 1) = I \frac{d\sigma_B}{d\Phi_n dM^2} \\
 \implies I &= \frac{\alpha_s}{2\pi^2} C_F \int_0^{\sqrt{\hat{s}}/2} \frac{dk k^2}{2k^3} (z_k^{N-1} - 1) \int_{-1}^1 \frac{4d \cos(\theta)}{1 - \cos^2(\theta)} \int_0^{2\pi} d\varphi \\
 &= 2 \frac{\alpha_s}{\pi} C_F \int_0^1 dz_k \frac{z_k^{N-1} - 1}{1 - z_k} \int_{-1}^1 \frac{d \cos(\theta)}{1 - \cos^2(\theta)}, \tag{2.14}
 \end{aligned}$$

where we used the definition: $z_k = 1 - 2k/\sqrt{\hat{s}}$ (with $k = E_k = \sqrt{\vec{k}^2}$) and integrated over the azimuthal angle φ . We can choose to parametrise the θ integration in terms of the transverse momentum of the soft gluon $k_t = \sqrt{\hat{s}} \sin(\theta)/2(1 - z_k)$. The emission factor I is quite general and encapsulates more regimes of gluon emission than strictly soft or collinear. However, we can see from the integrand that the leading behaviour appears in the regions where z_k is close to 1, or θ (or k_t) is close to 0. We recover the soft or collinear divergences, respectively regularised by virtual/real cancellation [62] and PDF counter terms. In fact, the gluon cannot be emitted at an arbitrary vanishing angle. The renormalised PDFs encapsulate emissions at small angles for $k_t \leq \mu_F$ (1.6), keeping the exchanged momentum safe from the non-perturbative regime. On the other hand, the upper limit for integration is usually set to around $k_t \lesssim M(1 - z_k)/2$ instead of $\sqrt{\hat{s}}(1 - z_k)/2$ as the softness of the emission is determined by comparison to M . Setting $z_k = z$ as a consequence of the phase space factorisation (2.8), we can write in the collinear limit:

$$\begin{aligned}
 I &= 2 \frac{\alpha_s}{2\pi} C_F \int_0^1 dz \frac{z^{N-1} - 1}{1 - z} \int_{\epsilon}^{\pi/2} \frac{2d\theta}{\sin(\theta)} \\
 &= 2 \frac{\alpha_s}{2\pi} C_F \int_0^1 dz \frac{z^{N-1} - 1}{1 - z} \int_{\mu_F}^{(1-z)M/2} \frac{2dk_t}{k_t \sqrt{1 - k_t^2/k^2}} \\
 &\simeq 2 \frac{\alpha_s}{2\pi} C_F \int_0^1 dz \frac{z^{N-1} - 1}{1 - z} \int_{\mu_F^2}^{(1-z)^2 M^2/4} \frac{dk_t^2}{k_t^2}. \tag{2.15}
 \end{aligned}$$

We can also consider the effects of the running coupling, since the momentum exchange occurs at the scale k_t . Now that we have the complete emission factor, we can do the actual resummation:

$$\sum_{n=0}^{+\infty} \frac{I^n}{n!} = \exp \left(2C_F \int_0^1 dz \frac{z^{N-1} - 1}{1 - z} \int_{\mu_F^2}^{(1-z)^2 M^2/4} \frac{dk_t^2}{k_t^2} \frac{\alpha_s(k_t)}{2\pi} \right). \tag{2.16}$$

For a detailed calculation of this Sudakov factor, see appendix A.8. The LL approximation only allows consideration of the first-order α_s term (see 1.1) and the resulting $\mathcal{O}(\alpha_s \ln^2 \bar{N})$ term, with $\bar{N} = Ne^{\gamma_E}$, γ_E being the Euler constant. Taking into account both of the incoming quark legs, we have the following Sudakov factor:

$$\begin{aligned} \exp(G_{LL}) &= \exp\left(g_1(2\lambda) \ln \bar{N}\right), \quad \lambda = \frac{\alpha_s}{2\pi} \beta_0 \ln \bar{N}, \\ g_1(2\lambda) &= \frac{A_q^{(1)}}{\beta_0 2\lambda} \left(2\lambda + (1 - 2\lambda) \ln(1 - 2\lambda)\right). \end{aligned} \quad (2.17)$$

where $A_q^{(1)} = 2C_F$, the Casimir operator relative to the emitting leg (can be adapted for other emitters like colour octets). To go beyond LL, we need to consider higher order cusp anomalous dimension

$$A_i = \sum_{j=1}^{+\infty} \left(\frac{\alpha_s}{2\pi}\right)^j A_i^{(j)},$$

as well as α_s running beyond one-loop. The cusp anomalous dimension appears order by order in the splitting functions (1.32), multiplying the + distribution terms. Now that we have derived the simplest case of soft gluon resummation, let us focus on the generalisation beyond LL accuracy and for processes with more complex colour structure.

2.1.4 Power counting

Firstly, we need to explicitly define the vocabulary of resummation and power counting in this document. As mentioned earlier, to perform resummation, we must specify the logarithmic accuracy we are considering. This requirement arises from the alternative power expansion in terms of $\alpha_s \ln \bar{N}$, in addition to the customary perturbative expansion in the coupling α_s . There are multiple methods for counting logarithmic powers. This section aims to clarify the various power countings found in the literature with as much detail as possible. From the expression of λ in (2.17), it is apparent that the Sudakov factor's functions g_i contain terms of the form $\alpha_s^m L^n$ with $L = \ln \bar{N}$. To determine m and n , we must expand g_i in $\alpha_s L$, for example, $g_1 = \mathcal{O}(\alpha_s L)$. With the usual definition of the g_i , we always have $m = n$, but, be careful that the LL factor is $g_1 L$ and not only g_1 . No matter what is the definition chosen for these functions (we could incorporate L in g_1 for example), the power counting should be done systematically to know which logarithms are resummed.

The literature [32, 58, 63–66] commonly classifies the accuracy of N^kLL resummation based on the power difference $m - n$, as $k = m - n + 1$. The LL accuracy corresponds to $\mathcal{O}(\alpha_s L^2)$ or $m - n = -1$, NLL to $\mathcal{O}(\alpha_s L)$ or $m - n = 0$, and so on. In particular, terms with $n = 0$ (hence beginning at N²LL), have a unique position since they don't depend on L . According to the classification, they are categorised as N^{m+1}LL level. Nevertheless, in some

Resummation accuracy	Cusp anom. dim. A	Anom. dim. Γ	Fixed order coeff.
LL	one-loop	\emptyset	tree-level
NLL	two-loop	one-loop	tree-level
N ² LL	three-loop	two-loop	one-loop
N ^{k} LL	$k + 1$ -loop	k -loop	$k - 1$ -loop

Table 2.1: SCET power counting

articles [58, 66], they are also considered as part of a modified version of N^mLL denoted as: N^mLL', N^mLL wC , or aN^{m+1}LL, in which the aforementioned terms are expanded at fixed order in α_s rather than exponentiated.

On the other hand, the power counting in the soft-collinear effective theory (SCET) [67] differs slightly as it is based on loop calculations. Indeed, [68–70] focus on the number of loops required to compute each resummation piece. We will provide further information on these ingredients later. SCET power counting is summarised in table 2.1.

The two ways of counting are typically consistent, but caution is advised in determining which pieces should be included (or omitted) in the resummation. For example, the fixed order coefficients of order $\mathcal{O}(\alpha_s)$ are included at the N²LL accuracy on both sides. Refer to [71] for a more detailed comparison between the SCET and perturbative QCD formalisms.

Within this document, we use the convention that terms of order $\mathcal{O}(\alpha_s)$ with no dependence on L should not be exponentiated, but rather included in the fixed order coefficients that enter the resummation computation. Refer to section 2.3 for further details. Now that we have a clear understanding of the essential concepts of resummation, let us focus on deriving the components involved in resummation computations.

2.2 General expression

2.2.1 Total cross section and PDF factorisation

In the following sections, we will provide a detailed description of the general resummation formalism. We will consider a generic process of $2 \rightarrow n + n_X$, whereby n coloured particles are present in the final states (able to emit soft gluon) and n_X are colourless particles. The latter will not contribute to the resummation on its own but will affect the kinematics. Having started from the factorisation formula (1.6), we can write the following:

$$\sigma(\tau) = \frac{1}{\mathcal{N}} \int_0^1 dx_1 dx_2 f_{\mathcal{I}_1}(x_1, \mu_F) f_{\mathcal{I}_2}(x_2, \mu_F) \frac{\langle \mathcal{A} | \mathcal{A} \rangle}{2s x_1 x_2 \omega(\mathcal{I}_1) \omega(\mathcal{I}_2)} d\Phi_{n+n_X}, \quad (2.18)$$

where $\tau = M^2/s$, \mathcal{N} is the symmetry factor for incoming partons \mathcal{I}_1 and \mathcal{I}_2 , $|\mathcal{A}\rangle$ the matrix element amplitude, and ω represents the average factors relative to spin and colour. In dimensional regularisation with $d = 4 - 2\epsilon$, we find that $\omega(q) = 2N_c$ and $\omega(g) = 2(1 - \epsilon)(N_c^2 - 1)$. The ϵ dependence for the gluon polarisation is employed in the Conventional Dimensional Regularisation (CDR) scheme [72]. However, in numerical applications, the 't Hooft-Veltman (HV) scheme [73] is preferred so that the ϵ dependence is dropped for external gluons. We can notice that in equation (2.18), we did not mention the symmetrisation $x_1 \leftrightarrow x_2$ that needs to be taken into account. Indeed, we cannot distinguish the two processes where the fraction x_1 comes from parton \mathcal{I}_1 or \mathcal{I}_2 , hence each contribution should be added to the cross section. In practice, it will lead to an additional factor of 2 in (2.22). Regarding the phase space, we reformulate (2.7) as:

$$\begin{aligned} d\Phi_{n+n_X} &= \frac{dM^2}{2\pi} d\Phi_n(M) \frac{dQ^2}{2\pi} d\Phi_{n_X}(Q) dk^2 \delta^{(4)}(k - p_k) d^4 p_k \delta(p_k^2 - M^2) d\Phi_2(P; \{Q, k\}) \\ &= \frac{dM^2}{2\pi} d\Phi_n(M) \frac{dQ^2}{2\pi} d\Phi_{n_X}(Q) d\Phi_2(P; \{Q, M\}) \\ &= \frac{dM^2}{2\pi} d\Phi_n(M) d\Phi_{1+n_X}. \end{aligned} \quad (2.19)$$

This allows us to define the partonic differential cross section:

$$\frac{d\hat{\sigma}(z)}{dM^2 d\Phi_n} = \frac{1}{2\pi \mathcal{N}} \int \frac{\langle \mathcal{A} | \mathcal{A} \rangle(z)}{\omega(\mathcal{I}_1) \omega(\mathcal{I}_2)} d\Phi_{1+n_X}, \quad (2.20)$$

where $z = \frac{M^2}{s x_1 x_2} = \frac{M^2}{\hat{s}}$ so that:

$$\begin{aligned} \sigma(\tau) &= \int_0^1 dx_1 dx_2 f_{\mathcal{I}_1}(x_1, \mu_F) f_{\mathcal{I}_2}(x_2, \mu_F) \frac{1}{2s x_1 x_2} \frac{d\hat{\sigma}(z)}{dM^2 d\Phi_n} d\Phi_n dM^2 \\ &= \int_0^1 dx_1 dx_2 dz \delta(\tau - x_1 x_2 z) x_1 f_{\mathcal{I}_1}(x_1, \mu_F) x_2 f_{\mathcal{I}_2}(x_2, \mu_F) \frac{z}{2M^2} \frac{d\hat{\sigma}(z)}{dM^2 d\Phi_n} d\Phi_n dM^2. \end{aligned} \quad (2.21)$$

This makes it easy to perform the Mellin transformation with respect to τ . Denoting the Mellin transform of PDF f_i as F_i , we have:

$$\begin{aligned}
 \sigma(N) &= \int_0^1 dx_1 dx_2 dz x_1^N f_{\mathcal{I}_1}(x_1, \mu_F) x_2^N f_{\mathcal{I}_2}(x_2, \mu_F) \frac{z^N}{2M^2} \frac{d\hat{\sigma}(z)}{dM^2 d\Phi_n} d\Phi_n dM^2 \\
 &= F_1(N+1, \mu_F) F_2(N+1, \mu_F) \int \frac{dM^2}{2M^2} \frac{d\hat{\sigma}(N+1)}{dM^2 d\Phi_n} d\Phi_n .
 \end{aligned} \tag{2.22}$$

Equation (2.22) is not specific to the context of resummation, it is simply a way to express PDF factorisation (1.6). In the following section, we detail the factorisation between the process-dependent hard part and the universal soft pieces.

2.2.2 Partonic cross section and Hard/Soft factorisation

We can now concentrate on the partonic differential cross section and its factorisation properties. At NLL accuracy, we can limit our consideration to one-loop level and $n_X = 1$. We can break down the generic amplitude $|\mathcal{A}\rangle$ into three parts: tree level $|\mathcal{A}_n^{(0)}\rangle$, one loop virtual $|\mathcal{A}_n^{(1)}\rangle$, and real emission $|\mathcal{A}_{n+1}^{(0)}\rangle$ contributions. The expansion at NLO gives:

$$\langle \mathcal{A} | \mathcal{A} \rangle = \langle \mathcal{A}_n^{(0)} | \mathcal{A}_n^{(0)} \rangle + \langle \mathcal{A}_n^{(1)} | \mathcal{A}_n^{(0)} \rangle + \langle \mathcal{A}_n^{(0)} | \mathcal{A}_n^{(1)} \rangle + \langle \mathcal{A}_{n+1}^{(0)} | \mathcal{A}_{n+1}^{(0)} \rangle . \tag{2.23}$$

Within the eikonal approximation, the latter can be expressed in terms of the tree-level amplitude and an eikonal factor, as in (2.2). With p_l the momentum of the leg l emitting the gluon k , we have:

$$\lim_{k \rightarrow 0} |\mathcal{A}_{n+1}^{(0)}\rangle = g_s \sum_l |\mathcal{A}_n^{(0)}\rangle_{\text{soft}, l} = -g_s \sum_l \frac{p_l \cdot \epsilon^*(k)}{k \cdot p_l} \mathbf{t}^l |\mathcal{A}_n^{(0)}\rangle . \tag{2.24}$$

In addition, any amplitude can be expanded over the orthogonal colour tensor basis, see section 1.3.1:

$$|\mathcal{A}\rangle = \sum_i \frac{\langle C_i | \mathcal{A} \rangle}{\langle C_i | C_i \rangle} |C_i\rangle . \tag{2.25}$$

From there, we can define the hard and soft matrices in colour space, up to one-loop level:

$$\begin{aligned}
 \mathbf{H}_{ij}^{(0)} &= \frac{1}{2\pi\mathcal{N}} \frac{1}{\omega(\mathcal{I}_1)\omega(\mathcal{I}_2)} \frac{\langle C_i | \mathcal{A}_n^{(0)} \rangle \langle \mathcal{A}_n^{(0)} | C_j \rangle}{\langle C_i | C_i \rangle \langle C_j | C_j \rangle} , \\
 \mathbf{H}_{ij}^{(1)} &= \frac{1}{2\pi\mathcal{N}} \frac{1}{\omega(\mathcal{I}_1)\omega(\mathcal{I}_2)} \frac{\langle C_i | \mathcal{A}_n^{(1)} \rangle \langle \mathcal{A}_n^{(0)} | C_j \rangle + \langle C_i | \mathcal{A}_n^{(0)} \rangle \langle \mathcal{A}_n^{(1)} | C_j \rangle}{\langle C_i | C_i \rangle \langle C_j | C_j \rangle} , \\
 \mathbf{S}_{ij}^{(0)} &= \langle C_i | C_j \rangle , \\
 \mathbf{S}_{ij}^{(1)} &= \sum_{kl} \hat{\mathcal{E}}_{kl} \langle C_i | \mathbf{t}^k \cdot \mathbf{t}^l | C_j \rangle ,
 \end{aligned} \tag{2.26}$$

where $\hat{\mathcal{E}}_{kl}$ is an eikonal factor that will be derived later in section 2.3.1. We recognise in (2.26) the expression of the colour factors of section 1.3.3, up to a multiplication by $\mathbf{S}^{(0)}$. As previously stated, PDF factorisation enables us to focus on the partonic cross section. However, we must also take into account the renormalisation of the PDF themselves in the $\overline{\text{MS}}$ scheme. In particular, it leads to PDF counterterms that are essential to cancel the infrared divergences arising from the hard function, as detailed in [36]. We reformulate slightly this result by introducing the beam functions multiplying the PDFs:

$$B_i(N) = \sum_j \hat{B}_{ij}(N, \mu, \mu_F) F_j(N, \mu_F), \quad (2.27)$$

where $\hat{B}_{ij}(N, \mu, \mu_F)$ corresponds to the Mellin transform of matching coefficients (or parton operators, see section 4 of [36]), including both singular and μ dependent parts. μ is the common scale chosen for the evaluation of the cross section, see (2.32), that can be different from μ_F . Then, up to first order, we have:

$$\hat{B}_{ij}^{(0)}(N, \mu, \mu_F) = \delta_{ij} \quad \hat{B}_{ij}^{(1)}(N, \mu, \mu_F) = \frac{(4\pi)^\epsilon}{\Gamma(1-\epsilon)} \left[\frac{1}{\epsilon} + \ln\left(\frac{\mu^2}{\mu_F^2}\right) \right] P_{ij}^{(1)}(N), \quad (2.28)$$

with the general perturbative expansion in terms of α_s for any quantity \mathbf{X} :

$$\mathbf{X} = \sum_{k=0}^n \mathbf{X}^{(k)} \left(\frac{\alpha_s}{2\pi} \right)^k. \quad (2.29)$$

In the large N limit, we have for the splitting kernels:

$$P_{ij}^{(1)}(N) = \delta_{ij} \left(-2C_i \ln \bar{N} + \gamma_i \right), \quad (2.30)$$

where γ_i is the collinear anomalous dimension, see (1.31):

$$\gamma_q = \frac{3}{2} C_F, \quad \gamma_g = \beta_0. \quad (2.31)$$

So that, at one-loop level, the beam functions are diagonal in flavour space. Therefore, we can maintain the original PDFs in (2.22) whilst incorporating the beam functions into the partonic cross-section. We can focus on the regular term alone in (2.28), after the cancellation of poles since we consider the renormalised quantities, free of divergences. In addition, as we have seen in section 2.1.3, resummation implies the introduction of exponential factors like the colour-diagonal Sudakov form factor (see appendix A.8), noted as $G(\lambda, \mu_R, \mu_F) = \exp\left(g_1(\lambda) \ln \bar{N} + g_2(\lambda)\right)$ at NLL. Finally, we can formulate the

differential cross section using the soft and hard colour matrices, incorporating the beam functions:

$$\frac{d^2\hat{\sigma}^{\text{res.}}(N, \mu)}{dM^2 d\Phi_n} = \text{Tr}\left(\mathbf{H}(\mu, \mu_R) \cdot \mathbf{S}(\mu, \mu_S)\right) \hat{B}_1(N, \mu, \mu_F) \hat{B}_2(N, \mu, \mu_F) G(\lambda, \mu_R, \mu_F). \quad (2.32)$$

The hard matrix \mathbf{H} encapsulates the underlying high-energy partonic process. Order by order it includes the virtual loops that are N independent, as we can see from the definitions in (2.26). On the other hand, \mathbf{S} encodes the soft radiations arising in the process. In particular, it contains the N dependent threshold logarithms that we aim to resum. The matching coefficients have the following expansion at a fixed order in α_s :

$$\mathbf{S} = \sum_{k=0}^n \mathbf{S}^{(k)} \left(\frac{\alpha_s}{2\pi}\right)^k, \quad \mathbf{H} = \sum_{k=0}^n \mathbf{H}^{(k)} \left(\frac{\alpha_s}{2\pi}\right)^k. \quad (2.33)$$

In (2.32), we detailed the scale dependence of each piece, including the common scale μ as well as the respective initial scales: μ_R from α_s renormalisation, μ_F from PDF factorisation and μ_S from the soft matrix renormalisation. In principle, any scale μ could be chosen to evaluate the partonic cross section. However, in order to avoid the use of more scales than necessary, the renormalisation scale μ_R is used as a common scale for the evaluation: $\mu = \mu_R$. Therefore, the hard function is directly evaluated at the relevant scale, while the soft and beam functions have to be evolved, as described in sections 2.3.2 and 2.3.3. We chose to evaluate at μ_R to focus on the soft physics involved in the evolution of the soft function but other choices exist in the literature.

The following sections aim to provide further information on the pieces mentioned above, particularly the soft matrix $\mathbf{S}^{(1)}$. In the soft approximation, the elements of the resummation are, to some extent, universal. This implies that the soft parts of a given process do not depend on hard-scale physics or fixed-order loop computations outside the soft regime. Although they depend on the particle content of the process, they can also be employed for other calculations. This essential resummation property will be extensively used in chapter 3 to repurpose the commonly known functions associated with the Drell-Yan process for the case of exotic BSM lepton production.

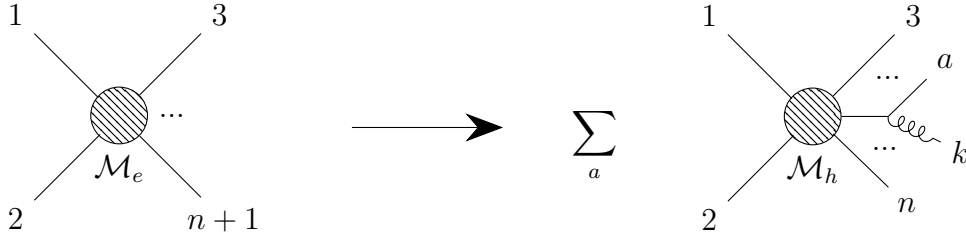
2.3 Colour matrices

2.3.1 Soft matrix

At tree level we can simply express the soft function as products of the colour basis tensors, see (2.26). As we chose an orthogonal basis, $\mathbf{S}^{(0)}$ is diagonal:

$$\mathbf{S}_{ij}^{(0)} = \langle C_i | C_j \rangle = \delta_{ij} \langle C_i | C_i \rangle . \quad (2.34)$$

At first loop level, we can use the previous eikonal Feynman rules (2.2) and phase space factorisation (2.7) to compute the soft function matrix. The eikonal decomposition at amplitude level can be represented diagrammatically as following, with the sum running on all partons (incoming or outgoing):



This translates at the differential cross section level as:

$$\begin{aligned} d\Phi_{n+1} \overline{\sum} |\mathbf{M}_e|^2 &= d\Phi_n \overline{\sum} |\mathbf{M}_h|^2 g_s^2 \mu^{2\epsilon} \sum_{ab} \mathbf{t}^a \cdot \mathbf{t}^b \frac{-p_a \cdot p_b}{p_a \cdot k p_b \cdot k} \frac{d^{d-1}k}{(2\pi)^{d-1} 2|k|} dM^2 \delta((P-k)^2 - M^2) \\ &= -d\sigma_B \frac{\alpha_s \mu^{2\epsilon}}{4\pi^2 \hat{s}} \sum_{ab} \mathbf{t}^a \cdot \mathbf{t}^b \frac{p_a \cdot p_b k^2}{p_a \cdot k p_b \cdot k} \frac{dk k^{-1-2\epsilon}}{(2\pi)^{-2\epsilon}} dM^2 \delta\left(1 - z - \frac{2k}{\sqrt{\hat{s}}}\right) d\Omega_{3-2\epsilon} , \end{aligned} \quad (2.35)$$

with $d\Omega_i$ the differential for angles in i dimensions. Dropping the dM^2 integration and performing the integration on the gluon momentum k , we obtain:

$$d\sigma_B d\mathbf{S}^{(1)} = -d\sigma_B \frac{\alpha_s}{4\pi^2} \sum_{ab} \mathbf{t}^a \cdot \mathbf{t}^b (4\pi)^{2\epsilon} \left(\frac{\mu^2}{M^2}\right)^\epsilon z^\epsilon (1-z)^{-1-2\epsilon} d\Omega_{3-2\epsilon} k^2 \frac{p_a \cdot p_b}{p_a \cdot k p_b \cdot k} . \quad (2.36)$$

We need to expand the factor $(1-z)^{-1-2\epsilon}$ as follows:

$$(1-z)^{-1-2\epsilon} = -\frac{\delta(1-z)}{2\epsilon} + \frac{1}{1-z} \Big|_+ - 2\epsilon \frac{\ln(1-z)}{1-z} \Big|_+ + \mathcal{O}(\epsilon^2) . \quad (2.37)$$

The soft matrix is obtained by the integration over the angles in $d-1 = 3-2\epsilon$ dimensions:

$$\begin{aligned}
 \frac{\alpha_s}{2\pi} \mathbf{S}^{(1)} &= - \sum_{a,b} \mathbf{t}^a \cdot \mathbf{t}^b \frac{\alpha_s}{4\pi^2} (4\pi)^{2\epsilon} \left(\frac{\mu^2}{M^2} \right)^\epsilon z^\epsilon (1-z)^{-1-2\epsilon} \int d\Omega_{3-2\epsilon} k^2 \frac{p_a \cdot p_b}{p_a \cdot k p_b \cdot k} \\
 &= - \sum_{a,b} \mathbf{t}^a \cdot \mathbf{t}^b \frac{\alpha_s}{4\pi^2} (4\pi)^\epsilon \left(\frac{\mu^2}{M^2} \right)^\epsilon z^\epsilon \frac{4\pi}{\Gamma(1-\epsilon)} \\
 &\quad \left(- \frac{\delta(1-z)}{2\epsilon} + \frac{1}{1-z} \Big|_+ - 2\epsilon \frac{\ln(1-z)}{1-z} \Big|_+ \right) \left(\frac{\Omega_{-1}^{ab}}{\epsilon} + \Omega_0^{ab} + \Omega_1^{ab} \epsilon \right) \\
 &= \sum_{a,b} \mathbf{t}^a \cdot \mathbf{t}^b \frac{\alpha_s}{\pi} \frac{(4\pi)^\epsilon}{\Gamma(1-\epsilon)} \left(\frac{\mu^2}{M^2} \right)^\epsilon \left(\frac{\delta(1-z)\Omega_{-1}}{2\epsilon^2} - \frac{\Omega_{-1}}{\epsilon} \frac{1}{1-z} \Big|_+ \right. \\
 &\quad \left. + \frac{\delta(1-z)\Omega_0}{2\epsilon} + 2\Omega_{-1} \frac{\ln(1-z)}{1-z} \Big|_+ - \Omega_0 \frac{1}{1-z} \Big|_+ - \Omega_{-1} \frac{\ln(z)}{1-z} + \frac{\delta(1-z)\Omega_1}{2} \right), \tag{2.38}
 \end{aligned}$$

where we omitted the ab superscript on Ω_i^{ab} for simplicity, but we should keep in mind that the Ω_i coefficients still depend on the corresponding partons (a, b). Applying the Mellin transform to the previous expression is relatively straightforward (refer to A.35):

$$\begin{aligned}
 \mathbf{S}^{(1)} &= \sum_{a,b} \mathbf{t}^a \cdot \mathbf{t}^b \frac{(4\pi)^\epsilon}{\Gamma(1-\epsilon)} \left(\frac{\mu^2}{M^2} \right)^\epsilon \left[\frac{\Omega_{-1}}{\epsilon^2} + \frac{2\Omega_{-1}}{\epsilon} \ln \bar{N} + \frac{\Omega_0}{\epsilon} \right. \\
 &\quad \left. + 2\Omega_{-1} \left(\ln^2 \bar{N} + \frac{\pi^2}{6} \right) + 2\Omega_0 \ln \bar{N} + \Omega_1 \right] + \mathcal{O}\left(\frac{1}{N}\right) + \mathcal{O}(\epsilon). \tag{2.39}
 \end{aligned}$$

The expressions of Ω_i , depending on the masses of partons a and b , are detailed in table 2.2, with:

$$v_{ab} = \sqrt{1 - \left(\frac{m_a m_b}{p_a \cdot p_b} \right)^2} \quad \text{and} \quad \beta_a = \sqrt{1 - \left(\frac{m_a}{E_a} \right)^2}.$$

From (2.39), it can be observed that $\mathbf{S}^{(1)}$ contains poles, a scale dependence as well as finite reminders, including both L dependent and independent terms. The soft matrix is not expressed in the colour tensor basis but directly in terms of colour factors from section 1.3.2. In order to obtain a comparable formula to (2.26), projection on $\langle C_i | \bullet | C_j \rangle$ is required.

Ω coefficients

In order to obtain the expression of the Ω coefficients, we need to perform the angular integral in $d-1$ dimensions. We can extract those results from the eikonal integral in [57], where we have the following expressions:

	$a = b \ m_a = 0$	$a = b \ m_a \neq 0$	$m_a = 0 = m_b$	$m_a = 0 \ m_b \neq 0$	$m_a m_b \neq 0$
Ω_{-1}	0	0	-1	-1/2	0
Ω_0	0	1	$\ln \frac{p_a \cdot p_b}{2E_a E_b}$	$\ln \frac{p_a \cdot p_b}{E_a m_b}$	$\frac{1}{2v_{ab}} \ln \left(\frac{1 + v_{ab}}{1 - v_{ab}} \right)$
Ω_1	0	$\frac{1}{\beta_a} \ln \left(\frac{1 + \beta_a}{1 - \beta_a} \right)$	$\frac{\pi^2}{6} + \text{Li}_2 \left(1 - \frac{2E_a E_b}{p_a \cdot p_b} \right)$	ϑ_1	ϑ_2

Table 2.2: Eikonal coefficients $\Omega_{-1/0/1}$ for each combination of massive/massless Wilson lines

$$\mathcal{E}_{ij} = -\frac{\xi^{-2\epsilon}}{2\epsilon} \frac{2^{2\epsilon}}{(2\pi)^{1-2\epsilon}} \left(\frac{s}{\mu^2} \right)^{-\epsilon} \int d\Omega_k^{(d-1)} E_k^2 \frac{p_i \cdot p_j}{(p_i \cdot k)(p_j \cdot k)} = \frac{(4\pi)^\epsilon}{\Gamma(1-\epsilon)} \left(\frac{\mu^2}{M^2} \right)^\epsilon \left[\frac{\mathcal{E}_{-2}}{\epsilon^2} + \frac{\mathcal{E}_{-1}}{\epsilon} + \mathcal{E}_0 \right]. \quad (2.40)$$

where we omitted the ij dependence in the same manner as we did for the Ω coefficients. The connection between the eikonal factor \mathcal{E}_{ij} and Ω^{ij} is straightforward, simply cancelling the $\ln \left(\frac{s\xi^2}{M^2} \right)$ component.

$$\begin{aligned} \bullet \Omega_1 &= -\mathcal{E}_0 - \mathcal{E}_{-1} \ln \left(\frac{s\xi^2}{M^2} \right) - \frac{\mathcal{E}_{-2}}{2} \ln^2 \left(\frac{s\xi^2}{M^2} \right), \\ \bullet \Omega_0 &= -\mathcal{E}_{-1} - \mathcal{E}_{-2} \ln \left(\frac{s\xi^2}{M^2} \right), \\ \bullet \Omega_{-1} &= -\mathcal{E}_{-2}. \end{aligned} \quad (2.41)$$

All the simple expressions of the Ω coefficients can be checked from the results in [57]. We only detail the complex formulas, namely ϑ_1 and ϑ_2 from table 2.2. However, before going any further we should clarify the expression in the massless scenario:

- For $m_a = m_b = 0$, we have:

$$\Omega_1 = \text{Li}_2 \frac{p_a \cdot p_b}{2E_a E_b} - \frac{1}{2} \ln^2 \frac{p_a \cdot p_b}{2E_a E_b} + \ln \frac{p_a \cdot p_b}{2E_a E_b} \ln \left(1 - \frac{p_a \cdot p_b}{2E_a E_b} \right) = \frac{\pi^2}{6} + \text{Li}_2 \left(1 - \frac{2E_a E_b}{p_a \cdot p_b} \right). \quad (2.42)$$

- For ϑ_1 , in the case $m_b = 0 \neq m_a$, we have:

$$\begin{aligned}
 \vartheta_1 &= \frac{\pi^2}{12} + \frac{1}{4} \ln^2\left(\frac{1 + \beta_a}{1 - \beta_a}\right) + \text{Li}_2\left(1 - \frac{E_a E_b (1 + \beta_a)}{p_a \cdot p_b}\right) - \text{Li}_2\left(1 - \frac{p_a \cdot p_b}{E_a E_b (1 - \beta_a)}\right) - \frac{1}{2} \ln^2\left(\frac{p_a \cdot p_b}{E_a E_b (1 - \beta_a)}\right) \\
 &= \frac{\pi^2}{12} + \frac{1}{4} \ln^2\left(\frac{1 + \beta_a}{1 - \beta_a}\right) + \text{Li}_2\left(1 - \frac{E_a E_b (1 + \beta_a)}{p_a \cdot p_b}\right) + \text{Li}_2\left(1 - \frac{E_a E_b (1 - \beta_a)}{p_a \cdot p_b}\right).
 \end{aligned} \tag{2.43}$$

- For ϑ_2 , in the case $m_a \neq 0$, $m_b \neq 0$, $a \neq b$, we have:

$$\vartheta_2 = \frac{-(1 + v_{ab})(p_a \cdot p_b)^2}{2m_a^2} \left(J^{(A_{kl})}(\alpha_{ab} E_a, \alpha_{ab} E_a \beta_a) - J^{(A_{kl})}(E_b, E_b \beta_b) \right), \tag{2.44}$$

with:

$$J^{(A_{kl})}(x, y) = \frac{1}{2\nu_{kl}\lambda_{kl}} \left[\ln^2\left(\frac{x - y}{x + y}\right) + 4\text{Li}_2\left(1 - \frac{x + y}{\nu_{kl}}\right) + 4\text{Li}_2\left(1 - \frac{x - y}{\nu_{kl}}\right) \right], \tag{2.45}$$

$$\text{where : } \quad \nu_{kl} = \frac{\alpha_{kl}^2 m_k^2 - m_l^2}{2\lambda_{kl}}, \quad \lambda_{kl} = \alpha_{kl} E_k - E_l \quad \text{and} \quad \alpha_{kl} = \frac{1 + v_{kl}}{m_k^2} p_k \cdot p_l.$$

In the specific case of top (or other heavy quark) pair production, these expressions become slightly simpler (see A.7.1). We now have the generic expression for the scale dependent $\mathbf{S}^{(1)}$ before any resummation or cancellation of poles. Henceforth, we will assume that the cancellation of the poles has been achieved and focus on the regular part of $\mathbf{S}^{(1)}$. It is important to note that the structure of the poles is crucial for the expansion of the scale-dependent factor. Even if we don't include them *per se* in the soft matrix, the poles echo in the scale dependence. Let us collect the regular components of $\mathbf{S}^{(1)}$, including the μ dependence.

$$\mathbf{S}^{(1)} = \frac{(4\pi)^\epsilon}{\Gamma(1 - \epsilon)} \sum_{a,b} \mathbf{t}^a \cdot \mathbf{t}^b \left\{ \Omega_{-1} \left[\frac{1}{2} \ln^2\left(\frac{\mu^2 \bar{N}^2}{M^2}\right) + \frac{\pi^2}{3} \right] + \Omega_0 \ln\left(\frac{\mu^2 \bar{N}^2}{M^2}\right) + \Omega_1 \right\}. \tag{2.46}$$

From this, it is apparent that the scale choice $\mu = M/\bar{N} \equiv \mu_S$ is special since it cancels the logarithmic contributions and L dependence. This scale corresponds physically to the soft scale that governs gluon emission under the eikonal approximation. It will be used as the initial condition for $\mathbf{S}^{(1)}$ in the renormalisation group evolution, as it renders the matching coefficient independent of L . However, it is crucial to select a consistent evaluation scale for all resummation components. If the partonic cross section is evaluated

at renormalisation scale μ_R , we need to evolve $\mathbf{S}^{(1)}$ accordingly from μ_S to μ_R . We can link expression (2.47) with the definition (2.32) by setting:

$$\hat{\mathcal{E}}_{kl} = \frac{(4\pi)^\epsilon}{\Gamma(1-\epsilon)} \left(\Omega_{-1} \frac{\pi^2}{3} + \Omega_1 \right). \quad (2.47)$$

2.3.2 Soft anomalous dimension matrix

The soft anomalous dimension matrix determines how the soft function evolves with the scale. Therefore, it should satisfy the following RGE order by order:

$$\frac{d\mathbf{S}}{d \ln(\mu^2)} = \Gamma_S \cdot \mathbf{S} + \mathbf{S} \cdot \Gamma_S^\dagger. \quad (2.48)$$

Which gives at first order in α_s ($\Gamma_S^{(0)} = 0$):

$$\frac{d\mathbf{S}^{(1)}}{d \ln(\mu^2)} = \Gamma_S^{(1)} \cdot \mathbf{S}^{(0)} + \mathbf{S}^{(0)} \cdot \Gamma_S^{(1)\dagger}. \quad (2.49)$$

We can formally solve this equation:

$$\mathbf{S}(\mu) = \mathcal{P} \exp \left[\int_{\mu_S^2}^{\mu^2} \frac{d\mu'^2}{\mu'^2} \frac{\alpha_s(\mu')}{2\pi} \Gamma_S^{(1)} \right] \mathbf{S}(\mu_S) \mathcal{P} \exp \left[\int_{\mu_S^2}^{\mu^2} \frac{d\mu'^2}{\mu'^2} \frac{\alpha_s(\mu')}{2\pi} \Gamma_S^{(1)\dagger} \right], \quad (2.50)$$

where the \mathcal{P} stands for path ordering, needed for formal integration of matrices in exponentials. The equation (2.49) alone is insufficient to determine Γ_S uniquely, although the final result should satisfy it. Actually, the anomalous dimension is defined from the renormalisation factors \mathbf{Z}_S acting on the soft amplitude. We can write the (renormalised) soft matrix as a product of soft amplitudes:

$$\mathbf{S}^{\overline{\text{MS}}} = \left| A_S^{\overline{\text{MS}}} \right\rangle \left\langle A_S^{\overline{\text{MS}}} \right| \quad \left| A_S^{\overline{\text{MS}}} \right\rangle = \lim_{\epsilon \rightarrow 0} \mathbf{Z}_S^{-1} |A_S\rangle. \quad (2.51)$$

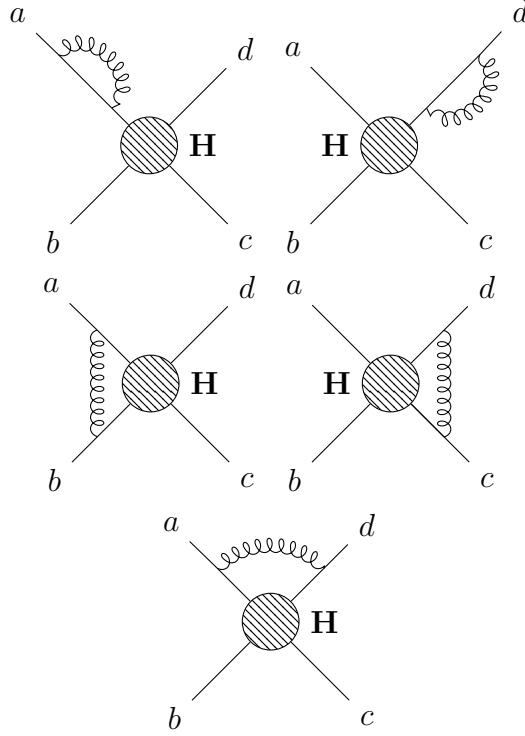
Then we can define Γ_S from the renormalisation factors:

$$\frac{d \left| A_S^{\overline{\text{MS}}} \right\rangle}{d \ln(\mu^2)} = \Gamma_S \cdot \left| A_S^{\overline{\text{MS}}} \right\rangle \implies \Gamma_S = \frac{d\mathbf{Z}_S^{-1}}{d \ln(\mu^2)} \cdot \mathbf{Z}_S. \quad (2.52)$$

At tree-level, the renormalisation factor is simply the identity: $\mathbf{Z}_S^{(0)} = 1$. Once expressed in the colour tensor basis, we recover (2.34). We can easily express:

$$\Gamma_S^{(1)} = \frac{d\mathbf{Z}_S^{(1)-1}}{d \ln(\mu^2)} \cdot \mathbf{Z}_S^{(0)} = -\mathbf{Z}_S^{(0)-1} \cdot \frac{d\mathbf{Z}_S^{(1)}}{d \ln(\mu^2)}. \quad (2.53)$$

In the $\overline{\text{MS}}$ scheme, the renormalisation factor eliminates the UV divergences for both the soft and hard functions individually. The remaining IR divergences arising from the virtual contribution have to cancel out exactly the real emission poles order by order (see A.6). Thus, by calculating the virtual one-loop poles, we can determine the soft poles (with a minus sign). We consider two external Wilson lines connected through a soft gluon, with a and b massless, c and d massive:



Here, we consider the case of four external legs in order to cover all possible combinations of massive or massless Wilson lines. Nevertheless, this reasoning also applies if there are fewer or more external particles. In general, the virtual integral connecting the Wilson lines i and j , in the eikonal approximation, can be expressed as:

$$|A_S\rangle^{ij} = (-1)^{\delta_{ij}} \mathbf{t}^i \cdot \mathbf{t}^j \int \frac{d^d k}{(2\pi)^d} \frac{2ig_s^2 \sigma_{ij} p_i \cdot p_j}{k^2 ((k + p_i)^2 - m_i^2) ((k + \sigma_{ij} p_j)^2 - m_j^2)}, \quad (2.54)$$

where $\sigma_{ij} = -1$ for different Wilson lines from the same side (incoming or outgoing), otherwise (opposite sides or same Wilson line) $\sigma_{ij} = 1$. This term is equivalent to $\mathcal{S}_{ij} = \delta_i \delta_j \Delta_i \Delta_j$ in the original formulation [27]. Therefore, the $\mathbf{Z}_S^{(1)}$ factor corresponds to the poles resulting from the integral (2.54). The poles will be subtracted from $|A_S\rangle$ to obtain the finite $|A_S^{\overline{\text{MS}}}\rangle$. In fact, we can use once again the eikonal integrals from [57] as

we did in section 2.35 to derive the poles. With $\mathbf{Z}_S^{(1)} = \sum_{ij} \mathbf{Z}_S^{(1)ij}$, we can express $\mathbf{Z}_S^{(1)ij}$, noting the Binoth factor as $\mathcal{S}_\epsilon = \frac{(4\pi)^\epsilon}{\Gamma(1-\epsilon)}$, for each case depicted in the diagrams above:

$$\begin{aligned}
 &\bullet \ i = j, \ m_i = 0 & \mathbf{Z}_S^{(1)ii} &= 0, \\
 &\bullet \ i = j, \ m_i \neq 0 & \mathbf{Z}_S^{(1)ii} &= -\frac{\alpha_s}{4\pi} \mathcal{S}_\epsilon \left(\frac{\mu^2}{M^2} \right)^\epsilon \frac{C_i}{\epsilon} \mathbf{1}, \\
 &\bullet \ i \neq j, \ m_i = m_j = 0 & \mathbf{Z}_S^{(1)ij} &= 2 \frac{\alpha_s}{4\pi} \mathcal{S}_\epsilon \left(\frac{\mu^2}{M^2} \right)^\epsilon \mathbf{t}^i \cdot \mathbf{t}^j \left[\frac{1}{\epsilon^2} - \frac{1}{\epsilon} \ln \left(\frac{\sigma_{ij} p_i \cdot p_j}{2E_i E_j} \right) \right], \\
 &\bullet \ i \neq j, \ m_i m_j \neq 0 & \mathbf{Z}_S^{(1)ij} &= \frac{\alpha_s}{4\pi} \mathcal{S}_\epsilon \left(\frac{\mu^2}{M^2} \right)^\epsilon \mathbf{t}^i \cdot \mathbf{t}^j \frac{2}{\epsilon} \frac{1}{v_{ij}} \left[-\ln \left(\frac{1+v_{ij}}{1-v_{ij}} \right) + 2i\pi \right], \\
 &\bullet \ m_i \neq m_j = 0 & \mathbf{Z}_S^{(1)ij} &= \frac{\alpha_s}{4\pi} \mathcal{S}_\epsilon \left(\frac{\mu^2}{M^2} \right)^\epsilon \mathbf{t}^i \cdot \mathbf{t}^j \left[\frac{1}{\epsilon^2} - \frac{2}{\epsilon} \ln \left(\frac{p_i \cdot p_j}{E_j m_i} \right) \right].
 \end{aligned} \tag{2.55}$$

We have double poles in the massless components of $\mathbf{Z}_S^{(1)}$ due to soft collinear divergence. However, this behaviour should not be considered when calculating the soft anomalous dimension since it also includes collinear divergence, which is not present in pure soft objects. Soft-collinear resummation will be included at the level of the Sudakov form factor, see appendix A.8.

At the one-loop level, we can derive the soft anomalous dimension colour matrix:

$$\frac{\alpha_s}{2\pi} \Gamma_{S,kl}^{(1)} = \left(\frac{d\mathbf{Z}_S^{(1)}}{d \ln(\mu^2)} \cdot \mathbf{Z}_S^{(0)} \right)_{kl} = -\frac{1}{\langle C_k | C_k \rangle} \frac{d\mathbf{Z}_{S,kl}^{(1)}}{d \ln(\mu^2)} = -\frac{\alpha_s}{2\pi} \mathcal{S}_\epsilon \sum_{ij} \omega^{ij} \frac{\langle C_k | \mathbf{t}^i \cdot \mathbf{t}^j | C_l \rangle}{\langle C_k | C_k \rangle}, \tag{2.56}$$

where we introduced the eikonal factors ω^{ij} , which encode the result of the $\mathbf{Z}_S^{(1)}$ derivation. The derivation with respect to $\ln(\mu^2)$ is equivalent to cancelling $(\mu^2/M^2)^\epsilon/\epsilon$ in (2.55), as we already argued that double poles should not affect the computation. This decomposition allows for the separation of the anomalous dimension matrix computation into two independent pieces, namely the colour factors $\mathbf{t}^i \cdot \mathbf{t}^j$ expressed in the colour basis, and the eikonal factors ω^{ij} arising from the previous eikonal integrals. The colour factors are the matrix representation of the colour tensors established in section 1.3.2, in the colour tensor basis used for the process. We simply ensure that the normalisation is correct by checking the quadratic case:

$$\frac{\langle C_k | \mathbf{t}^i \cdot \mathbf{t}^i | C_l \rangle}{\langle C_k | C_k \rangle} = C_i \delta_{kl},$$

where the right hand side C_i is the quadratic Casimir operator. These colour factors depend only on the colour representation and contain no information about the kinematics of the process. In a sense they are just a family of matrices spanning Γ_S with eikonal weights.

Once the global normalisation is settled, we can express the eikonal factors ω^{ij} . However, we must stress out that there is no unique expression of these eikonal factors. We can illustrate this by using the colour conservation and shifting the weight by an arbitrary quantity: $\tilde{\omega}^{ij} = \omega^{ij} + \delta^i$. Then, by colour conservation we have:

$$\begin{aligned} \sum_{ij} \tilde{\omega}^{ij} \frac{\langle C_k | \mathbf{t}^i \cdot \mathbf{t}^j | C_l \rangle}{\langle C_k | C_k \rangle} &= \sum_{ij} \omega^{ij} \frac{\langle C_k | \mathbf{t}^i \cdot \mathbf{t}^j | C_l \rangle}{\langle C_k | C_k \rangle} + \sum_i \delta^i \frac{\langle C_k | \mathbf{t}^i \cdot \left(\sum_j \mathbf{t}^j \right) | C_l \rangle}{\langle C_k | C_k \rangle} \\ &= \sum_{ij} \omega^{ij} \frac{\langle C_k | \mathbf{t}^i \cdot \mathbf{t}^j | C_l \rangle}{\langle C_k | C_k \rangle}, \end{aligned} \quad (2.57)$$

Here is a set of expressions for the eikonal factors that are coherent with [27] or [74]:

$$\begin{aligned} \bullet \quad i = j, \quad m_i = 0 \quad &\omega^{ii} = 0, \\ \bullet \quad i = j, \quad m_i \neq 0 \quad &\omega^{ii} = -\frac{1}{2}, \\ \bullet \quad i \neq j, \quad m_i = m_j = 0 \quad &\omega^{ij} = -\ln \left(\frac{p_i \cdot p_j}{2E_i E_j} \right) - \frac{i\pi}{2} (1 - \sigma_{ij}), \\ \bullet \quad m_i \neq m_j = 0 \quad &\omega^{ij} = -\ln \left(\frac{p_i \cdot p_j}{E_j m_i} \right), \\ \bullet \quad i \neq j, \quad m_i, m_j \neq 0 \quad &\omega^{ij} = -\frac{1}{v_{ij}} \left[\ln \left(\frac{1 + v_{ij}}{1 - v_{ij}} \right) + 2i\pi \right]. \end{aligned} \quad (2.58)$$

For simplicity gauge dependent terms, like the ν_i in [27], have been excluded from the ω factors, as Γ_S should be gauge invariant. Of course gauge terms should not have any physical contribution, and we can check that they either cancel or give a pure-imaginary diagonal contribution not affecting the evolution of the soft function. For explicit examples of soft anomalous dimension matrices, refer to appendix A.7.2.

It should be noted that $\Gamma_S^{(1)}$ does not depend on any arbitrary scale μ . As a result, the soft anomalous dimension can be positioned in front of the integration in (2.50) and the path ordering \mathcal{P} can be omitted. With this simplification, we can perform the evolution integral from μ_S to μ_R , using the x definition from (1.3):

$$\begin{aligned}
 \Gamma_S^{(1)} \int_{\mu_S^2}^{\mu_R^2} \frac{d\mu'^2}{\mu'^2} \frac{\alpha_s}{2\pi} \frac{1}{1+x(\mu')} &= -\frac{\alpha_s}{2\pi} \Gamma_S^{(1)} \frac{2\pi}{\alpha_s \beta_0} \int_0^{x(\mu_S)} \frac{dx}{x} \frac{1}{1+x} \\
 &= -\frac{\Gamma_S^{(1)}}{\beta_0} \ln \left[1 - \frac{\alpha_s}{\pi} \beta_0 \ln \left(\frac{\mu_R \bar{N}}{M} \right) \right] \\
 &= -\frac{\Gamma_S^{(1)}}{\beta_0} \left[\ln(1-2\lambda) + \ln \left(1 + \frac{x(M)}{1-2\lambda} \right) \right] \\
 &\simeq -\frac{\Gamma_S^{(1)}}{\beta_0} \left[\ln(1-2\lambda) + \frac{\alpha_s}{2\pi} \beta_0 \ln \left(\frac{M^2}{\mu_R^2} \right) \left(1 + \frac{2\lambda}{1-2\lambda} \right) \right].
 \end{aligned} \tag{2.59}$$

We observe that the integration results in a part that depends on N , which contributes to the resummation through an exponential factor and a second term that contains an N -independent piece that should be expanded at fixed order. The final term, proportional to $2\lambda/(1-2\lambda)$, is of order $\mathcal{O}(\alpha_s^2 L)$ and only contributes to N²LL accuracy, which is beyond the scope of this study.

2.3.3 Beam functions

In order to evolve the renormalised beam functions from μ_F to μ_R , similarly to the soft function's evolution from μ_S to μ_R , the corresponding RGEs for the beam functions need to be solved. The kernels of the RGEs are simply the splitting kernels (1.32) as the beam functions account for the PDFs and their counter terms. At first order, the beam functions and splitting kernels are diagonal in flavour space. We have the following RGE, including the PDF, expanded at order $\mathcal{O}(\alpha_s)$:

$$\begin{aligned}
 \frac{dB_i}{d \ln(\mu^2)} &= \sum_j P_{ij} B_j, \\
 \frac{dB_i^{(1)}}{d \ln(\mu^2)} &= P_{ii}^{(1)} f_i(\mu_F),
 \end{aligned} \tag{2.60}$$

with the formal solution for the beam functions:

$$\hat{B}_i(N, \mu, \mu_F) = \exp \left[\int_{\mu_0^2}^{\mu^2} \frac{d\mu'^2}{\mu'^2} \frac{\alpha_s(\mu')}{2\pi} P_{ii}^{(1)}(N) \right] \hat{B}_i(N, \mu_0, \mu_F), \tag{2.61}$$

with $\hat{B}_i(N, \mu_F, \mu_F) = 1$. Since $P_{ii}^{(1)}(N) = -2C_i \ln(\bar{N}) + \gamma_i$, the L independent part should be expanded, while the N dependent part is included in the g_2 function of the Sudakov factor (see A.78). Indeed, the integration gives:

$$\begin{aligned}
 \int_{\mu_F^2}^{\mu_R^2} \frac{d\mu'^2}{\mu'^2} \frac{\alpha_s}{2\pi} \frac{-2C_i \ln(\overline{N}) + \gamma_i}{1+x(\mu')} &= -\frac{\alpha_s}{2\pi} \left(-2C_i \ln(\overline{N}) + \gamma_i \right) \frac{2\pi}{\alpha_s \beta_0} \int_0^{x(\mu_F)} \frac{dx}{1+x} \\
 &= -\frac{-2C_i \ln(\overline{N}) + \gamma_i}{\beta_0} \ln \left[1 + \frac{\alpha_s}{\pi} \beta_0 \ln \left(\frac{\mu_F}{\mu_R} \right) \right] \\
 &\simeq -\frac{\alpha_s}{2\pi} \left(-2C_i \ln(\overline{N}) + \gamma_i \right) \ln \left(\frac{\mu_F^2}{\mu_R^2} \right) + \mathcal{O}(\alpha_s^2).
 \end{aligned} \tag{2.62}$$

After expansion, we have the N -independent beam contribution at one-loop:

$$\tilde{B}_i(\mu_R, \mu_F) = \tilde{B}_i^{(0)}(\mu_R, \mu_F) + \frac{\alpha_s}{2\pi} \tilde{B}_i^{(1)}(\mu_R, \mu_F) = 1 + \frac{\alpha_s}{2\pi} \ln \left(\frac{\mu_R^2}{\mu_F^2} \right) \gamma_i. \tag{2.63}$$

And the resummed contribution entering the Sudakov, see the last term in (A.78):

$$\ln \left(\frac{\hat{B}_i}{\tilde{B}_i} \right) (\mu_R, \mu_F) = \frac{2C_i \lambda}{\beta_0} \ln \left(\frac{\mu_F^2}{\mu_R^2} \right). \tag{2.64}$$

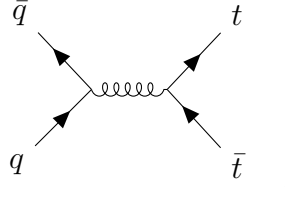
2.3.4 Hard matrix

The hard matrices may be defined order by order *via* the coloured loop amplitudes $\left| \mathcal{A}_n^{(k)} \right\rangle$ and their contraction with the colour tensor basis, as defined in section 2.3.1. The amplitudes $\left| \mathcal{A}_n^{(k)} \right\rangle$ are process-specific and cannot be generically computed, unlike the soft functions. Nevertheless, the Born and one-loop amplitudes can be automatically computed by codes like MG5AMC [75, 76]. Assuming that the setup (particle masses, couplings, PDFs, hadronic centre of mass energy...) is coherent between the different parts of the calculation, we can extract the coloured amplitudes $\left| \mathcal{A}_n^{(0)} \right\rangle$ and $\left| \mathcal{A}_n^{(1)} \right\rangle$, from the MADLOOP tool used in MG5AMC. This method was used in the case of the processes in chapter 4 to generate the hard parts needed in (2.26).

In simpler cases, we can compute $\mathbf{H}^{(0)}$ directly, for example in the $pp \rightarrow t\bar{t}$ process. We introduce the reduced Mandelstam variables $t_1 = (p_1 - p_t)^2 - m_t^2 = t - m_t^2$ and $u_1 = (p_1 - p_{\bar{t}})^2 - m_t^2 = u - m_t^2$, with m_t is the mass of the top quark, p_1 and p_2 the four momenta of the incoming partons. For this process, we have the following parton channels:

$$q_1 \bar{q}_2 \longrightarrow t_3 \bar{t}_4$$

The quark channel can be represented diagrammatically as:



We can associate the singlet-octet colour basis:

$$\{\delta_{c_2c_1}\delta_{c_3c_4}; \mathbf{T}_{c_2c_1}^i \mathbf{T}_{c_3c_4}^i\}, \quad (2.65)$$

which gives at Born level, after taking the matrix element squared, with M the invariant mass of the $t\bar{t}$ final state:

$$\mathbf{H}^{(0)} = \frac{128\pi^2\alpha_s^2}{8N_c^2M^2} \left(\frac{t_1^2 + u_1^2 + 2m_t^2M^2}{M^4} \right) \begin{pmatrix} 0 & 0 \\ 0 & 1 \end{pmatrix}, \quad (2.66)$$

$$g_1g_2 \longrightarrow t_3\bar{t}_4$$

For the gluon fusion channel, we have the following diagrams:



We can choose the colour basis obtained by the symmetrisation and antisymmetrisation of the two octets together with a singlet:

$$\{\delta^{c_1c_2}\delta_{c_3c_4}; if^{c_1c_2j}\mathbf{T}_{c_3c_4}^j; d^{c_1c_2j}\mathbf{T}_{c_3c_4}^j\}. \quad (2.67)$$

Then at the hard matrix level:

$$\mathbf{H}^{(0)} = \frac{32\pi^2\alpha_s^2}{8(N_c^2 - 1)^2} \left(\frac{t_1^2 + u_1^2 + 4m_t^2M^2}{M^2t_1u_1} - \frac{4m_t^4M^2}{t_1^2u_1^2} \right) \begin{pmatrix} \frac{1}{N_c^2} & \frac{1}{N_c} \frac{t_1 - u_1}{M^2} & \frac{1}{N_c} \\ \frac{1}{N_c} \frac{t_1 - u_1}{M^2} & \left(\frac{t_1 - u_1}{M^2} \right)^2 & \frac{t_1 - u_1}{M^2} \\ \frac{1}{N_c} & \frac{t_1 - u_1}{M^2} & 1 \end{pmatrix}. \quad (2.68)$$

2.4 General expression and implementation

2.4.1 Resummation formula

When all previous results are gathered, a closed formula for the resummed differential cross section at NLL can be obtained:

$$\begin{aligned} \frac{d^2 \hat{\sigma}^{\text{res.}}(N, \mu_F, \mu_R)}{dM^2 d\Phi_n} &= \exp\left(g_1(\lambda) \ln \bar{N} + g_2(\lambda)\right) \tilde{B}_1(\mu_R, \mu_F) \tilde{B}_2(\mu_R, \mu_F) \text{Tr} \left[\left(\mathbf{H}^{(0)} + \frac{\alpha_s}{2\pi} \mathbf{H}^{(1)}(\mu_R) \right) \cdot \right. \\ &\quad \exp\left(\frac{\ln(1-2\lambda)}{\beta_0} \Gamma_S^{(1)}\right) \cdot \left(\mathbf{S}^{(0)} + \frac{\alpha_s}{2\pi} \left[\mathbf{S}^{(1)}(\mu_S) + \ln\left(\frac{M^2}{\mu_R^2}\right) \left\{ \Gamma_S^{(1)} \cdot \mathbf{S}^{(0)} + \mathbf{S}^{(0)} \cdot \Gamma_S^{(1)\dagger} \right\} \right] \right) \cdot \\ &\quad \left. \exp\left(\frac{\ln(1-2\lambda)}{\beta_0} \Gamma_S^{(1)\dagger}\right) \right]. \end{aligned} \quad (2.69)$$

The exponential factor $\exp(g_1(\lambda) \ln \bar{N} + g_2(\lambda))$ corresponds to the Sudakov factor, see appendix A.8 for more details. We can notice that the formula (2.69) contains matrixial exponents coming from the soft anomalous dimension. In general we need to diagonalise these matrices to evaluate the exponentials, like in [77]. In some specific regimes, like the absolute threshold limit (see section 4.1.1) for heavy (s)quark pair production [78] in some particular colour basis, the soft anomalous dimension matrix becomes diagonal so that we can avoid the cost of the diagonalisation procedure. In fact, the choice of a particular colour basis can be motivated by the diagonalisation properties of the soft anomalous dimension as in [31].

Equation (2.69) details the content of the partonic differential cross section. In order to calculate the physical cross section, we need to obtain the PDFs in Mellin space as they appear in (2.22).

2.4.2 Implementation of PDFs

In order to avoid the numerical cost of performing the Mellin transform of the PDFs, we follow the implementation performed in [79] by making use of a MSTW-like parameterisation:

$$f(x) = A_0 x^{A_1} (1-x)^{A_2} \left(1 + A_3 \sqrt{x} + A_4 x + A_5 x^{3/2} + A_6 x^2 + A_7 x^{5/2} \right). \quad (2.70)$$

This yields the following analytical Mellin transform (see A.35), where we introduce the Euler beta function $B(x, y) = \Gamma(x)\Gamma(y)/\Gamma(x+y)$:

$$\begin{aligned}
F(N) = A_0 & \left[B(A_1 + N, A_2 + 1) + A_3 B\left(A_1 + N + \frac{1}{2}, A_2 + 1\right) \right. \\
& + A_4 B(A_1 + N + 1, A_2 + 1) + A_5 B\left(A_1 + N + \frac{3}{2}, A_2 + 1\right) \\
& \left. + A_6 B(A_1 + N + 2, A_2 + 1) + A_7 B\left(A_1 + N + \frac{5}{2}, A_2 + 1\right) \right]. \tag{2.71}
\end{aligned}$$

In addition, each PDF also depends on the factorisation scale μ_F . This means that, for every chosen value of μ_F and for each parton (both gluon and active quark flavours), we need to fit the eight parameters A_i . One potential approach is to fit the PDFs at one scale and then evolve them. However this process becomes quite complex beyond the first order addressed in appendix A.4. Dedicated codes, such as `QCD-Pegasus` [80] are dedicated to PDF evolution, but we chose another approach suitable for the work presented in this document. A more practical solution is to perform the fit for each desired μ_F value. While the fitting procedure is not excessively time-consuming, this approach ensures that we can accurately describe the PDFs at each distinct scale of interest. As a drawback, it becomes more difficult to integrate the differential cross section using a dynamical factorisation scale since the fit has to be performed locally.

Fit results

Figure 2.1 displays the ratios of the fit to the original LHAPDF output from the CT18NLO set, as well as its Mellin transform brought back in x space after Mellin inversion (see section 2.4.3 for more details).

The parameterisation and fitting procedure demonstrate high precision for x values below 0.1. However, beyond this value, the fit oscillates up to $x \simeq 0.4$ and then drops rapidly compared to the original PDF. This behaviour is also observed in [79], which uses the same kind of PDF parameterisation. Nevertheless, this mismatch is not expected to significantly impact the physical predictions. Indeed, as we can see in figure 1.2, PDFs are highly suppressed in the high x region, indicating virtual partons have little chance of monopolising the momentum of a hadron. Hence, the high x region hardly contributes when computing physical observables like the cross section. On the other hand, the numerical inverse of the Mellin transform is extremely precise and do not involve further mismatch compared to the analytical fit. We must highlight that the fit in figure 2.1 was obtained by successively fitting the PDF on four ranges, each one corresponding to one order of magnitude in x . It implies that small discontinuities are expected at $x \in \{10^{-3}, 10^{-2}, 10^{-1}\}$. In the actual implementation for practical use, we take care to choose a single range of x to fit the LHAPDF input. This range should be selected around a representative x value, in the relevant region of interest to calculate the observable, and

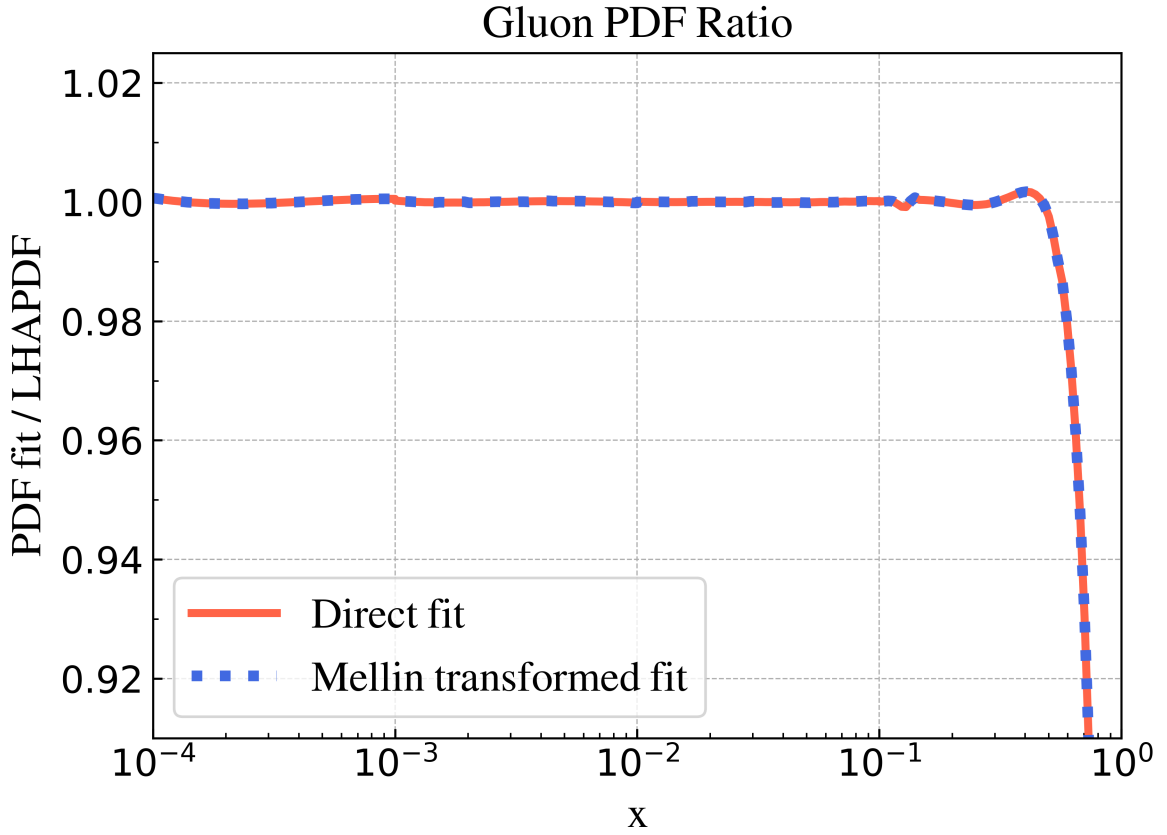


Figure 2.1: Ratio of direct fit and inversed Mellin transformed analytical fit with respect to CT18NLO gluon PDF at $\mu_F = 10$ GeV

not cover too many orders of magnitude for the fit to be accurate. Later on, to assess the quality of the fit, we consistently compare our tree-level predictions with those generated by the Monte-Carlo event generator MADGRAPH5_AMC@NLO [75, 76] (MG5AMC). Any significant discrepancies at tree level could indicate issues with the fitting procedure. As the PDFs should have a similar impact on tree-level, resummed or higher-order computations, checking at the lowest complexity level is relevant.

It is important to note that this parameterisation is not the only approach to obtain analytical Mellin transform. For instance, Chebyshev polynomials can be used to fit the PDFs, as in [81]. According to the authors of this article, using Chebyshev polynomials increases numerical accuracy for practical purposes while reducing computational cost compared to splines or other polynomial fits. On the other hand, the Chebyshev interpolation seems more sensitive to fine-tuning effects regarding the intervals slicing or the maximal degree chosen. While it is not technically difficult, the analytical Mellin transform is also less direct than for the MSTW parameterisation. Having a complementary Chebyshev fitting procedure would certainly be of use for the work presented in this document but is

left for future development. In the same way, we can completely avoid using an analytic parameterisation to obtain the Mellin transform of PDFs. Indeed, we can use the trick described in appendix B of [82] which consist in incorporating the PDFs in a luminosity factor and use an *ansatz* to improve numerical convergence.

2.4.3 Physical result in direct space

Inverse Mellin transform

The cross section in (2.22) has been transformed into Mellin space. To obtain a physical result, the inverse Mellin transform (A.37) must be carried out:

$$d\hat{\sigma}^{\text{res.}}(\tau, \mu_F, \mu_R) = \frac{1}{2i\pi} \int_{C-i\infty}^{C+i\infty} dN \tau^{-N} d\sigma^{\text{res.}}(N, \mu_F, \mu_R). \quad (2.72)$$

The inverse Mellin transform is an integration in the complex plane parametrised by two quantities, namely $C \in \mathbb{R}$ the real axis offset and $\Phi \in [\pi/2, \pi]$ the angle tilting the integration lines in the \mathbb{C} plane. This enables us to parametrise N along the integration path:

$$\begin{aligned} N(x) &= C + xe^{i\Phi} & x > 0 & \text{ for } \text{Im}(N) > 0, \\ N(x) &= C + xe^{-i\Phi} & x > 0 & \text{ for } \text{Im}(N) < 0, \end{aligned} \quad (2.73)$$

with the corresponding illustration:

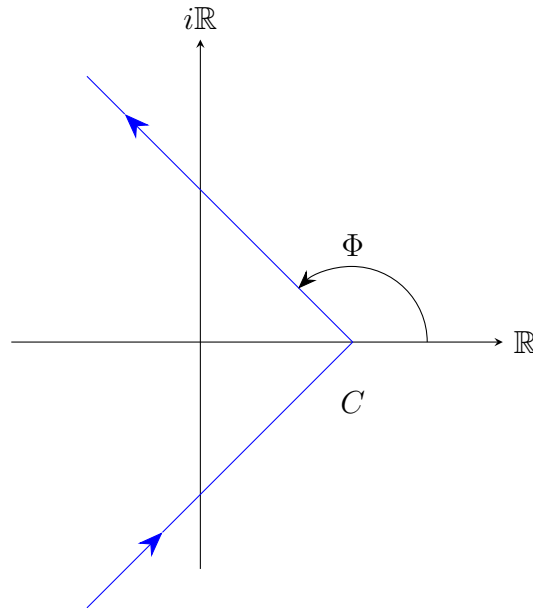


Figure 2.2: N integration path for the inverse Mellin transform

The integration parameters C and Φ are only necessary to ensure the numerical convergence of the integration. The actual result should not depend on them, this property will be used as a test for numerical stability. C should be selected to avoid the Landau pole on the right ($2\lambda = 1$) and the pomeron singularity on the left. Following the minimal prescription of [82], we have $2 < C < \exp(\pi/\alpha_s\beta_0)$. A good empirical choice for these parameters is $C \gtrsim 2.01$ and $\Phi \simeq 3\pi/4$. In fact we can simplify the integration by using the complex conjugation between the two branches:

$$\begin{aligned} \frac{1}{2i\pi} \int_{C-i\infty}^{C+i\infty} dN z^{-N} f(N) &= \int_{C-i\infty}^C \frac{dN}{2i\pi} z^{-N} f(N) + \int_C^{C+i\infty} \frac{dN}{2i\pi} z^{-N} f(N) \\ &= - \int_C^{C+i\infty} \frac{dN}{2i\pi} \overline{z^{-N} f(N)} + \int_C^{C+i\infty} \frac{dN}{2i\pi} z^{-N} f(N) \quad (2.74) \\ &= \frac{1}{\pi} \operatorname{Im} \left(\int_C^{C+i\infty} dN z^{-N} f(N) \right), \end{aligned}$$

under the hypothesis that f is a real function when N is real. In the end, it is only necessary to integrate over one branch, for example the upper one.

Matching

Now that we have all access to the result of resummation in physical space, it is crucial to understand how it can be matched with fixed-order predictions. Indeed, the resummed observable should adjust the fixed-order prediction in the target region, where the fixed order exhibits pathological behaviour (namely, threshold logarithms). However, in order to produce meaningful predictions in all situations, we need to have a matching procedure that combines both fixed-order and resumed results. The main concept is to add the fixed order and the resummed observables coherently, for each scale value. However, we need to take into account the double counting between the two terms. This can be resolved by expanding the resummed prediction to the desired fixed order and subtract it from the matching. We denote the differential cross section computed at NLO, evaluated at scale μ_R as $d\sigma_{|\mu_R}^{\text{f.o.}}$, the resummed prediction as $d\sigma_{|\mu_R}^{\text{res.}}$ and the resummed cross section expanded at NLO as $d\sigma_{|\text{f.o.}, \mu_R}^{\text{res.}}$. Then the matching simply reads:

$$d\sigma_{|\mu_R}^{\text{match.}} = d\sigma_{|\mu_R}^{\text{f.o.}} + d\sigma_{|\mu_R}^{\text{res.}} - d\sigma_{|\text{f.o.}, \mu_R}^{\text{res.}}. \quad (2.75)$$

To derive the expansion of the resummed result, we start from (2.69) and expand at $\mathcal{O}(\alpha_s)$:

$$\begin{aligned}
d\sigma_{\text{f.o.}, \mu}^{\text{res.}} = & \text{Tr} \left[\mathbf{H}^{(0)} \cdot \mathbf{S}^{(0)} \left(1 + \frac{\alpha_s}{2\pi} (\tilde{B}_1^{(1)} + \tilde{B}_2^{(1)}) + g_{1\text{f.o.}} \ln \bar{N} + g_{2\text{f.o.}} \right) \right. \\
& \left. + \frac{\alpha_s}{2\pi} \mathbf{H}^{(0)} \cdot \mathbf{S}^{(1)} + \frac{\alpha_s}{2\pi} \mathbf{H}^{(1)} \cdot \mathbf{S}^{(0)} - \frac{\alpha_s}{2\pi} \beta_0 \ln \bar{N} \mathbf{H}^{(0)} \cdot \left(\Gamma_S^{(1)} \cdot \mathbf{S}^{(0)} + \mathbf{S}^{(0)} \cdot \Gamma_S^{(1)\dagger} \right) \right]. \quad (2.76)
\end{aligned}$$

The expressions of $g_{1\text{f.o.}}$ and $g_{2\text{f.o.}}$ are available in appendix A.8.2.

Scale variation and theoretical uncertainty

To evaluate the effectiveness of the resummation procedure, it is crucial to appreciate the theoretical uncertainty arising from the different scales introduced into the calculation. As we are carrying out a perturbative approach, either at fixed order alone or including the resummation, we need to truncate the expansion at some point. This truncation introduces a dependence on arbitrary scales introduced by the perturbative computation. To prevent any physical artifacts, it's typical to evaluate these scales as close to physical values as possible. To obtain an estimate of the unaccounted higher-order information in the computation, we calculate the relative change in results when the scales are varied. Specifically, we estimate the theoretical error as the maximum and minimum values of the prediction when the scales are varied by a factor of two around the central value. It is standard practice to avoid using extreme variations when dealing with multiple scales. In our case, the arbitrary scales are μ_F from the PDF factorisation and μ_R from the hard matrix's renormalisation. μ_S , relative to the soft matrix is fixed at M/\bar{N} and is not included in the scales variation. By selecting a central scale μ_0 that is shared by both μ_F and μ_R , we can explore variations within a 7-point set:

$$(\mu_F, \mu_R) \in \mu_0 \times \left\{ \left(\frac{1}{2}, \frac{1}{2} \right); \left(\frac{1}{2}, 1 \right); \left(1, \frac{1}{2} \right); (1, 1); (1, 2); (2, 1); (2, 2) \right\}. \quad (2.77)$$

3

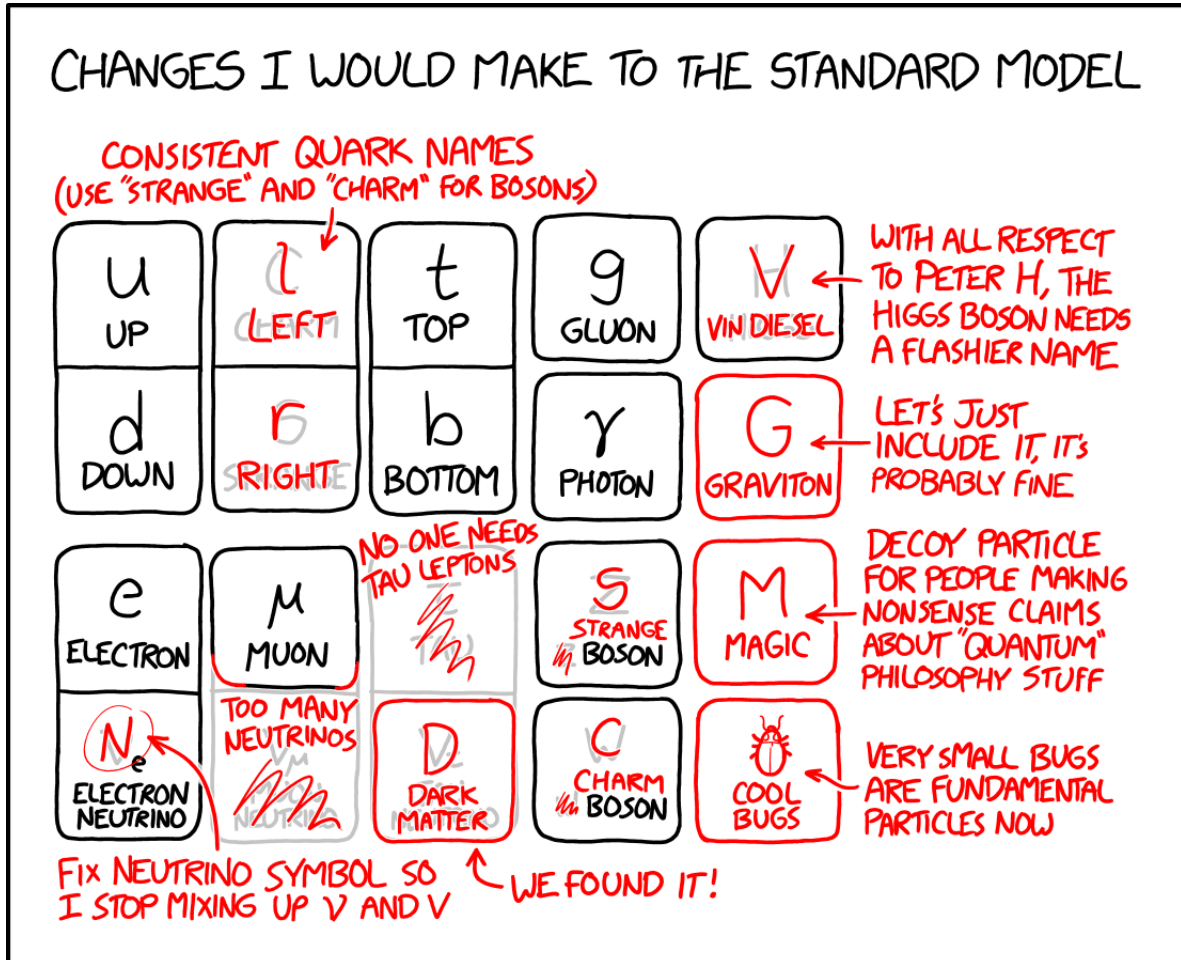
Drell-Yan like processes: VLL & Seesaw

Summary

3.1	BSM and exotic leptons searches	71
3.2	Theoretical models and their implementation	72
3.2.1	A simplified model for VLL phenomenology	72
3.2.2	An effective Type-III seesaw Lagrangian	75
3.2.3	From Lagrangian to events at the LHC	79
3.3	Improving theory accuracy beyond NLO: threshold resummation . . .	80
3.4	Cross sections for extra lepton production at the LHC	82
3.4.1	Total cross sections at the LHC	82
3.4.2	Invariant mass distributions	86
3.4.3	Transverse momentum spectra	90
3.5	Conclusion	91

Science must begin with myths, and with the criticism of myths

Karl Popper



xkcd comics n°2351, Standard Model Changes

THE following chapter is widely inspired from the published work carried out in [83]. Slight modifications are made, in order to include the results presented there in the broader framework of this document. We refer to pair production of colour singlet final states, such as $pp \rightarrow l^+l^-$, as Drell-Yan like processes. Consistency was checked between the codes used in this chapter and chapter 4.

3.1 BSM and exotic leptons searches

Several extensions of the Standard Model (SM) predict the existence of new exotic heavy leptons. These arise in particular in composite models [84–86], grand unified theories [87, 88], supersymmetric models [89–91], left-right symmetric models [92–95], dark matter scenarios [96] or in Type I [97–104] and Type-III [97, 105] seesaw models. In composite scenarios, the new physics particle spectrum often features vector-like leptons (VLLs) transforming as electroweak $SU(2)_L$ singlets or doublets. In contrast, in some seesaw and left-right models, neutrino masses are generated from Yukawa interactions of new electroweak singlets or triplets of fermions with the SM Higgs field and lepton weak doublet. Consequently, searches for new heavy leptons consist of an important component of the experimental beyond the SM (BSM) search programme at the Large Hadron Collider (LHC).

The ATLAS and CMS collaborations have explored the associated parameter spaces, both for promptly-decaying [106–123] and long-lived [111, 124] extra leptons, and for a variety of mass ranges. Limits have been set on the mixing properties of long-lived heavy charge-neutral leptons for masses of 3–15 GeV, while short-lived neutral and charged leptons must have masses of at least about 950 GeV in Type-III seesaw models (for branching ratios of 1 in the final state considered). Moreover, in left-right models neutral lepton masses must be larger than 3 TeV for W_R boson masses smaller than 4–5 TeV, and indirect probes for heavy neutrinos via vector-boson-fusion processes additionally constrain masses ranging up to 20 TeV for large mixings with the SM leptons and neutrinos. Finally, bounds on VLLs strongly depend on their representation under the electroweak symmetry group and on the VLL couplings to SM leptons. For instance, whereas weak doublets of VLL coupling to tau leptons are constrained to be heavier than about 1 TeV [108], the limit drops in the 100 – 200 GeV range in the singlet case [122]. On the other hand, LEP bounds on light VLLs are still relevant, and they impose a lower limit on the VLL mass. Such a limit lies in the 100 GeV range at best, depending on the details of the model [125–128].

From the theoretical side, total and differential cross section calculations for collider processes involving extra neutrinos are known at next-to-leading order (NLO) in QCD in a generic simplified model describing the dynamics of the heavy neutrinos [129, 130], for an effective left-right-symmetric scenario [131] and for the production of type III seesaw leptons [132]. In addition, NLO-QCD predictions matched with threshold resummation at the next-to-leading-logarithmic (NLL) accuracy [133–135] and approximate next-to-next-to-leading-order cross section matched with next-to-next-to-leading-logarithmic (NNLL) threshold resummation [136] can also be obtained from electroweakino pair-production processes in the Minimal Supersymmetric Standard Model, after decoupling all supersymmetric states but the produced electroweakinos. Beside differential and total rates,

precision collider simulations in which NLO calculations are matched with parton showers (PS) are available for heavy neutrino simplified models [129–131], as well as for VLL models for well-defined mixings between the composite and the SM sectors [137]. However, simulations for Type-III seesaw scenarios and generic composite VLL setups are only available at leading order (LO) so far.

The goal of this chapter is to fill this gap, and to report about the development of two new publicly available UFO [138] model libraries allowing for event generation at the NLO+PS accuracy. Our implementation is suitable in particular to describe VLL and Type-III seesaw lepton production processes from computations achieved by means of the precision Monte Carlo event generator MADGRAPH5_AMC@NLO [75, 76] (MG5AMC). Moreover, we take the opportunity to update predictions for the total rates and the invariant mass distributions of the BSM Drell-Yan-like processes inherent to the models considered, and present results at NLO in QCD matched with threshold resummation at NNLL, following the formalism of [139–141].

The rest of this chapter is organised as follows. In section 3.2, we introduce two effective theoretical frameworks suitable for our calculations, a first one dedicated to a simplified VLL model and a second one to Type-III seesaw scenarios, and we report details about their implementation. In section 3.3, we briefly describe the formalism that we use to resum large threshold logarithms. In section 3.4, we make use of the MG5AMC platform to study the phenomenology of the two models at the NLO+PS accuracy, as well as of an in-house programme to handle predictions at NLO+NNLL in the strong coupling. We compute total rates for the production of extra leptons (section 3.4.1), invariant-mass distributions (section 3.4.2), and we additionally present for the first time NLO+PS-accurate differential distributions relevant for experimental searches for VLLs and Type-III seesaw fermions (section 3.4.3). We summarise our work and conclude in section 3.5.

3.2 Theoretical models and their implementation

In order to study the phenomenology of the considered models, we construct two effective frameworks, one for each of the models. We minimally extend the SM in terms of fields and interactions, so that the resulting new physics parameter spaces are of small dimensionality.

3.2.1 A simplified model for VLL phenomenology

We begin by considering an extension of the SM in which the theory field content includes a set of VLL fields. They are all colour singlet, but each of them lies in a different $SU(2)_L$ representation. They are correspondingly assigned different hypercharge $U(1)_Y$ quantum numbers. In order to be as model independent as possible, we adopt a simplified

model approach and focus on extra leptons that are either electrically neutral or with an electric charge $Q = \pm 1$. These leptons are organised in (vector-like) $SU(2)_L$ doublets and singlets,

$$L^0 = \begin{pmatrix} N^0 \\ E^0 \end{pmatrix}, \quad \tilde{E}^0, \quad \tilde{N}^0, \quad (3.1)$$

where in this notation the superscript ‘0’ indicates that the fields are gauge eigenstates, and the tilde above a field indicates that it is an $SU(2)_L$ singlet. We next implement the mixing between the SM and the new lepton fields. To this aim, we introduce an effective parametrisation apt to capture the main phenomenological features of the vector-like fields in a model-independent way, following guidelines introduced for vector-like quark setups [142, 143].

In practice, we assume that the mixing between the SM fields and the new leptons is small, so that the gauge interactions of the different fields are unaffected to first order. Moreover, we implement the off-diagonal interactions of the exotic leptons with the SM ones through generic free parameters, which further open the VLL decay channels into a SM lepton and an electroweak boson. The corresponding Lagrangian, given in terms of mass eigenstates (the superscript ‘0’ being therefore dropped), reads

$$\begin{aligned} \mathcal{L}_{\text{VLL}} = & \mathcal{L}_{\text{SM}} + i\bar{L}\not{D}L - m_N\bar{N}N - m_E\bar{E}E + i\bar{\tilde{N}}\not{D}\tilde{N} - m_{\tilde{N}}\bar{\tilde{N}}\tilde{N} + i\bar{\tilde{E}}\not{D}\tilde{E} - m_{\tilde{E}}\bar{\tilde{E}}\tilde{E} \\ & + \sum_{\Psi=E,\tilde{E}} \left[h\bar{\Psi} \left(\hat{\kappa}_L^\Psi P_L + \hat{\kappa}_R^\Psi P_R \right) \ell + \frac{g}{\sqrt{2}} \bar{\Psi} W^- \kappa_L^\Psi P_L \nu_\ell + \frac{g}{2c_W} \bar{\Psi} Z \left(\tilde{\kappa}_L^\Psi P_L + \tilde{\kappa}_R^\Psi P_R \right) \ell + \text{H.c.} \right] \\ & + \sum_{\Psi=N,\tilde{N}} \left[h\bar{\Psi} \hat{\kappa}_L^\Psi P_L \nu_\ell + \frac{g}{2c_W} \bar{\Psi} Z \tilde{\kappa}_L^\Psi P_L \nu_\ell + \frac{g}{\sqrt{2}} \bar{\Psi} W^+ \left(\kappa_L^\Psi P_L + \kappa_R^\Psi P_R \right) \ell + \text{H.c.} \right], \end{aligned} \quad (3.2)$$

where \mathcal{L}_{SM} is the SM Lagrangian, and the parameters m_N , m_E , $m_{\tilde{N}}$ and $m_{\tilde{E}}$ stand for the masses of the four new fields in the physical basis, assuming that the masses of the doublet component fields can be different after electroweak symmetry breaking and particle mixing. The first two lines in this Lagrangian include, additionally to the SM Lagrangian, all gauge-invariant kinetic and mass terms for the new states. The gauge-covariant derivative operator D_μ is defined, for a generic field ψ , by

$$D_\mu \psi = \partial_\mu \psi - ig' B_\mu Y \psi - ig W_\mu^k T^k \psi. \quad (3.3)$$

Here, the coupling constants g and g' respectively stand for the weak $SU(2)_L$ and hypercharge $U(1)_Y$ coupling constants, and B_μ and W_μ^k are the associated gauge fields. The action of the hypercharge operator Y on the field ψ can be deduced from table 3.1, as the representation to adopt for the $SU(2)$ generators T^k . In particular, $T^k = 0$ for an

Field	Spin	Representation	Name
L^0	$(1/2, 1/2)$	$(\mathbf{1}, \mathbf{2})_{-1/2}$	VLL0
\tilde{N}^0	$(1/2, 1/2)$	$(\mathbf{1}, \mathbf{1})_0$	VLN0
\tilde{E}^0	$(1/2, 1/2)$	$(\mathbf{1}, \mathbf{1})_{-1}$	VLE0

Table 3.1: Gauge eigenstates complementing the SM field content, their spin given as their representation under the $SO(1, 3)$ group (second column), their $SU(3)_c \times SU(2)_L \times U(1)_Y$ (third column) representation and their name in the FEYNRULES implementation (last column).

Field	Spin	Name	PDG	Mass	Width
N	$(1/2, 1/2)$	VLLN	9000001	MVLLN	WVLLN
E	$(1/2, 1/2)$	VLLE	9000002	MVLLE	WVLLE
\tilde{N}	$(1/2, 1/2)$	VLN	9000003	MVLN	WVLN
\tilde{E}	$(1/2, 1/2)$	VLE	9000004	MVLE	WVLE

Table 3.2: Mass eigenstates supplementing the SM, with their spin quantum number (second column), name used in the FEYNRULES convention (third column) and adopted PDG identifier (fourth column). In the last two columns, we provide the FEYNRULES symbols associated with the particle masses and widths.

$SU(2)_L$ singlet, and $T^k = \sigma^k/2$ for an $SU(2)_L$ doublet, with σ^k being the Pauli matrices. In other words, we approximate mass eigenstates by gauge eigenstates in all kinetic terms, *i.e.* $L^0 \approx L$, $\tilde{E}^0 \approx \tilde{E}$ and $\tilde{N}^0 \approx \tilde{N}$.

The last four lines of the Lagrangian (3.2) collect the effective interactions of each of the four VLLs considered with a SM lepton (ℓ standing for the charged lepton field and ν_ℓ for the neutrino one), and either the Higgs boson h , the W boson or the Z boson. In (3.2), all flavour indices are understood so that each of the κ , $\hat{\kappa}$ and $\tilde{\kappa}$ couplings has to be seen as a vector in the flavour space. Moreover, c_w refers to the cosine of the electroweak mixing angle.

In the following, the exact values of the κ , $\hat{\kappa}$ and $\tilde{\kappa}$ coupling vectors are irrelevant, provided that they are not too large to guarantee that the VLL states have a narrow width, and not too small so that they can promptly decay into a lepton+electroweak boson system within LHC detector scales. In a hadron collision process in which the new leptons are pair produced, such couplings indeed only appear in the heavy particle decays.

In order to allow for phenomenological studies of the model, we implement it in the FEYNRULES package [144, 145], starting from the SM implementation that is shipped with the programme. We include the definitions of the gauge eigenstates (3.1), together with the corresponding mass eigenstates appearing in the Lagrangian (3.2). Information on these

Couplings	Names	Les Houches blocks
$(\hat{\kappa}_L^E)_i, (\hat{\kappa}_R^E)_i$	KLLEH[i], KRLEH[i]	KLLEH, KRLEH
$(\hat{\kappa}_L^{\tilde{E}})_i, (\hat{\kappa}_R^{\tilde{E}})_i$	KLEH[i], KREH[i]	KLEH, KREH
$(\hat{\kappa}_L^N)_i$	KLLNH[i]	KLLNH
$(\hat{\kappa}_L^{\tilde{N}})_i$	KLNH[i]	KLNH
$(\tilde{\kappa}_L^E)_i, (\tilde{\kappa}_R^E)_i$	KLLEZ[i], KRLEZ[i]	KLLEZ, KRLEZ
$(\tilde{\kappa}_L^{\tilde{E}})_i, (\tilde{\kappa}_R^{\tilde{E}})_i$	KLEZ[i], KREZ[i]	KLEZ, KREZ
$(\tilde{\kappa}_L^N)_i$	KLLNZ[i]	KLLNZ
$(\tilde{\kappa}_L^{\tilde{N}})_i$	KLNZ[i]	KLNZ
$(\kappa_L^E)_i$	KLLEW[i]	KLLEW
$(\kappa_L^{\tilde{E}})_i$	KLEW[i]	KLEW
$(\kappa_L^N)_i, (\kappa_R^N)_i$	KLLNW[i], KRLNW[i]	KLLNW, KRLNW
$(\kappa_L^{\tilde{N}})_i, (\kappa_R^{\tilde{N}})_i$	KLNW[i], KRNW[i]	KLNW, KRNW

Table 3.3: Three-point VLL coupling strengths to a SM lepton and an electroweak boson, given together with the associated FEYNRULES symbol and the corresponding Les Houches block. The indice i denotes a generation index ranging from 1 to 3.

fields, their names in the FEYNRULES conventions, and the Particle Data Group (PDG) identifiers that we have adopted for the physical fields, are provided in tables 3.1 and 3.2. These tables also include the symbols associated with the mass and width of the physical fields. All BSM couplings appearing in (3.2) have been implemented as three-vectors in the flavour space, following the convention of table 3.3. This table also includes information on the Les Houches block structure used to organise all model external parameters [146], as required by all high-energy physics programmes relying on FEYNRULES for model implementation. Moreover, their specific contributions to any process can be turned off through a dedicated interaction order named VLL (see the FEYNRULES manual [144]).

3.2.2 An effective Type-III seesaw Lagrangian

In Type-III seesaw models, neutrino masses are generated through the interactions of the SM Higgs field Φ with the SM leptons and at least two generations of extra fermions lying in the adjoint representation of $SU(2)_L$ and with zero hypercharge. In the following, we make use of two-component Weyl fermion notation for all fields, and omit all SM and BSM generation indices for clarity. In such a formalism, the Lagrangian of the model is expressed in terms of the SM weak doublet of left-handed leptons L_L , the SM weak

singlet of right-handed charged leptons E_R^c (E_R being thus the corresponding left-handed Weyl spinor), and the weak triplet of extra lepton Σ^k (with $k = 1, 2, 3$ being an $SU(2)_L$ adjoint index). The three gauge eigenstates Σ^k can be conveniently related to states of definite electric charge $E^\pm \equiv \Sigma^\pm$ (of charge $Q = \pm 1$) and $N \equiv \Sigma^0$ (of charge $Q = 0$) by introducing the matrix representation for the $SU(2)_L$ triplets Σ^i_j , with i and j referring to fundamental indices of $SU(2)_L$. We obtain,

$$\Sigma^i_j = \frac{1}{\sqrt{2}}(\sigma^k)^i_j \Sigma^k = \begin{pmatrix} \frac{1}{\sqrt{2}}N & E^+ \\ E^- & -\frac{1}{\sqrt{2}}N \end{pmatrix}. \quad (3.4)$$

The Type-III Lagrangian is given by

$$\begin{aligned} \mathcal{L}_{\text{TypeIII}} &= \overline{\mathcal{L}}_{\text{SM}} + \mathcal{L}_{\text{kin}} \\ &+ \left(y_\ell \Phi^\dagger L_L \cdot E_R + 2y_\Sigma \Phi \cdot \left[\Sigma^k T^k L_L \right] + \text{H.c.} \right). \end{aligned} \quad (3.5)$$

In our notation, $\overline{\mathcal{L}}_{\text{SM}}$ stands for the reduced SM Lagrangian in which all terms involving a leptonic field have been removed, and \mathcal{L}_{kin} collects all gauge-invariant kinetic terms for the (two-component) leptonic fields L_L , E_R and Σ , and a mass term for the Σ field (of mass m_Σ). Moreover, the matrices $T^k = \sigma^k/2$ stand for the generators of $SU(2)_L$ in the fundamental representation, and the scalar product appearing on the second line refers to the $SU(2)$ -invariant product of two fields lying in its fundamental representation, similarly to (1.40). In Type-III models, charged lepton and neutrino masses are driven by the SM leptonic 3×3 Yukawa matrix y_ℓ , and the heavy neutrino Yukawa matrix y_Σ whose size depends on the number of generations of new fermions.

From the LHC physics point of view, we can simplify the model presented above by emphasising the focus on the lightest of all Σ states, that are assumed to be the only ones to which the LHC would be sensitive. This strategy follows that introduced in ref. [147]. Under such an assumption, the relevant part of the Yukawa matrix y_Σ (in the Σ -flavour \times SM-flavour space) becomes a vector in the SM-flavour space, that we take real for simplicity.

The mass eigenstates of the model hence include three generations of physical up-type and down-type quarks, and four generations of charged leptons (ℓ') and Majorana neutrinos (ν'). After electroweak symmetry breaking, the Lagrangian (3.5) induces a mixing between the three SM leptons and the new states Σ , rendering at least two neutrinos massive. Introducing the three 4×4 mixing matrices in the lepton flavour space U_L^ℓ , U_R^ℓ and U^ν , lepton gauge and mass eigenstates are related by [148],

$$\begin{pmatrix} E_L \\ E^- \end{pmatrix} = U_L^\ell \ell'_L, \quad \begin{pmatrix} E_R \\ E^{+c} \end{pmatrix} = U_R^\ell \ell'_R, \quad \begin{pmatrix} \nu_L \\ N \end{pmatrix} = U^\nu \nu', \quad (3.6)$$

where the three-component vector in the flavour space E_L (ν_L) stands for the down-type (up-type) component of the weak doublet of left-handed SM leptons. As the new fermion masses of $\mathcal{O}(m_\Sigma)$ are expected to be heavy compared with the neutrino masses of $\mathcal{O}(y_\Sigma v)$, with v being the SM Higgs vacuum expectation value, the three mixing matrices can be expanded at the first order in yv/m_Σ [149, 150],

$$\begin{aligned} U_L^\ell &= \begin{pmatrix} \mathbb{1} - \varepsilon & \frac{v}{m_\Sigma} y_\Sigma \\ -\frac{v}{m_\Sigma} y_\Sigma^\dagger & 1 - \varepsilon' \end{pmatrix}, & U_R^\ell &= \begin{pmatrix} \mathbb{1} & \frac{M_\ell v}{m_\Sigma^2} y_\Sigma \\ -\frac{M_\ell v}{m_\Sigma^2} y_\Sigma^\dagger & 1 \end{pmatrix}, \\ U^\nu &= \begin{pmatrix} [\mathbb{1} - \frac{1}{2}\varepsilon] U_{\text{PMNS}} & \frac{v}{\sqrt{2}m_\Sigma} y_\Sigma \\ -\frac{v}{\sqrt{2}m_\Sigma} y_\Sigma^\dagger & 1 - \frac{1}{2}\varepsilon' \end{pmatrix}. \end{aligned} \quad (3.7)$$

These expressions depend on the quantities ε and ε' , that are 3×3 and scalar objects in the SM flavour space respectively,

$$\varepsilon = \frac{v^2}{2m_\Sigma^2} y_\Sigma y_\Sigma^\dagger \quad \text{and} \quad \varepsilon' = \frac{v^2}{2m_\Sigma^2} y_\Sigma^\dagger y_\Sigma, \quad (3.8)$$

as well as on the SM lepton mass matrix M_ℓ (that is diagonal in the flavour space) and on the Pontecorvo-Maki-Nakagawa-Sakata (PMNS) matrix U_{PMNS} . The latter can be defined from the neutrino oscillation parameters, namely the neutrino mixing angles θ_{ij} (with $i, j = 1, 2, 3$), the Dirac CP -violating phase φ_{CP} and the two Majorana CP -violating phases φ_1 and φ_2 . Setting $c_{ij} = \cos(\theta_{ij})$ and $s_{ij} = \sin(\theta_{ij})$, we can parametrise the PMNS matrix as follows (see section 7 of [151] for current values):

$$U_{\text{PMNS}} = \begin{pmatrix} c_{12}c_{13} & s_{12}c_{13} & s_{13}e^{-i\varphi_{CP}} \\ -s_{12}c_{23} - c_{12}s_{13}s_{23}e^{i\varphi_{CP}} & c_{12}c_{23} - s_{12}s_{13}s_{23}e^{i\varphi_{CP}} & s_{23}c_{13} \\ s_{12}s_{23} - c_{12}s_{13}c_{23}e^{i\varphi_{CP}} & -c_{12}s_{23} - s_{12}s_{13}c_{23}e^{i\varphi_{CP}} & c_{23}c_{13} \end{pmatrix} \begin{pmatrix} e^{i\varphi_1} & 0 & 0 \\ 0 & e^{i\varphi_2} & 0 \\ 0 & 0 & 1 \end{pmatrix},$$

We implement the Type-III model described above in the FEYNRULES package [144, 145] following the same method that has been used for the Type II seesaw implementation [152]. We begin with the implementation of the SM shipped with FEYNRULES, from which all lepton definitions and related Lagrangian terms have been modified. In practice, we have modified all lepton and neutrino definitions so that two-component left-handed Weyl fermions [153] are used for the gauge eigenstates of the model (E_R^c , L_L). Next, we add definitions for the fermionic triplets Σ^k , still using left-handed Weyl fermions, and

Field	Spin	Representation	# generations	Name
L_L	(1/2, 0)	$(\mathbf{1}, \mathbf{2})_{-1/2}$	3	LLw
E_R	(1/2, 0)	$(\mathbf{1}, \mathbf{1})_1$	3	ERw
Σ^k	(1/2, 0)	$(\mathbf{1}, \mathbf{3})_0$	1	Sigw

Table 3.4: Gauge eigenstates associated with the leptonic sector of the Type-III seesaw model, their spin given as their representation under the $SO(1,3)$ group (second column), their $SU(3)_c \times SU(2)_L \times U(1)_Y$ representation (third column), and their name in the FEYNRULES implementation (last column).

Field	Spin	Name	PDG	Mass	Width
e^-	(1/2, 1/2)	e	11	Me	–
μ^-	(1/2, 1/2)	mu	13	MMu	–
τ^-	(1/2, 1/2)	ta	15	MTA	–
E^-	(1/2, 1/2)	SigM	9000017	MSigma	WSigM
ν_1	(1/2, 1/2)	v1	12	Mv1	–
ν_2	(1/2, 1/2)	v2	14	Mv2	–
ν_3	(1/2, 1/2)	v3	16	Mv3	–
N	(1/2, 1/2)	Sig0	9000018	MSigma	WSig0

Table 3.5: Mass eigenstates that either supplement the SM or whose definition is altered relatively to the SM, with their spin representation (second column), name used in the FEYNRULES convention (third column) and adopted PDG identifier (fourth column). In the last two columns, we provide the FEYNRULES symbols associated with the particle masses and widths.

incorporate the mixing relations (3.6) for the definition of the four physical charged lepton states and the four physical neutrino states in terms of all gauge eigenstates. Finally, we map the physical two-component fermions of the model into the corresponding Dirac fields (charged leptons) and Majorana fields (neutrinos). More information on all fields included in the model implementation is given in tables 3.4 and 3.5 (representation, names in the FEYNRULES conventions, PDG identifiers, symbols for masses and widths).

The new physics parameters y_Σ and m_Σ appearing in the Lagrangian (3.5) are implemented in a standard way, together with the neutrino oscillation parameters dictating the values of the PMNS matrix. Moreover, we assume a normal neutrino mass hierarchy and set the masses of the three lightest neutrinos m_{ν_1} , m_{ν_2} and m_{ν_3} from the value of the smallest neutrino mass (m_{ν_1} in our case), and the neutrino squared mass differences Δm_{21}^2 and Δm_{31}^2 ,

$$m_{\nu_2} = \sqrt{m_{\nu_1}^2 + \Delta m_{21}^2} \quad \text{and} \quad m_{\nu_3} = \sqrt{m_{\nu_1}^2 + \Delta m_{31}^2}. \quad (3.9)$$

Parameter	Name	LH block	LH counter
$(y_\Sigma)_e$	ySigma[1]	YSIGMA	1
$(y_\Sigma)_\mu$	ySigma[2]	YSIGMA	2
$(y_\Sigma)_\tau$	ySigma[3]	YSIGMA	3
m_Σ	MSigma	MASS	9000017
m_{ν_1}	Mv1	MASS	12
Δm_{21}^2	dmsq21	MNU	2
Δm_{31}^2	dmsq31	MNU	3
θ_{12}	th12	PMNS	1
θ_{23}	th23	PMNS	2
θ_{13}	th13	PMNS	3
φ_{CP}	delCP	PMNS	4
φ_1	PhiM1	PMNS	5
φ_2	PhiM2	PMNS	6

Table 3.6: External parameters defining the leptonic sector of the Type-III seesaw model, including the neutrino parameters in the context of a normal mass hierarchy (so that $m_{\nu_1} < m_{\nu_2} < m_{\nu_3}$). Each parameter is given together with the symbol used in the FEYNRULES implementation, and the corresponding Les Houches (LH) block and counter information.

More information on the free parameters of the leptonic/neutrino sector of the model is provided in table 3.6 (FEYNRULES names and Les Houches block structure).

3.2.3 From Lagrangian to events at the LHC

In order to handle LHC simulations at NLO-QCD matched with PS, we make use of the two FEYNRULES model implementations detailed in sections 3.2.1 and 3.2.2, and jointly use them with the MOGRE package (version 1.1) [154], NLOCT (version 1.0.1) [155] and FEYNARTS (version 3.9) [156]. This allows us to renormalise the bare Lagrangians (3.2) and (3.5) relatively to $\mathcal{O}(\alpha_s)$ QCD interactions, and generate UFO model files [138] including both tree-level interactions, UV counterterms, and the so-called R_2 Feynman rules required for the numerical evaluation of numerators of one-loop integrals in a four-dimensional spacetime. Such UFO models can subsequently be used with MG5AMC [75, 76] for LO and NLO calculations in QCD, as well as by HERWIG7 [157] and SHERPA [158] at LO.

Before closing this subsection, we provide information on the MG5AMC framework [75, 76] which employ to carry out fixed-order (N)LO and (N)LO+PS calculations. MG5AMC

handles infrared singularities inherent to NLO calculations via the FKS method [159, 160], in an automated way through the MADFKS module [161, 162]. The evaluation of UV-renormalised one-loop amplitudes is achieved by switching dynamically between several integral-reduction techniques that work either at the integrand level (like the OPP method [163] or Laurent-series expansion [164]) or through tensor-integral reduction [165–167]. This has been automated in the MADLOOP module [75, 168], that exploits the public codes CUTTOOLS [169], NINJA [170, 171] and COLLIER [172]. Moreover, one-loop computations have been optimised at the integrand level through an in-house procedure inspired by the idea of OPENLOOPS [173]. Finally, NLO+PS predictions are obtained by matching fixed-order calculations with PS according to the MC@NLO method [174].

3.3 Improving theory accuracy beyond NLO: threshold resummation

For the Drell-Yan-like processes considered, it is well-known that large logarithms spoil the convergence of the perturbative series when the invariant mass M of the final-state system approaches the hadronic centre-of-mass energy \sqrt{s} . This calls for a proper resummation of soft-gluon radiation, or at least a matching with PS as achieved in the MG5AMC framework. In this section, we briefly describe, for the convenience of readers, the theoretical formalism that we adopt for fixed-order calculations matched with threshold resummation. Additional details and an extensive description can be found in section 2 of [32].

At the partonic level, the corresponding kinematic region is defined in terms of the partonic scaling variable $z = M^2/\hat{s}$ when $z \rightarrow 1$, with $\sqrt{\hat{s}}$ being the partonic centre-of-mass energy. In this limit, the perturbative coefficients in the cross sections get contributions in the form of $\alpha_s \ln(1 - z)$ originating from soft gluon emission, which could be of $\mathcal{O}(1)$ and thus potentially spoil the perturbative convergence of the usual series in α_s . This issue can be resolved by reorganising the perturbative expansion in an alternative manner, and resumming the large logarithms in $\alpha_s \ln(1 - z)$ to all orders in α_s .

Resummation calculations are conveniently carried out in the Mellin N -space conjugate to z , where the $z \rightarrow 1$ limit thus corresponds to the large N region. The resummed partonic cross section in the Mellin space, denoted by $\Delta_{q\bar{q}}^{\text{res}}(N, M^2, \mu_F^2)$ with μ_F being the factorisation scale, is defined in eq. (2.47) from [32] for a generic process with a colourless final state. For a Drell-Yan-like process and at the k^{th} logarithmic accuracy ($N^k\text{LL}$), it

reads

$$\Delta_{q\bar{q}}^{\text{res}}(N, M^2, \mu_F^2) \Big|_{\text{N}^{\text{kLL}}} = \tilde{g}_{0,q\bar{q}}(M^2, \mu_F^2, \mu_R^2) \Big|_{\text{N}^{\text{kLO}}} \exp \left(g_{1,q\bar{q}}(\lambda) \ln \bar{N} + \sum_{j=2}^{k+1} a_s^{j-2}(\mu_R^2) g_{j,q\bar{q}}(\lambda) \right). \quad (3.10)$$

In this expression, the $\tilde{g}_{0,q\bar{q}}|_{\text{N}^{\text{kLO}}}$ factor collects the N -independent terms of the first $k + 1$ coefficients of the usual a_s perturbative expansion (in Mellin space), where we have introduced the short-hand notation $a_s(\mu_R^2) = \alpha_s(\mu_R^2)/4\pi$ with μ_R denoting the renormalisation scale. We can connect \tilde{g}_0 to the quantities introduced in (2.69) in the particular case of Drell-Yan-like processes (colourless final state):

$$\begin{aligned} \tilde{g}_{0,q\bar{q}}(M^2, \mu_F^2, \mu_R^2) &= \tilde{B}_q(\mu_R, \mu_F) \tilde{B}_{\bar{q}}(\mu_R, \mu_F) \exp \left(2 \frac{\ln(1-2\lambda)}{\beta_0} \text{Re} \left[\Gamma_S^{(1)} \right] \right) \\ &\left(H^{(0)} S^{(0)} + \frac{\alpha_s}{2\pi} \left[H^{(1)}(\mu_R) S^{(0)} + H^{(0)} S^{(1)}(\mu_S) + 2 \ln \left(\frac{M^2}{\mu_R^2} \right) \text{Re} \left[\Gamma_S^{(1)} \right] H^{(0)} S^{(0)} \right] \right). \end{aligned} \quad (3.11)$$

This factor is process dependent, and it gets contributions from virtual corrections and soft real emission. In the exponent, the process-independent (*i.e.* universal) coefficients $g_{j,q\bar{q}}(\lambda)$ with $j > 0$ receive contributions from the threshold logarithmic terms originating from real emission. Given $\lambda = 2\beta_0 a_s(\mu_R^2) \ln \bar{N} \sim \mathcal{O}(1)$ with β_0 being the first coefficient of the QCD beta function, they effectively resum these logarithmic contributions to all orders in α_s . We refer to appendix A.9 for the analytical form of the various coefficients appearing in (3.10) and that are relevant for NLO+NNLL calculations for the Drell-Yan-like processes considered.

As the separation of the N -independent and N -dependent pieces in (3.10) is not unambiguous, different resummation schemes have been proposed and described in section 2.4 of [32]. In this document, we consider the so-called \bar{N}_1 resummation scheme for simplicity.

Resummed calculations must then have to be matched with fixed-order predictions at (N)LO. This is achieved by adding the resummed and (N)LO results and subtracting of all double-counted contributions. The latter correspond to the (N)LO soft-virtual terms of the partonic cross section, which can be obtained by expanding $\Delta_{q\bar{q}}^{\text{res}}(N, M^2, \mu_F^2)$ at $\mathcal{O}(\alpha_s^{b(+1)})$, where b stands for the power in α_s of the LO contributions (that is 0 here).

3.4 Cross sections for extra lepton production at the LHC

In this section, we compute total and differential cross sections relevant for the production of additional leptons such as those appearing in the models introduced in section 3.2. Predictions at (N)LO and (N)LO+PS are obtained within the MG5AMC framework (version 3.3.0), using the UFO models developed in this work, and we employ PYTHIA 8.2 [175] to deal with the simulation of the QCD environment (parton showering and hadronisation). On the other hand, total rate calculations matching fixed-order predictions with soft-gluon resummation are derived with an in-house code.

We define the electroweak sector through three independent input parameters that we choose to be the Z -boson mass m_Z , the electromagnetic coupling constant evaluated at the Z -pole $\alpha(m_Z)$, and the Fermi constant G_F ,

$$\begin{aligned} m_Z &= 91.1876 \text{ GeV}, & \alpha^{-1}(m_Z) &= 127.9, \\ G_F &= 1.1663787 \cdot 10^{-5} \text{ GeV}^{-2}. \end{aligned} \tag{3.12}$$

In addition, the CKM matrix is taken diagonal, the pole mass of the top quark $m_t = 172.7 \text{ GeV}$, and we consider $n_f = 5$ active quark flavours. Moreover, the widths of all particles appearing in the relevant diagrams have been set to zero. Our predictions make use of the CT18NNLO [49] set of parton distribution functions (PDFs), which are provided by LHAPDF [176] that we also use to control the renormalisation group running of the strong coupling α_s . For predictions in the Type-III seesaw model, we safely set the elements of the ε matrix to zero, as they turn to be negligible once bounds from flavour and electroweak precision data are accounted for [177].

The central value of the renormalisation and factorisation scales is set to the invariant mass M of the produced di-lepton system, $\mu_R = \mu_F = M$. Scale uncertainties are evaluated through the usual seven-point variation method described in section 2.4.3, in which the renormalisation and factorisation scales are varied independently by a factor of two up and down relative to their central value with the two extreme cases $\mu_R/\mu_F = 4$ or $1/4$ being excluded.

3.4.1 Total cross sections at the LHC

We dedicate this section to an overview of the behaviour of the total cross sections for exotic lepton production at the LHC with $\sqrt{s} = 14 \text{ TeV}$, as a function of the lepton mass. We study the production of a pair of electrically-charged VLLs, and we consider both the

cases of an $SU(2)_L$ singlet and doublet of VLLs,

$$pp \rightarrow \tilde{E}^+ \tilde{E}^-, \quad pp \rightarrow E^+ E^-. \quad (3.13)$$

Moreover, we also explore the production of a pair of singly-charged Type-III leptons that are mostly weak triplets,

$$pp \rightarrow E^+ E^- \equiv \Sigma^+ \Sigma^-. \quad (3.14)$$

For the last process, we introduced the abusive notation $\Sigma^\pm \equiv E^\pm$ to make an explicit distinction between the VLLs appearing in the model of section 3.2.1 (process (3.13) and notation of table 3.2), and those inherent to the Type-III seesaw model of section 3.2.2 (process (3.14) and notation of table 3.5). We do not consider any other pair-production mechanism (*i.e.* the production of a pair of neutral or doubly-charged leptons, or of an associated pair of leptons of different charges), as cross section predictions are not expected to exhibit a fundamentally different behaviour due to the purely electroweak nature of the processes involved. We indeed focus, in the following, on the impact of higher-order corrections that only depends on the quark/gluon nature of the initial state. Our analysis therefore equally applies to charged-current and neutral-current production processes, the only difference between the various channels being the normalisation of the (differential) rates. However, as our UFO model files are public and MG5AMC is a general-purpose event generator, interested readers can study by themselves any other process, both at (N)LO and (N)LO+PS.

In the left panel of figure 3.1, we report LO production cross sections for the three processes of eqs. (3.13) and (3.14). The cross sections are found to span about 7 orders of magnitude for exotic lepton masses varying from 200 GeV to 2.5 TeV. Cross sections around 100–1000 fb are found for small lepton masses of a few hundreds of GeV, whereas the production rates drop to the 0.001–1 fb regime for leptons of 1–2 TeV, making the potential observation of such BSM particles at the LHC more challenging. Moreover, for a given lepton mass, the production of a pair of weak-triplet states ($pp \rightarrow \Sigma^+ \Sigma^-$; red) is favoured over that of weak-doublet states ($pp \rightarrow E^+ E^-$; blue), while the latter is favoured over the production of weak-singlet states ($pp \rightarrow \tilde{E}^+ \tilde{E}^-$; green). Such a hierarchy, as well as the relative differences observed between the rates that are factors of a few, can be understood from the different $SU(2)_L$ representations of the fields considered, together with the Drell-Yan-like nature of the lepton pair-production mechanism.

In the right panel of figure 3.1, we present the corresponding K -factors, that we define, for a given lepton mass, as the ratio of a cross section to the associated LO one at central scale. K -factors are shown both at LO (shaded area) and NLO (hatched area), together with the associated scale uncertainties. We observe mild K -factor values at NLO, which vary in the 1.15–1.40 range as a function of the exotic lepton mass. Moreover, the K -factors are found to be (almost) independent of the process. Such a result is not surprising

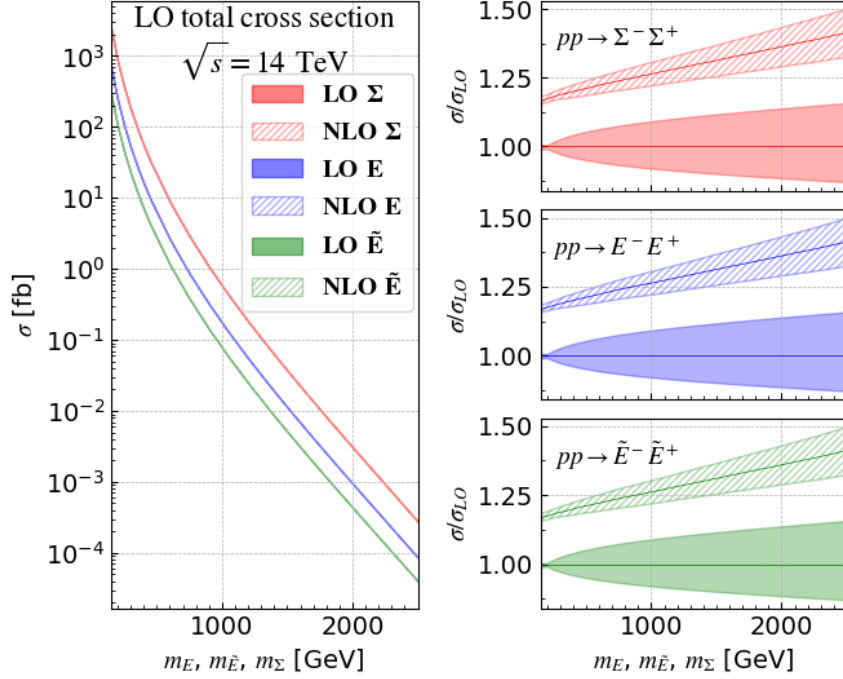


Figure 3.1: Total cross sections for the production of charged leptons typical from VLL and Type-III seesaw models, presented as a function of the lepton mass. We consider $SU(2)_L$ singlet (green), doublet (blue) and triplet (red) leptons, and the LHC at 14 TeV. Predictions are shown at LO (left panel), as well as in the form of LO and NLO K -factors together with the associated scale uncertainties (right panel).

as the underlying Born contribution factorises in the case of a Drell-Yan-like process. Uncertainties are significantly larger at LO than at NLO, and vary in the last case from a few percents at small lepton masses to about 10% for larger masses. This behaviour stems from the typically larger invariant masses associated with heavier di-lepton systems, that naturally enhance the importance of the threshold logarithms that ought to be resummed.

In the upper panel of figure 3.2, we show the production rates obtained after matching NLO predictions with soft gluon resummation at the NNLL accuracy, these results being currently the best theoretical predictions of the total cross sections for the processes considered. In order to estimate the associated impact, we present, in the three lower panels of figure 3.2, the ratio of the NLO, NLO+NLL and NLO+NNLL rates to the NLO one for the three processes. By virtue of the factorisation properties of the Born contributions, the predictions for these ratios are mostly independent of the process. We observe a mild increase of the total rate once threshold resummation is included, although this increase is mostly driven by the leading and next-to-leading logarithmic contributions. NNLL contributions indeed barely modify the total rates. Numerically, these enhancements with respect to the NLO predictions are found to be about 5% for scenarios with light leptons, and range to about 10% for scenarios featuring heavier leptons. In addition, it is

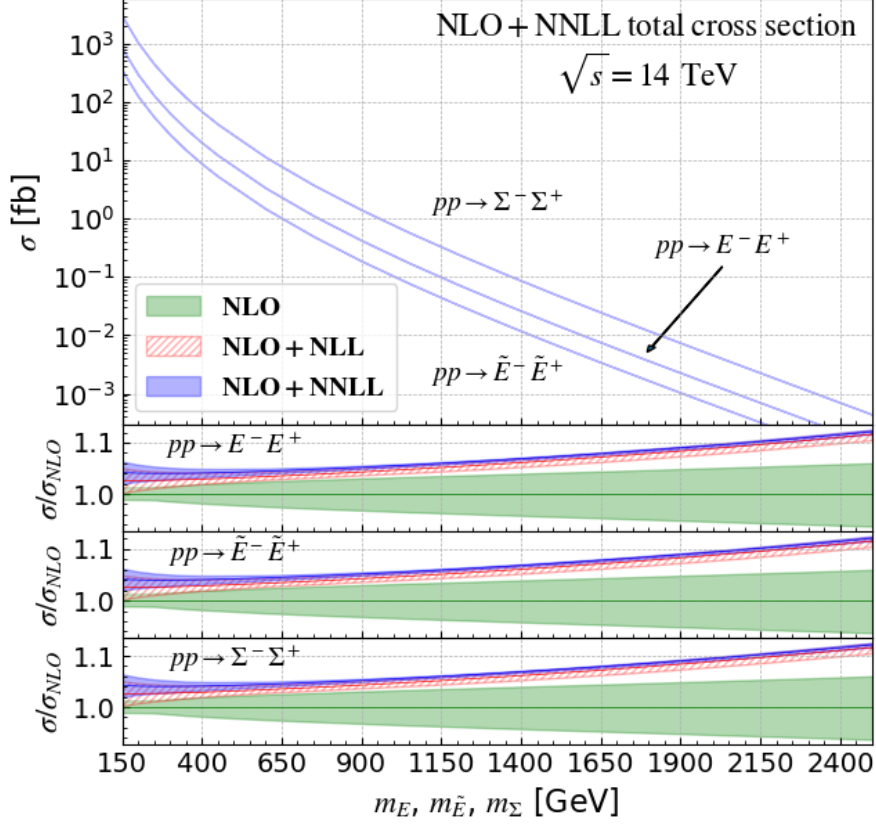


Figure 3.2: Total NLO+NNLL cross sections (upper panel) for the production of vector-like and Type-III seesaw leptons, presented as a function of the mass of the exotic lepton and for the LHC at a centre-of-mass energy of 14 TeV. We also display the ratios of the NLO (green), NLO+NLL (red) and NLO+NNLL (blue) rates to the NLO ones (with a central scale choice), together with the associated scale uncertainties.

observed that the resummed results (at NLO+NLL and NLO+NNLL) lie above the error bands of the NLO ones when a lepton mass of a few hundreds GeV is considered. This situation is similar to the case of the SM Drell-Yan process (see the rapidity distributions in [33]).

As typical from resummation calculations, the most notable feature of the NLO+NNLL rate concerns the drastic reduction of the scale uncertainties inherent to the predictions, that are reduced below the percent level in average, regardless of the lepton mass. The necessity of incorporating soft gluon resummation in the predictions is made even more evident for scenarios featuring heavy exotic leptons. Here, the scale uncertainty bands at NLO+(N)NLL drastically decrease, which could be anticipated as we deal with a perturbative calculations in which α_s is even smaller (the scale at which it is evaluated

being trivially larger). This essentially cures the counter-intuitive large scale uncertainties observed at NLO. These uncertainties in the large lepton mass region are mainly due to μ_F variation, hence the PDF contribution. This explains why we recover a behaviour similar to the PDF uncertainties presented in figure 20 of [178].

3.4.2 Invariant mass distributions

In this section, we consider again the processes (3.13) and (3.14), and we calculate the associated invariant-mass distributions $d\sigma/dM$, with M standing for the invariant mass of the di-lepton system. As an illustration, we choose three typical exotic lepton masses of 600 GeV, 900 GeV and 1.5 TeV, which correspond to three scenarios that have not been fully excluded yet by LHC experiments. The definition of these scenarios is driven by current experimental search results. The CMS collaboration has indeed observed an excess of 2.8σ when searching for VLLs with a mass of 600 GeV [106], whereas VLLs of 900 GeV can already be probed by existing run 2 CMS and ATLAS searches. In contrast, extra leptons with a mass of 1500 GeV lie beyond the current reach, but they could potentially be probed at future LHC runs. In addition, all chosen extra lepton masses lead to PDF uncertainties under fair control [154]. The results are shown in figures 3.3 and 3.4.

In the upper inset in each plot, we display fixed-order predictions and the associated scale uncertainties at LO (red) and NLO (blue), as well as after matching them with threshold resummation at LO+LL (cyan), NLO+NLL (yellow) and NLO+NNLL (purple). We have checked that for invariant mass distributions, (N)LO+PS results coincide with (N)LO calculations since this observable is insensitive to PS effects. (N)LO+PS predictions are therefore not included in the figures. In general, we observe a rapid increase of the differential cross section close to the kinematic threshold M_0 equals to twice the heavy lepton mass, until it peaks at $M \approx 1.06M_0$ before falling off toward higher invariant-mass values.

For any given M value, fixed-order LO predictions (red) are found to be notably smaller. Their matching with predictions including the resummation of the LL contributions (cyan) yields a significant enhancement of the central value. It reaches 15%–25% in the peak region, and 30% at larger invariant masses where the relevant phase space region is closer to the partonic threshold ($z \rightarrow 1$). Resummation effects are therefore more prominent in the latter case. Nevertheless, scale uncertainties in both cases remain large, and the two sets of predictions do not overlap within their error bands. This effect can be tamed down after including NLO corrections. In this case, both NLO+NLL and NLO+NNLL predictions are found to agree with each other once uncertainties are accounted for, whereas NLO spectra are slightly smaller for all considered M values.

In order to better assess the impact of threshold resummation, we display in the lower insets of figures 3.3 and 3.4 bin-by-bin ratios of the NLO, NLO+NLL and NLO+NNLL

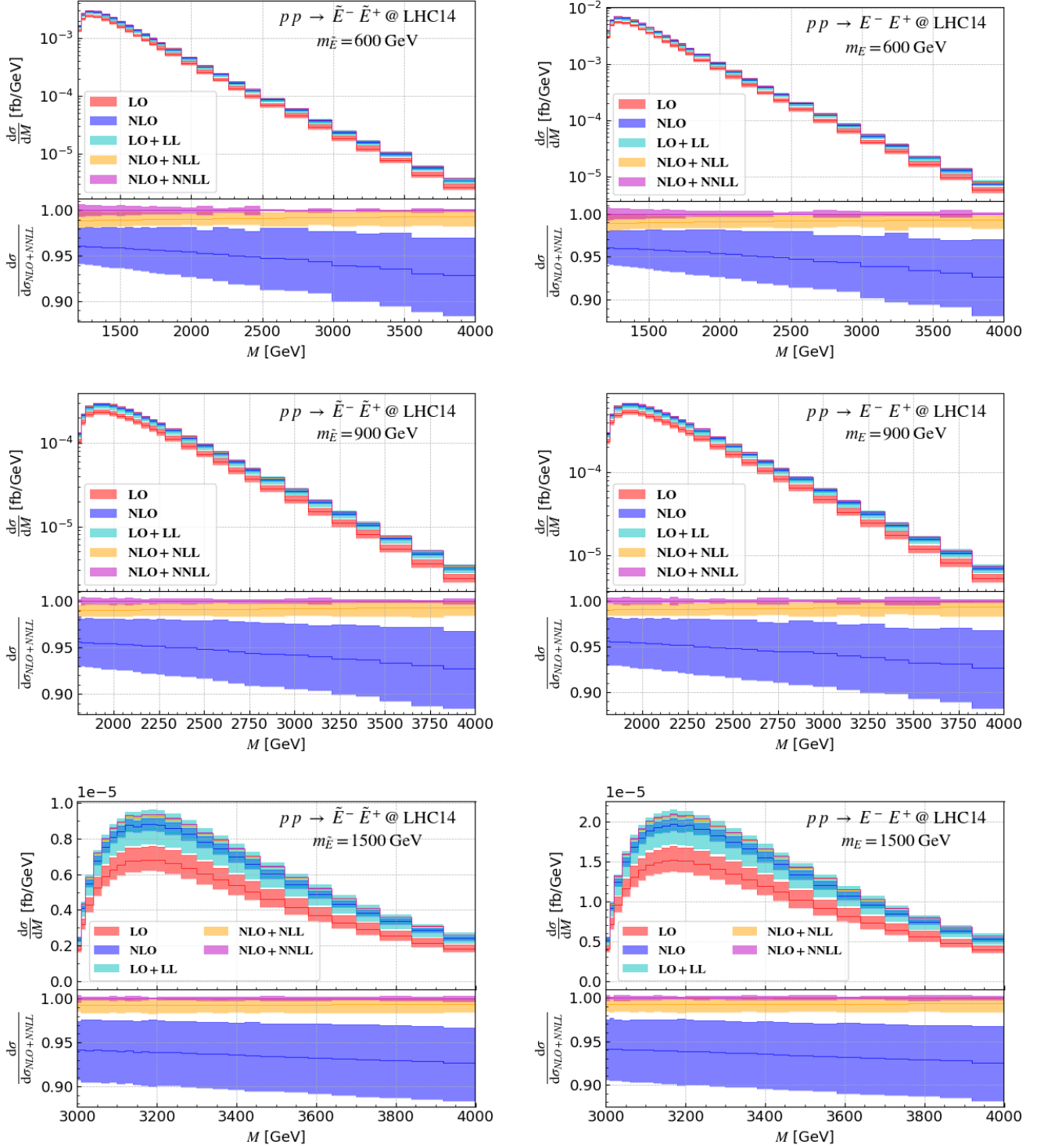


Figure 3.3: Invariant mass spectrum for the processes (3.13), together with the associated scale uncertainties (upper inset of each panel). We show fixed-order results at LO (red) and NLO (blue), as well as after matching them with threshold resummation at LO+LL (cyan), NLO+NLL (yellow) and NLO+NNLL (purple), and we consider new lepton masses of 600 GeV (top row), 900 GeV (middle row) and 1.5 TeV (bottom row). We additionally present the bin-by-bin ratios of the NLO, NLO+NLL and NLO+NNLL spectra to the NLO+NNLL ones, with the associated uncertainties (lower inset in each panel).

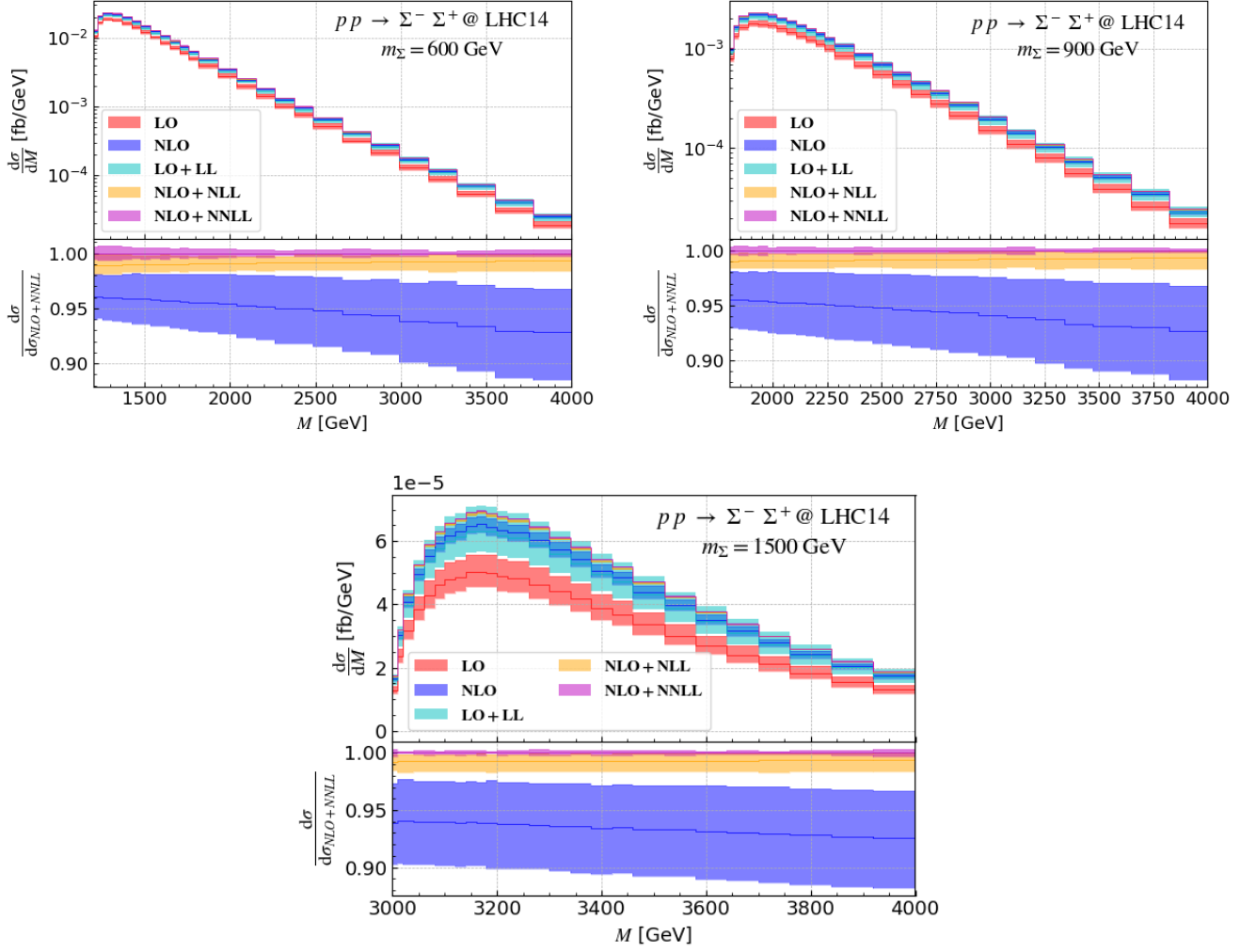


Figure 3.4: Same as figure 3.3 but for Type-III seesaw leptons and the process (3.14).

rates to the most precise NLO+NNLL predictions evaluated with central scale choices. The bands represent again the associated scale uncertainties. We observe that the increase of the differential NLO cross section induced by NLL or NNLL resummation (or equivalently, the decrease of the NLO cross sections, shown in blue, relative to the most precise NLO+NNLL predictions) depends on the invariant mass of the di-lepton system M , and therefore indirectly on the mass of the lepton species produced that fix the kinematic production threshold M_0 . Preferred configurations hence naturally target larger z values closer to 1 for heavy lepton production than for light lepton production. Resummation effects are therefore expected to be more important for heavy leptons, when considering M values lying at a given relative distance from M_0 . Again, we observe that NLO+(N)NLL results are generally outside the NLO error bands.

Nevertheless, the shape of the spectrum is stabilised after including threshold resummation at NLL (yellow). NNLL resummation (purple) only yields a mild increase of the

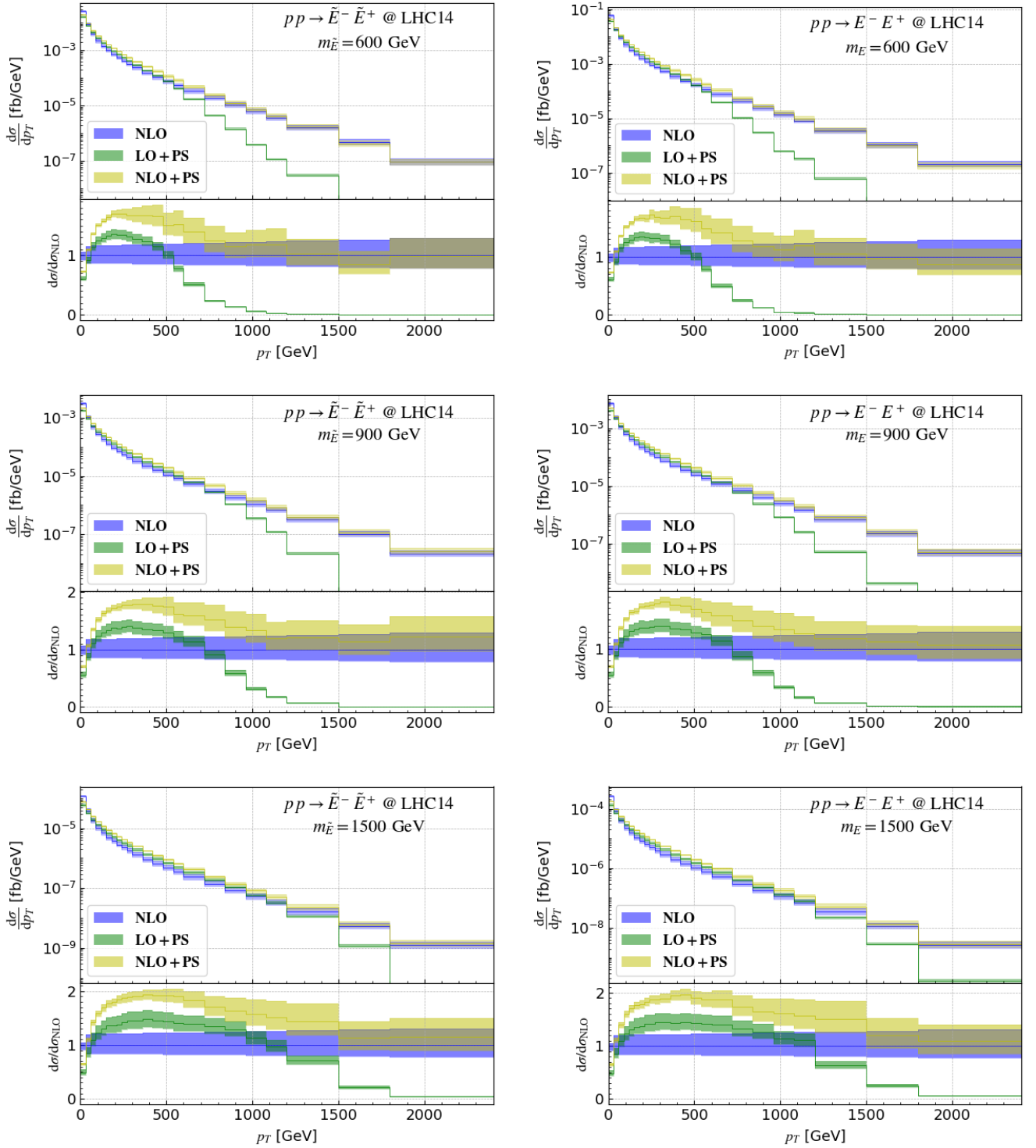


Figure 3.5: Transverse momentum spectrum for the processes (3.13), together with the associated scale uncertainties (upper inset in each panel). We show fixed-order results at NLO (blue), as well as LO+PS (green) and NLO+PS (olive) predictions. We consider lepton masses of 600 GeV (top row), 900 GeV (middle row) and 1.5 TeV (bottom row), and we additionally present the corresponding bin-by-bin ratios to the NLO spectra with the associated scale uncertainties (lower inset in each panel).

rate by less than 1%, which is largely independent of the di-lepton invariant mass M . This shows that a good perturbative convergence has been achieved at NLO+NNLL. Moreover, NLO+NNLL predictions are crucial to reduce the scale uncertainties to be less than 0.5%, hence motivating using more precise predictions for BSM signals when available.

3.4.3 Transverse momentum spectra

We now turn to the study of the distribution in the transverse momentum (p_T) of the lepton pair, which is an observable relevant to show that the inclusion of PS is essential. Although the MG5AMC framework practically allows for investigations of any observable, we only focus, for the sake of an example, on this distribution in the p_T of the di-lepton system. In figures 3.5 and 3.6, we present $d\sigma/dp_T$ distributions at NLO (blue), LO+PS (green) and NLO+PS (olive), whereas the LO distributions are trivially located at $p_T = 0$. As in section 3.4.2, we choose three benchmark scenarios featuring extra leptons with masses of 600 GeV, 900 GeV and 1.5 TeV respectively. The different p_T spectra are shown in the upper insets of the figures, whereas the lower insets display their bin-by-bin ratios to the (fixed-order) NLO predictions.

While NLO predictions (blue) in principle diverge at small p_T due to uncanceled soft and/or collinear singularities originating from real emission, the integration of the differential cross section within a given bin regularises this divergence, the bin-by-bin results shown in the figures being normalised by the bin size. It is similar to the cancellation described in appendix A.6: the virtual singularity sits at $p_T = 0$, we need to cancel it with the real emission contribution by integrating over a finite bin size. We therefore observe a finite cross section with a pronounced maximum in the low p_T region, with $p_T \lesssim 30$ GeV (which corresponds to the first bin shown in the plots). The cross sections in the small p_T regime are therefore expected to be better described by matching fixed-order predictions with PS. Showering, as well as the non-perturbative intrinsic transverse momentum k_T of the constituents of the protons, should additionally distort the shapes of the spectra in the low p_T regime. NLO+PS predictions are hence smaller than NLO ones at small $p_T \lesssim 30$ GeV, before becoming considerably greater at intermediate transverse momenta ($p_T \in [60, 500]$ GeV). At larger p_T values, QCD radiation encoded in the real matrix elements dominates, so that NLO+PS predictions agree with NLO ones.

This last effect can be even more evidenced by studying the LO+PS curves (green). As the LO cross section does not allow any emission (hence is proportional to $\delta(p_T)$), non-zero p_T values are here purely arising from shower effects. As such, they cannot capture the NLO behaviour and they give rise to a too soft spectrum in the high- p_T regime. In conclusion, NLO+PS should be the best for describing such an observable, while NLO (LO+PS) predictions fail at low (high) p_T . Finally, we can note that multiplying LO+PS predictions by an overall K -factor, as traditionally done in many experimental and phenomenological

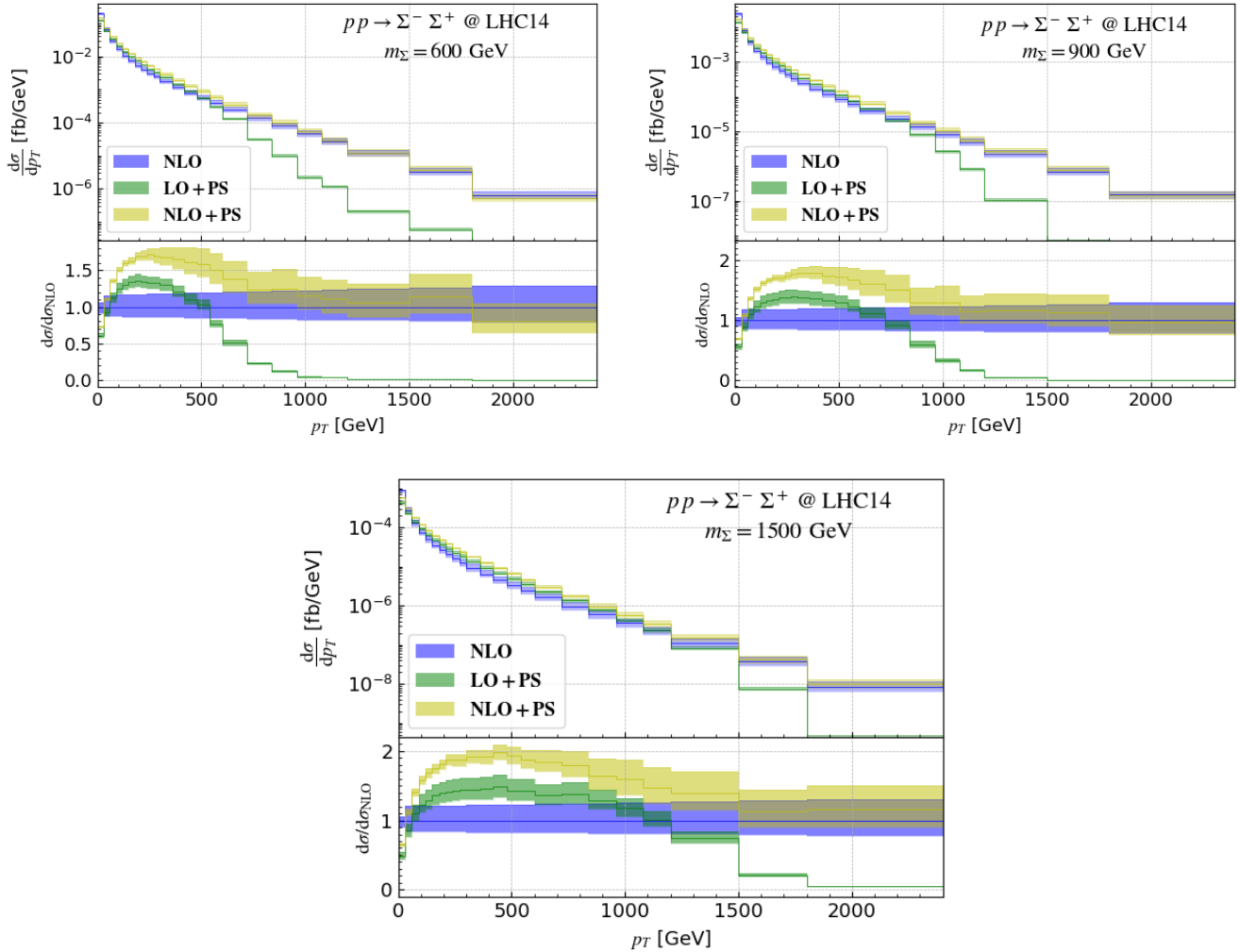


Figure 3.6: Same as figure 3.5 but for Type-III seesaw leptons.

studies, is unjustified in the aim of an accurate signal description, and will even yield qualitatively wrong results at high p_T .

3.5 Conclusion

Numerous extensions of the Standard Model feature additional leptons that carry a variety of different electric charges. They are consequently actively searched for at collider experiments. In this work, we have studied the production of these extra leptons in effective frameworks representative of the TeV-scale phenomenology of several models featuring additional leptons. By providing FEYNRULES implementations and the associated UFO libraries for Type-III seesaw models and new physics scenarios with VLLs, we complete the set of publicly available models suitable for calculations relevant for the production of

new leptons at colliders beyond the LO or LO+PS accuracy. With these public models, VLL and Type-III lepton production can now be simulated at NLO+PS accuracy, as was already the case for other neutrino mass models or left-right-symmetric scenarios which both involve new non-coloured fermions. The corresponding model files can be downloaded from <https://feynrules.irmp.ucl.ac.be/wiki/NLOModels>.

We have reported the most precise calculations of total rates to date for the production of a pair of Type-III leptons or VLLs lying in the trivial or fundamental representations of $SU(2)_L$. Our predictions include both NLO QCD corrections and threshold resummation effects at NNLL. Higher-order QCD effects increase the production rates by 25%–30%, the exact value depending on the scenario and the extra lepton mass, and scale uncertainties are reduced below 1%. We have additionally investigated the impact of these corrections on the distributions in the invariant mass of the produced heavy lepton system and observed a notable increase in the differential rates and a significant reduction of the scale uncertainties.

Finally, we have made use of the designed UFO models to highlight the joint impact of NLO corrections and PS matching on an example of observable relevant for existing searches for extra leptons. We have chosen the distribution in the transverse momentum of the dilepton system. We have illustrated how NLO+PS improves fixed-order NLO computations at low p_T , and provides a better modelling of the physical spectra at intermediate p_T values below 1 TeV. These calculations have been achieved fully automatically, in the MG5AMC framework, in a setup similar to that used in ATLAS and CMS studies as well as in many existing phenomenological explorations. Upgrades of existing studies and searches to include NLO corrections matched with PS should therefore be straightforward.

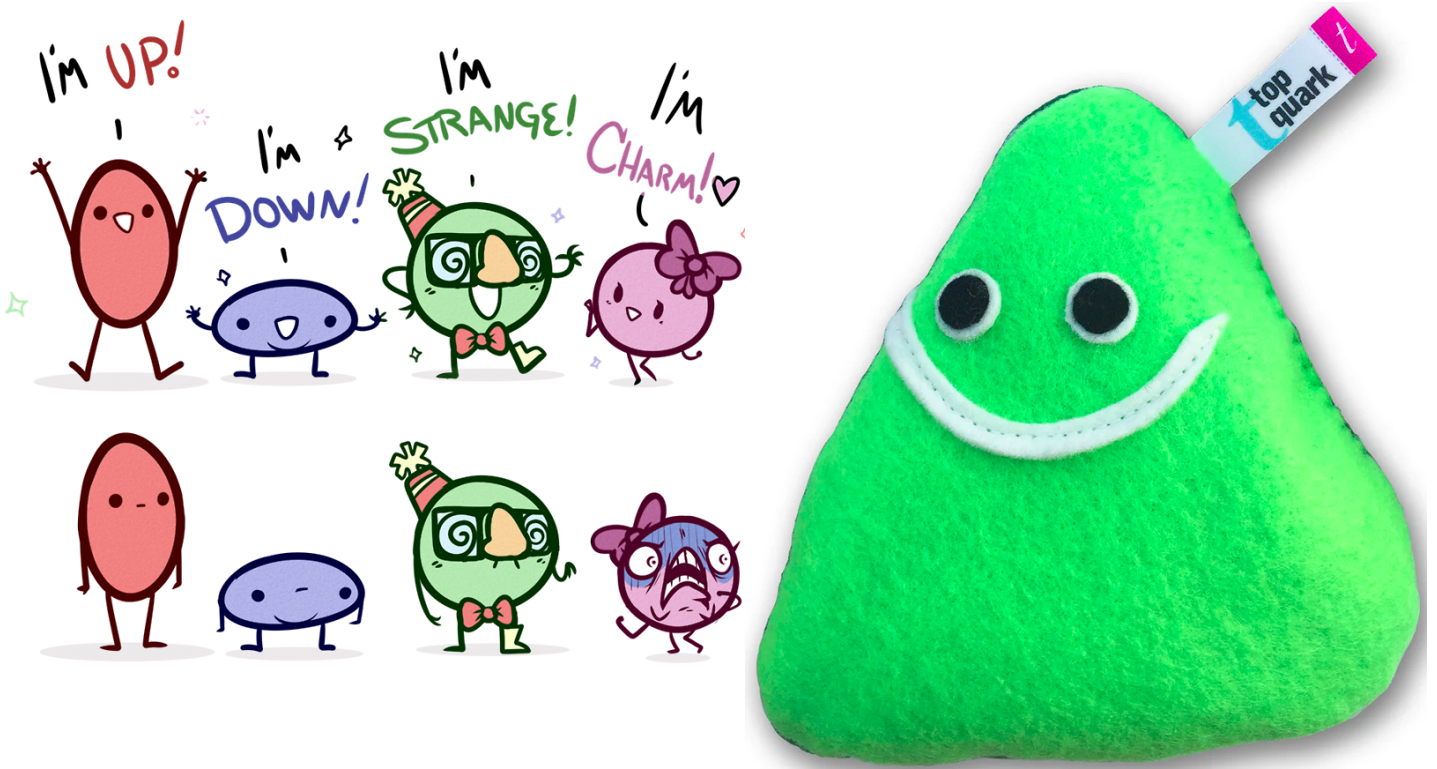
4

Colourful processes: top pair(s) production

Summary

4.1	Pair production: $pp \rightarrow t\bar{t}$	95
4.1.1	Absolute threshold <i>vs</i> invariant mass threshold	95
4.1.2	Differential cross section	96
4.2	Increasing multiplicity: $pp \rightarrow t\bar{t}t\bar{t}$	99
4.2.1	NLO prediction	100
4.2.2	Feynman diagrams and partonic channels	100
4.2.3	Colour Basis	101
4.2.4	Soft function and anomalous dimension	103
4.2.5	Resummation results	103

Celui qui trouve sans chercher est celui qui a longtemps cherché sans trouver
Gaston Bachelard



Cartoon representation of quarks, light quarks and top quark

THIS chapter focuses on the analysis of processes related to top pair(s) production. Initially, we will examine the well-known $2 \rightarrow 2$ process of a single pair production. The intricacies of resummation in this context arise due to the coloured and massive particles present in the final states. Hence, we need the complete general resummation formalism detailed in section 2.4.1. However, the resummation calculation for this process has already been discussed in the literature [20, 68, 179–182]. This provides us with an opportunity to validate our procedure and identify any deviations in the setup when compared to the literature. We will conclude by examining the four-top production, a process of great interest for SM and BSM studies, which displays greater multiplicity and has not been extensively covered by the resummation literature [31]. The results presented in this chapter were obtained using the MSTW2008nnlo68cl PDF set.

4.1 Pair production: $pp \longrightarrow t\bar{t}$

In this section, we detail the resummed results related to the top pair production process. The formalism was detailed in chapter 3, we focus only on the physical results in this section. Firstly, let us precise the resummation setup we consider to compare with the literature.

4.1.1 Absolute threshold *vs* invariant mass threshold

In the literature, the threshold limit can have two distinct meanings. The “absolute” threshold limit and the “invariant mass” threshold are distinct frameworks that we detail here:

- Absolute threshold: this limit corresponds to $\tilde{z} = \tilde{M}^2/\hat{s} \rightarrow 1$, where \tilde{M} is the mass of the final state at rest. In the case of top pair production, we have $\tilde{M}^2 = 4m_t^2$, for four top production $\tilde{M}^2 = 16m_t^2$.
- Invariant mass threshold: here the threshold limit corresponds to $z = M^2/\hat{s} \rightarrow 1$, with M the invariant mass of the Born-level system.

We always have $M \geq \tilde{M}$, so that the absolute threshold limit can be seen as a limit case of the invariant mass approach. Even if the two approaches are related, we must stress that they are not equivalent. The absolute threshold approach assumes that the final state particles are produced almost at rest. In that case, the fixed order coefficients should also take into account Coulomb corrections that encode gluon exchange between particles that are nearly at rest. These corrections are typically of order $\mathcal{O}(\alpha_s/\beta_C)$, where $\beta_C = \sqrt{1 - \tilde{z}}$. Hence, they become significant when \tilde{z} approaches 1. However, in the context of LHC and top pair production we can evaluate $\tilde{M} = 2m_t \simeq 345$ GeV and $\sqrt{\hat{s}}$ can reach up to $\sqrt{s} = 13$ TeV, implying that β_C is a generic $\mathcal{O}(1)$ parameter, as detailed in the introduction of [68]. Furthermore, in the context of the absolute threshold, it is commonly expected that there will be a natural diagonalisation of the soft anomalous matrix that helps the computations, as reported in [78]. For illustration, an instance is provided in appendix A.7.2.

To better understand the regimes, we can display the (M^2, \hat{s}) phase space, as shown in figure 13 of [68]. In figure 4.1, the blue region corresponds to the invariant mass threshold regime, where $z \rightarrow 1$ but the invariant mass can be far from the mass shell. The green region corresponds to the absolute threshold regime, where M is close to \tilde{M} and where Coulomb singularities appear that need to be considered.

In this document, we will only consider the invariant mass threshold approach as it allows to access the differential cross section $\frac{d\sigma}{dM}$.

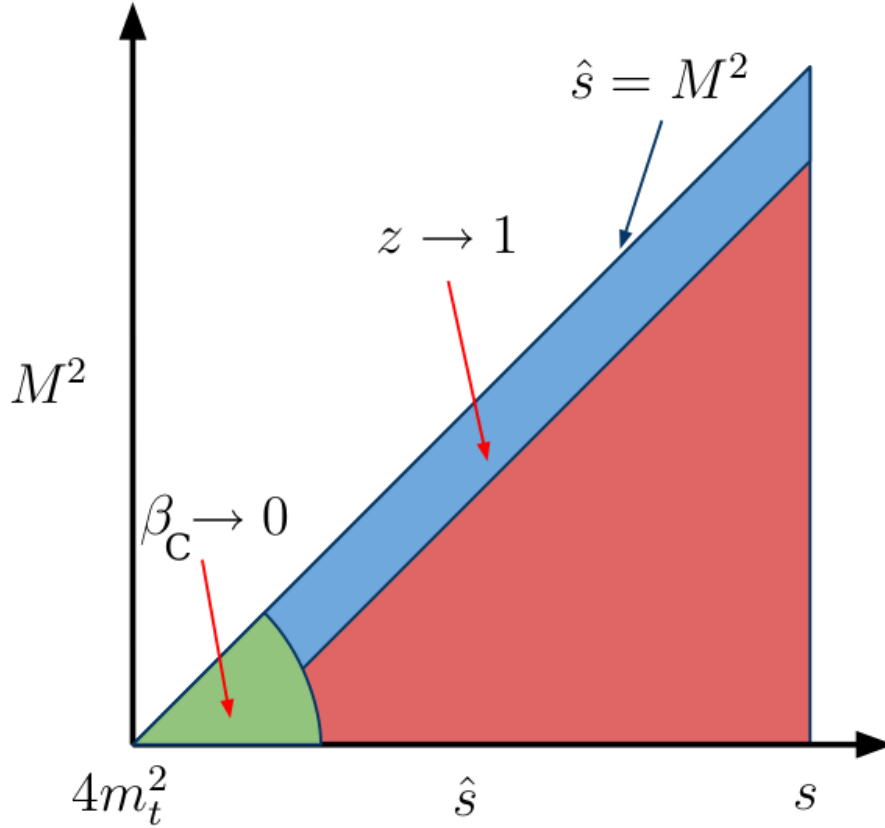


Figure 4.1: Figure 13 of [68] displaying the $(M, \sqrt{\hat{s}})$ phase space and different threshold regions

4.1.2 Differential cross section

In this section we present some results for the differential cross section with respect to the invariant mass.

First, we plot the differential cross section in the region close to the production threshold to assess the effect of resummation. Figure 4.2 displays the fixed-order cross section (LO and NLO) alongside the matched resummed result at NLL accuracy. The hadronic center-of-mass energy is set to 7 TeV and an initial central scale of $\mu_0 = M/2$ is chosen. As we will discuss later in this section, this selection is motivated by a comparison with [68].

As previously noted in section 3.4.2, a global increase in the matched result over the corresponding fixed-order NLO is observed. This enhancement ranges from 3% at the production threshold to 12% at $M = 500$ GeV. Additionally, there is a modest reduction in the scale uncertainties with respect to the fixed-order prediction. Indeed, the average relative error across the range of invariant mass is 26.6% for NLO, whereas it is only 21.4% for the matched prediction. This reduction is less pronounced than in section 3.4.2 for Drell-Yan like processes, but similar to what can be found in the literature, see Figure

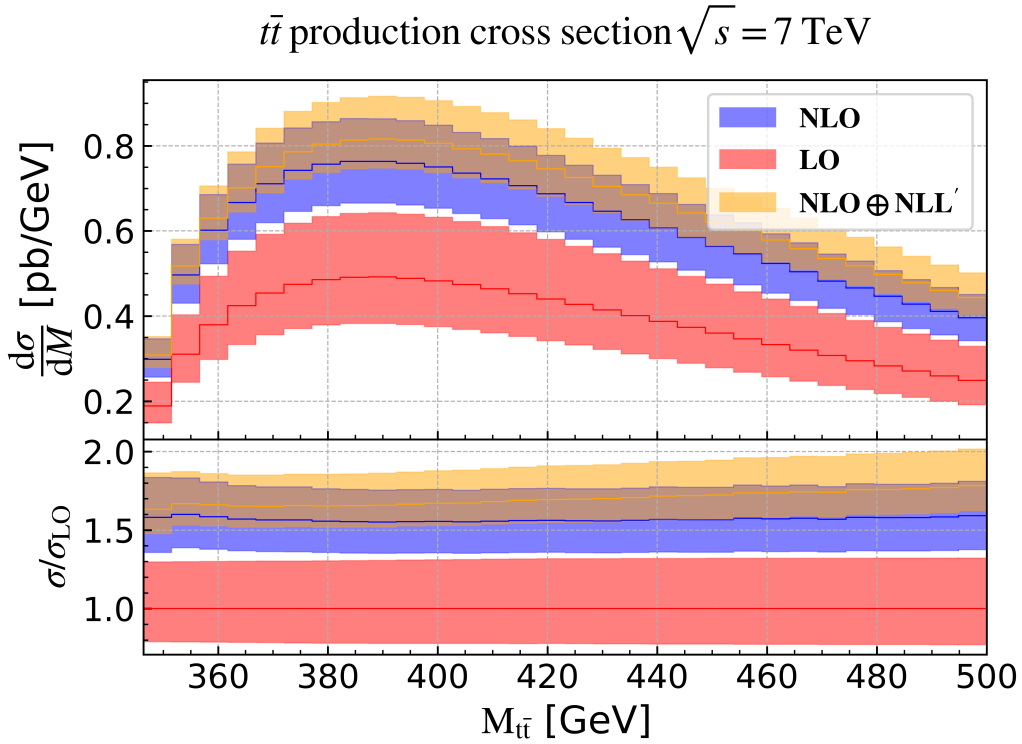


Figure 4.2: Differential cross section for top pair production at LO, NLO and matched resummed at NLL accuracy, compare to [68]

2 & 8 of [68]. A discerning reader would notice that the resummation featured in [68] differs from the one developed in this document, as it includes elements of N^2LL accuracy. Therefore, we cannot make a direct comparison of the obtained values with the literature and must instead compare qualitatively.

A more quantitative comparison with the literature may be achievable using the setup in [182]. Figure 4.3 displays the differential cross section for both the fixed order prediction at NLO and the matched prediction at NLL accuracy, for $\sqrt{s} = 8$ TeV and $\mu_0 = M$. To ensure a direct comparison, we replicated the setup used in figure 3 of [182]. We can extract the data that come from the ATLAS analysis [183] and compare with the matched prediction.

Firstly, it is clear that the overall shape of figure 4.3 is very similar to figure 3 of [182]. The most remarkable feature of the plot is the clear gain in accuracy of the matched prediction compared to NLO, relative to the ATLAS data. There is no obvious reduction in scale uncertainty due to the increase in normalisation of the matched prediction. However, it is clear that the enhancement induced by the resummation matching brings the ATLAS data within the error bars of the prediction. A complete comparison with the $NLO+N^2LL'$ resummation conducted in [182] (in brown in figure 4.3) would need the inclusion of

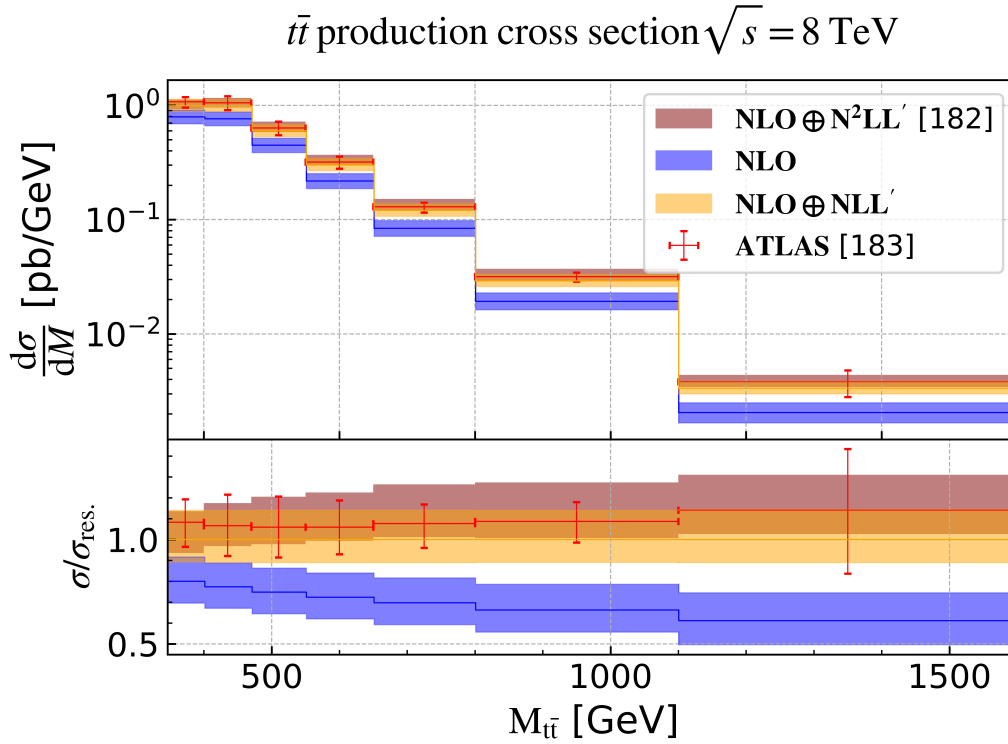


Figure 4.3: Differential cross section for top pair production at LO, NLO and matched resummed at NLL accuracy, compared to matching N²LL' of [182] and ATLAS data [183]

transverse mass logarithms. These logarithms significantly affect the high M domain, improving further the matched prediction and enhancing the accuracy in comparison to the ATLAS data. Given that the resummation configuration in our research is not precisely identical to that of [182], we should not be overly concerned about the disparities in the two predictions. The main takeaway is that, in both scenarios, the situation improves with the inclusion of resummation relative to NLO.

The authors in [182] note that choosing a central scale of $\mu_0 = M/2$ increases the value of the NLO cross section, in contrast to using $\mu_0 = M$. This outcome is in line with the resummation effect, resulting in improved accuracy in regions where higher order corrections are prominent. Although the third figure in their paper is obtained with $\mu_0 = M$, they conclude that it is more appropriate to use $M/2$ later. This decision motivated our choice of scale in both figures 4.2 and 4.3.

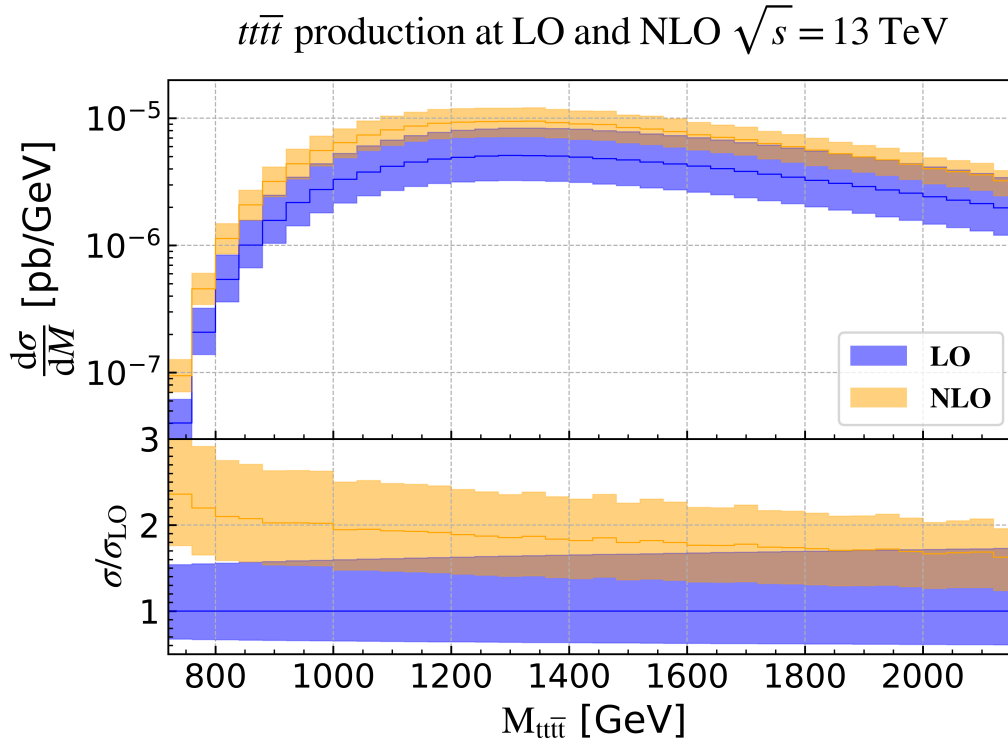


Figure 4.4: Fixed order differential cross section with respect to the final state invariant mass. Computed automatically with MG5AMC for $\sqrt{s} = 13$ TeV at LO and NLO, $\mu_0 = 2m_t$

4.2 Increasing multiplicity: $pp \longrightarrow t\bar{t}\bar{t}$

As it has been discussed in introduction, the four top process is of great interest in the context of LHC physics.

Its cross section has only recently been measured experimentally [29, 30]. As a result, there are still considerable error bars on both theoretical and experimental sides, approximately $\pm 25\%$. Investigating this rare process is certainly worthwhile as the top sector holds a special role in the SM due to the mass of the top. Top physics serves as a pathway to comprehend the properties of Higgs since the coupling correlates with the mass. When considering BSM physics, research such as that carried out in [184] explores the possible connections between the top sector and the NP through the use of Standard Model Effective Theory (SMEFT). In this context, the four-top production process presents a great opportunity to probe NP, as such a massive final state suffers little physical background from other processes. After this brief motivation for the study of the four top production process, let us present some results for the (differential) cross section, first in the known case of fixed order prediction and finally for resummation.

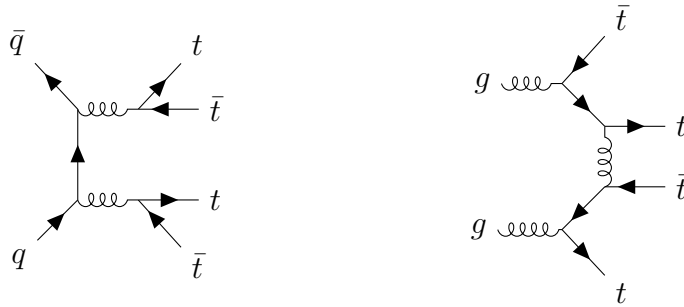
4.2.1 NLO prediction

For the selected MG5AMC configuration, with a fixed central scale of $2m_t$, the total cross section for the production of four top quarks at LO and NLO, for $\sqrt{s} = 13$ TeV, are respectively: $5.88^{+67.8\%}_{-37.7\%}$ fb and $10.47^{+24.9\%}_{-24.4\%}$ fb. This choice of central scale was motivated by comparison with [31], in order to obtain a comparable normalisation of the total cross section.

Figure 4.4 illustrates the differential cross section for the production of four top quarks, generated by MG5AMC. The shape closely resembles that of the differential cross section in figures 3.4 and 4.2. The NLO is increased by a global K factor of about 1.79 (+79%) compared to the LO. However the K factor is not constant over the entire range of M as it is higher than 2 near production threshold and decreases as M increases. Although the NLO error bar appears larger on the lower plot, it is merely a result of the enhancement, since NLO and LO do not share the same normalisation. In accordance with our expectations upon increasing the perturbative order, we observe a decrease in the relative error bars.

4.2.2 Feynman diagrams and partonic channels

To tackle the four top production process we need the full toolbox introduced in this document. Firstly, let us look at some tree-level diagrams for this process, see A.10 for the other geometries.



From the given diagrams, it is clear that we have two parton channels for this process: quark-antiquark and gluon-gluon. A colour basis is required for each subprocess, which is elaborated in section 1.3.1.

4.2.3 Colour Basis

Let us first detail the simple representation decomposition for the final state. In the case of four top production it reads:

$$\begin{aligned}
 \underline{\mathbf{3}} \otimes \overline{\underline{\mathbf{3}}} \otimes \underline{\mathbf{3}} \otimes \overline{\underline{\mathbf{3}}} &= (1, 0) \otimes (0, 1) \otimes (1, 0) \otimes (0, 1) = \left((1, 1) \oplus (0, 0) \right) \otimes \left((1, 1) \oplus (0, 0) \right) \\
 &= (1, 1) \otimes (1, 1) \oplus (1, 1) \otimes (0, 0) \oplus (1, 1) \otimes (0, 0) \oplus (0, 0) \otimes (0, 0) \\
 &= \mathbf{27} \oplus \underline{\mathbf{10}} \oplus \overline{\underline{\mathbf{10}}} \oplus \mathbf{8} \oplus \mathbf{8} \oplus \mathbf{8} \oplus \mathbf{8} \oplus \mathbf{1} \oplus \mathbf{1}.
 \end{aligned} \tag{4.1}$$

Since $\underline{\mathbf{3}} \otimes \overline{\underline{\mathbf{3}}} = \mathbf{8} \oplus \mathbf{1}$, the quark channel can only populate the octets or singlets in the decomposition (4.1). Following the same method used in 1.41 for the gluon channel, and after orthogonalisation, we derive the six-dimensional colour basis for the quark channel.

$$\begin{aligned}
 q_1 \bar{q}_2 &\longrightarrow t_3 t_4 \bar{t}_5 \bar{t}_6 \\
 &\left\{ \delta_{c_2 c_1} \delta_{c_3 c_5} \delta_{c_4 c_6}; \delta_{c_2 c_1} \frac{N_c \delta_{c_3 c_6} \delta_{c_4 c_5} - \delta_{c_3 c_5} \delta_{c_4 c_6}}{N_c}; \delta_{c_4 c_6} \frac{N_c \delta_{c_2 c_5} \delta_{c_3 c_1} - \delta_{c_2 c_1} \delta_{c_3 c_5}}{N_c}; \right. \\
 &\frac{1}{N_c^2} \left(N_c \delta_{c_2 c_5} (N_c \delta_{c_3 c_6} \delta_{c_4 c_1} - \delta_{c_3 c_1} \delta_{c_4 c_6}) + \delta_{c_2 c_1} (\delta_{c_3 c_5} \delta_{c_4 c_6} - N_c \delta_{c_3 c_6} \delta_{c_4 c_5}) \right); \\
 &\frac{1}{N_c^2 - 1} \left((N_c^2 - 1) \delta_{c_2 c_6} \delta_{c_3 c_1} \delta_{c_4 c_5} + \delta_{c_2 c_5} (\delta_{c_3 c_6} \delta_{c_4 c_1} - N_c \delta_{c_3 c_1} \delta_{c_4 c_6}) + \delta_{c_2 c_1} (\delta_{c_3 c_5} \delta_{c_4 c_6} - N_c \delta_{c_3 c_6} \delta_{c_4 c_5}) \right); \\
 &\frac{1}{N_c^2 - 2} \left[\delta_{c_2 c_6} \left((N_c^2 - 2) \delta_{c_3 c_5} \delta_{c_4 c_1} - N_c \delta_{c_3 c_1} \delta_{c_4 c_5} \right) + \delta_{c_2 c_5} (2 \delta_{c_3 c_1} \delta_{c_4 c_6} - N_c \delta_{c_3 c_6} \delta_{c_4 c_1}) \right. \\
 &\quad \left. + \delta_{c_2 c_1} (2 \delta_{c_3 c_6} \delta_{c_4 c_5} - N_c \delta_{c_3 c_5} \delta_{c_4 c_6}) \right] \left. \right\}.
 \end{aligned} \tag{4.2}$$

To perform the orthogonalisation, the `Mathematica` software package `ColorMath` [185] was utilised. This package is specifically developed to manage $SU(N_c)$ algebra and is optimised for this purpose. We used the same package for determining the colour factors in the context of four top production. Regarding the gluon channel, the colour basis was previously discussed in (1.41), and therefore our focus now is on its orthogonalisation.

$$g_1 g_2 \longrightarrow t_3 t_4 \bar{t}_5 \bar{t}_6$$

We take $N_c = 3$ to simplify the basis writing. Consequently, we have 13 tensors in the basis, instead of 14, as one of the orthogonalized tensor norm is vanishing when $N_c = 3$:

$$\begin{aligned}
 &\mathbf{T}_{c_4 c_6}^{c_1} \cdot \mathbf{T}_{c_3 c_5}^{c_2} + \mathbf{T}_{c_3 c_5}^{c_1} \cdot \mathbf{T}_{c_4 c_6}^{c_2} - \mathbf{T}_{c_4 c_5}^{c_1} \cdot \mathbf{T}_{c_3 c_6}^{c_2} - \mathbf{T}_{c_4 c_5}^{c_2} \cdot \mathbf{T}_{c_3 c_6}^{c_1} + \delta_{c_4 c_6} (\mathbf{T}_{c_3 \alpha}^{c_1} \cdot \mathbf{T}_{\alpha c_5}^{c_2} + \mathbf{T}_{c_3 \alpha}^{c_2} \cdot \mathbf{T}_{\alpha c_5}^{c_1}) \\
 &- \delta_{c_4 c_5} (\mathbf{T}_{c_3 \alpha}^{c_1} \cdot \mathbf{T}_{\alpha c_6}^{c_2} + \mathbf{T}_{c_3 \alpha}^{c_2} \cdot \mathbf{T}_{\alpha c_6}^{c_1}) + \delta_{c_3 c_5} (\mathbf{T}_{c_4 \alpha}^{c_1} \cdot \mathbf{T}_{\alpha c_6}^{c_2} + \mathbf{T}_{c_4 \alpha}^{c_2} \cdot \mathbf{T}_{\alpha c_6}^{c_1}) \\
 &- \delta_{c_3 c_6} (\mathbf{T}_{c_4 \alpha}^{c_1} \cdot \mathbf{T}_{\alpha c_5}^{c_2} + \mathbf{T}_{c_4 \alpha}^{c_2} \cdot \mathbf{T}_{\alpha c_5}^{c_1}) + \frac{\delta^{c_1 c_2}}{2} (\delta_{c_3 c_6} \delta_{c_4 c_5} - \delta_{c_3 c_5} \delta_{c_4 c_6}).
 \end{aligned}$$

The rest of the colour basis reads:

$$\begin{aligned}
 & \left\{ \mathbf{T}_{c_4\alpha}^{c_1} \cdot \mathbf{T}_{\alpha c_6}^{c_2} \delta_{c_3 c_5}; \left(\mathbf{T}_{c_4\alpha}^{c_1} \cdot \mathbf{T}_{\alpha c_6}^{c_2} + 8 \mathbf{T}_{c_4\alpha}^{c_2} \cdot \mathbf{T}_{\alpha c_6}^{c_1} \right) \frac{\delta_{c_3 c_5}}{8}; \mathbf{T}_{c_3 c_5}^{c_1} \cdot \mathbf{T}_{c_4 c_6}^{c_2}; \right. \\
 & \mathbf{T}_{c_4 c_6}^{c_1} \cdot \mathbf{T}_{c_3 c_5}^{c_2} - \frac{1}{8} \mathbf{T}_{c_3 c_5}^{c_1} \cdot \mathbf{T}_{c_4 c_6}^{c_2}; \mathbf{T}_{c_3\alpha}^{c_1} \cdot \mathbf{T}_{\alpha c_5}^{c_2} \delta_{c_4 c_6} - \frac{\delta_{c_3 c_5}}{7} \left(\mathbf{T}_{c_4\alpha}^{c_1} \cdot \mathbf{T}_{\alpha c_6}^{c_2} + \mathbf{T}_{c_4\alpha}^{c_2} \cdot \mathbf{T}_{\alpha c_6}^{c_1} \right); \\
 & \mathbf{T}_{c_3\alpha}^{c_2} \cdot \mathbf{T}_{\alpha c_5}^{c_1} \delta_{c_4 c_6} + \frac{1}{6} \left(\mathbf{T}_{c_3\alpha}^{c_1} \cdot \mathbf{T}_{\alpha c_5}^{c_2} \delta_{c_4 c_6} - \left(\mathbf{T}_{c_4\alpha}^{c_1} \cdot \mathbf{T}_{\alpha c_6}^{c_2} + \mathbf{T}_{c_4\alpha}^{c_2} \cdot \mathbf{T}_{\alpha c_6}^{c_1} \right) \delta_{c_3 c_5} \right); \mathbf{T}_{c_4\alpha}^{c_1} \cdot \mathbf{T}_{\alpha c_5}^{c_2} \delta_{c_3 c_6} \\
 & - \frac{1}{189} \left(-7 \left(\delta_{c_3 c_5} \mathbf{T}_{c_4\alpha}^{c_2} \cdot \mathbf{T}_{\alpha c_6}^{c_1} + \delta_{c_4 c_6} \mathbf{T}_{c_3\alpha}^{c_2} \cdot \mathbf{T}_{\alpha c_5}^{c_1} \right) - 16 \mathbf{T}_{c_3 c_5}^{c_1} \cdot \mathbf{T}_{c_4 c_6}^{c_2} + 56 \left(\mathbf{T}_{c_3\alpha}^{c_1} \cdot \mathbf{T}_{\alpha c_5}^{c_2} + \mathbf{T}_{c_4\alpha}^{c_1} \cdot \mathbf{T}_{\alpha c_6}^{c_2} \right) \right. \\
 & \left. + 65 \mathbf{T}_{c_4 c_6}^{c_1} \cdot \mathbf{T}_{c_3 c_5}^{c_2} \right); \mathbf{T}_{c_4\alpha}^{c_2} \cdot \mathbf{T}_{\alpha c_5}^{c_1} \delta_{c_3 c_6} + \frac{1}{309} \left(7 \left(\mathbf{T}_{c_3\alpha}^{c_1} \cdot \mathbf{T}_{\alpha c_5}^{c_2} \delta_{c_4 c_6} + \mathbf{T}_{c_4\alpha}^{c_1} \cdot \mathbf{T}_{\alpha c_6}^{c_2} \delta_{c_3 c_5} \right) \right. \\
 & \left. + 15 \mathbf{T}_{c_4\alpha}^{c_1} \cdot \mathbf{T}_{\alpha c_5}^{c_2} \delta_{c_3 c_6} + 21 \mathbf{T}_{c_4 c_6}^{c_1} \cdot \mathbf{T}_{c_3 c_5}^{c_2} - 91 \left(\mathbf{T}_{c_3\alpha}^{c_2} \cdot \mathbf{T}_{\alpha c_5}^{c_1} \delta_{c_4 c_6} + \mathbf{T}_{c_4\alpha}^{c_2} \cdot \mathbf{T}_{\alpha c_6}^{c_1} \delta_{c_3 c_5} \right) - 105 \mathbf{T}_{c_4 c_6}^{c_2} \cdot \mathbf{T}_{c_3 c_5}^{c_1} \right); \\
 & \mathbf{T}_{c_3 c_6}^{c_1} \cdot \mathbf{T}_{c_4 c_5}^{c_2} - \frac{1}{36} \left(\mathbf{T}_{c_4\alpha}^{c_1} \cdot \mathbf{T}_{\alpha c_6}^{c_2} \delta_{c_3 c_5} + \mathbf{T}_{c_3\alpha}^{c_2} \cdot \mathbf{T}_{\alpha c_5}^{c_1} \delta_{c_4 c_6} - 9 \delta_{c_3 c_6} \left(\mathbf{T}_{c_4\alpha}^{c_1} \cdot \mathbf{T}_{\alpha c_5}^{c_2} + \mathbf{T}_{c_4\alpha}^{c_2} \cdot \mathbf{T}_{\alpha c_5}^{c_1} \right) \right. \\
 & \left. + 13 \left(\mathbf{T}_{c_3\alpha}^{c_1} \cdot \mathbf{T}_{\alpha c_5}^{c_2} \delta_{c_4 c_6} + \mathbf{T}_{c_4\alpha}^{c_2} \cdot \mathbf{T}_{\alpha c_6}^{c_1} \delta_{c_3 c_5} + \mathbf{T}_{c_4 c_6}^{c_1} \cdot \mathbf{T}_{c_3 c_5}^{c_2} + \mathbf{T}_{c_3 c_5}^{c_1} \cdot \mathbf{T}_{c_4 c_6}^{c_2} \right) \right); \mathbf{T}_{c_4 c_5}^{c_1} \cdot \mathbf{T}_{c_3 c_6}^{c_2} \\
 & - \frac{1}{30} \left(3 \left(\mathbf{T}_{c_3\alpha}^{c_1} \cdot \mathbf{T}_{\alpha c_5}^{c_2} \delta_{c_4 c_6} + \mathbf{T}_{c_4\alpha}^{c_2} \cdot \mathbf{T}_{\alpha c_6}^{c_1} \delta_{c_3 c_5} \right) - 6 \mathbf{T}_{c_4 c_5}^{c_2} \cdot \mathbf{T}_{c_3 c_6}^{c_1} - 9 \left(\mathbf{T}_{c_4\alpha}^{c_1} \cdot \mathbf{T}_{\alpha c_5}^{c_2} \delta_{c_3 c_6} + \mathbf{T}_{c_4\alpha}^{c_2} \cdot \mathbf{T}_{\alpha c_5}^{c_1} \delta_{c_3 c_6} \right) \right. \\
 & \left. + 11 \left(\mathbf{T}_{c_4\alpha}^{c_1} \cdot \mathbf{T}_{\alpha c_6}^{c_2} \delta_{c_3 c_5} + \mathbf{T}_{c_3\alpha}^{c_2} \cdot \mathbf{T}_{\alpha c_5}^{c_1} \delta_{c_4 c_6} \right) + 13 \left(\mathbf{T}_{c_4 c_6}^{c_1} \cdot \mathbf{T}_{c_3 c_5}^{c_2} + \mathbf{T}_{c_3 c_5}^{c_1} \cdot \mathbf{T}_{c_4 c_6}^{c_2} \right) \right); \mathbf{T}_{c_3\alpha}^{c_1} \cdot \mathbf{T}_{\alpha c_6}^{c_2} \delta_{c_4 c_5} \\
 & - \frac{1}{168} \left(14 \left(\mathbf{T}_{c_3\alpha}^{c_2} \cdot \mathbf{T}_{\alpha c_5}^{c_1} \delta_{c_4 c_6} + \mathbf{T}_{c_4\alpha}^{c_2} \cdot \mathbf{T}_{\alpha c_6}^{c_1} \delta_{c_3 c_5} \right) - 18 \mathbf{T}_{c_4\alpha}^{c_2} \cdot \mathbf{T}_{\alpha c_5}^{c_1} \delta_{c_3 c_6} + 35 \mathbf{T}_{c_4 c_6}^{c_1} \cdot \mathbf{T}_{c_3 c_5}^{c_2} - 39 \mathbf{T}_{c_4\alpha}^{c_1} \cdot \mathbf{T}_{\alpha c_5}^{c_2} \delta_{c_3 c_6} \right. \\
 & \left. - 63 \left(\mathbf{T}_{c_4 c_5}^{c_1} \cdot \mathbf{T}_{c_3 c_6}^{c_2} + \mathbf{T}_{c_3 c_6}^{c_1} \cdot \mathbf{T}_{c_4 c_5}^{c_2} \right) + 77 \left(\mathbf{T}_{c_3\alpha}^{c_1} \cdot \mathbf{T}_{\alpha c_5}^{c_2} \delta_{c_4 c_6} + \mathbf{T}_{c_4\alpha}^{c_1} \cdot \mathbf{T}_{\alpha c_6}^{c_2} \delta_{c_3 c_5} \right) + 98 \mathbf{T}_{c_3 c_5}^{c_1} \cdot \mathbf{T}_{c_4 c_6}^{c_2} \right); \\
 & \mathbf{T}_{c_3\alpha}^{c_2} \cdot \mathbf{T}_{\alpha c_6}^{c_1} \delta_{c_4 c_5} - \frac{1}{400} \left(-67 \mathbf{T}_{c_4\alpha}^{c_1} \cdot \mathbf{T}_{\alpha c_5}^{c_2} \delta_{c_3 c_6} + 81 \left(\mathbf{T}_{c_3\alpha}^{c_1} \cdot \mathbf{T}_{\alpha c_5}^{c_2} \delta_{c_4 c_6} + \mathbf{T}_{c_4\alpha}^{c_1} \cdot \mathbf{T}_{\alpha c_6}^{c_2} \delta_{c_3 c_5} \right) \right. \\
 & \left. - 104 \left(\mathbf{T}_{c_3\alpha}^{c_1} \cdot \mathbf{T}_{\alpha c_6}^{c_2} \delta_{c_4 c_5} + \mathbf{T}_{c_4\alpha}^{c_2} \cdot \mathbf{T}_{\alpha c_5}^{c_1} \delta_{c_3 c_6} \right) + 144 \mathbf{T}_{c_3 c_5}^{c_1} \cdot \mathbf{T}_{c_4 c_6}^{c_2} - 189 \left(\mathbf{T}_{c_3 c_6}^{c_1} \cdot \mathbf{T}_{c_4 c_5}^{c_2} + \mathbf{T}_{c_4 c_5}^{c_1} \cdot \mathbf{T}_{c_3 c_6}^{c_2} \right) \right. \\
 & \left. + 192 \left(\mathbf{T}_{c_3\alpha}^{c_2} \cdot \mathbf{T}_{\alpha c_5}^{c_1} \delta_{c_4 c_6} + \mathbf{T}_{c_4\alpha}^{c_2} \cdot \mathbf{T}_{\alpha c_6}^{c_1} \delta_{c_3 c_5} \right) + 255 \mathbf{T}_{c_4 c_6}^{c_1} \cdot \mathbf{T}_{c_3 c_5}^{c_2} \right); \\
 & \frac{1}{74} \left(26 \delta_{c_3 c_6} \left(\mathbf{T}_{c_4\alpha}^{c_1} \cdot \mathbf{T}_{\alpha c_5}^{c_2} + \mathbf{T}_{c_4\alpha}^{c_2} \cdot \mathbf{T}_{\alpha c_5}^{c_1} \right) + 26 \delta_{c_4 c_5} \left(\mathbf{T}_{c_3\alpha}^{c_2} \cdot \mathbf{T}_{\alpha c_6}^{c_1} + \mathbf{T}_{c_3\alpha}^{c_1} \cdot \mathbf{T}_{\alpha c_6}^{c_2} \right) \right. \\
 & \left. - 36 \left(\mathbf{T}_{c_4 c_6}^{c_1} \cdot \mathbf{T}_{c_3 c_5}^{c_2} + \mathbf{T}_{c_4 c_6}^{c_2} \cdot \mathbf{T}_{c_3 c_5}^{c_1} \right) + 37 \delta_{c_3 c_5} \delta_{c_4 c_6} \delta^{c_1 c_2} + 38 \left(\mathbf{T}_{c_4 c_5}^{c_1} \cdot \mathbf{T}_{c_3 c_6}^{c_2} + \mathbf{T}_{c_4 c_5}^{c_2} \cdot \mathbf{T}_{c_3 c_6}^{c_1} \right) \right. \\
 & \left. - 48 \delta_{c_4 c_6} \left(\mathbf{T}_{c_3\alpha}^{c_1} \cdot \mathbf{T}_{\alpha c_5}^{c_2} + \mathbf{T}_{c_3\alpha}^{c_2} \cdot \mathbf{T}_{\alpha c_5}^{c_1} \right) - 48 \delta_{c_3 c_5} \left(\mathbf{T}_{c_4\alpha}^{c_1} \cdot \mathbf{T}_{\alpha c_6}^{c_2} + \mathbf{T}_{c_4\alpha}^{c_2} \cdot \mathbf{T}_{\alpha c_6}^{c_1} \right) \right) \left. \right\}. \tag{4.3}
 \end{aligned}$$

Such an example of a complex colour basis demonstrates the importance of a minimal set for determining colour factors, as outlined in section 1.3.2. As the size of the tensor basis and the length of each individual tensor increases, the use of the minimal set becomes more and more necessary.

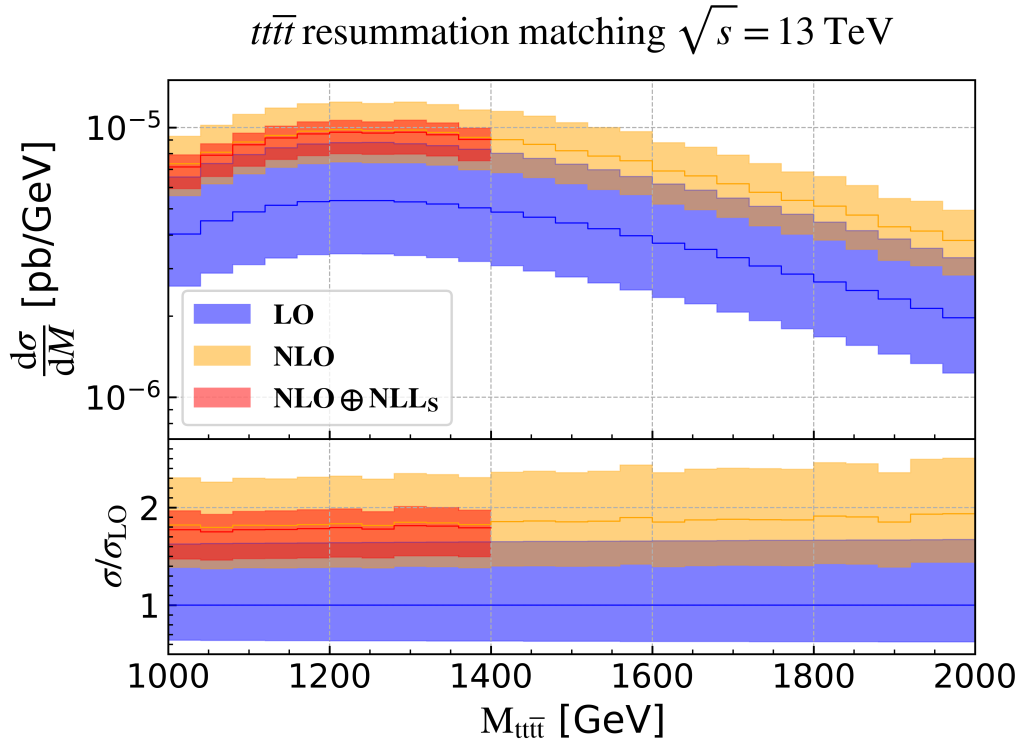


Figure 4.5: Matching of fixed order NLO to resummed cross section at NLL accuracy, except the hard function at one loop, for $\sqrt{s} = 13$ TeV, $\mu_0 = M/4$

4.2.4 Soft function and anomalous dimension

Having determined the colour basis and known the particle content of the process, we have all the ingredients to derive the soft functions. However, due to the length of the functional forms of these matrices, we will not present them in this document. Indeed, the kinematics of the $2 \rightarrow 4$ processes allow fewer simplifications than the $2 \rightarrow 2$, which greatly increases the complexity of the functions that constitute the coefficients of the matrices. Thorough checks were conducted to verify that the analytical `Mathematica` derivation of these matrices was accurately implemented numerically.

4.2.5 Resummation results

In figure 4.5, the figure displays the matching between the fixed order NLO and the resummed NLL predictions. Due to the substantial CPU cost, we could not integrate the $\mathbf{H}^{(1)}$ contribution into the resummation procedure for the four-top process at the time of thesis writing. The loop calculation, which was automated using the `MADLOOP` module, requires significant computing power. Although the framework has been validated and the code is designed to include these contributions, we have decided to postpone their

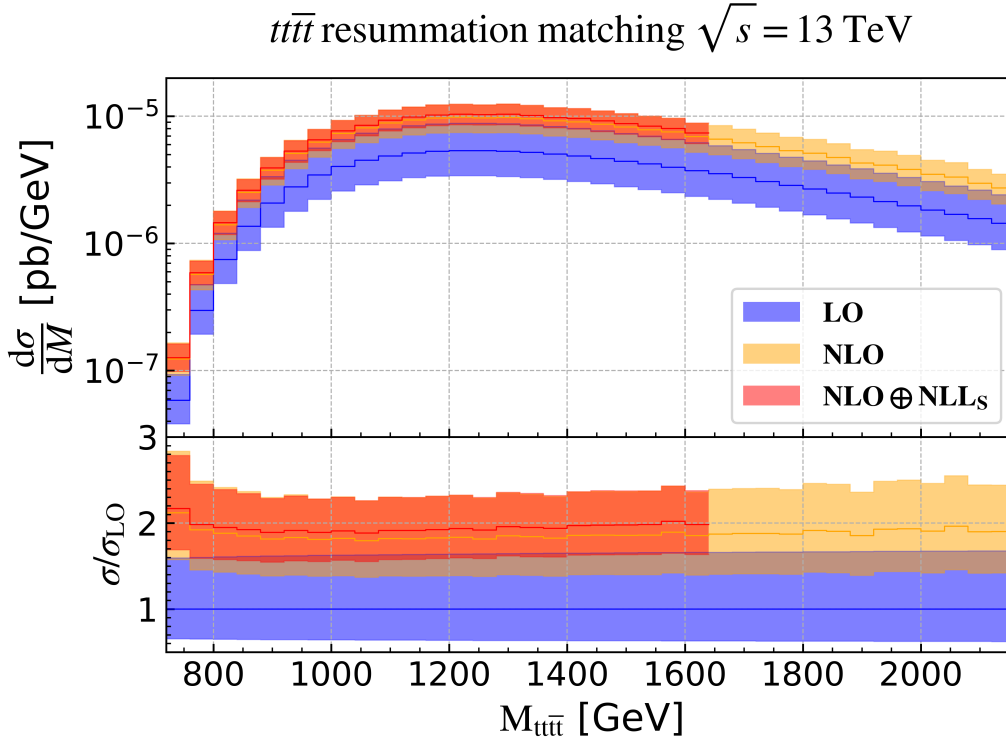


Figure 4.6: Matching of fixed order NLO to resummed cross section at NLL accuracy, except the hard function at one loop, for $\sqrt{s} = 13$ TeV, $\mu_0 = M/2$

treatment to achieve a meaningful result more quickly. For example, switching off the loop calculation and exclusively involving the fundamental hard function at Born level $\mathbf{H}^{(0)}$ results in a factor of 200 speed-up, whereas a single call of MADLOOP alone could take up to 35 seconds, in the case of the gluon channel, when including the loops. The integration method used for the four-top process, both for the inverse Mellin transform and the phase space integration, is based on Monte Carlo integration with *Vegas* [186]. To attain precision at an order of $\mathcal{O}(0.5\%)$, typically $\mathcal{O}(10^5)$ *Vegas* points are required in this setup, rendering the incorporation of $\mathbf{H}^{(1)}$ too demanding as an initial step. Further work is required to decrease the CPU time needed for incorporating the one-loop virtual contribution. In subsequent sections, we will designate the NLL, with the exception of the $\mathbf{H}^{(1)}$ contribution, as NLL_S . By using NLL_S only, we observe that the matching in figure 4.5 exhibits a decrease in error bars compared to the fixed order. For the bins that have been calculated up to this point, the relative error for NLO is $+26.3\% - 24.1\%$, whereas for the matching, it is $+10.7\% - 16.7\%$ with a central value reduction of 3.2%.

The application of the resummation formalism to the four-top production process enhances precision as we observe a reduction in the error bars related to scale. Figure 4.5 illustrates this and constitutes the initial step towards achieving complete NLO+NLL

matching at the differential cross section level. The small decrease of the central value is not expected for the matched prediction as the measurement lies above the NLO prediction (see 5). As reported in [31], the full matching at NLL accuracy should result in a global increase of the cross section around 15%. The central scale choice appears to be crucial in this case as taking $\mu_0 = M/2$ results in a increase of the central value of the matched prediction of 6% instead of the previous decrease, see figure 4.6. To compare coherently with [31], we would need the full NLO+NLL matching with a similar scale choice. However, we observe a reduction of the scale-induced error bars in both cases $\mu_0 = M/2$ and $\mu_0 = M/4$. This development is promising as it exhibits the robustness of resummation's ability to enhance the asymptotic convergence of predictions compared to fixed order computations.

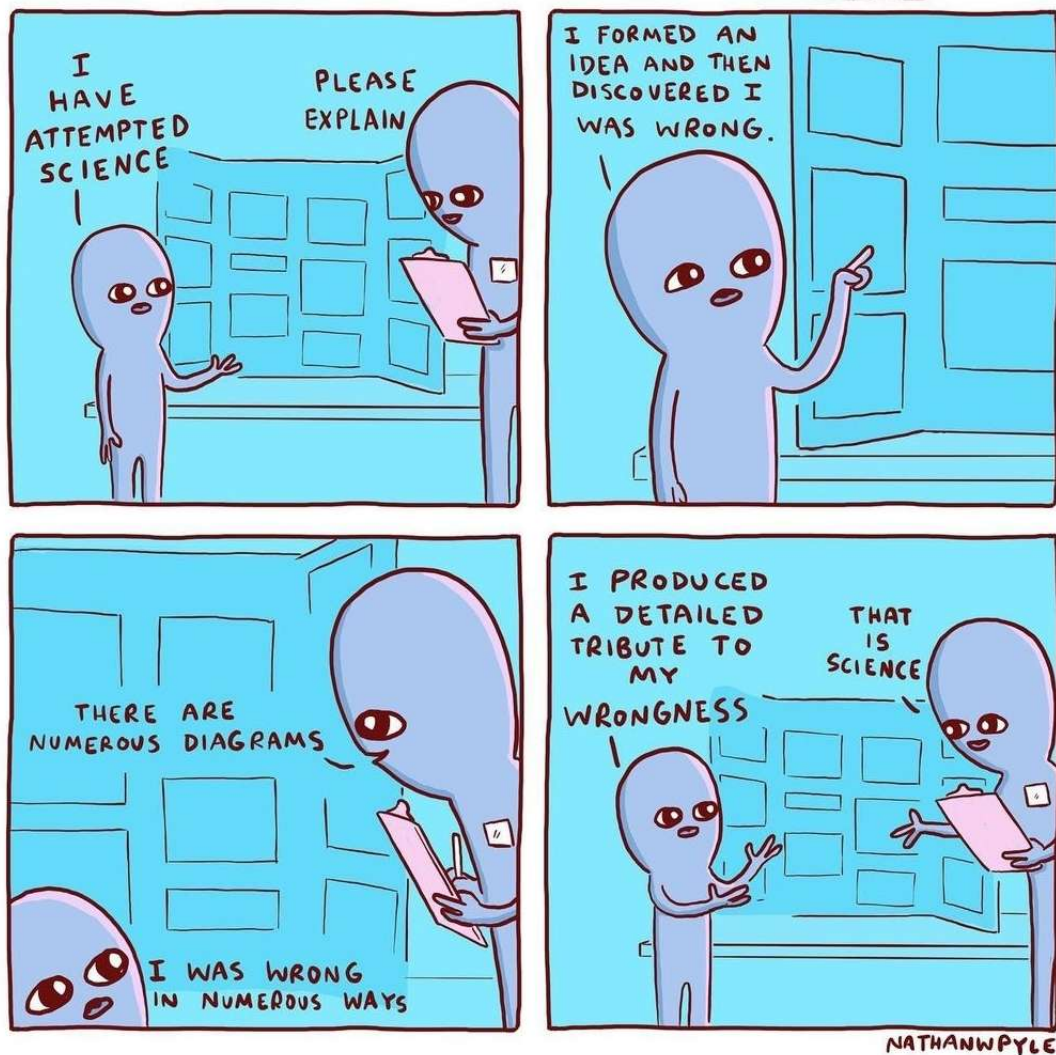
To conclude, we will briefly summarise the results presented in this thesis, before providing an outlook on possible future studies.

5

Conclusion

Le savant n'étudie pas la nature parce que cela est utile. Il l'étudie parce qu'il y prend plaisir et il y prend plaisir parce qu'elle est belle

Henri Poincaré



Strange Planet, Nathan W. Pyle

As a conclusion, the work presented in this thesis is summarised before prospects are outlined. More technical details are given in the following appendix. Finally, the references can be found in the bibliography section. A small abstract concludes this document.

Summary

After introducing general aspects of perturbative QCD in chapter 1, we focused on the threshold resummation formalism in chapter 2. The “toy resummation” section provided an opportunity to introduce threshold resummation’s fundamental principles before extending the framework to more intricate colour structures. The general expression (2.69) indeed includes cases with non-colour singlets in the final state, which may produce non-factorisable colour algebras, as detailed in section 1.3.2. This implies the determination of matrices in the colour space, in particular the soft matrix and its anomalous dimension. After establishing the theoretical framework, we can proceed with the resummation of observables for processes of interest.

In chapter 3 we consider the pair production of exotic leptons arising in various BSM models. The study of VLL pair production or weak triplets from Type-III seesaw models has many similarities to the well-known Drell-Yan process. The kinematics and corresponding diagrams are identical, with only the couplings being different. It follows that only the absolute value of the observable will vary for each individual case. Specifically, the normalised observables, whether they are total or differential cross sections, exhibit identical behaviour for the three pair productions studied. Furthermore, since only the initial partons in this scenario are coloured particles, it is possible to use directly the Sudakov form factor at N²LL from Drell-Yan. The resummation’s universality properties enable a precise treatment of these BSM models with minimal effort, even though they were initially known only at LO before the work of [83]. The study yielded improved results for fixed order prediction with NLO, while the inclusion of N²LL resummation further improved accuracy (central value) and precision (error bars) by reducing the scale uncertainty below the $\mathcal{O}(1\%)$ level.

For processes involving more than four coloured particles, it is necessary to use the general formalism specified in chapter 2, as the colour space has a dimension greater than one. In chapter 4, we focus on the application of resummation to top pairs production. Firstly, we replicate some previously published results for top pair production, which, although not new, help to validate the methodology and authenticate our implementation. Subsequently, we investigate the four top production process. As previously discussed, this topic is of great interest, particularly in the context of Run 3 at the LHC since we expect an improvement of statistics compared to the first measurement [29, 30]. Preliminary results are presented relative to the matching of resummed prediction to fixed order NLO in section 4.2.5. Even without the full NLL implementation, we already see a reduction of the error bars relative to scale variation. The numbers are coherent with the existing literature [31], although caution is advised since the resummation setup is not equivalent. Further work is needed to claim to have performed the complete NLO+NLL matching for four top production in the invariant mass threshold framework. Nevertheless, we can

consider that the theoretical framework as well as the code implementation are already done and validated on several examples. The only remaining task is to optimise the loop evaluation and integration to have a complete the matching at NLO+NLL. Apart from this direct continuation of the work presented in this thesis, we outline a few directions for future research following the present study.

Outlook

After briefly summarising the main content of this thesis, we will now provide an overview of potential future work following this study.

Before moving forward with the current implementation and exploring new applications, it is worth reconsidering the setup of PDFs. It was previously mentioned that the MSTW parametrisation we use is not the only option available. Firstly, the parametrisation can be adjusted to feature smaller polynomials in the fit function. Additionally, we could opt for Chebyshev parametrisation instead of regular polynomials. Concurrently, we may explore the use of different PDF sets. For instance, the NNPDF collaboration [52] proposes PDF sets determined through the use of neural networks. Recently, the MSTW authors also updated the PDF sets with the latest MSHT global fit [187].

When considering the application to Drell-Yan like processes, a potentially interesting project might be to push the threshold resummation to the N³LL level. Indeed, the resummation components for standard Drell-Yan are known, so the adaptation in the case of exotic lepton productions should be possible. Incorporating q_T resummation appears to be promising as we can see from the parton-shower matching in section 3.4.3. In the context of regular Drell-Yan q_T resummation, it has been established up to N³LL accuracy [188]. Incorporating both would pave the way for joint resummation [189].

Firstly, an attempt should be made to retrieve the findings of [31] using the absolute threshold limit. It should be possible to achieve this in the $M \rightarrow \tilde{M}$ region. Comparing these results for the total cross section would provide a strong cross-check of the two approaches. Including higher-order terms could improve the accuracy of our predictions. Due to limited computational resources, the $\mathbf{H}^{(1)}$ contribution was not included in our results. However, for the sake of consistency, it should be included. This would require some optimisation for the integration of virtual loop contribution as well as more computational resources. Similarly, incorporating N²LL contributions that are available for the Sudakov form factor is feasible. As the complexity of the N²LO fixed order prediction lies beyond the scope of current research, enhancing the resummation accuracy is a worthwhile area for investigation. The inclusion of electro-weak corrections is outside the scope of this document but is already available in the literature [31, 190] and should be a valuable addition to the present study.

Another interesting direction could be to add collinear improvement to the current resummation. This only concerns the Sudakov form factor, hence requires a moderate effort to implement. Elements to go in this direction are detailed in appendix A.8.3. We could also explore the next-to-leading power resummation [191] that is considering the inclusion of terms suppressed by a power of the threshold parameter $1 - z$ and could further improve the gain in precision.

To extend this work, we could apply the procedure to other processes of interest. $2 \rightarrow 3$ processes would be suitable choices as resummation is not systematically performed in these cases. Notable examples include $pp \rightarrow t\bar{t}\gamma/H/Z/W$ [192, 193], $\gamma\gamma g$, and BSM processes such as the production of squarks or gluino beyond pair production.

On a longer timescale, it would be worthwhile to explore the potential for automating resummation, particularly at NLL accuracy. Indeed, if widely used automated fixed order prediction tools such as MG5AMC are utilised, it would be worthwhile to develop a corresponding software to incorporate resummation in our predictions. A software of this kind could be developed against a well-established meta-code like MG5AMC, which furnishes numerous ingredients necessary for resummation. Indeed, if fixed order computations are process-specific, resummation has a certain degree of universality, as noted earlier in chapter 2. In principle, automating it should be possible in the same way that generic next-to-leading order computations has been achieved. As it would be less process-specific, and that some components from the fixed order calculation can be reused, it would benefit from existing codes as MG5AMC. For example, in our study, we employed the MADLOOP module [75, 168] integrated into MG5AMC for determining \mathbf{H} . Although this is far from being automatised, this is clearly possible with current technology. Subsequently, after setting up the colour basis and extracting the hard function, the only remaining function to be computed is the soft one. Instructions for computing the soft matrices up to first order in the general case are provided in sections 2.3.1 and 2.3.2. For complex processes such as the production of four tops, the matrices can become quite large, with many functional coefficients. Hence further efforts in optimisation should be done before considering automating resummation.

A

Appendix

Summary

A.1	Lagrangian and Feynman rules	113
A.1.1	Lagrangian	113
A.1.2	Feynman rules	113
A.2	$SU(N_c)$ colour algebra	114
A.2.1	$SU(N_c)$ relations	114
A.2.2	Colour Factors	115
A.3	Spinors and polarisation tensors	115
A.4	PDF Evolution	116
A.4.1	Decoupling, singlets and non-singlet states	117
A.4.2	Evolution operators	118
A.5	Mellin transform	120
A.5.1	Miscellaneous	120
A.5.2	Splitting kernels	122
A.6	Subtraction method	123
A.7	Soft and Anomalous dimension color matrices	124
A.7.1	Soft color matrix	125
A.7.2	Soft anomalous dimension color matrix	125

A.8	Sudakov factor	126
A.8.1	Derivation	126
A.8.2	Expansion $\mathcal{O}(\alpha_s)$	131
A.8.3	Collinearly improved resummation	131
A.9	Resummation coefficients	132
A.10	Four top production tree level diagrams	135
A.10.1	Quark channel	135
A.10.2	Gluon channel	135

A.1 Lagrangian and Feynman rules

A.1.1 Lagrangian

QED

$$\mathcal{L}_{QED} = -\frac{1}{4}F_{\mu\nu}F^{\mu\nu} + \sum_l \bar{\psi}_l(i\cancel{\partial} - m)\psi_l - e\bar{\psi}_l\gamma^\mu\psi_l A_\mu \quad (\text{A.1})$$

Where the field tensor $F_{\mu\nu}$ is given by:

$$F_{\mu\nu} = \partial_\mu A_\nu - \partial_\nu A_\mu \quad (\text{A.2})$$

QCD

$$\mathcal{L}_{QCD} = -\frac{1}{4}F_{\mu\nu}^i F^{i\mu\nu} + \sum_f \bar{\psi}_{f,a}(i\delta_{ab}\cancel{\partial} - \delta_{ab}m_f)\psi_{f,b} - g_s\bar{\psi}_{f,a}\gamma^\mu\mathbf{T}_{ab}^i\psi_{f,b}\mathcal{A}_\mu^i \quad (\text{A.3})$$

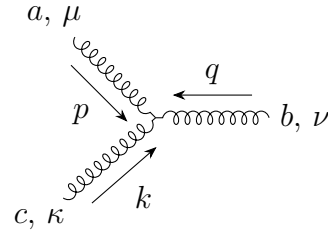
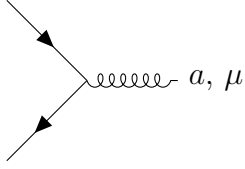
where the ψ_f represent the quark fields, γ^μ a Dirac matrix and \mathbf{T}^i a generator of SU(3). The field tensor $F_{\mu\nu}^i$ can be expressed in term of the colour potential \mathcal{A} and the SU(3) group structure constants f^{ijk} :

$$F_{\mu\nu}^i = \partial_\mu\mathcal{A}_\nu^i - \partial_\nu\mathcal{A}_\mu^i - g_s f^{ijk}\mathcal{A}_\mu^j\mathcal{A}_\nu^k \quad (\text{A.4})$$

A.1.2 Feynman rules

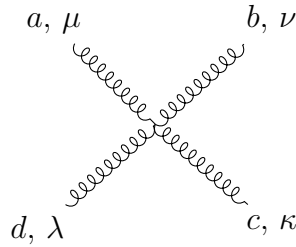
QED

$$\frac{-ie\gamma^\mu}{p^2 - m^2 + i\varepsilon} \quad \frac{-i}{p^2 + i\varepsilon} \left(g^{\mu\nu} - (1 - \xi) \frac{p^\mu p^\nu}{p^2} \right) \quad (\text{A.5})$$

QCD


$$ig_s \gamma^\mu \mathbf{T}^a$$

$$g_s f^{abc} [g^{\mu\nu} (q-p)^\kappa + g^{\mu\kappa} (p-k)^\nu + g^{\nu\kappa} (k-q)^\mu]$$



$$-ig_s^2 [f^{abi} f^{cdi} (g^{\mu\kappa} g^{\nu\lambda} - g^{\mu\lambda} g^{\nu\kappa}) + f^{aci} f^{bdi} (g^{\mu\nu} g^{\lambda\kappa} - g^{\mu\lambda} g^{\nu\kappa}) + f^{adi} f^{bci} (g^{\mu\nu} g^{\lambda\kappa} - g^{\mu\kappa} g^{\nu\lambda})] \quad (\text{A.6})$$

A.2 SU(N_c) colour algebra

A.2.1 SU(N_c) relations

$$\text{Tr}(\mathbf{t}^a \cdot \mathbf{t}^b) = T_R \delta^{ab} \quad \mathbf{t}^a \cdot \mathbf{t}^a = C_R \mathbf{1} \quad \text{Tr}(\mathbf{t}^a) = 0 \quad (\text{A.7})$$

For the fundamental representation, we have $T_F = \frac{1}{2}$ and $C_F = \frac{N_c^2 - 1}{2N_c}$

For the adjoint, $T_A = N_c = C_A$

$$\begin{aligned} \mathbf{T}_{ij}^a \mathbf{T}_{kl}^a &= \frac{1}{2} \left(\delta_{il} \delta_{jk} - \frac{1}{N_c} \delta_{ij} \delta_{kl} \right) & \mathbf{T}^a \cdot \mathbf{T}^b \cdot \mathbf{T}^a &= \left(C_F - \frac{C_A}{2} \right) \mathbf{T}^b \\ f^{\alpha bc} f^{\beta bc} &= N_c \delta^{\alpha\beta} & f^{abc} d^{\beta bc} &= 0 & d^{abc} d^{\beta bc} &= \frac{N_c^2 - 4}{N_c} \delta^{\alpha\beta} \\ i f^{abc} \mathbf{T}^b \mathbf{T}^c &= -\frac{C_A}{2} \mathbf{T}^a \end{aligned} \quad (\text{A.8})$$

Jacobi identities:

$$\begin{aligned}
f^{ab\sigma} f^{\sigma cd} + f^{cb\sigma} f^{a\sigma d} + f^{db\sigma} f^{a\sigma c} &= 0 \\
f^{ab\sigma} d^{\sigma cd} + f^{cb\sigma} d^{a\sigma d} + f^{db\sigma} d^{a\sigma c} &= 0
\end{aligned} \tag{A.9}$$

A.2.2 Colour Factors

$q\bar{q} \longrightarrow t\bar{t}$

$$\mathbf{t}_q \cdot \mathbf{t}_{\bar{q}} = \begin{pmatrix} -C_F & 0 \\ 0 & \frac{C_A}{2} - C_F \end{pmatrix} \quad \mathbf{t}_q \cdot \mathbf{t}_t = \begin{pmatrix} 0 & -1 \\ \frac{-C_F}{2N_c} & \frac{C_A}{2} - 2C_F \end{pmatrix} \tag{A.10}$$

$g_1 g_2 \longrightarrow t\bar{t}$

$$\mathbf{t}_{g_1} \cdot \mathbf{t}_{g_2} = \begin{pmatrix} -C_A & 0 & 0 \\ 0 & \frac{-C_A}{2} & 0 \\ 0 & 0 & \frac{-C_A}{2} \end{pmatrix} \quad \mathbf{t}_{g_1} \cdot \mathbf{t}_t = \begin{pmatrix} 0 & -1 & 0 \\ \frac{-1}{2} & \frac{-C_A}{2} & \frac{-C_A}{2} \\ 0 & -\frac{N_c^2 - 4}{4N_c} & \frac{-C_A}{4} \end{pmatrix} \tag{A.11}$$

A.3 Spinors and polarisation tensors

The following identities are valid for spinors in the respective cases of particles (u) and anti-particles (v), incoming (x) and outgoing (\bar{x}) of mass m and momentum p :

$$\begin{aligned}
(\not{p} - m)u(p) &= \bar{u}(p)(\not{p} - m) = 0 \\
(\not{p} + m)v(p) &= \bar{v}(p)(\not{p} + m) = 0
\end{aligned} \tag{A.12}$$

where $\not{p} = \gamma^\mu p_\mu$, the spin indices being omitted.

We also have:

$$\sum_{spin} u(p)\bar{u}(p) = \not{p} + m \quad \sum_{spin} v(p)\bar{v}(p) = \not{p} - m \tag{A.13}$$

The gauge boson polarisation are transverse in the massless case (on-shell gluon or photon):

$$\epsilon^\mu = (0, \vec{\epsilon}), \quad \vec{p} \cdot \vec{\epsilon}(p) = 0 \tag{A.14}$$

When summing over all polarisation, we have the following gauge-dependant identity:

$$\sum_{pol.} \epsilon_\mu^*(p) \epsilon_\nu(p) = -g_{\mu\nu} + (1 - \xi) \frac{p_\mu p_\nu}{p^2} \quad (\text{A.15})$$

We should notice that the gauge boson can be off-shell, so that p^2 does not vanish.

Although, in principle, all gauge choices are equivalent, we try to select the most convenient one for the computation.

We can highlight three common gauge fixing:

- $\xi = 1$ 't Hooft – Feynman gauge
 - $\xi = 0$ Lorenz gauge
 - $\xi \rightarrow \infty$ unitary gauge
- (A.16)

In the context of QCD, we will mainly use the first two gauge fixing, while the last one is more useful when studying the weak interaction.

A.4 PDF Evolution

PDFs evolve with the factorisation scale according to the coupled DGLAP equations. For simplicity, we will focus only on PDFs of quarks and gluon in the proton. However the same reasoning can be applied to other cases.

$$Q^2 \partial_{Q^2} \begin{pmatrix} q_i(x, Q^2) \\ \bar{q}_i(x, Q^2) \\ g(x, Q^2) \end{pmatrix} = \frac{\alpha_s(Q^2)}{2\pi} \int_x^1 \frac{d\xi}{\xi} \begin{pmatrix} P_{q_i q_j}^{(1)} & P_{q_i \bar{q}_j}^{(1)} & P_{q_i g}^{(1)} \\ P_{\bar{q}_i q_j}^{(1)} & P_{\bar{q}_i \bar{q}_j}^{(1)} & P_{\bar{q}_i g}^{(1)} \\ P_{g q_j}^{(1)} & P_{g \bar{q}_i}^{(1)} & P_{g g}^{(1)} \end{pmatrix} \begin{pmatrix} x \\ \bar{x} \\ \xi \end{pmatrix} \begin{pmatrix} q_j(\xi, Q^2) \\ \bar{q}_j(\xi, Q^2) \\ g(\xi, Q^2) \end{pmatrix} \quad (\text{A.17})$$

These equations can be written in the Mellin space through the Mellin transform (A.35):

$$Q^2 \partial_{Q^2} \begin{pmatrix} q_i(N, Q^2) \\ \bar{q}_i(N, Q^2) \\ g(N, Q^2) \end{pmatrix} = \frac{\alpha_s(Q^2)}{2\pi} \begin{pmatrix} P_{q_i q_j}^{(1)} & P_{q_i \bar{q}_j}^{(1)} & P_{q_i g}^{(1)} \\ P_{\bar{q}_i q_j}^{(1)} & P_{\bar{q}_i \bar{q}_j}^{(1)} & P_{\bar{q}_i g}^{(1)} \\ P_{g q_j}^{(1)} & P_{g \bar{q}_i}^{(1)} & P_{g g}^{(1)} \end{pmatrix} (N) \begin{pmatrix} q_j(N, Q^2) \\ \bar{q}_j(N, Q^2) \\ g(N, Q^2) \end{pmatrix} \quad (\text{A.18})$$

Moreover we can significantly simplify the couplings by considering the following

properties of the splitting functions at NLO:

$$\begin{aligned}
P_{q_i q_j}^{(1)} &= P_{\bar{q}_i \bar{q}_j}^{(1)} = P_{qq}^{(1)} \delta_{ij} & P_{q_i g}^{(1)} &= P_{\bar{q}_i g}^{(1)} = P_{qg}^{(1)} \\
P_{g \bar{q}_i}^{(1)} &= P_{g q_i}^{(1)} = P_{gq}^{(1)} & P_{\bar{q}_i q_j}^{(1)} &= P_{q_i \bar{q}_j}^{(1)} = 0
\end{aligned} \tag{A.19}$$

A.4.1 Decoupling, singlets and non-singlet states

The DGLAP equations remain highly coupled in the physical base of partons. To diagonalize the $(2n_f + 1) \times (2n_f + 1)$ matrix in flavour space, we can choose a different base and decompose our partons in $2n_f - 1$ non-singlet states (NS) and 2 coupled singlet states.

Let us first define the \pm quark states:

$$q_i^\pm = q_i \pm \bar{q}_i \tag{A.20}$$

We can already observe that we obtain n_f decoupled equations from the $q_i^- \equiv V_i$ states:

$$\forall i \in \llbracket 1, n_f \rrbracket \quad Q^2 \partial_{Q^2} V_i = \frac{\alpha_s}{2\pi} \left(P_{qq}^{(1)} q_i + P_{qg}^{(1)} g - P_{q\bar{q}}^{(1)} \bar{q}_i - P_{gq}^{(1)} g \right) = \frac{\alpha_s}{2\pi} P_{qq}^{(1)} V_i \tag{A.21}$$

The other NS states are less trivial but still easy to write down:

$$\forall i \in \llbracket 1, n_f - 1 \rrbracket \quad T_i = \sum_{j=1}^i q_j^+ - i q_{i+1}^+ \tag{A.22}$$

It is easy to verify that, just like for the V_i , we have decoupled equations for the T_i :

$$\forall i \in \llbracket 1, n_f - 1 \rrbracket \quad Q^2 \partial_{Q^2} T_i = \frac{\alpha_s}{2\pi} P_{qq}^{(1)} T_i \tag{A.23}$$

Hence, we have $2n_f - 1$ decoupled equations, leaving two coupled equations in the singlet sector.

Singlet sector

The singlet sector is composed of two coupled states: the gluon g and $\Sigma = \sum_{i=1}^{n_f} q_i^+$.

We have the following coupled equations:

$$Q^2 \partial_{Q^2} \begin{pmatrix} \Sigma \\ g \end{pmatrix} = \frac{\alpha_s(Q^2)}{2\pi} \begin{pmatrix} P_{qq}^{(1)} & 2n_f P_{qg}^{(1)} \\ P_{gq} & P_{gg}^{(1)} \end{pmatrix} \begin{pmatrix} \Sigma \\ g \end{pmatrix} \tag{A.24}$$

This 2×2 basis can be diagonalized with the following eigenvalues:

$$r_{\pm} = \frac{1}{2} \left(P_{qq}^{(1)} + P_{gg}^{(1)} \pm \sqrt{(P_{qq}^{(1)} - P_{gg}^{(1)})^2 + 8n_f P_{qg}^{(1)} P_{gq}^{(1)}} \right) \quad (\text{A.25})$$

Each eigenvalue is associated to an eigenstate:

$$\Sigma' = \alpha_+ \Sigma + \beta_+ g \quad g' = \alpha_- \Sigma + \beta_- g \quad (\text{A.26})$$

With: $\alpha_{\pm} = \beta_{\pm} \frac{r_{\pm} - P_{gg}^{(1)}}{P_{gq}^{(1)}} \neq 0$ or equivalently: $\beta_{\pm} = \alpha_{\pm} \frac{r_{\pm} - P_{qq}^{(1)}}{2n_f P_{qg}^{(1)}}$, up to a global normalization (we can choose for example $\beta_{\pm} = 1$).

Ultimately, we obtain:

$$Q^2 \partial_{Q^2} \begin{pmatrix} \Sigma' \\ g' \end{pmatrix} = \frac{\alpha_s(Q^2)}{2\pi} \begin{pmatrix} r_+ & 0 \\ 0 & r_- \end{pmatrix} \begin{pmatrix} \Sigma' \\ g' \end{pmatrix} \quad (\text{A.27})$$

With :

$$\begin{pmatrix} \Sigma' \\ g' \end{pmatrix} = P^{-1} \begin{pmatrix} \Sigma \\ g \end{pmatrix} \quad \text{with } P = \begin{pmatrix} \alpha_+ & \alpha_- \\ \beta_+ & \beta_- \end{pmatrix} \quad \text{and } P^{-1} = \frac{1}{\alpha_+ \beta_- - \alpha_- \beta_+} \begin{pmatrix} \beta_- & -\alpha_- \\ -\beta_+ & \alpha_+ \end{pmatrix}$$

Having recovered our $2n_f + 1$ equations, we now have a complete set of decoupled equations that we can solve to find the evolution operators.

A.4.2 Evolution operators

In the evolution basis, all the equations are decoupled and take the form:

$$Q^2 \partial_{Q^2} \Xi(N, Q^2) = \frac{\alpha_s(Q^2)}{2\pi} \Lambda(N) \Xi(N, Q^2) \quad \Rightarrow \quad \Xi(N, Q^2) = \Xi(N, \mu_F^2) \exp \left(\int_{\mu_F^2}^{Q^2} \frac{dk^2}{k^2} \frac{\alpha_s(k^2)}{2\pi} \Lambda(N) \right) \quad (\text{A.28})$$

With $\Lambda \in \{r_+; r_-; P_{qq}^{(1)}\}$, $\Xi \in \{\Sigma'; g'; (V_i)_{1 \leq i \leq n_f}; (T_i)_{1 \leq i \leq n_f - 1}\}$ respectively for the singlets eigenstates and the non singlets states.

We can define the corresponding evolution operators:

$$\hat{\varepsilon}_\Lambda(N, Q, \mu_F) \equiv \exp \left(\int_{\mu_F^2}^{Q^2} \frac{dk^2}{k^2} \frac{\alpha_s(k^2)}{2\pi} \Lambda(N) \right) \quad (\text{A.29})$$

From evolution back to physical basis

Once the evolution is done in the eigenspace, we need to rotate the PDF back to the physical basis. For clarity, we will avoid explicitly writing the scales and instead denote the evolved quantities with a *tilde*.

First, let us go back to the original singlet basis:

$$\begin{aligned} \tilde{\Sigma}' &= \hat{\varepsilon}_{r_+} \frac{\beta_- \Sigma - \alpha_- g}{\alpha_+ \beta_- - \alpha_- \beta_+} = \frac{\beta_- \tilde{\Sigma} - \alpha_- \tilde{g}}{\alpha_+ \beta_- - \alpha_- \beta_+} \\ \tilde{g}' &= \hat{\varepsilon}_{r_-} \frac{\alpha_+ g - \beta_+ \Sigma}{\alpha_+ \beta_- - \alpha_- \beta_+} = \frac{\alpha_+ \tilde{g} - \beta_+ \tilde{\Sigma}}{\alpha_+ \beta_- - \alpha_- \beta_+} \end{aligned} \quad (\text{A.30})$$

$$\begin{aligned} \tilde{\Sigma} &= \hat{\varepsilon}_{r_+} \frac{\alpha_+ \beta_- \Sigma - \alpha_+ \alpha_- g}{\alpha_+ \beta_- - \alpha_- \beta_+} - \hat{\varepsilon}_{r_-} \frac{\alpha_- \beta_+ \Sigma - \alpha_+ \alpha_- g}{\alpha_+ \beta_- - \alpha_- \beta_+} \\ \tilde{g} &= \hat{\varepsilon}_{r_-} \frac{\alpha_+ \beta_- g - \beta_+ \beta_- \Sigma}{\alpha_+ \beta_- - \alpha_- \beta_+} - \hat{\varepsilon}_{r_+} \frac{\alpha_- \beta_+ g - \beta_+ \beta_- \Sigma}{\alpha_+ \beta_- - \alpha_- \beta_+} \end{aligned}$$

Without any loss of generality, we can express $\alpha_\pm = \beta_\pm \frac{r_\pm - P_{gg}^{(1)}}{P_{gq}^{(1)}}$ and $\beta_\pm = \alpha_\pm \frac{r_\pm - P_{qq}^{(1)}}{2n_f P_{qg}^{(1)}}$, allowing us to recover:

$$\begin{aligned} \tilde{\Sigma} &= \hat{\varepsilon}_{r_+} \frac{(r_- - P_{qq}^{(1)})\Sigma - 2n_f P_{qg}^{(1)}g}{r_- - r_+} - \hat{\varepsilon}_{r_-} \frac{(r_+ - P_{qq}^{(1)})\Sigma - 2n_f P_{qg}^{(1)}g}{r_- - r_+} \\ \tilde{g} &= \hat{\varepsilon}_{r_-} \frac{(r_+ - P_{gg}^{(1)})g - P_{gq}^{(1)}\Sigma}{r_+ - r_-} - \hat{\varepsilon}_{r_+} \frac{(r_- - P_{gg}^{(1)})g - P_{gq}^{(1)}\Sigma}{r_+ - r_-} \end{aligned} \quad (\text{A.31})$$

Hence we have already access to the evolved gluon PDF in the physical basis.

Furthermore, we can recover the physical quark PDFs as follows:

$$\begin{aligned} \tilde{q}_i &= \frac{1}{2} \left(\frac{\tilde{\Sigma}}{n_f} - \frac{\tilde{T}_{i-1}}{i} + \sum_{j=i}^{n_f-1} \frac{\tilde{T}_j}{j(j+1)} + \tilde{V}_i \right) \\ \tilde{\bar{q}}_i &= \frac{1}{2} \left(\frac{\tilde{\Sigma}}{n_f} - \frac{\tilde{T}_{i-1}}{i} + \sum_{j=i}^{n_f-1} \frac{\tilde{T}_j}{j(j+1)} - \tilde{V}_i \right) \end{aligned} \quad (\text{A.32})$$

With $\tilde{V}_i = \hat{\varepsilon}_{qq} V_i$ and $\tilde{T}_i = \hat{\varepsilon}_{qq} T_i$, of course: $T_0 = T_{n_f} = 0$

Expansion at NLO

Finally, in order to be consistent with the 1-loop computation, we can expand the evolved PDF at $\mathcal{O}(\alpha_s)$ in terms of initial PDFs. Assuming that Λ only depends on N , we can write:

$$\hat{\varepsilon}_\Lambda(N, Q^2/\mu_F^2) = 1 + \frac{\alpha_s(\mu_R^2)}{2\pi} \ln\left(\frac{Q^2}{\mu_F^2}\right) \Lambda(N) + \mathcal{O}(\alpha_s^2) \quad (\text{A.33})$$

Then,

$$\begin{aligned} \tilde{g}(N, Q^2) &= g(N, \mu_F^2) \left(1 + \frac{\alpha_s(\mu_R^2)}{2\pi} \ln\left(\frac{Q^2}{\mu_F^2}\right) P_{gg}^{(1)}(N) \right) \\ &\quad + \frac{\alpha_s(\mu_R^2)}{2\pi} \ln\left(\frac{Q^2}{\mu_F^2}\right) P_{gq}^{(1)}(N) \Sigma(N, \mu_F^2) + \mathcal{O}(\alpha_s^2) \end{aligned} \quad (\text{A.34})$$

$$\begin{aligned} \tilde{q}_i(N, Q^2) &= q_i(N, \mu_F^2) \left(1 + \frac{\alpha_s(\mu_R^2)}{2\pi} \ln\left(\frac{Q^2}{\mu_F^2}\right) P_{qq}^{(1)}(N) \right) \\ &\quad + \frac{\alpha_s(\mu_R^2)}{2\pi} \ln\left(\frac{Q^2}{\mu_F^2}\right) P_{qg}^{(1)}(N) g(N, \mu_F^2) + \mathcal{O}(\alpha_s^2) \end{aligned}$$

A.5 Mellin transform

A.5.1 Miscellaneous

Here is a collection of some useful Mellin transform.

Let us remind the definition first:

$$\mathcal{M}[f](N) \equiv F(N) \equiv \int_0^1 dz z^{N-1} f(z) \quad (\text{A.35})$$

In general, Mellin transform is useful to express convolutions as regular products after transformation:

$$\begin{aligned} H(x) &= \int g(x/y) f(y) \frac{dy}{y} = \int g(z) f(y) \delta(zy - x) dy dz \\ \Rightarrow H(N) &= \int g(z) f(y) (zy)^{N-1} \delta(zy - x) dx dy dz = g(N) f(N) \end{aligned} \quad (\text{A.36})$$

We also have the Mellin inverse transform from N to z space:

$$f(z) = \frac{1}{2i\pi} \int_{C-i\infty}^{C+i\infty} dN z^{-N} F(N) \quad (\text{A.37})$$

We can apply the Mellin transform to distributions like $\delta_a(x) = \delta(x - a)$:

$$\mathcal{M}[\delta_a](N) = a^{N-1} \quad (\text{A.38})$$

$$\mathcal{M}[z^a] = \int_0^1 dz z^{N-1+a} = \frac{1}{N+a} \quad (\text{A.39})$$

$$\begin{aligned} \mathcal{M}[\ln(1-z)] &= \int_0^1 dz z^{N-1} \ln(1-z) = - \sum_{k=0}^{+\infty} \frac{1}{(k+1)(N+k+1)} = - \frac{\gamma + \psi(N+1)}{N} \\ &\underset{|N| \gg 1}{=} - \frac{\ln(\bar{N})}{N} + \mathcal{O}\left(\frac{1}{N^2}\right) \end{aligned} \quad (\text{A.40})$$

where $\psi(N) = \frac{\Gamma'(N)}{\Gamma(N)}$ and $\bar{N} = Ne^\gamma$. See eq B.4.9a in [194]:

$$\mathcal{M}\left[\left.\frac{\ln(1-z)}{1-z}\right|_+\right] = \frac{1}{2} \left(\psi(N)^2 + 2\gamma\psi(N) - \psi'(N) + \gamma^2 + \frac{\pi^2}{6} \right) \underset{|N| \gg 1}{\simeq} \frac{1}{2} \left(\ln^2(\bar{N}) + \frac{\pi^2}{6} \right) + \mathcal{O}(1) \quad (\text{A.41})$$

$$\begin{aligned} \mathcal{M}\left[\frac{\ln(z)}{1-z}\right] &= \int_0^1 dz z^{N-1} \frac{\ln(z)}{1-z} = - \sum_{p=1}^{+\infty} \sum_{k=0}^{+\infty} \int_0^1 dz z^{N-1+k} \frac{(1-z)^p}{p} \\ &= - \sum_{p=1}^{+\infty} \sum_{k=0}^{+\infty} \frac{\Gamma(N+k)\Gamma(p+1)}{p\Gamma(N+k+1+p)} = - \sum_{p=1}^{+\infty} \frac{\Gamma(N)\Gamma(p)}{p\Gamma(N+p)} \\ &= - \psi'(N) \underset{|N| \gg 1}{\simeq} - \frac{1}{N} \end{aligned} \quad (\text{A.42})$$

We recall that:

$$\psi(N) = \frac{1}{N-1} + \psi(N-1) \quad \psi(N) \underset{|N| \gg 1}{\simeq} \sum_{k=1}^{N-1} \frac{1}{k} - \gamma = \ln(N) - \frac{1}{2N} + \mathcal{O}\left(\frac{1}{N^2}\right) \quad (\text{A.43})$$

We can easily deduce the Mellin transform of the MSTW parametrization (2.71) from the definition of the beta function:

$$B(x, y) = \frac{\Gamma(x)\Gamma(y)}{\Gamma(x+y)} = \int_0^1 dt t^{x-1}(1-t)^{y-1} \quad (\text{A.44})$$

Before considering the Mellin transform of the splitting kernels, let us remind the + distribution prescription:

$$\int_0^1 dx f(x) \frac{1}{1-x} \Big|_+ = \int_0^1 dx \frac{f(x) - f(1)}{1-x} \quad (\text{A.45})$$

In general, the + distribution prescription can be applied to functions with a divergence (here in $x = 1$). So that we also have for example:

$$\int_0^1 dx f(x) \frac{\ln(1-x)}{1-x} \Big|_+ = \int_0^1 dx (f(x) - f(1)) \frac{\ln(1-x)}{1-x} \quad (\text{A.46})$$

A.5.2 Splitting kernels

$$\begin{aligned} \gamma_{qq}^{(1)}(N) &= \mathcal{M}[P_{qq}^{(1)}] = C_F \int_0^1 dz z^{N-1} \left(\frac{3}{2} \delta(1-z) + (z^2 + 1) \frac{1}{1-z} \Big|_+ \right) \\ &= C_F \left(\frac{3}{2} + \int_0^1 dz \frac{z^{N-1}(z^2 + 1) - 2}{1-z} \right) \\ &= C_F \left(\frac{3}{2} - \sum_{k=0}^N \int_0^1 dz z^k - \sum_{k=0}^{N-2} \int_0^1 dz z^k \right) \\ &= C_F \left(\frac{3}{2} - 2 \sum_{k=1}^N \frac{1}{k} + \frac{1}{N} - \frac{1}{N+1} \right) = C_F \left(\frac{3}{2} - 2 \sum_{k=1}^N \frac{1}{k} + \frac{1}{N(N+1)} \right) \\ &\stackrel{|N| \gg 1}{=} C_F \left(-2 \ln(\overline{N}) + \frac{3}{2} \right) + \mathcal{O}\left(\frac{1}{N}\right) \end{aligned} \quad (\text{A.47})$$

$$\begin{aligned} \gamma_{qg}^{(1)}(N) &= \mathcal{M}[P_{qg}^{(1)}] = T_F \int_0^1 dz z^{N-1} (z^2 + (1-z^2)) = T_F \left(\frac{2}{N+2} + \frac{1}{N} - \frac{2}{N+1} \right) \\ &= T_F \frac{2 + N + N^2}{N(N+1)(N+2)} \stackrel{|N| \gg 1}{\sim} \frac{T_F}{N} \end{aligned} \quad (\text{A.48})$$

$$\begin{aligned} \gamma_{gq}^{(1)}(N) &= \mathcal{M}[P_{gq}^{(1)}] = C_F \int_0^1 dz z^{N-1} \frac{1 + (1-z)^2}{z} = C_F \left(\frac{2}{N-1} + \frac{1}{N+1} - \frac{2}{N} \right) \\ &= C_F \frac{2 + N + N^2}{N(N+1)(N-1)} \stackrel{|N| \gg 1}{\sim} \frac{C_F}{N} \end{aligned} \quad (\text{A.49})$$

$$\begin{aligned}
\gamma_{gg}^{(1)}(N) &= \mathcal{M}[P_{gg}^{(1)}] = \int_0^1 dz z^{N-1} \left[2C_A \left(\frac{1-z}{z} + z(1-z) + z \frac{1}{1-z} \Big|_+ \right) + \beta_0 \delta(1-z) \right] \\
&= \beta_0 + 2C_A \left(\frac{1}{N-1} - \frac{1}{N} + \frac{1}{N+1} - \frac{1}{N+2} - \sum_{k=1}^N \frac{1}{k} \right) \\
&= \beta_0 + 2C_A \left(2 \frac{N^2 + N + 1}{(N-1)N(N+1)(N+2)} - \sum_{k=1}^N \frac{1}{k} \right) \\
&\stackrel{|N| \gg 1}{=} -2C_A \ln(\overline{N}) + \beta_0 + \mathcal{O}\left(\frac{1}{N}\right)
\end{aligned} \tag{A.50}$$

A.6 Subtraction method

Assuming a collision between two partons resulting in the production of m particles in the final state, we can formally write the Born cross section:

$$\sigma_B = \int_m d\sigma_B \tag{A.51}$$

Where we take into account all the $3m - 4$ degrees of freedom in the integration. To calculate the NLO cross section, we must include both the virtual contribution and the real emissions. As the virtual part arises from one-loop diagrams, it has the same degrees of freedom as the Born-level cross section. However, the real emission term involves a production of an additional final-state particle, resulting in more degrees of freedom:

$$\sigma_{\text{NLO}} = \int_m d\sigma^V + \int_{m+1} d\sigma^R \tag{A.52}$$

After the renormalisation procedure, both of these two quantities are UV-finite, however, they still contain infrared poles. If the incoming partons are massless, the KLN theorem [62] guarantees the cancellation of these divergences, resulting in the total cross section, an IR-safe observable, being free of all divergences. It is worth noting, however, that while the divergences cancel formally, it is impossible in practice to obtain a numerically stable evaluation of $d\sigma^V$ and $d\sigma^R$. Thus, subtraction methods are employed to address this issue. The general approach is to introduce a new cancelling contribution, denoted as $d\sigma^A$, to capture the singular behavior of $d\sigma^R$ in the related phase space. Formally, we express this as follows:

$$\sigma_{\text{NLO}} = \int_m \left[d\sigma^V + \int_1 d\sigma^A \right] + \int_{m+1} \left[d\sigma^R - d\sigma^A \right] \quad (\text{A.53})$$

Of course, there is no unicity regarding the choice of $d\sigma^A$ since we can freely move any finite contribution from $d\sigma^R$ or $d\sigma^V$ in the local counter term. Once a suitable $d\sigma^A$ is produced, the two integrals become individually finite and can be evaluated without significant cancellation from the poles. However, depending on the method of choosing $d\sigma^A$, some numerical instabilities may still occur. In the case of the dipole subtraction method [39,195], the subtraction counter-term is designed to temper the threshold logarithms arising in the context of soft gluon emissions.

Massive final states

We did not use the dipole formalism in this document although it brings many information, such as an alternative way to compute the soft matrix $\mathbf{S}^{(1)}$. This choice was motivated by the specific treatment of the multiple massive final states in the context of the dipole formalism. Indeed, as stated in appendix C. of [196], the dipole phase space integration must be handled with caution when multiple massive partons appear in the final state. Specifically, the velocity factors introduced in [195] to simplify the phase space integration, modify the finite reminders, which is precisely what we aim to calculate. The dipole formalism is coherent and predicts the correct infrared pole structure in all cases. However, when dealing with multiple massive final states, we are unable to use equation (5.16) from [195] and the resulting finite terms (5.35) directly, hence our choice of an alternative computation in section 2.3.1.

A.7 Soft and Anomalous dimension color matrices

Let us define the reduced Mandelstam variables:

$$\begin{aligned} t_1 &= t - m_t^2 \\ u_1 &= u - m_t^2 \end{aligned} \quad (\text{A.54})$$

$$\text{so that : } M^2 + t_1 + u_1 = 0$$

with $\beta = \sqrt{1 - \frac{4m_t^2}{M^2}}$ and $L_\beta = \frac{1 + \beta^2}{2\beta} \left[\ln \left(\frac{1 - \beta}{1 + \beta} \right) + i\pi \right]$, useful for the top pair production process.

A.7.1 Soft color matrix

$$q\bar{q} \longrightarrow t\bar{t}$$

$$\mathbf{S}^{(0)} = \begin{pmatrix} N_c^2 & 0 \\ 0 & \frac{C_F}{2}N_c \end{pmatrix} \quad (\text{A.55})$$

$$gg \longrightarrow t\bar{t}$$

$$\mathbf{S}^{(0)} = \begin{pmatrix} N_c(N_c^2 - 1) & 0 & 0 \\ 0 & (N_c^2 - 1)N_c & 0 \\ 0 & 0 & \frac{N_c^2 - 1}{2N_c}(N_c^2 - 4) \end{pmatrix} \quad (\text{A.56})$$

A.7.2 Soft anomalous dimension color matrix

$$q\bar{q} \longrightarrow t\bar{t}$$

$$\Gamma_S^{(1)} = 2 \begin{pmatrix} -C_F(1 + L_\beta) & \frac{C_F}{N_c} \ln\left(\frac{t_1}{u_1}\right) \\ 2 \ln\left(\frac{t_1}{u_1}\right) & \frac{1 + L_\beta}{2N_c} - \frac{2}{N_c} \ln\left(\frac{t_1}{u_1}\right) + \frac{N_c}{2} \left[i\pi - 1 + \ln\left(\frac{t_1 u_1}{M^2 m_t^2}\right) \right] \end{pmatrix}$$

$$gg \longrightarrow t\bar{t}$$

$$\Gamma_S^{(1)} = 2 \begin{pmatrix} -C_F(1 + L_\beta) & \ln\left(\frac{t_1}{u_1}\right) & 0 \\ 2 \ln\left(\frac{t_1}{u_1}\right) & \frac{1 + L_\beta}{2N_c} + \frac{N_c}{2} \left[i\pi - 1 + \ln\left(\frac{t_1 u_1}{M^2 m_t^2}\right) \right] & \frac{N_c^2 - 4}{2N_c} \ln\left(\frac{t_1 u_1}{M^2 m_t^2}\right) \\ 0 & \frac{N_c}{2} \ln\left(\frac{t_1 u_1}{M^2 m_t^2}\right) & \frac{1 + L_\beta}{2N_c} + \frac{N_c}{2} \left[i\pi - 1 + \ln\left(\frac{t_1 u_1}{M^2 m_t^2}\right) \right] \end{pmatrix}$$

Absolute mass threshold limit

In the absolute mass threshold limit, we have $t_1 \rightarrow -2m_t^2$, $u_1 \rightarrow -2m_t^2$ and $M^2 \rightarrow 4m_t^2$. Which gives diagonal soft anomalous dimension matrices:

$q\bar{q} \longrightarrow t\bar{t}$

$$\Gamma_S^{(1)} = 2 \begin{pmatrix} -C_F(1 + L_\beta) & 0 \\ 0 & \frac{1 + L_\beta}{2N_c} + \frac{N_c}{2}(i\pi - 1) \end{pmatrix}$$

 $gg \longrightarrow t\bar{t}$

$$\Gamma_S^{(1)} = 2 \begin{pmatrix} -C_F(1 + L_\beta) & 0 & 0 \\ 0 & \frac{1 + L_\beta}{2N_c} + \frac{N_c}{2}(i\pi - 1) & 0 \\ 0 & 0 & \frac{1 + L_\beta}{2N_c} + \frac{N_c}{2}(i\pi - 1) \end{pmatrix}$$

A.8 Sudakov factor

A.8.1 Derivation

Using the $\overline{\text{MS}}$ scheme in renormalization (scale μ_R) and factorization (scale μ_F) we have the Sudakov form factor for initial partons i and j :

$$G_{ij} = G_i + G_j = \int_0^1 dz \frac{z^{N-1} - 1}{1 - z} \int_{\mu_F^2}^{(1-z)^2 Q^2} \frac{dq^2}{q^2} \left(A_i(\alpha_s(q^2)) + A_j(\alpha_s(q^2)) \right) \quad (\text{A.57})$$

A_i is the cusp anomalous dimension, multiplying the $\frac{1}{1-z}|_+$ part of the parton splitting function $P_{ii}(z)$, with $i \in \{q, g\}$. This anomalous dimension can be expanded in terms of $\frac{\alpha_s}{2\pi}$ order by order:

$$A_i(\alpha_s) = \sum_{k=1}^{+\infty} A_i^{(k)} \left(\frac{\alpha_s}{2\pi} \right)^k \quad (\text{A.58})$$

Here we stop at $A^{(2)}$ as we consider only NLL accuracy (see the power counting in 2.1), namely:

$$A_i^{(1)} = 2C_i \quad A_q^{(2)} = 2C_i \left(\left(\frac{67}{18} - \frac{\pi^2}{6} \right) C_A - \frac{5n_f}{9} \right) \equiv 2C_i K \quad (\text{A.59})$$

This factor accounts for the resummation of soft-collinear radiated gluons, giving the usual Leading Logarithmic terms. We also have to expand $\alpha_s(q^2)$ in term of the evaluation at μ_R due to the running:

$$\alpha_s(q^2) = \frac{\alpha_s(\mu_R^2)}{1 + \frac{\alpha_s(\mu_R^2)}{2\pi}\beta_0 \ln(q^2/\mu_R^2)} - \frac{\alpha_s^2(\mu_R^2)}{2\pi} \frac{\beta_1}{\beta_0} \frac{\ln(1 + \beta_0\alpha_s(\mu_R^2) \ln(q^2/\mu_R^2)/2\pi)}{(1 + \beta_0\alpha_s(\mu_R^2) \ln(q^2/\mu_R^2)/2\pi)^2} + \mathcal{O}(\alpha_s^3(\mu_R^2)) \quad (\text{A.60})$$

From now on we will note $\alpha_s(\mu_R^2) = \alpha_s$ as it is the common scale used for the evaluation of the observable. For simplicity, we will focus on a single parton contribution G_i . With the notation $x(q)$ from (1.3), we have three terms to compute:

$$\begin{aligned} G_i &= \int_0^1 dz \frac{z^{N-1} - 1}{1 - z} \int_{\mu_F^2}^{(1-z)^2 Q^2} \frac{dq^2}{q^2} 2C_i \frac{\alpha_s}{2\pi} \frac{1}{1 + x(q)} \\ &\quad - \int_0^1 dz \frac{z^{N-1} - 1}{1 - z} \int_{\mu_F^2}^{(1-z)^2 Q^2} \frac{dq^2}{q^2} 2C_i \frac{\alpha_s^2}{4\pi^2} \frac{\beta_1}{\beta_0} \frac{\ln(1 + x(q))}{(1 + x(q))^2} \\ &\quad + \int_0^1 dz \frac{z^{N-1} - 1}{1 - z} \int_{\mu_F^2}^{(1-z)^2 Q^2} \frac{dq^2}{q^2} 2C_i K \frac{\alpha_s^2}{4\pi^2} \left(\frac{1}{1 + x(q)} \right)^2 \end{aligned} \quad (\text{A.61})$$

First we must take care of the integrals over q^2 :

$$\begin{aligned} \int_{\mu_F^2}^{(1-z)^2 Q^2} \frac{dq^2}{q^2} \frac{1}{1 + x(q)} &= \frac{2\pi}{\beta_0\alpha_s} \left[\ln \left(1 + x(Q(1-z)) \right) - \ln \left(1 + x(\mu_F) \right) \right] \\ \int_{\mu_F^2}^{(1-z)^2 Q^2} \frac{dq^2}{q^2} \frac{\ln(1 + x(q))}{(1 + x(q))^2} &= -\frac{2\pi}{\beta_0\alpha_s} \left[\frac{1 + \ln \left(1 + x(Q(1-z)) \right)}{1 + x(Q(1-z))} - \frac{1 + \ln \left(1 + x(\mu_F) \right)}{1 + x(\mu_F)} \right] \\ \int_{\mu_F^2}^{(1-z)^2 Q^2} \frac{dq^2}{q^2} \left(\frac{1}{1 + x(q)} \right)^2 &= -\frac{2\pi}{\beta_0\alpha_s} \left(\frac{1}{1 + x(Q(1-z))} - \frac{1}{1 + x(\mu_F)} \right) \end{aligned} \quad (\text{A.62})$$

All the terms that doesn't depend on z are lumped together in:

$$\Lambda = \frac{2C_i}{\beta_0} \int_0^1 dz \frac{z^{N-1} - 1}{1 - z} \left[-\ln \left(1 + x(\mu_F) \right) - \frac{\alpha_s}{2\pi} \frac{\beta_1}{\beta_0} \frac{1 + \ln \left(1 + x(\mu_F) \right)}{1 + x(\mu_F)} + \frac{\alpha_s}{2\pi} K \frac{1}{1 + x(\mu_F)} \right] \quad (\text{A.63})$$

We keep in mind that:

$$\int_0^1 dz \frac{z^{N-1} - 1}{1 - z} = - \int_0^1 dz \sum_{k=0}^{N-2} z^k = - \sum_{k=1}^{N-1} \frac{1}{k} = -\psi(N) - \gamma_E \approx -\ln(Ne^{\gamma_E}) + \frac{1}{2N} + \mathcal{O}(1/N^2) \quad (\text{A.64})$$

In the limit $\alpha_s \ll 1$, $|N| \gg 1$, $\alpha_s |\ln(N)| < 1$, with $\bar{N} = Ne^{\gamma_E}$:

$$\Lambda = -\frac{2C_i}{\beta_0} \frac{\alpha_s}{2\pi} \beta_0 \ln(\bar{N}) \left(-\ln(\mu_F^2/\mu_R^2) - \frac{\beta_1}{\beta_0^2} + \frac{K}{\beta_0} \right) + \mathcal{O}(\alpha_s^2 \ln(N)) \quad (\text{A.65})$$

To go further we need to perform the z integration on the parts depending on z . To do so, we perform an expansion in $\beta_0 \frac{\alpha_s}{2\pi} \ln(Q^2(1-z)^2/\mu_R^2)$. This is possible because of the regularisation in 1 due to the $\frac{1}{1-z} \Big|_+$ prescription. For the following calculation we will use the approximation (5.3) in [139]: $z^{N-1} - 1 \simeq -\Theta(1 - 1/\bar{N} - z)$. Moreover, we make the change of variable $\tilde{z} = \frac{Q(1-z)}{\mu_R}$. Altogether we have:

$$\begin{aligned} G_i = \Lambda &+ \frac{2C_i}{\beta_0} \int_{Q/\mu_R \bar{N}}^{Q/\mu_R} \frac{d\tilde{z}}{\tilde{z}} \sum_{k=1}^{+\infty} \frac{\left(-\beta_0 \frac{\alpha_s}{\pi} \ln(\tilde{z})\right)^k}{k} + \frac{2C_i}{\beta_0} K \frac{\alpha_s}{2\pi} \int_{Q/\mu_R \bar{N}}^{Q/\mu_R} \frac{d\tilde{z}}{\tilde{z}} \sum_{k=0}^{+\infty} \left(-\beta_0 \frac{\alpha_s}{\pi} \ln(\tilde{z})\right)^k \\ &- \frac{2C_i}{\beta_0} \frac{\beta_1}{\beta_0} \frac{\alpha_s}{2\pi} \int_{Q/\mu_R \bar{N}}^{Q/\mu_R} \frac{d\tilde{z}}{\tilde{z}} \left(1 - \sum_{q=1}^{+\infty} \frac{\left(-\beta_0 \frac{\alpha_s}{\pi} \ln(\tilde{z})\right)^q}{q}\right) \sum_{k=0}^{+\infty} \left(-\beta_0 \frac{\alpha_s}{\pi} \ln(\tilde{z})\right)^k \end{aligned} \quad (\text{A.66})$$

Everything converges so we can invert the infinite sums and the integrals. We need to compute:

$$\int_{Q/\mu_R \bar{N}}^{Q/\mu_R} \frac{d\tilde{z}}{\tilde{z}} \ln^k(\tilde{z}) = \frac{\ln^{k+1}(Q/\mu_R) - \ln^{k+1}(Q/\mu_R \bar{N})}{k+1} \quad (\text{A.67})$$

In the end:

$$\begin{aligned} G_i = \Lambda &+ \frac{2C_i}{\beta_0} \sum_{k=1}^{+\infty} \left(-\beta_0 \frac{\alpha_s}{\pi}\right)^k \left(\ln^{k+1}(Q/\mu_R) - \ln^{k+1}(Q/\mu_R \bar{N})\right) \left(\frac{1}{k} - \frac{1}{k+1}\right) \\ &+ \frac{2C_i}{\beta_0} \left(K - \frac{\beta_1}{\beta_0}\right) \frac{\alpha_s}{2\pi} \sum_{k=0}^{+\infty} \left(-\beta_0 \frac{\alpha_s}{\pi}\right)^k \left(\ln^{k+1}(Q/\mu_R) - \ln^{k+1}(Q/\mu_R \bar{N})\right) \frac{1}{k+1} \quad (\text{A.68}) \\ &+ \frac{2C_i}{\beta_0} \frac{\beta_1}{\beta_0} \frac{\alpha_s}{2\pi} \sum_{q=1}^{+\infty} \sum_{k=0}^{+\infty} \frac{\left(-\beta_0 \frac{\alpha_s}{\pi}\right)^{q+k}}{(q+k+1)q} \left(\ln^{k+q+1}(Q/\mu_R) - \ln^{k+q+1}(Q/\mu_R \bar{N})\right) \end{aligned}$$

By noting that:

$$\begin{aligned} \sum_{q=1}^{+\infty} \sum_{k=0}^{+\infty} \frac{X^{q+k}}{(q+k+1)q} &= \frac{1}{2} \left(\sum_{q=1}^{+\infty} \sum_{k=0}^{+\infty} \frac{X^{q+k}}{(q+k+1)q} + \frac{X^{q+k}}{(q+k+1)(k+1)} \right) \\ &= \frac{1}{2X} \sum_{q=1}^{+\infty} \sum_{k=0}^{+\infty} \frac{X^{q+k+1}}{(k+1)q} = \frac{1}{2X} \ln^2(1-X) \end{aligned} \quad (\text{A.69})$$

We have:

$$\begin{aligned} G_i &= \Lambda + \frac{2C_i}{\beta_0} \left(-\ln(Q/\mu_R) \ln\left(1 + \beta_0 \frac{\alpha_s}{\pi} \ln(Q/\mu_R)\right) + \ln(Q/\mu_R \bar{N}) \ln\left(1 + \beta_0 \frac{\alpha_s}{\pi} \ln(Q/\mu_R \bar{N})\right) \right) \\ &+ \frac{2C_i}{\beta_0} \left(-\frac{\ln\left(1 + \beta_0 \frac{\alpha_s}{\pi} \ln(Q/\mu_R)\right)}{\beta_0 \frac{\alpha_s}{\pi}} + \ln(Q/\mu_R) + \frac{\ln\left(1 + \beta_0 \frac{\alpha_s}{\pi} \ln(Q/\mu_R \bar{N})\right)}{\beta_0 \frac{\alpha_s}{\pi}} - \ln(Q/\mu_R \bar{N}) \right) \\ &+ \frac{C_i}{\beta_0^2} \left(K - \frac{\beta_1}{\beta_0} \right) \left(\ln\left(1 + \beta_0 \frac{\alpha_s}{\pi} \ln(Q/\mu_R)\right) - \ln\left(1 + \beta_0 \frac{\alpha_s}{\pi} \ln(Q/\mu_R \bar{N})\right) \right) \\ &- \frac{C_i \beta_1}{\beta_0^2} \frac{1}{2} \left(\ln^2\left(1 + \beta_0 \frac{\alpha_s}{\pi} \ln(Q/\mu_R)\right) - \ln^2\left(1 + \beta_0 \frac{\alpha_s}{\pi} \ln(Q/\mu_R \bar{N})\right) \right) \end{aligned} \quad (\text{A.70})$$

At this stage we can make some simplifications considering that the expansion parameter is $\beta_0 \frac{\alpha_s}{\pi} \ln(\bar{N})$ so if α_s is alone (without $\ln(\bar{N})$) it's small and expandable at $\mathcal{O}(\alpha_s)$ level.

Else, with noting, $\lambda = \frac{\alpha_s}{2\pi} \beta_0 \ln(\bar{N})$:

$$\begin{aligned} &-\ln(Q/\mu_R) \ln\left(1 + \beta_0 \frac{\alpha_s}{\pi} \ln(Q/\mu_R)\right) + \ln(Q/\mu_R \bar{N}) \ln\left(1 + \beta_0 \frac{\alpha_s}{\pi} \ln(Q/\mu_R \bar{N})\right) \\ &= \ln(Q/\mu_R) \ln(1-2\lambda) - \ln(\bar{N}) \ln(1-2\lambda) - \ln(\bar{N}) \ln\left(1 + \beta_0 \frac{\alpha_s}{\pi} \ln(Q/\mu_R)/(1-2\lambda)\right) \\ &= \ln(Q/\mu_R) \ln(1-2\lambda) - \ln(\bar{N}) \ln(1-2\lambda) - \frac{2\lambda}{1-2\lambda} \ln(Q/\mu_R) \end{aligned} \quad (\text{A.71})$$

And:

$$\begin{aligned} &-\frac{\ln\left(1 + \beta_0 \frac{\alpha_s}{\pi} \ln(Q/\mu_R)\right)}{\beta_0 \frac{\alpha_s}{\pi}} + \ln(Q/\mu_R) + \frac{\ln\left(1 + \beta_0 \frac{\alpha_s}{\pi} \ln(Q/\mu_R \bar{N})\right)}{\beta_0 \frac{\alpha_s}{\pi}} - \ln(Q/\mu_R \bar{N}) \\ &= \frac{\ln(\bar{N})}{2\lambda} (2\lambda + \ln(1-2\lambda)) + \frac{2\lambda}{1-2\lambda} \ln(Q/\mu_R) \end{aligned} \quad (\text{A.72})$$

Finally:

$$\ln^2\left(1 + \beta_0 \frac{\alpha_s}{\pi} \ln(Q/\mu_R)\right) - \ln^2\left(1 + \beta_0 \frac{\alpha_s}{\pi} \ln(Q/\mu_R \bar{N})\right) = \ln^2(1 - 2\lambda) \quad (\text{A.73})$$

Thus, we have:

$$\begin{aligned} G_i = & \Lambda + \frac{2C_i}{\beta_0} \ln(Q/\mu_R \bar{N}) \ln\left(1 - \beta_0 \frac{\alpha_s}{\pi} \ln(\bar{N})\right) + \frac{2C_i}{\beta_0} \left(\frac{\ln\left(1 - \beta_0 \frac{\alpha_s}{\pi} \ln(\bar{N})\right)}{\beta_0 \frac{\alpha_s}{\pi}} + \ln(\bar{N}) \right) \\ & - \frac{C_i}{\beta_0^2} \left(K - \frac{\beta_1}{\beta_0}\right) \ln\left(1 - \beta_0 \frac{\alpha_s}{\pi} \ln(\bar{N})\right) + \frac{C_i}{\beta_0} \frac{\beta_1}{\beta_0^2} \frac{1}{2} \ln^2\left(1 - \beta_0 \frac{\alpha_s}{\pi} \ln(\bar{N})\right) \end{aligned} \quad (\text{A.74})$$

Finally we replace Λ by its expression:

$$\begin{aligned} G_i = & \frac{2C_i}{\beta_0} \lambda \left(\ln(\mu_F^2/\mu_R^2) + \frac{\beta_1}{\beta_0^2} - \frac{K}{\beta_0} \right) \\ & + \frac{C_i}{\beta_0} \ln(Q^2/\mu_R^2) \ln(1 - 2\lambda) + \frac{C_i \ln(\bar{N})}{\beta_0 \lambda} \left((1 - 2\lambda) \ln(1 - 2\lambda) + 2\lambda \right) \\ & - \frac{C_i}{\beta_0^2} \left(K - \frac{\beta_1}{\beta_0}\right) \ln(1 - 2\lambda) + \frac{C_i}{\beta_0} \frac{\beta_1}{\beta_0^2} \frac{1}{2} \ln^2(1 - 2\lambda) \\ G_i = & \frac{C_i \ln(\bar{N})}{\beta_0 \lambda} \left(2\lambda + (1 - 2\lambda) \ln(1 - 2\lambda) \right) - \frac{C_i}{\beta_0^2} K \left(2\lambda + \ln(1 - 2\lambda) \right) \\ & + \frac{C_i \beta_1}{\beta_0^3} \left(2\lambda + \ln(1 - 2\lambda) + \frac{1}{2} \ln^2(1 - 2\lambda) \right) + \frac{C_i}{\beta_0} \ln(Q^2/\mu_R^2) \ln(1 - 2\lambda) + \frac{C_i}{\beta_0} 2\lambda \ln(\mu_F^2/\mu_R^2) \end{aligned} \quad (\text{A.75})$$

We can distinguish the Leading-Logarithmic part of G_i , namely the first term and the others constituting the Next-to-Leading-Logarithmic part. In the case of $i = j = q$, we have:

$$G_{qq} = g_1(2\lambda) \ln(\bar{N}) + g_2\left(2\lambda, \frac{Q^2}{\mu_R^2}, \frac{\mu_F^2}{\mu_R^2}\right) \quad (\text{A.76})$$

$$g_1(2\lambda) = \frac{2A_q^{(1)}}{2\lambda\beta_0} \left(2\lambda + (1 - 2\lambda) \ln(1 - 2\lambda) \right) \quad (\text{A.77})$$

$$\begin{aligned}
g_2(2\lambda, \frac{Q^2}{\mu_R^2}, \frac{\mu_F^2}{\mu_R^2}) &= -\frac{A_q^{(2)}}{\beta_0^2} \left(2\lambda + \ln(1 - 2\lambda)\right) + \frac{A_q^{(1)}\beta_1}{\beta_0^3} \left(2\lambda + \ln(1 - 2\lambda) + \frac{1}{2} \ln^2(1 - 2\lambda)\right) \\
&\quad + \frac{A_q^{(1)}}{\beta_0} \ln(Q^2/\mu_R^2) \ln(1 - 2\lambda) + 2\lambda \frac{A_q^{(1)}}{\beta_0} \ln(\mu_F^2/\mu_R^2)
\end{aligned} \tag{A.78}$$

A.8.2 Expansion $\mathcal{O}(\alpha_s)$

At order $\mathcal{O}(\alpha_s)$ we have:

$$g_1(\ln(\bar{N})) = \frac{\alpha_s}{2\pi} 2A_i^{(1)} \ln(\bar{N}) \tag{A.79}$$

$$g_2(\ln(\bar{N}), \frac{\mu_F^2}{Q^2}) = \frac{\alpha_s}{2\pi} A_i^{(1)} \ln(\bar{N}) \ln\left(\frac{\mu_F^2}{Q^2}\right) \tag{A.80}$$

A.8.3 Collinearly improved resummation

We can improve collinearly the resummation by taking into account up to $\mathcal{O}(1/N)$ terms. To do so we extract from the soft and hard parts the terms to build two diagonal evolution operators like:

$$\begin{aligned}
\ln(E^{(1)}) &= \int_{\mu_F^2}^{Q^2/\bar{N}^2} \frac{dq^2}{q^2} \frac{\alpha_s(q^2)}{2\pi} P'_{qq}(N) \\
&= \int_{\mu_F^2}^{Q^2/\bar{N}^2} \frac{dq^2}{q^2} \frac{\alpha_s}{2\pi} \frac{1}{1 + \beta_0 \frac{\alpha_s}{2\pi} \ln(q^2/\mu_R^2)} \int_0^1 dz \frac{z^{N-1} - 1}{1 - z} A_1 - \delta(1 - z) z^{N-1} \frac{B_1}{2}
\end{aligned} \tag{A.81}$$

Where $P'_{qq}(N)$ is the large N (or $z \simeq 1$) equivalent of the splitting function

$$P_{qq}(N) = C_F \int_0^1 dz z^{N-1} \left(\frac{2}{1-z} \Big|_+ - (1+z) + \frac{3}{2} \delta(1-z) \right) \tag{A.82}$$

When can identify the B_1 coefficient to the $\delta(1 - z)$ term, sometimes noted as: $\delta P_{qq}^{(1)} = -\frac{B_1}{2} = \frac{3C_F}{2}$.

After integration it gives :

$$\ln(E^{(1)}) = -\frac{1}{2} \left(2 \ln(\bar{N}) A_1 + B_1 \right) \left(\frac{\ln(1-2\lambda)}{\beta_0} + \frac{\alpha_s \ln(Q^2/\mu_R^2)}{2\pi} \right) \quad (\text{A.83})$$

Remembering that we have two evolution operators like the previous one (one for each incoming parton possibly emitting soft gluons), this leads to the changes:

$$g^{(1)}(2\lambda) \hookrightarrow \tilde{g}^{(1)}(2\lambda) = g^{(1)}(2\lambda) + \frac{2A_1}{\beta_0} \ln(1-2\lambda) \quad (\text{A.84})$$

$$g^{(2)}\left(\lambda, \frac{Q^2}{\mu_R^2}, \frac{\mu_F^2}{\mu_R^2}\right) \hookrightarrow \tilde{g}^{(2)}\left(2\lambda, \frac{Q^2}{\mu_R^2}, \frac{\mu_F^2}{\mu_R^2}\right) = g^{(2)}\left(2\lambda, \frac{Q^2}{\mu_R^2}, \frac{\mu_F^2}{\mu_R^2}\right) + \frac{B_1}{\beta_0} \ln(1-2\lambda) + 2\lambda \frac{A_1}{\beta_0} \ln(Q^2/\mu_R^2) \quad (\text{A.85})$$

$$H^{(1)} = \mathcal{A}_0 + 2\delta P_{qq}^{(1)} + \frac{\pi^2}{3} A_1 \hookrightarrow \tilde{H}^{(1)} = H^{(1)} + H^{(0)} B_1 \ln(Q^2/\mu_R^2) = \mathcal{A}_0 + \frac{\pi^2}{3} A_1 \quad (\text{A.86})$$

A.9 Resummation coefficients

In this section, we provide analytical results for the resummation coefficients appearing in (3.10) in the case of a Drell-Yan-like process. Those comprise the process-dependent term $\tilde{g}_{0,q\bar{q}}$, as well as the universal coefficients of the exponent $g_{k,q\bar{q}}$ with $k > 0$. The latter are identical to those given in appendix A of [197]. We then provide below the expression for the process-dependent coefficient $\tilde{g}_{0,q\bar{q}}(M^2, \mu_F^2, \mu_R^2)$ that can be expanded in a_s as

$$\tilde{g}_{0,q\bar{q}}(M^2, \mu_F^2, \mu_R^2) = \frac{d\hat{\sigma}_{q\bar{q}}^{(0)}}{d\ln M^2} \left(1 + \sum_{k=1} a_s^k(\mu_R^2) \tilde{g}_{0,q\bar{q}}^{(k)} \right), \quad (\text{A.87})$$

where $\frac{d\hat{\sigma}_{q\bar{q}}^{(0)}}{d\ln M^2}$ is the Born partonic cross section differentiating with respect to $\ln M^2$. The $\tilde{g}_{0,q\bar{q}}^{(1)}$ and $\tilde{g}_{0,q\bar{q}}^{(2)}$ coefficients in QCD (for $n_f = 5$) relevant for resummation at N²LL explicitly

read

$$\begin{aligned}
\tilde{g}_{0,q\bar{q}}^{(1)} &= \frac{-64}{3} + \frac{64}{3}\zeta_2 - 8L_{fr} + 8L_{qr}, \\
\tilde{g}_{0,q\bar{q}}^{(2)} &= \frac{-1291}{9} + \frac{64\zeta_2}{9} + \frac{368\zeta_2^2}{3} + \frac{4528\zeta_3}{27} \\
&\quad + \frac{188L_{fr}^2}{3} + \frac{4L_{qr}^2}{3} \\
&\quad + L_{fr} \left(\frac{1324}{9} - \frac{1888\zeta_2}{9} + \frac{32\zeta_3}{3} \right) \\
&\quad + L_{qr} \left(\frac{148}{9} - 64L_{fr} + \frac{416\zeta_2}{9} - \frac{32\zeta_3}{3} \right),
\end{aligned} \tag{A.88}$$

with $L_{qr} = \ln \frac{M^2}{\mu_R^2}$, $L_{fr} = \ln \frac{\mu_F^2}{\mu_R^2}$ and ζ_n being the Riemann zeta function $\zeta(n)$.

In the processes (3.13) and (3.14), the di-lepton system is produced either through an s -channel virtual photon exchange, or through an s -channel Z -boson exchange. In other words, the Born partonic cross section can be split into three pieces, namely the square of photon-exchange diagram, that of the Z -exchange diagram, and the interference between the two diagrams. Mathematically, this can be written as

$$\hat{\sigma}_{q\bar{q}}^{(0)} = \hat{\sigma}_{q\bar{q}}^{(0),\gamma} + \hat{\sigma}_{q\bar{q}}^{(0),Z} + \hat{\sigma}_{q\bar{q}}^{(0),\text{int}}. \tag{A.89}$$

The photon exchange contribution depends on the electric charge of the initial-state quarks Q_q , and on that of the final-state leptons Q_ℓ ,

$$\hat{\sigma}_{q\bar{q}}^{(0),\gamma} = Q_q^2 Q_\ell^2 \frac{4\pi\alpha^2}{9M^2} \sqrt{1 - \frac{4m_\ell^2}{M^2}} \left(1 + \frac{2m_\ell^2}{M^2} \right). \tag{A.90}$$

In this expression, m_ℓ is the mass of the produced lepton, and it is thus respectively given by $m_{\bar{E}}$, m_E and m_Σ in the three processes shown in (3.13) and (3.14). As all exotic leptons produced in these processes satisfy $Q_\ell = -1$, $\hat{\sigma}_{q\bar{q}}^{(0),\gamma}$ is identical in all three cases.

The Z -boson exchange contribution and the interference term read

$$\begin{aligned}
\hat{\sigma}_{q\bar{q}}^{(0),Z} &= f_\ell^2 \frac{(V_q^2 + A_q^2)}{4} \frac{M^4}{(M^2 - m_Z^2)^2 + \Gamma_Z^2 m_Z^2} \frac{\hat{\sigma}_{q\bar{q}}^{(0),\gamma}}{Q_q^2}, \\
\hat{\sigma}_{q\bar{q}}^{(0),\text{int}} &= f_\ell Q_q V_q \frac{M^2(M^2 - m_Z^2)}{(M^2 - m_Z^2)^2 + \Gamma_Z^2 m_Z^2} \frac{\hat{\sigma}_{q\bar{q}}^{(0),\gamma}}{Q_q^2},
\end{aligned} \tag{A.91}$$

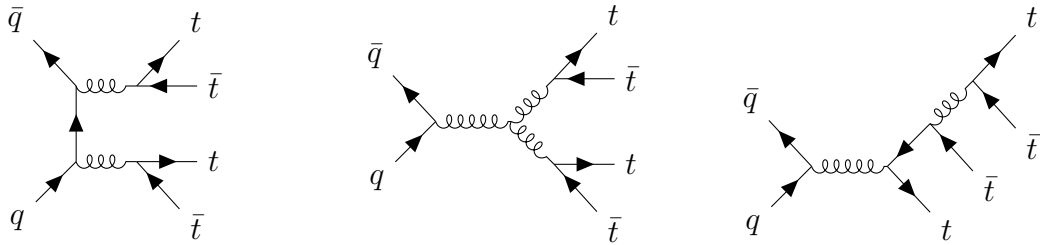
where $V_q = I_q - 2s_W^2 Q_q$ and $A_q = I_q$ represent the vector and axial couplings between the initial quarks and the Z boson respectively. Here, the parameters c_W and s_W are the cosine

and sine of the electroweak mixing angle, and I_q is the weak isospin quantum number of the quark q , that is thus equal to $1/2$ for up-type quarks and $-1/2$ for down-type quarks. In addition, Γ_Z denotes the width of the Z boson, and the prefactor f_ℓ depends on the quantum numbers of the lepton ℓ produced. It is thus given by

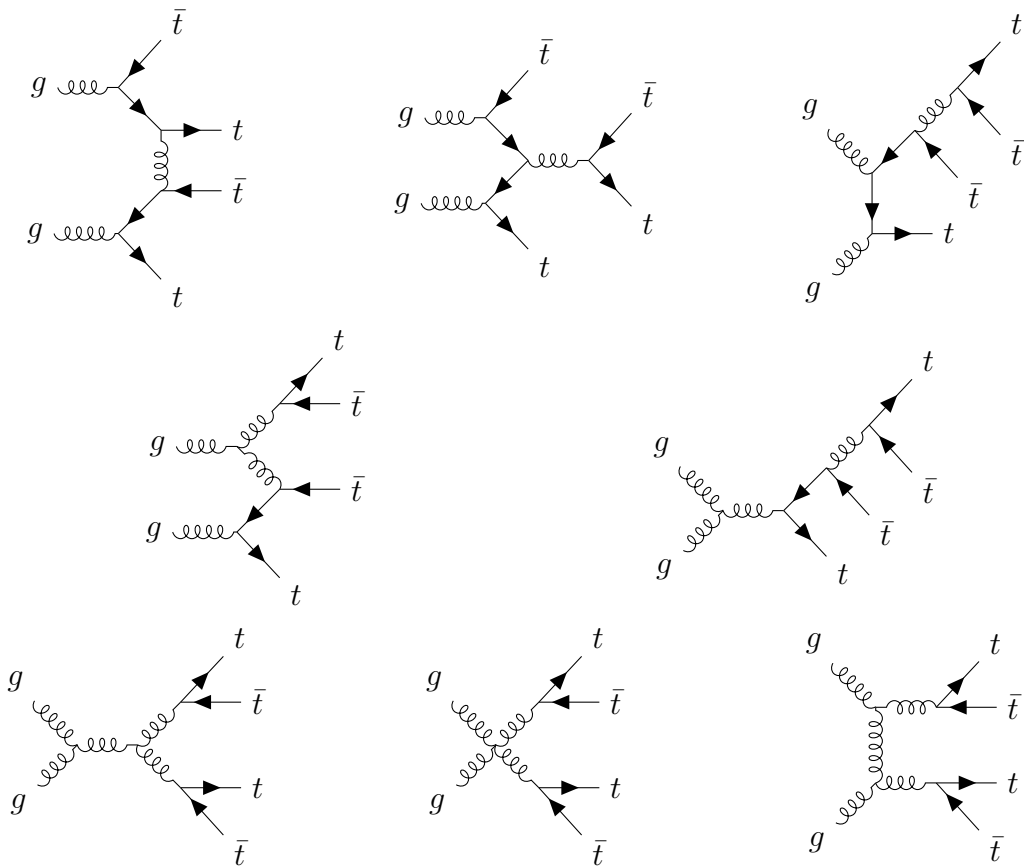
$$f_\ell = \begin{cases} -c_W^{-2} & \text{for } \ell = \tilde{E}, \\ \frac{c_W^2 - s_W^2}{2s_W^2 c_W^2} & \text{for } \ell = E, \\ s_W^{-2} & \text{for } \ell = \Sigma. \end{cases} \quad (\text{A.92})$$

A.10 Four top production tree level diagrams

A.10.1 Quark channel



A.10.2 Gluon channel



These diagrams represent all possible geometries for four top production in the SM at tree-level. Of course, the fermion lines can be exchanged so more diagrams should be taken into account for the actual computation. When generated with MG5AMC the tree level process generates 14 diagrams for the quark channel (28 if we take into account the exchange of initial quarks) and 72 for the gluon channel.

B

Bibliography

References

- [1] S. L. Glashow, “Partial-symmetries of weak interactions,” *Nuclear Physics* **22** no. 4, (1961) 579–588.
- [2] S. Weinberg, “A model of leptons,” *Phys. Rev. Lett.* **19** (Nov, 1967) 1264–1266.
- [3] H. David Politzer, “Asymptotic freedom: An approach to strong interactions,” *Physics Reports* **14** no. 4, (1974) 129–180.
- [4] S. L. Glashow, J. Iliopoulos, and L. Maiani, “Weak interactions with lepton-hadron symmetry,” *Phys. Rev. D* **2** (Oct, 1970) 1285–1292.
- [5] **ATLAS** Collaboration, “Standard model summary plots,” tech. rep., CERN. <http://atlas.web.cern.ch/Atlas/GROUPS/PHYSICS/CombinedSummaryPlots/SM>.
- [6] P. Charitos, M. Chrzaszcz, and R. Tores, “Experimental physics goals captured,” Dec., 2022. <https://doi.org/10.5281/zenodo.7468100>.
- [7] M. Mangano, P. Azzi, M. Benedikt, A. Blondel, D. A. Britzger, A. Dainese, M. Dam, J. de Blas, D. Enterria, O. Fischer, C. Grojean, J. Gutleber, C. Gwenlan, C. Hensens, P. Janot, M. Klein, U. Klein, M. P. McCullough, S. Monteil, J. Poole, M. Ramsey-Musolf, C. Schwanenberger, M. Selvaggi, F. Zimmermann, and T. You, “FCC Physics Opportunities: Future Circular Collider Conceptual Design Report Volume 1. Future Circular Collider,” Tech. Rep. 6, CERN, Geneva, 2019.
- [8] J. Gutleber, E. Sirtori, F. Giffoni, F. Guadagno, and G. Catalano, “Plan for research infrastructure socio-economic impact analysis,” Nov., 2021. <https://doi.org/10.5281/zenodo.5725806>.
- [9] G. Apollinari, O. Brüning, T. Nakamoto, and L. Rossi, “High luminosity large hadron collider HL-LHC,” 2015. <https://cds.cern.ch/record/2120673>.
- [10] **Particle Data Group** Collaboration, R. L. Workman *et al.*, “Review of Particle Physics,” *PTEP* **2022** (2022) 083C01.
- [11] F. Cascioli, T. Gehrmann, M. Grazzini, S. Kallweit, P. Maierhöfer, A. von Manteuffel, S. Pozzorini, D. Rathlev, L. Tancredi, and E. Weihs, “ZZ production at hadron colliders in NNLO QCD,” *Physics Letters B* **735** (2014) 311–313.

- [12] T. Gehrmann, M. Grazzini, S. Kallweit, P. Maierhöfer, A. von Manteuffel, S. Pozzorini, D. Rathlev, and L. Tancredi, “ W^+W^- production at hadron colliders in next to next to leading order QCD,” *Phys. Rev. Lett.* **113** (Nov, 2014) 212001.
- [13] S. Catani, L. Cieri, D. de Florian, G. Ferrera, and M. Grazzini, “Diphoton production at hadron colliders: A fully differential QCD calculation at next-to-next-to-leading order,” *Phys. Rev. Lett.* **108** (Feb, 2012) 072001.
- [14] M. Grazzini, S. Kallweit, D. Rathlev, and A. Torre, “ $Z\gamma$ production at hadron colliders in NNLO QCD,” *Physics Letters B* **731** (2014) 204–207.
- [15] X. Chen, T. Gehrmann, N. Glover, M. Höfer, and A. Huss, “Isolated photon and photon+jet production at NNLO QCD accuracy,” *Journal of High Energy Physics* **2020** no. 4, (Apr, 2020) .
- [16] A. Gehrmann-De Ridder, T. Gehrmann, E. W. N. Glover, A. Huss, and D. M. Walker, “Next-to-next-to-leading-order QCD corrections to the transverse momentum distribution of weak gauge bosons,” *Phys. Rev. Lett.* **120** (Mar, 2018) 122001.
- [17] R. Boughezal, F. Caola, K. Melnikov, F. Petriello, and M. Schulze, “Higgs boson production in association with a jet at next-to-next-to-leading order,” *Phys. Rev. Lett.* **115** (Aug, 2015) 082003.
- [18] M. Czakon, D. Heymes, and A. Mitov, “High-precision differential predictions for top-quark pairs at the LHC,” *Physical Review Letters* **116** no. 8, (Feb, 2016) .
- [19] S. Catani, S. Devoto, M. Grazzini, S. Kallweit, and J. Mazzitelli, “Top-quark pair production at the LHC: fully differential QCD predictions at NNLO,” *Journal of High Energy Physics* **2019** no. 7, (Jul, 2019) .
- [20] N. Kidonakis, M. Guzzi, and A. Tonerio, “Top-quark cross sections and distributions at approximate n^3 LO,” *Phys. Rev. D* **108** (Sep, 2023) 054012.
- [21] C. Duhr, F. Dulat, and B. Mistlberger, “Drell-yan cross section to third order in the strong coupling constant,” *Physical Review Letters* **125** no. 17, (Oct, 2020) .
- [22] S. Kallweit, V. Sotnikov, and M. Wiesemann, “Triphoton production at hadron colliders in NNLO QCD,” *Physics Letters B* **812** (Jan, 2021) 136013.
- [23] M. Czakon, A. Mitov, and R. Poncelet, “Next-to-next-to-leading order study of three-jet production at the LHC,” *Physical Review Letters* **127** no. 15, (Oct, 2021) .
- [24] H. A. Chawdhry, M. Czakon, A. Mitov, and R. Poncelet, “NNLO QCD corrections to diphoton production with an additional jet at the LHC,” *Journal of High Energy Physics* **2021** no. 9, (Sep, 2021) .
- [25] **ATLAS** Collaboration, “Top cross section summary plots - september 2023,” tech. rep., CERN, Geneva, 2023. <http://cds.cern.ch/record/2872786>.

- [26] S. Catani, D. de Florian, and M. Grazzini, “Universality of non-leading logarithmic contributions in transverse-momentum distributions,” *Nuclear Physics B* **596** no. 1, (2001) 299–312.
- [27] J. Botts and G. F. Sterman, “Hard Elastic Scattering in QCD: Leading Behavior,” *Nucl. Phys. B* **325** (1989) 62–100.
- [28] E. Laenen, G. Sterman, and W. Vogelsang, “Recoil and threshold corrections in short-distance cross sections,” *Physical Review D* **63** no. 11, (May, 2001) .
- [29] C. Collaboration, “Observation of four top quark production in proton-proton collisions at $\sqrt{s} = 13$ tev,” [arXiv:2305.13439 \[hep-ex\]](#).
- [30] A. collaboration, “Observation of four-top-quark production in the multilepton final state with the atlas detector,” *The European Physical Journal C* **83** no. 6, (Jun, 2023) 496.
- [31] M. van Beekveld, A. Kulesza, and L. M. Valero, “Threshold resummation for the production of four top quarks at the LHC,” [arXiv:2212.03259 \[hep-ph\]](#).
- [32] A. H. Ajjath and H.-S. Shao, “N3LO+N3LL QCD improved higgs pair cross sections,” *Journal of High Energy Physics* **2023** no. 2, (Feb, 2023) .
- [33] A. H. Ajjath, P. Mukherjee, V. Ravindran, A. Sankar, and S. Tiwari, “Resummed higgs boson cross section at next-to SV to NNLO+NNLL,” *The European Physical Journal C* **82** no. 9, (Sep, 2022) .
- [34] M. Bonvini, S. Marzani, C. Muselli, and L. Rottoli, “On the higgs cross section at N3LO+N3LL and its uncertainty,” *Journal of High Energy Physics* **2016** no. 8, (Aug, 2016) .
- [35] S. Mandelstam, “II. vortices and quark confinement in non-abelian gauge theories,” *Physics Reports* **23** no. 3, (1976) 245–249.
- [36] J. C. Collins, D. E. Soper, and G. Sterman, “Factorization of hard processes in QCD,” [arXiv:hep-ph/0409313 \[hep-ph\]](#).
- [37] A. D. Martin, W. J. Stirling, R. S. Thorne, and G. Watt, “Parton distributions for the LHC,” *The European Physical Journal C* **63** no. 2, (Jul, 2009) 189–285.
- [38] S. Coleman, “Fun with SU(3),” in *Seminar on high-energy physics and elementary particles*, pp. 331–352. 1965.
- [39] S. Catani and M. Seymour, “A general algorithm for calculating jet cross sections in nlo qcd,” *Nuclear Physics B* **485** no. 1-2, (Feb, 1997) 291–419.
- [40] W. A. Bardeen, A. J. Buras, D. W. Duke, and T. Muta, “Deep-inelastic scattering beyond the leading order in asymptotically free gauge theories,” *Phys. Rev. D* **18** (Dec, 1978) 3998–4017.

- [41] T. van Ritbergen, J. Vermaseren, and S. Larin, “The four-loop β -function in quantum chromodynamics,” *Physics Letters B* **400** no. 3, (1997) 379–384.
- [42] H. D. Politzer, “Reliable perturbative results for strong interactions?,” *Phys. Rev. Lett.* **30** (Jun, 1973) 1346–1349.
- [43] R. Feynman, *Photon-hadron interactions*. Taylor Francis, 1972.
- [44] M. Gell-Mann, “A Schematic Model of Baryons and Mesons,” *Phys. Lett.* **8** (1964) 214–215.
- [45] G. Zweig, *An $SU(3)$ model for strong interaction symmetry and its breaking. Version 2*, pp. 22–101. 2, 1964.
- [46] V. Bertone, M. Cacciari, S. Frixione, and G. Stagnitto, “The partonic structure of the electron at the next-to-leading logarithmic accuracy in QED,” *Journal of High Energy Physics* **2020** no. 3, (Mar, 2020) .
- [47] G. Altarelli and G. Parisi, “Asymptotic Freedom in Parton Language,” *Nucl. Phys.* **B126** (1977) 298–318.
- [48] M. E. Peskin and D. V. Schroeder, *An Introduction to Quantum Field Theory*. Westview Press, 1995. Reading, USA: Addison-Wesley (1995) 842 p.
- [49] T.-J. Hou *et al.*, “New CTEQ global analysis of quantum chromodynamics with high-precision data from the LHC,” *Phys. Rev. D* **103** no. 1, (2021) 014013, [arXiv:1912.10053 \[hep-ph\]](#).
- [50] L. D. Debbio, “An overview of lattice results for parton distribution functions,” [arXiv:2211.00977 \[hep-lat\]](#).
- [51] X. Ji, “Parton physics on a euclidean lattice,” *Phys. Rev. Lett.* **110** (Jun, 2013) 262002.
- [52] S. Forte and S. Carrazza, “Parton distribution functions,” [arXiv:2008.12305 \[hep-ph\]](#).
- [53] A. Buckley, J. Ferrando, S. Lloyd, K. Nordström, B. Page, M. Rüfenacht, M. Schönherr, and G. Watt, “LHAPDF6: parton density access in the LHC precision era,” *The European Physical Journal C* **75** no. 3, (Mar, 2015) .
- [54] A. D. Martin, A. J. T. M. Mathijssen, W. J. Stirling, R. S. Thorne, B. J. A. Watt, and G. Watt, “Extended parameterisations for MSTW PDFs and their effect on lepton charge asymmetry from w decays,” *The European Physical Journal C* **73** no. 2, (Feb, 2013) .
- [55] R. S. Thorne and W. K. Tung, “pQCD formulations with heavy quark masses and global analysis,” [arXiv:0809.0714 \[hep-ph\]](#).

- [56] S. Keppeler and M. Sjö Dahl, “Orthogonal multiplet bases in $SU(n_c)$ color space,” *Journal of High Energy Physics* **2012** no. 9, (Sep, 2012) , [arXiv:1207.0609 \[hep-ph\]](#) .
- [57] R. Frederix, S. Frixione, F. Maltoni, and T. Stelzer, “Automation of next-to-leading order computations in QCD: the FKS subtraction,” *Journal of High Energy Physics* **2009** no. 10, (Oct, 2009) .
- [58] A. Kulesza, L. M. Valero, and V. Theeuwes, “On soft gluon resummation for associated single top production with a Higgs boson at the LHC,” *Eur. Phys. J. Plus* **138** no. 2, (2023) 178, [arXiv:2109.15039 \[hep-ph\]](#) .
- [59] V. M. Theeuwes, *Soft Gluon Resummation for Heavy Particle Production at the Large Hadron Collider*. Phd thesis, University of Munster, March, 2016.
- [60] M. Lévy and J. Sucher, “Eikonal approximation in quantum field theory,” *Phys. Rev.* **186** (Oct, 1969) 1656–1670.
- [61] C. G. Papadopoulos, “PHEGAS: A phase-space generator for automatic cross-section computation,” *Computer Physics Communications* **137** no. 2, (Jun, 2001) 247–254.
- [62] T. D. Lee and M. Nauenberg, “Degenerate systems and mass singularities,” *Phys. Rev.* **133** (Mar, 1964) B1549–B1562.
- [63] A. Banfi, B. K. El-Menoufi, and P. F. Monni, “The sudakov radiator for jet observables and the soft physical coupling,” *Journal of High Energy Physics* **2019** no. 1, (Jan, 2019) .
- [64] S. Catani, D. De Florian, and M. Grazzini, “Soft-gluon effective coupling and cusp anomalous dimension,” *Eur. Phys. J. C* **79** no. 8, (2019) 685, [arXiv:1904.10365 \[hep-ph\]](#) .
- [65] S. Catani, D. de Florian, M. Grazzini, and P. Nason, “Soft-gluon resummation for higgs boson production at hadron colliders,” *Journal of High Energy Physics* **2003** no. 07, (Jul, 2003) 028–028.
- [66] N. Kidonakis and N. Yamanaka, “Soft-gluon corrections for tqZ production,” *Phys. Lett. B* **838** (2023) 137708, [arXiv:2210.09542 \[hep-ph\]](#) .
- [67] C. W. Bauer, S. Fleming, D. Pirjol, and I. W. Stewart, “An effective field theory for collinear and soft gluons: Heavy to light decays,” *Phys. Rev. D* **63** (May, 2001) 114020.
- [68] V. Ahrens, A. Ferroglia, M. Neubert, B. D. Pecjak, and L. L. Yang, “Renormalization-group improved predictions for top-quark pair production at hadron colliders,” *Journal of High Energy Physics* **2010** no. 9, (Sep, 2010) .

- [69] A. Broggio, A. Ferroglia, G. Ossola, and B. D. Pecjak, “Associated production of a top pair and a w boson at next-to-next-to-leading logarithmic accuracy,” *Journal of High Energy Physics* **2016** no. 9, (Sep, 2016) .
- [70] W.-L. Ju, Y. Xu, L. L. Yang, and B. Zhou, “Thrust distribution in higgs decays up to the fifth logarithmic order,” *Phys. Rev. D* **107** (Jun, 2023) 114034.
- [71] M. Bonvini, S. Forte, M. Ghezzi, and G. Ridolfi, “Threshold resummation in scet vs. perturbative qcd: An analytic comparison,” *Nuclear Physics B* **861** no. 3, (2012) 337–360.
- [72] J. C. Collins, *Renormalization: An Introduction to Renormalization, the Renormalization Group and the Operator-Product Expansion*. Cambridge Monographs on Mathematical Physics. Cambridge University Press, 1984.
- [73] G. 't Hooft and M. Veltman, “Regularization and renormalization of gauge fields,” *Nuclear Physics B* **44** no. 1, (1972) 189–213.
- [74] N. Kidonakis and G. Sterman, “Resummation for QCD hard scattering,” *Nuclear Physics B* **505** no. 1-2, (Nov, 1997) 321–348.
- [75] J. Alwall, R. Frederix, S. Frixione, V. Hirschi, F. Maltoni, O. Mattelaer, H. S. Shao, T. Stelzer, P. Torrielli, and M. Zaro, “The automated computation of tree-level and next-to-leading order differential cross sections, and their matching to parton shower simulations,” *JHEP* **07** (2014) 079, [arXiv:1405.0301 \[hep-ph\]](#).
- [76] R. Frederix, S. Frixione, V. Hirschi, D. Pagani, H. S. Shao, and M. Zaro, “The automation of next-to-leading order electroweak calculations,” *JHEP* **07** (2018) 185, [arXiv:1804.10017 \[hep-ph\]](#). [Erratum: *JHEP* 11, 085 (2021)].
- [77] N. Kidonakis, G. Oderda, and G. Sterman, “Evolution of color exchange in QCD hard scattering,” *Nuclear Physics B* **531** no. 1-3, (Oct, 1998) 365–402.
- [78] A. Kulesza and L. Motyka, “Soft gluon resummation for the production of gluino-gluino and squark-antisquark pairs at the LHC,” *Physical Review D* **80** no. 9, (Nov, 2009) .
- [79] B. Fuks, M. Klasen, D. R. Lamprea, and M. Rothering, “Precision predictions for electroweak superpartner production at hadron colliders with resumino,” *The European Physical Journal C* **73** no. 7, (Jul, 2013) .
- [80] A. Vogt, “Efficient evolution of unpolarized and polarized parton distributions with QCD-pegasus,” *Computer Physics Communications* **170** no. 1, (Jul, 2005) 65–92.
- [81] M. Diehl, R. Nagar, and F. J. Tackmann, “ChiliPDF: Chebyshev interpolation for parton distributions,” *The European Physical Journal C* **82** no. 3, (Mar, 2022) .
- [82] S. Catani, “The resummation of soft gluons in hadronic collisions,” *Nuclear Physics B* **478** no. 1-2, (Oct, 1996) 273–310.

- [83] A. H. Ajjath, B. Fuks, H.-S. Shao, and Y. Simon, “Precision predictions for exotic lepton production at the large hadron collider,” *Phys. Rev. D* **107** (Apr, 2023) 075011.
- [84] G. Cacciapaglia, A. Deandrea, and K. Sridhar, “Review of fundamental composite dynamics,” *Eur. Phys. J. ST* **231** no. 7, (2022) 1221–1222.
- [85] G. Cacciapaglia, C. Pica, and F. Sannino, “Fundamental Composite Dynamics: A Review,” *Phys. Rept.* **877** (2020) 1–70, [arXiv:2002.04914 \[hep-ph\]](#).
- [86] G. Panico and A. Wulzer, *The Composite Nambu-Goldstone Higgs*, vol. 913. Springer, 2016. [arXiv:1506.01961 \[hep-ph\]](#).
- [87] A. P. Morais, R. Pasechnik, and W. Porod, “Prospects for new physics from gauge left-right-colour-family grand unification hypothesis,” *Eur. Phys. J. C* **80** no. 12, (2020) 1162, [arXiv:2001.06383 \[hep-ph\]](#).
- [88] A. P. Morais, R. Pasechnik, and W. Porod, “Grand Unified Origin of Gauge Interactions and Families Replication in the Standard Model,” *Universe* **7** no. 12, (2021) 461, [arXiv:2001.04804 \[hep-ph\]](#).
- [89] J. Y. Araz, S. Banerjee, M. Frank, B. Fuks, and A. Goudelis, “Dark matter and collider signals in an MSSM extension with vector-like multiplets,” *Phys. Rev. D* **98** no. 11, (2018) 115009, [arXiv:1810.07224 \[hep-ph\]](#).
- [90] M. Endo, K. Hamaguchi, S. Iwamoto, and N. Yokozaki, “Higgs Mass and Muon Anomalous Magnetic Moment in Supersymmetric Models with Vector-Like Matters,” *Phys. Rev. D* **84** (2011) 075017, [arXiv:1108.3071 \[hep-ph\]](#).
- [91] S. P. Martin, “Extra vector-like matter and the lightest Higgs scalar boson mass in low-energy supersymmetry,” *Phys. Rev. D* **81** (2010) 035004, [arXiv:0910.2732 \[hep-ph\]](#).
- [92] R. N. Mohapatra and J. C. Pati, “A Natural Left-Right Symmetry,” *Phys. Rev. D* **11** (1975) 2558.
- [93] R. N. Mohapatra, F. E. Paige, and D. P. Sidhu, “Symmetry Breaking and Naturalness of Parity Conservation in Weak Neutral Currents in Left-Right Symmetric Gauge Theories,” *Phys. Rev. D* **17** (1978) 2462.
- [94] J. C. Pati and A. Salam, “Lepton Number as the Fourth Color,” *Phys. Rev. D* **10** (1974) 275–289. [Erratum: *Phys.Rev.D* 11, 703–703 (1975)].
- [95] G. Senjanovic and R. N. Mohapatra, “Exact Left-Right Symmetry and Spontaneous Violation of Parity,” *Phys. Rev. D* **12** (1975) 1502.
- [96] J. Halverson, N. Orlofsky, and A. Pierce, “Vectorlike Leptons as the Tip of the Dark Matter Iceberg,” *Phys. Rev. D* **90** no. 1, (2014) 015002, [arXiv:1403.1592 \[hep-ph\]](#).

- [97] Y. Cai, T. Han, T. Li, and R. Ruiz, “Lepton Number Violation: Seesaw Models and Their Collider Tests,” *Front. in Phys.* **6** (2018) 40, [arXiv:1711.02180 \[hep-ph\]](#).
- [98] M. Gell-Mann, P. Ramond, and R. Slansky, “Complex Spinors and Unified Theories,” *Conf. Proc. C* **790927** (1979) 315–321, [arXiv:1306.4669 \[hep-th\]](#).
- [99] S. L. Glashow, “The Future of Elementary Particle Physics,” *NATO Sci. Ser. B* **61** (1980) 687.
- [100] P. Minkowski, “ $\mu \rightarrow e\gamma$ at a Rate of One Out of 10^9 Muon Decays?,” *Phys. Lett. B* **67** (1977) 421–428.
- [101] R. N. Mohapatra and G. Senjanovic, “Neutrino Mass and Spontaneous Parity Nonconservation,” *Phys. Rev. Lett.* **44** (1980) 912.
- [102] J. Schechter and J. W. F. Valle, “Neutrino Masses in SU(2) x U(1) Theories,” *Phys. Rev. D* **22** (1980) 2227.
- [103] R. E. Shrock, “General Theory of Weak Leptonic and Semileptonic Decays. 1. Leptonic Pseudoscalar Meson Decays, with Associated Tests For, and Bounds on, Neutrino Masses and Lepton Mixing,” *Phys. Rev. D* **24** (1981) 1232.
- [104] T. Yanagida, “Horizontal gauge symmetry and masses of neutrinos,” *Conf. Proc. C* **7902131** (1979) 95–99.
- [105] R. Foot, H. Lew, X. G. He, and G. C. Joshi, “Seesaw Neutrino Masses Induced by a Triplet of Leptons,” *Z. Phys. C* **44** (1989) 441.
- [106] CMS Collaboration, “Search for pair-produced vector-like leptons in final states with third-generation leptons and at least three b quark jets in proton-proton collisions at $\sqrt{s} = 13$ TeV,” [arXiv:2208.09700 \[hep-ex\]](#).
- [107] CMS Collaboration, “Search for resonant and nonresonant production of pairs of dijet resonances in proton-proton collisions at $\sqrt{s} = 13$ TeV,” *Journal of High Energy Physics* **2023** no. 7, (Jul, 2023) .
- [108] ATLAS Collaboration, “Search for third-generation vector-like leptons in pp collisions at $\sqrt{s} = 13$ TeV with the ATLAS detector,” *Journal of High Energy Physics* **2023** no. 7, (Jul, 2023) .
- [109] ATLAS Collaboration, M. Aaboud *et al.*, “Search for a right-handed gauge boson decaying into a high-momentum heavy neutrino and a charged lepton in pp collisions with the ATLAS detector at $\sqrt{s} = 13$ TeV,” *Phys. Lett. B* **798** (2019) 134942, [arXiv:1904.12679 \[hep-ex\]](#).
- [110] ATLAS Collaboration, M. Aaboud *et al.*, “Search for heavy Majorana or Dirac neutrinos and right-handed W gauge bosons in final states with two charged leptons and two jets at $\sqrt{s} = 13$ TeV with the ATLAS detector,” *JHEP* **01** (2019) 016, [arXiv:1809.11105 \[hep-ex\]](#).

- [111] **ATLAS** Collaboration, G. Aad *et al.*, “Search for heavy neutral leptons in decays of W bosons produced in 13 TeV pp collisions using prompt and displaced signatures with the ATLAS detector,” *JHEP* **10** (2019) 265, [arXiv:1905.09787 \[hep-ex\]](#).
- [112] **ATLAS** Collaboration, G. Aad *et al.*, “Search for type-III seesaw heavy leptons in dilepton final states in pp collisions at $\sqrt{s} = 13$ TeV with the ATLAS detector,” *Eur. Phys. J. C* **81** no. 3, (2021) 218, [arXiv:2008.07949 \[hep-ex\]](#).
- [113] **ATLAS** Collaboration, G. Aad *et al.*, “Search for new phenomena in three- or four-lepton events in pp collisions at $\sqrt{s} = 13$ TeV with the ATLAS detector,” *Phys. Lett. B* **824** (2022) 136832, [arXiv:2107.00404 \[hep-ex\]](#).
- [114] **ATLAS Collaboration** Collaboration, G. Aad *et al.*, “Search for type-III seesaw heavy leptons in leptonic final states in pp collisions at $\sqrt{s} = 13$ TeV with the ATLAS detector,” *Eur. Phys. J. C* **82** (Feb, 2022) 988, [arXiv:2202.02039 \[hep-ex\]](#).
- [115] **CMS** Collaboration, A. M. Sirunyan *et al.*, “Search for Evidence of the Type-III Seesaw Mechanism in Multilepton Final States in Proton-Proton Collisions at $\sqrt{s} = 13$ TeV,” *Phys. Rev. Lett.* **119** no. 22, (2017) 221802, [arXiv:1708.07962 \[hep-ex\]](#).
- [116] **CMS** Collaboration, A. M. Sirunyan *et al.*, “Search for a heavy right-handed W boson and a heavy neutrino in events with two same-flavor leptons and two jets at $\sqrt{s} = 13$ TeV,” *JHEP* **05** (2018) 148, [arXiv:1803.11116 \[hep-ex\]](#).
- [117] **CMS** Collaboration, A. M. Sirunyan *et al.*, “Search for heavy neutral leptons in events with three charged leptons in proton-proton collisions at $\sqrt{s} = 13$ TeV,” *Phys. Rev. Lett.* **120** no. 22, (2018) 221801, [arXiv:1802.02965 \[hep-ex\]](#).
- [118] **CMS** Collaboration, A. M. Sirunyan *et al.*, “Search for heavy Majorana neutrinos in same-sign dilepton channels in proton-proton collisions at $\sqrt{s} = 13$ TeV,” *JHEP* **01** (2019) 122, [arXiv:1806.10905 \[hep-ex\]](#).
- [119] **CMS** Collaboration, A. M. Sirunyan *et al.*, “Search for heavy neutrinos and third-generation leptoquarks in hadronic states of two τ leptons and two jets in proton-proton collisions at $\sqrt{s} = 13$ TeV,” *JHEP* **03** (2019) 170, [arXiv:1811.00806 \[hep-ex\]](#).
- [120] **CMS** Collaboration, A. M. Sirunyan *et al.*, “Search for vector-like leptons in multilepton final states in proton-proton collisions at $\sqrt{s} = 13$ TeV,” *Phys. Rev. D* **100** no. 5, (2019) 052003, [arXiv:1905.10853 \[hep-ex\]](#).
- [121] **CMS** Collaboration, A. M. Sirunyan *et al.*, “Search for physics beyond the standard model in multilepton final states in proton-proton collisions at $\sqrt{s} = 13$ TeV,” *JHEP* **03** (2020) 051, [arXiv:1911.04968 \[hep-ex\]](#).

- [122] **CMS Collaboration**, A. Tumasyan *et al.*, “Inclusive nonresonant multilepton probes of new phenomena at $\sqrt{s}=13$ TeV,” *Phys. Rev. D* **105** no. 11, (2022) 112007, [arXiv:2202.08676 \[hep-ex\]](#).
- [123] **CMS Collaboration**, A. Tumasyan *et al.*, “Search for a right-handed W boson and a heavy neutrino in proton-proton collisions at $\sqrt{s} = 13$ TeV,” *JHEP* **04** (2022) 047, [arXiv:2112.03949 \[hep-ex\]](#).
- [124] **ATLAS Collaboration** Collaboration, “Search for heavy neutral leptons in decays of W bosons using a dilepton displaced vertex in $\sqrt{s} = 13$ TeV *pp* collisions with the ATLAS detector,” *Phys. Rev. Lett.* **131** (Aug, 2023) 061803.
- [125] **OPAL Collaboration**, G. Abbiendi *et al.*, “Search for charged excited leptons in e^+e^- collisions at $\sqrt{s} = 183$ -GeV to 209-GeV,” *Phys. Lett. B* **544** (2002) 57–72, [arXiv:hep-ex/0206061](#).
- [126] **DELPHI Collaboration**, J. Abdallah *et al.*, “Search for excited leptons in e^+e^- collisions at $\sqrt{s} = 189$ -GeV to 209-GeV,” *Eur. Phys. J. C* **46** (2006) 277–293, [arXiv:hep-ex/0603045](#).
- [127] **L3 Collaboration**, P. Achard *et al.*, “Search for heavy neutral and charged leptons in e^+e^- annihilation at LEP,” *Phys. Lett. B* **517** (2001) 75–85, [arXiv:hep-ex/0107015](#).
- [128] **ALEPH Collaboration**, D. Buskulic *et al.*, “Search for heavy lepton pair production in e^+e^- collisions at center-of-mass energies of 130-GeV and 136-GeV,” *Phys. Lett. B* **384** (1996) 439–448.
- [129] C. Degrande, O. Mattelaer, R. Ruiz, and J. Turner, “Fully-Automated Precision Predictions for Heavy Neutrino Production Mechanisms at Hadron Colliders,” *Phys. Rev. D* **94** no. 5, (2016) 053002, [arXiv:1602.06957 \[hep-ph\]](#).
- [130] B. Fuks, J. Neundorff, K. Peters, R. Ruiz, and M. Saimpert, “Majorana neutrinos in same-sign $W^\pm W^\pm$ scattering at the LHC: Breaking the TeV barrier,” *Phys. Rev. D* **103** no. 5, (2021) 055005, [arXiv:2011.02547 \[hep-ph\]](#).
- [131] O. Mattelaer, M. Mitra, and R. Ruiz, “Automated Neutrino Jet and Top Jet Predictions at Next-to-Leading-Order with Parton Shower Matching in Effective Left-Right Symmetric Models,” [arXiv:1610.08985 \[hep-ph\]](#).
- [132] R. Ruiz, “QCD Corrections to Pair Production of Type III Seesaw Leptons at Hadron Colliders,” *JHEP* **12** (2015) 165, [arXiv:1509.05416 \[hep-ph\]](#).
- [133] J. Debove, B. Fuks, and M. Klasen, “Threshold resummation for gaugino pair production at hadron colliders,” *Nucl. Phys. B* **842** (2011) 51–85, [arXiv:1005.2909 \[hep-ph\]](#).

- [134] B. Fuks, M. Klasen, D. R. Lamprea, and M. Rothering, “Gaugino production in proton-proton collisions at a center-of-mass energy of 8 TeV,” *JHEP* **10** (2012) 081, [arXiv:1207.2159 \[hep-ph\]](#).
- [135] B. Fuks, M. Klasen, D. R. Lamprea, and M. Rothering, “Precision predictions for electroweak superpartner production at hadron colliders with Resummino,” *Eur. Phys. J. C* **73** (2013) 2480, [arXiv:1304.0790 \[hep-ph\]](#).
- [136] J. Fiaschi and M. Klasen, “Higgsino and gaugino pair production at the LHC with aNNLO+NNLL precision,” *Phys. Rev. D* **102** no. 9, (2020) 095021, [arXiv:2006.02294 \[hep-ph\]](#).
- [137] P. N. Bhattiprolu and S. P. Martin, “Prospects for vectorlike leptons at future proton-proton colliders,” *Phys. Rev. D* **100** no. 1, (2019) 015033, [arXiv:1905.00498 \[hep-ph\]](#).
- [138] C. Degrande, C. Duhr, B. Fuks, D. Grellscheid, O. Mattelaer, and T. Reiter, “UFO - The Universal FeynRules Output,” *Comput. Phys. Commun.* **183** (2012) 1201–1214, [arXiv:1108.2040 \[hep-ph\]](#).
- [139] S. Catani and L. Trentadue, “Resummation of the QCD Perturbative Series for Hard Processes,” *Nucl. Phys. B* **327** (1989) 323–352.
- [140] G. F. Sterman, “Summation of Large Corrections to Short Distance Hadronic Cross-Sections,” *Nucl. Phys. B* **281** (1987) 310–364.
- [141] A. Vogt, “Next-to-next-to-leading logarithmic threshold resummation for deep inelastic scattering and the Drell-Yan process,” *Phys. Lett. B* **497** (2001) 228–234, [arXiv:hep-ph/0010146](#).
- [142] M. Buchkremer, G. Cacciapaglia, A. Deandrea, and L. Panizzi, “Model Independent Framework for Searches of Top Partners,” *Nucl. Phys. B* **876** (2013) 376–417, [arXiv:1305.4172 \[hep-ph\]](#).
- [143] B. Fuks and H.-S. Shao, “QCD next-to-leading-order predictions matched to parton showers for vector-like quark models,” *Eur. Phys. J. C* **77** no. 2, (2017) 135, [arXiv:1610.04622 \[hep-ph\]](#).
- [144] A. Alloul, N. D. Christensen, C. Degrande, C. Duhr, and B. Fuks, “FeynRules 2.0 - A complete toolbox for tree-level phenomenology,” *Comput. Phys. Commun.* **185** (2014) 2250–2300, [arXiv:1310.1921 \[hep-ph\]](#).
- [145] N. D. Christensen, P. de Aquino, C. Degrande, C. Duhr, B. Fuks, M. Herquet, F. Maltoni, and S. Schumann, “A Comprehensive approach to new physics simulations,” *Eur. Phys. J. C* **71** (2011) 1541, [arXiv:0906.2474 \[hep-ph\]](#).
- [146] P. Z. Skands *et al.*, “SUSY Les Houches accord: Interfacing SUSY spectrum calculators, decay packages, and event generators,” *JHEP* **07** (2004) 036,

- arXiv:hep-ph/0311123.
- [147] C. Biggio and F. Bonnet, “Implementation of the Type III Seesaw Model in FeynRules/MadGraph and Prospects for Discovery with Early LHC Data,” *Eur. Phys. J. C* **72** (2012) 1899, arXiv:1107.3463 [hep-ph].
 - [148] T. Li and X.-G. He, “Neutrino Masses and Heavy Triplet Leptons at the LHC: Testability of Type III Seesaw,” *Phys. Rev. D* **80** (2009) 093003, arXiv:0907.4193 [hep-ph].
 - [149] A. Abada, C. Biggio, F. Bonnet, M. B. Gavela, and T. Hambye, “Low energy effects of neutrino masses,” *JHEP* **12** (2007) 061, arXiv:0707.4058 [hep-ph].
 - [150] A. Abada, C. Biggio, F. Bonnet, M. B. Gavela, and T. Hambye, “ $\mu \rightarrow e$ gamma and $\tau \rightarrow l$ gamma decays in the fermion triplet seesaw model,” *Phys. Rev. D* **78** (2008) 033007, arXiv:0803.0481 [hep-ph].
 - [151] C. Giganti, S. Lavignac, and M. Zito, “Neutrino oscillations: The rise of the PMNS paradigm,” *Progress in Particle and Nuclear Physics* **98** (Jan, 2018) 1–54.
 - [152] B. Fuks, M. Nemevšek, and R. Ruiz, “Doubly Charged Higgs Boson Production at Hadron Colliders,” *Phys. Rev. D* **101** no. 7, (2020) 075022, arXiv:1912.08975 [hep-ph].
 - [153] C. Duhr and B. Fuks, “A superspace module for the FeynRules package,” *Comput. Phys. Commun.* **182** (2011) 2404–2426, arXiv:1102.4191 [hep-ph].
 - [154] S. Frixione, B. Fuks, V. Hirschi, K. Mawatari, H.-S. Shao, P. A. Sunder, and M. Zaro, “Automated simulations beyond the Standard Model: supersymmetry,” *JHEP* **12** (2019) 008, arXiv:1907.04898 [hep-ph].
 - [155] C. Degrande, “Automatic evaluation of UV and R2 terms for beyond the Standard Model Lagrangians: a proof-of-principle,” *Comput. Phys. Commun.* **197** (2015) 239–262, arXiv:1406.3030 [hep-ph].
 - [156] T. Hahn, “Generating Feynman diagrams and amplitudes with FeynArts 3,” *Comput. Phys. Commun.* **140** (2001) 418–431, arXiv:hep-ph/0012260.
 - [157] J. Bellm *et al.*, “Herwig 7.0/Herwig++ 3.0 release note,” *Eur. Phys. J. C* **76** no. 4, (2016) 196, arXiv:1512.01178 [hep-ph].
 - [158] T. Gleisberg, S. Hoeche, F. Krauss, M. Schonherr, S. Schumann, F. Siegert, and J. Winter, “Event generation with SHERPA 1.1,” *JHEP* **02** (2009) 007, arXiv:0811.4622 [hep-ph].
 - [159] S. Frixione, Z. Kunszt, and A. Signer, “Three jet cross-sections to next-to-leading order,” *Nucl. Phys. B* **467** (1996) 399–442, arXiv:hep-ph/9512328.
 - [160] S. Frixione, “A General approach to jet cross-sections in QCD,” *Nucl. Phys. B* **507** (1997) 295–314, arXiv:hep-ph/9706545.

- [161] R. Frederix, S. Frixione, F. Maltoni, and T. Stelzer, “Automation of next-to-leading order computations in QCD: The FKS subtraction,” *JHEP* **10** (2009) 003, [arXiv:0908.4272 \[hep-ph\]](#).
- [162] R. Frederix, S. Frixione, A. S. Papanastasiou, S. Prestel, and P. Torrielli, “Off-shell single-top production at NLO matched to parton showers,” *JHEP* **06** (2016) 027, [arXiv:1603.01178 \[hep-ph\]](#).
- [163] G. Ossola, C. G. Papadopoulos, and R. Pittau, “Reducing full one-loop amplitudes to scalar integrals at the integrand level,” *Nucl. Phys. B* **763** (2007) 147–169, [arXiv:hep-ph/0609007](#).
- [164] P. Mastrolia, E. Mirabella, and T. Peraro, “Integrand reduction of one-loop scattering amplitudes through Laurent series expansion,” *JHEP* **06** (2012) 095, [arXiv:1203.0291 \[hep-ph\]](#). [Erratum: *JHEP* **11**, 128 (2012)].
- [165] A. I. Davydychev, “A Simple formula for reducing Feynman diagrams to scalar integrals,” *Phys. Lett. B* **263** (1991) 107–111.
- [166] A. Denner and S. Dittmaier, “Reduction schemes for one-loop tensor integrals,” *Nucl. Phys. B* **734** (2006) 62–115, [arXiv:hep-ph/0509141](#).
- [167] G. Passarino and M. J. G. Veltman, “One Loop Corrections for $e^+ e^-$ Annihilation Into $\mu^+ \mu^-$ in the Weinberg Model,” *Nucl. Phys. B* **160** (1979) 151–207.
- [168] V. Hirschi, R. Frederix, S. Frixione, M. V. Garzelli, F. Maltoni, and R. Pittau, “Automation of one-loop QCD corrections,” *JHEP* **05** (2011) 044, [arXiv:1103.0621 \[hep-ph\]](#).
- [169] G. Ossola, C. G. Papadopoulos, and R. Pittau, “CutTools: A Program implementing the OPP reduction method to compute one-loop amplitudes,” *JHEP* **03** (2008) 042, [arXiv:0711.3596 \[hep-ph\]](#).
- [170] V. Hirschi and T. Peraro, “Tensor integrand reduction via Laurent expansion,” *JHEP* **06** (2016) 060, [arXiv:1604.01363 \[hep-ph\]](#).
- [171] T. Peraro, “Ninja: Automated Integrand Reduction via Laurent Expansion for One-Loop Amplitudes,” *Comput. Phys. Commun.* **185** (2014) 2771–2797, [arXiv:1403.1229 \[hep-ph\]](#).
- [172] A. Denner, S. Dittmaier, and L. Hofer, “Collier: a fortran-based Complex One-Loop Library in Extended Regularizations,” *Comput. Phys. Commun.* **212** (2017) 220–238, [arXiv:1604.06792 \[hep-ph\]](#).
- [173] F. Cascioli, P. Maierhofer, and S. Pozzorini, “Scattering Amplitudes with Open Loops,” *Phys. Rev. Lett.* **108** (2012) 111601, [arXiv:1111.5206 \[hep-ph\]](#).
- [174] S. Frixione and B. R. Webber, “Matching NLO QCD computations and parton shower simulations,” *JHEP* **06** (2002) 029, [arXiv:hep-ph/0204244](#).

- [175] T. Sjöstrand, S. Ask, J. R. Christiansen, R. Corke, N. Desai, P. Ilten, S. Mrenna, S. Prestel, C. O. Rasmussen, and P. Z. Skands, “An introduction to PYTHIA 8.2,” *Comput. Phys. Commun.* **191** (2015) 159–177, [arXiv:1410.3012 \[hep-ph\]](#).
- [176] A. Buckley, J. Ferrando, S. Lloyd, K. Nordström, B. Page, M. Rüfenacht, M. Schönherr, and G. Watt, “LHAPDF6: parton density access in the LHC precision era,” *Eur. Phys. J. C* **75** (2015) 132, [arXiv:1412.7420 \[hep-ph\]](#).
- [177] C. Biggio, E. Fernandez-Martinez, M. Filaci, J. Hernandez-Garcia, and J. Lopez-Pavon, “Global Bounds on the Type-III Seesaw,” *JHEP* **05** (2020) 022, [arXiv:1911.11790 \[hep-ph\]](#).
- [178] G. Das, C. Dey, M. Kumar, and K. Samanta, “Threshold enhanced cross sections for colorless productions,” *Physical Review D* **107** no. 3, (Feb, 2023) .
- [179] L. G. Almeida, G. Sterman, and W. Vogelsang, “Threshold resummation for the top quark charge asymmetry,” *Physical Review D* **78** no. 1, (Jul, 2008) .
- [180] R. Bonciani, S. Catani, M. L. Mangano, and P. Nason, “NLL resummation of the heavy quark hadroproduction cross-section,” *Nucl. Phys. B* **529** (1998) 424–450, [arXiv:hep-ph/9801375](#). [Erratum: *Nucl.Phys.B* 803, 234 (2008)].
- [181] N. Kidonakis, E. Laenen, S. Moch, and R. Vogt, “Sudakov resummation and finite order expansions of heavy quark hadroproduction cross sections,” *Physical Review D* **64** no. 11, (Oct, 2001) .
- [182] B. D. Pecjak, D. J. Scott, X. Wang, and L. L. Yang, “Resummed differential cross sections for top-quark pairs at the LHC,” *Physical Review Letters* **116** no. 20, (May, 2016) .
- [183] “Measurements of top-quark pair differential cross-sections in the lepton + jets channel in pp collisions at $\sqrt{s} = 8\text{TeV}$ using the ATLAS detector,” *The European Physical Journal C* **76** no. 10, (Oct, 2016) .
- [184] R. Aoude, H. E. Faham, F. Maltoni, and E. Vryonidou, “Complete SMEFT predictions for four top quark production at hadron colliders,” *Journal of High Energy Physics* **2022** no. 10, (Oct, 2022) .
- [185] M. Sjö Dahl, “ColorMath - a package for color summed calculations in $SU(n_c)$,” *The European Physical Journal C* **73** no. 2, (Feb, 2013) .
- [186] G. P. Lepage, “A New Algorithm for Adaptive Multidimensional Integration,” *J. Comput. Phys.* **27** (1978) 192.
- [187] S. Bailey, T. Cridge, L. A. Harland-Lang, A. D. Martin, and R. S. Thorne, “Parton distributions from LHC,HERA, tevatron and fixed target data: MSHT20 PDFs,” *The European Physical Journal C* **81** no. 4, (Apr, 2021) .

- [188] S. Camarda, L. Cieri, and G. Ferrera, “Drell–yan lepton-pair production: q_t resummation at N³LL accuracy and fiducial cross sections at N³LO,” *Physical Review D* **104** no. 11, (Dec, 2021) .
- [189] G. Lusterians, A. Papaefstathiou, and W. J. Waalewijn, “How much joint resummation do we need?,” *Journal of High Energy Physics* **2019** no. 10, (Oct, 2019) .
- [190] R. Frederix, D. Pagani, and M. Zaro, “Large NLO corrections in $t\bar{t}w^\pm$ and $t\bar{t}t\bar{t}$ hadroproduction from supposedly subleading ew contributions,” *Journal of High Energy Physics* **2018** no. 2, (Feb, 2018) .
- [191] N. Bahjat-Abbas, D. Bonocore, J. S. Damsté, E. Laenen, L. Magnea, L. Vernazza, and C. D. White, “Diagrammatic resummation of leading-logarithmic threshold effects at next-to-leading power,” *Journal of High Energy Physics* **2019** no. 11, (Nov, 2019) .
- [192] N. Kidonakis and A. Tonerio, “aNNLO results for $t\bar{t}\gamma$ cross sections,” [arXiv:2305.12305 \[hep-ph\]](#) .
- [193] F. Demartin, F. Maltoni, K. Mawatari, and M. Zaro, “Higgs production in association with a single top quark at the lhc,” [arXiv:1504.00611 \[hep-ph\]](#) .
- [194] M. Bovini, “Resummation of soft and hard gluon radiation in perturbative QCD,” [arXiv:1212.0480](#) .
- [195] S. Catani, S. Dittmaier, M. H. Seymour, and Z. Trócsányi, “The dipole formalism for next-to-leading order qcd calculations with massive partons,” *Nuclear Physics B* **627** no. 1-2, (Apr, 2002) 189–265.
- [196] W. Beenakker, S. Brensing, M. Krämer, A. Kulesza, E. Laenen, and I. Niessen, “NNLL resummation for squark-antisquark pair production at the LHC,” *Journal of High Energy Physics* **2012** no. 1, (Jan, 2012) .
- [197] A. H. Ajjath, A. Chakraborty, G. Das, P. Mukherjee, and V. Ravindran, “Resummed prediction for Higgs boson production through $b\bar{b}$ annihilation at N³LL,” *JHEP* **11** (2019) 006, [arXiv:1905.03771 \[hep-ph\]](#) .
- [198] L.-B. Chen, H. T. Li, H.-S. Shao, and J. Wang, “The gluon-fusion production of higgs boson pair: N³LO QCD corrections and top-quark mass effects,” *Journal of High Energy Physics* **2020** no. 3, (Mar, 2020) .
- [199] J. R. Gaunt, M. Stahlhofen, and F. J. Tackmann, “The quark beam function at two loops,” *Journal of High Energy Physics* **2014** no. 4, (Apr, 2014) .
- [200] A. H. Ajjath, G. Das, M. C. Kumar, P. Mukherjee, V. Ravindran, and K. Samanta, “Resummed drell-yan cross-section at N³LL,” *JHEP* **10** (2020) 153, [arXiv:2001.11377 \[hep-ph\]](#) .

- [201] S. Catani and M. Grazzini, “Collinear factorization and splitting functions for next-to-next-to-leading order QCD calculations,” *Physics Letters B* **446** no. 2, (Jan, 1999) 143–152.
- [202] R. Bonciani, S. Catani, M. L. Mangano, and P. Nason, “Nll resummation of the heavy-quark hadroproduction cross-section,” *Nuclear Physics B* **529** no. 1, (1998) 424–450.
- [203] J. Campbell, J. Huston, and F. Krauss, *The Black Book of Quantum Chromodynamics : a Primer for the LHC Era*. Oxford University Press, 2018.
- [204] T. Muta, *Foundations of Quantum Chromodynamics: An Introduction to Perturbative Methods in Gauge Theories, (3rd ed.)*, vol. 78 of *World scientific Lecture Notes in Physics*. World Scientific, Hackensack, N.J., 3rd ed., 2010.
- [205] R. K. Ellis and G. Zanderighi, “Scalar one-loop integrals for QCD,” *Journal of High Energy Physics* **2008** no. 02, (Feb, 2008) 002–002.
- [206] P. Skands, “Introduction to QCD,” in *Searching for New Physics at Small and Large Scales*. WORLD SCIENTIFIC, Sep, 2013.
- [207] M. L. Mangano, “Introduction to QCD,” CERN. 1999.
- [208] **LHCb** Collaboration, R. Aaij *et al.*, “Measurement of the ratio of branching fractions $\mathcal{B}(\bar{B}^0 \rightarrow D^{*+}\tau^-\bar{\nu}_\tau)/\mathcal{B}(\bar{B}^0 \rightarrow D^{*+}\mu^-\bar{\nu}_\mu)$,” *Phys. Rev. Lett.* **115** no. 11, (2015) 111803, [arXiv:1506.08614 \[hep-ex\]](#). [Erratum: *Phys.Rev.Lett.* 115, 159901 (2015)].
- [209] G. Altarelli, R. Ellis, and G. Martinelli, “Large Perturbative Corrections to the Drell-Yan Process in QCD,” *Nucl. Phys. B* **157** (1979) 461–497.
- [210] C. Uhlemann and N. Kauer, “Narrow-width approximation accuracy,” *Nuclear Physics B* **814** no. 1-2, (Jun, 2009) 195–211.
- [211] A. Kulesza, G. Sterman, and W. Vogelsang, “Joint resummation in electroweak boson production,” *Physical Review D* **66** no. 1, (Jul, 2002) .
- [212] J. J. Liu, C. S. Li, L. L. Yang, and L. G. Jin, “Next-to-leading order QCD corrections to the direct top quark production via model-independent FCNC couplings at hadron colliders,” *Physical Review D* **72** no. 7, (Oct, 2005) .
- [213] J. Muse, *Search for third generation vector-like leptons with the ATLAS detector*. Phd thesis, Oklahoma U., 2022.
- [214] **OPAL** Collaboration, G. Abbiendi *et al.*, “Search for unstable heavy and excited leptons at LEP 2,” *Eur. Phys. J. C* **14** (2000) 73–84, [arXiv:hep-ex/0001056](#).

Resommation en QCD à l'aune du Run 3 du LHC

Résumé : Les prédictions qui découlent du Modèle Standard de la physique des particules permettent de confronter la théorie aux expériences, notamment dans le cadre de la physique au LHC. C'est à la fois crucial dans le contexte des mesures de précision, pour détecter d'éventuels écarts au modèle standard, que pour des recherches directes de nouvelles particules. Les progrès rapides des mesures expérimentales, notamment avec le Run 3 du LHC, appellent à l'amélioration des prédictions théoriques de processus plus rares et complexes. Pour atteindre ce but, augmenter le nombre d'ordres perturbatifs pris en compte dans les calculs n'est pas la seule solution. Les techniques comme la resommation de seuil de gluons mous permettent de prendre en compte des termes à tous les ordres par exponentiation. Cela a pour conséquence de réduire les erreurs théoriques et améliorer la pertinence des résultats. Lors de cette thèse, nous nous sommes intéressés à l'application de la resommation à des processus comprenant des corrections de QCD à l'ordre sous dominant, d'une part dans le cadre de productions de leptons exotiques, et d'autre part pour la physique du quark top.

Mots clés : QFT, QCD, Resommation, NLO, Précision, Modèle Standard et au-delà.

QCD resummation in the light of the LHC run 3

Abstract: The predictions derived from the Standard Model of particle physics allow to compare theory with experimental measurements. As the LHC is currently running its third data taking campaign, it is of particular interest in the context of LHC physics. This comparison is crucial both in the context of precision measurements, to detect possible deviations from the Standard Model, and for direct searches for new particles. The recent progress in experimental measurements, particularly with Run 3 of the LHC, calls for improvements in theoretical predictions related to rarer and more complex processes. To achieve this goal, increasing the number of perturbative orders taken into account in the calculations is not the only solution. Techniques such as soft gluon threshold resummation allow terms at all orders to be taken into account by exponentiation. This typically reduces the theoretical error bars and improves the accuracy of the results. In this thesis, we focused on the application of resummation to processes involving QCD corrections at the subdominant order, firstly in the context of exotic lepton production, and secondly in quark top physics.

Keywords: QFT, QCD, Resummation, NLO, Precision, BSM, four-top.

Sorbonne Université, LPTHE, UMR 7589, Paris, France